

AD-A248 903

SC71002.FR

SC71002.FR

Copy No. 4

## TRANSFORMATION TOUGHENING OF CERAMICS

FINAL REPORT FOR THE PERIOD  
January 15, 1989 through January 14, 1992

CONTRACT NO. F49620-89-C-0031

Prepared for:

Air Force Office of Scientific Research  
Directorate of Electronic and Material Sciences  
Building 410  
Bolling AFB, DC 20332-6448

DTIC  
ELECTE  
APR 16 1992

D. B. Marshall  
Principal Investigator

MARCH 1992

Approved for public release; distribution unlimited.

92-09737



Rockwell International  
Science Center

# REPORT DOCUMENTATION PAGE

Form Approved  
OMB No. 0704-0188

Public reporting burden for this collection of information is estimated to average 1 hour per response, including the time for reviewing instructions, searching existing data sources, gathering and maintaining the data needed, and completing and reviewing the collection of information. Send comments regarding this burden estimate or any other aspect of this collection of information, including suggestions for reducing this burden, to Washington Headquarters Services, Directorate for Information Operations and Reports, 1215 Jefferson Davis Highway, Suite 1204, Arlington, VA 22202-4302, and to the Office of Management and Budget, Paperwork Reduction Project (0704-0188), Washington, DC 20503.

1. AGENCY USE ONLY (Leave blank)	2. REPORT DATE	3. REPORT TYPE AND DATES COVERED
	MARCH 1992	FINAL REPORT - 1/15/89 - 1/14/92
4. TITLE AND SUBTITLE		5. FUNDING NUMBERS
TRANSFORMATION TOUGHENING OF CERAMICS		
6. AUTHOR(S) D.B. MARSHALL		F49620-89-C-0031
7. PERFORMING ORGANIZATION NAME(S) AND ADDRESS(ES) ROCKWELL INTERNATIONAL Science Center 1049 Camino Dos Rios Thousand Oaks, CA 91360		8. PERFORMING ORGANIZATION REPORT NUMBER SC71002.FR
9. SPONSORING/MONITORING AGENCY NAME(S) AND ADDRESS(ES) Air Force Office of Scientific Research Boiling Air Force Base Washington, D.C. 20332 Attn: Lt. Col. Larry Burggraf		10. SPONSORING/MONITORING AGENCY REPORT NUMBER 61025 2306/A2
11. SUPPLEMENTARY NOTES Unlimited		
12a. DISTRIBUTION / AVAILABILITY STATEMENT  Approved for public release; distribution unlimited.		12b. DISTRIBUTION CODE
13. ABSTRACT (Maximum 200 words)  The results of a three-year study, aimed at developing a fundamental understanding of transformation toughening in ceramics and using that understanding to design and fabricate new microstructures with improved properties, are described. A new class of materials with dual scale (laminar) microstructures and greatly enhanced fracture toughness have been developed and tested; increases in fracture toughness from 5 to 18 MPAm <sup>1/2</sup> were measured. These new microstructures were designed by combining micromechanics modeling of the effects of zone shape on toughness with direct measurements of transformation zone characteristics (which provided critical testing of the theoretical modeling) and measurements of transformation thermodynamics. To fabricate these microstructures a new colloidal processing method, which allowed construction of multilayered structures with layer thicknesses as small as 10µm, was developed. The direct transformation zone measurements included Raman microprobe spectroscopy to measure the distribution of transformed phases within the zones, and moiré interferometry and high resolution strain mapping (by digital image correlation) to measure directly the transformation strains that are responsible for toughening. Calculations of crack tip shielding indicated modifications to transformation zone shapes that would increase the toughening.		
14. SUBJECT TERMS Ceramics, Zirconia, Toughening, Laminar Composites, Mechanical Properties, R-Curve Behavior, Fracture Mechanics, Transformation, Fatigue		15. NUMBER OF PAGES
		16. PRICE CODE
17. SECURITY CLASSIFICATION OF REPORT UNCLASSIFIED	18. SECURITY CLASSIFICATION OF THIS PAGE UNCLASSIFIED	19. SECURITY CLASSIFICATION OF ABSTRACT UNCLASSIFIED
		20. LIMITATION OF ABSTRACT UNLIMITED



## TABLE OF CONTENTS

	<u>Page</u>
1.0 INTRODUCTION.....	1
2.0 PUBLICATIONS, PERSONNEL AND TECHNICAL PRESENTATIONS .....	4
2.1 Publications.....	4
2.2 Patent Applications .....	5
2.3 Personnel .....	6
2.4 Technical Presentations .....	6
2.5 Awards.....	7
3.0 NEW MICROSTRUCTURES.....	8
3.1 Enhanced Fracture Toughness in Layered Microcomposites of Ce-ZrO <sub>2</sub> and Al <sub>2</sub> O <sub>3</sub> .....	9
3.2 The Design of High Toughness Laminar Zirconia Composites .....	10
3.3 Crack Resistance Curves in Layered Zirconia Ceramics .....	11
4.0 ANALYSIS OF CRACK SHIELDING AND ZONE SHAPE EFFECTS .....	12
4.1 Transformation Zone Shape Effects in Crack Shielding in Ceria-Partially Stabilized Zirconia (Ce-TZP)-Alumina Composites.....	13
4.2 Crack Shielding in Ceria-Partially Stabilized Zirconia.....	14
5.0 DIRECT MEASUREMENTS OF TRANSFORMATION ZONE CHARACTERISTICS .....	15
5.1 Direct Measurement of Transformation Zone Strains in Toughened Zirconia .....	16
5.2 Crack-Tip Transformation Zones in Toughened Zirconia.....	17
5.3 Cyclic Fatigue-Crack Propagation in Mg-PSZ Ceramics .....	18
6.0 TRANSFORMATION THERMODYNAMICS AND REVERSIBILITY .....	19
6.1 Recovery of Crack-Tip Transformation Zones in Zirconia After High Temperature Annealing.....	20
6.2 On the Thermoelastic Martensitic Transformation in Tetragonal ZrO <sub>2</sub> ....	21
6.3 Reversible Transformation and Elastic Anisotropy in Mg-ZrO <sub>2</sub> .....	22
6.4 Structural and Mechanical Property Changes in Toughened Magnesia-Partially-Stabilized Zirconia at Low Temperatures .....	23



## 1.0 INTRODUCTION

The goal of this research is to develop a basic scientific understanding of factors that dictate the mechanical properties of transformation toughened ceramics and to use that understanding to design and fabricate microstructures with improved properties. Our approach is to develop and use new methods, such as Raman spectroscopy and high resolution strain measurement techniques, to measure transformation characteristics directly within zones surrounding crack tips, and hence, in combination with mechanics modeling to deduce the toughening mechanisms and relationships between microstructural characteristics and macroscopic properties. With the guidance and insight gained from such experiments, new microstructures are being designed to optimize the desirable properties. Detailed results of the research are contained in papers that are included in Sections 3 to 6 of this report, and which have been published in or submitted to the journals noted on the cover pages. The results are briefly summarized below.

The fabrication and properties of new zirconia microstructures with greatly enhanced fracture toughness are described in Section 3. These new materials have dual scale microstructures containing barriers to transformation with a spatial scale ~ 100 times the grain size. Most work was done with laminar microstructures, although there is evidence that fibers and platelets will yield similar toughening effects. The microstructures were designed on the basis of micromechanics analysis of the effects of zone shape on toughening (Section 4), as well as direct measurements of crack tip transformation zone characteristics, which provided critical testing of the validity of toughening analyses (Section 5). A new colloidal-centrifugal consolidation method was developed in collaboration with Prof. F.F. Lange (U.C. Santa Barbara) to fabricate multilayered microstructures with layers as small as 10  $\mu\text{m}$ . The layered composites exhibited toughening effects that were much larger than expected; in addition to modifying the zone shape by preventing a detrimental autocatalytic transformation ahead of the crack as anticipated, there was a strong interaction of the transformation zone with the layers which caused the zone to spread normal to the crack plane (which is beneficial to toughening). Fracture toughnesses as high as 18  $\text{MPa}\cdot\text{m}^{1/2}$  were measured from direct *in situ* crack growth experiments in these laminar materials.

Analyses of the effects of the shape of crack tip transformation zones on the degree of toughening and comparisons of the analysis with measured R-curves in  $\text{Ce-ZrO}_2$  materials are given in Sections 4.1 and 4.2. High fracture toughnesses (in the range of 12-14  $\text{MPa}\cdot\text{m}^{1/2}$ ) have



been observed in Ce-ZrO<sub>2</sub> materials, in which the transformation zone extends ahead of the crack a distance  $\sim$  10 to 20 times the zone width (this shape contrasts with that of other ZrO<sub>2</sub> ceramics where the zone extends approximately equal distances ahead and to the side of the crack). Two important conclusions were drawn from the results: (1) the calculated stress intensity factors confirmed that the measured fracture toughness in Ce-TZP is consistent with the toughening being due to crack shielding from the observed transformation zones - this contrasts with speculation in the literature that crack tip shielding is not responsible for the toughening, but instead, a Dugdale zone mechanism operates; (2) given that transformation shielding is responsible for the observed toughening, the calculations show that if the microstructure could be modified to eliminate the elongation of the zone ahead of the crack, the toughness could be increased by a factor of approximately 2. These results provided the motivation to develop the layered microstructures to eliminate the elongated frontal zone.

More direct measurements of crack tip transformation zone characteristics and transformation thermodynamics are described in Sections 5 and 6. Detailed measurements have been made of the distributions of monoclinic phase within transformation zones in several Mg-PSZ materials of various peak toughesses using Raman spectroscopy (Section 5.2). The results allowed direct calculation of the crack tip shielding stress intensity factor, and thus comparison of transformation toughening theory with experimentally measured toughness (for steady state crack growth). The following zone characteristics were observed: (1) the volume fraction of stress-induced transformation was not uniform within the zone, (2) the transformation zone contours ahead of the crack were closer to semicircular in shape than they were to the contours of constant hydrostatic stress in the elastic crack tip field, (3) transformation of all the tetragonal phase was never observed adjacent to cracks (contrary to TEM observations of thin foils), and (4) the zone size increased during initial crack growth, correlating with the measured crack resistance curve. The calculated reductions in crack tip stress intensity factor due to transformation zone shielding, assuming that only the dilatational component of the transformation strains remained (i.e., that the long range shear component was relieved by twinning), accounted for a large fraction of the measured toughness increases, although there was a significant component ( $\sim 4 \text{ MPa}\cdot\text{m}^{1/2}$ ) which was not accounted for. This implies that either there is a significant component of transformation shear strain that is not relieved by twinning, or other toughening mechanisms operate.

The residual strains responsible for crack tip shielding have been measured directly within the transformation zones surrounding cracks in Mg-PSZ using two techniques (Section 5.1):



Moiré interferometry and high resolution strain mapping by digital image correlation. Both methods provide maps of differential in-plane displacements within the specimen surface that is intersected by the crack, the latter method with the higher resolution (by about an order of magnitude). The results were compared with finite element analysis to assess surface relaxation effects, and the measured strains were used to evaluate the crack tip stress intensity factor. The calculated shielding, assuming that the net transformation strain was only the hydrostatic component, was consistent with the equivalent calculation using Raman measurements. However, both were smaller than the observed toughening. An approach for determining the shielding contribution due to nonhydrostatic strain components, using in-plane and out-of-plane residual strain measurements with finite element modeling, was outlined.

Crack growth induced by cyclic tensile loading in a series of Mg-PSZ materials with systematically varied microstructures was demonstrated in a collaborative study with U.C. Berkeley (Section 5.3). Several crack growth effects were shown to result directly from the existence of a transformation zone that shields the crack tip from the applied loading: crack closure effects, which reduce the effective tip stress intensity range, transient acceleration or retardation following sudden changes in cyclic load amplitude, and retardation following single tensile overloads. However, the fatigue mechanism was shown not to involve degradation of the transformation toughening: Raman microprobe measurements of the transformation zones developed during crack growth under constant cyclic load were used to show that the shielding of the crack tips was not reduced by the cyclic nature of the load. This implies that an intrinsic mechanism is responsible for the observed fatigue crack growth. This result is important because it means that the beneficial effect of transformation toughening is not lost in fatigue loading. The resistance to cyclic fatigue (including the threshold for fatigue crack growth) was found to increase in proportion to the monotonic fracture toughness.



## 2.0 PUBLICATIONS, PERSONNEL AND TECHNICAL PRESENTATIONS

### 2.1 Publications

#### (a) Publications in press or in preparation from work done in 1989-1991:

1. "Enhanced Fracture Toughness in Layered Microcomposites of Ce-ZrO<sub>2</sub> and Al<sub>2</sub>O<sub>3</sub>," by D.B. Marshall, J.R. Ratto and F.F. Lange, *J. Am. Ceram. Soc.* 74[12], 2974-87 (1991).
2. "The Design of High Toughness Laminar Zirconia Composites," by D.B. Marshall, *Bull. Am. Ceram. Soc.*, in press.
3. "Crack Resistance Curves in Layered Zirconia Ceramics," by D.B. Marshall and J.R. Ratto, to be submitted to *J. Am. Ceram. Soc.*
4. "Transformation Zone Shape Effects on Crack Shielding in Ceria-Partially-Stabilized Zirconia (Ce-TZP)-Alumina Composites," by C-S. Yu, D.K. Shetty, M.C. Shaw and D.B. Marshall, submitted to *J. Amer. Ceram. Soc.*
5. "Recovery of Crack-tip Transformation Zones in Zirconia after High Temperature Annealing," by M.C. Shaw, D.B. Marshall, A.H. Heuer and E. Inghels, *J. Am. Ceram. Soc.* 75[2], 474-76 (1992).
6. "Direct Measurement of Transformation Zone Strains in Toughened Zirconia," by M.S. Dadkhah, D.B. Marshall, W.L. Morris and B.N. Cox, *J. Am. Ceram. Soc.* 74[3], 584-92 (1991).
7. "Resistance Curve Simulations in Transformation Toughened Materials," by C.L. Hom, R.M. McMeeking, A.G. Evans and D.B. Marshall, in preparation for *J. Am. Ceram. Soc.*
8. "Crack Shielding in Ceria-Partially Stabilized Zirconia," by D.B. Marshall, *J. Am. Ceram. Soc.* 73(10), 3119-21 (1990).



9. "Crack Tip Transformation Zones in Toughened Zirconia," by D.B. Marshall, M.C. Shaw, R.H. Dauskardt, R.O. Ritchie, M. Readey and A.H. Heuer, *J. Am. Ceram. Soc.* 73(9), 2659-66 (1990).
10. "Cyclic Fatigue Crack Propagation in Mg-PSZ Ceramics," by R.H. Dauskardt, D.B. Marshall and R.O. Ritchie, *J. Am. Ceram. Soc.* 73(4), 893-903 (1990).
11. "On the Thermoelastic Martensitic Transformation in Tetragonal ZrO<sub>2</sub>" by A.H. Heuer, M. Ruhle and D.B. Marshall, *J. Am. Ceram. Soc.* 73[4] 1084-93 (1990).

(b) Published in 1989 from previous year's work on AFOSR contract:

12. "Reversible Transformation and Elastic Anisotropy in Mg-PSZ," by D.B. Marshall and M.V. Swain, *J. Am. Ceram. Soc.* 72[8], 1530-32 (1989).
13. "Cyclic Fatigue-Crack Propagation in Ceramics: Behaviour in Overaged and Partially Stabilized MgO-ZrO<sub>2</sub>," by R.H. Dauskardt, D.B. Marshall and R.O. Ritchie, *Mat. Res. Soc. Proc. on Fracture Mechanics of Structural Ceramics*, 1989.
14. "Structural and Mechanical Property Changes in Toughened Mg-PSZ at Low Temperatures," by D.B. Marshall, M.R. James and J.R. Porter, *J. Am. Ceram. Soc.* 72[2], 218-27 (1989).

## 2.2 Patent Applications

"Laminar Ceramic Composites" by D.B. Marshall, F.F. Lange and J.J. Ratto, submitted to U.S. Patent Office September 1991.



### 2.3 Personnel

The principal investigator is Dr. D.B. Marshall. Other contributors from the Rockwell Science Center were Dr. M. Dadkhah, Dr. W.L. Morris, Dr. B.N. Cox, Mr. M. Shaw (also a part time graduate student at U.C. Santa Barbara), Mr. E. Wright and Mr. J. Ratto. The program has also benefitted from several informal collaborations with universities: Prof. F.F. Lange from U.C. Santa Barbara on colloidal processing of laminar composites, Profs. R. McMeeking and A.G. Evans and graduate student C.L. Hom, from U.C. Santa Barbara on modeling R-curve behavior; Dr. R.H. Dauskardt and Prof. R.O. Ritchie from U.C. Berkeley on fatigue crack growth; Prof. A.H. Heuer and Dr. M. Readey from Case Western Reserve University on thermodynamics and reversibility of transformations; and C-S. Yu and Prof. D.K. Shetty of University of Utah on analysis of zone shape effects on toughening.

### 2.4 Technical Presentations

Fulrath Award Symposium, "Design of New High Toughness Laminar Zirconia Composites," at Am. Ceram. Soc. Pacific Coast Meeting, San Diego, Oct. 1991.

AeroMat '91, Invited Lecture "Laminar Composites," Long Beach, May 1991.

Albrecht-Rabenau Symposium on Ceramic Science, Max-Plank-Institute (Tegernsee), June 1990 invited lecture, "Modeling of Mechanical Properties."

American Ceramic Society Annual Meeting, Dallas, April 1990, invited lecture, "Transformation Zones in  $ZrO_2$ ."

4th International Conference on Science and Technology of Zirconia, Anaheim, Nov. 1989, Invited keynote speaker: "Crack Tip Zones in Transformation Toughened Ceramics."

3rd Int. Conf. on Fundamentals of Fracture, Irsee, Germany, June 1989, Invited speaker: "Crack Tip Zones in Transformation Toughened Ceramics."



Rockwell International  
Science Center

SC71002.FR

American Ceramic Society Annual Meeting, Indianapolis, April 1989, "Characterization of Transformation Zones in Toughened Zirconia."

13th Annual Conf. on Composites and Advanced Ceramics, Cocoa Beach, Jan. 1989,  
"Cyclic Fatigue Crack Propagation in Advanced Ceramics."

## 2.5 Awards

American Ceramic Society Fulrath Award 1991 to D.B. Marshall.



Rockwell International  
Science Center

SC71002.FR

### 3.0 NEW MICROSTRUCTURES



**Rockwell International**  
**Science Center**

SC71002.FR

**3.1 ENHANCED FRACTURE TOUGHNESS IN LAYERED  
MICROCOMPOSITES OF Ce-ZrO<sub>2</sub> AND Al<sub>2</sub>O<sub>3</sub>**

published in J. Am. Ceram. Soc.

# Enhanced Fracture Toughness in Layered Microcomposites of Ce-ZrO<sub>2</sub> and Al<sub>2</sub>O<sub>3</sub>

David B. Marshall\* and Joseph J. Ratto

Rockwell International Science Center, Thousand Oaks, California 91360

Fred F. Lange\*

Materials Department, University of California, Santa Barbara, California 93106

Laminar composites, containing layers of Ce-ZrO<sub>2</sub> and either Al<sub>2</sub>O<sub>3</sub> or a mixture of Al<sub>2</sub>O<sub>3</sub> and Ce-ZrO<sub>2</sub>, have been fabricated using a colloidal method that allowed formation of layers with thicknesses as small as 10  $\mu\text{m}$ . Strong interactions between these layers and the martensitic transformation zones surrounding cracks and indentations have been observed. In both cases, the transformation zones spread along the region adjacent to the layer, resulting in an increased fracture toughness. The enhanced fracture toughness was observed for cracks growing parallel to the layers as well as for those that were oriented normal to the layers. [Key words: laminates, fracture toughness, cerium, zirconia, alumina.]

## I. Introduction

HIGH fracture toughnesses, in the range 10 to 14  $\text{MPa} \cdot \text{m}^{1/2}$ , have been achieved recently in ceria-partially-stabilized zirconia (Ce-TZP) that undergoes martensitic transformation from tetragonal to monoclinic phase.<sup>1-8</sup> However, the shapes of the transformation zones surrounding cracks in these materials are not optimal for producing large transformation toughening.<sup>9</sup> Whereas in other zirconia ceramics of comparable toughness (magnesia-partially-stabilized zirconia, Mg-PSZ) the transformation zone extends approximately equal distances ahead and to the side of a crack,<sup>10</sup> the zone in Ce-TZP is very elongated, extending ahead of the crack a distance of 10 to 20 times the zone width.<sup>1-4</sup> The extra transformed material ahead of the crack degrades the toughness; calculation of the crack tip shielding from zones with such shapes indicates that the increase in fracture toughness due to transformation shielding is about a factor of 2 smaller for an elongated frontal zone typical of Ce-TZP than for a semi-circular frontal zone shape characteristic of Mg-PSZ.<sup>9</sup> Therefore, substantial benefit should result if the microstructure of Ce-TZP could be modified to change the shape of the transformation zone.

The elongated frontal zone in Ce-TZP is thought to result from autocatalytic transformation, i.e., the sequential triggering of transformation in a grain by transformation strains in adjacent grains.<sup>5</sup> Autocatalytic transformation also occurs in Mg-PSZ, as evidenced by the formation of well-defined shear bands within grains.<sup>11</sup> The microstructure of Mg-PSZ may be

thought of as dual scale; the individual precipitates that transform from tetragonal to monoclinic phase are lenticular in shape ( $\sim 300$  nm in diameter) and are contained within grains that are larger by about 2 orders of magnitude ( $\sim 50$   $\mu\text{m}$  in diameter).<sup>12</sup> Although each transformation band contains many autocatalytically transformed precipitates, the grain boundaries are effective as barriers, which arrest the propagating band. In Ce-TZP, there is no such large-scale barrier to arrest a developing transformation band; in this case, the transforming units are the individual grains and there is no larger-scale microstructural unit.

In this paper, we describe an approach for introducing a large-scale microstructural unit into Ce-TZP, in the form of layers of either Al<sub>2</sub>O<sub>3</sub> or a mixture of Al<sub>2</sub>O<sub>3</sub> and Ce-TZP. Based on the above discussion, the optimum separation of the layers would be expected to be a factor of ~10 to 100 times the grain size (which is  $\sim 2$   $\mu\text{m}$ ), with individual layer thicknesses being at the lower end of the range. Layered structures satisfying this requirement have been fabricated using a colloidal method to consolidate powders. This approach has allowed formation of layers as thin as  $\sim 10$   $\mu\text{m}$ . Controlled crack growth experiments and indentation experiments are used to investigate the influence of these barrier layers on crack tip transformation zones and fracture toughness. The presence of the barrier layers leads to large increases in toughness and extensive *R*-curve behavior.

## II. Composite Fabrication

Composites of Ce-TZP with layers of either Al<sub>2</sub>O<sub>3</sub> or a mixture of 50% by volume of Al<sub>2</sub>O<sub>3</sub> and Ce-ZrO<sub>2</sub> were fabricated using a colloidal technique. The technique involved sequential centrifuging of solutions containing suspended particles to form the layered green body, followed by drying and sintering at 1600°C for 3 h. Use was made of a technique described recently by Velamakanni *et al.*,<sup>13</sup> and Chang *et al.*,<sup>14</sup> in which an aqueous electrolyte ( $\text{NH}_4\text{NO}_3$ ) was used to produce short-range repulsive hydration forces and to reduce the magnitudes of the longer-range electrostatic forces between the suspended particles. Such conditions produce a weakly attractive network of particles which prevents mass segregation during centrifugation, but, because of the lubricating action of the short-range repulsive forces, allows the particles to pack to high green density.

The relative green densities of the Al<sub>2</sub>O<sub>3</sub> and Ce-ZrO<sub>2</sub> powders (Al<sub>2</sub>O<sub>3</sub> powder from Sumitomo, Type AKP-30; Ce-ZrO<sub>2</sub> powder from Tosoh, Tokyo, grade TZ-12Ce) consolidated separately in this manner were approximately 60 and 50 vol%, respectively. The larger shrinkage of the Ce-ZrO<sub>2</sub> during subsequent sintering caused cracking in some layered composites that contained pure Al<sub>2</sub>O<sub>3</sub> layers (the exceptions being some thin layers,  $<30$   $\mu\text{m}$  thick). This mismatch was minimized by using the mixed composition of 50 vol% Al<sub>2</sub>O<sub>3</sub> and Ce-ZrO<sub>2</sub> instead of pure Al<sub>2</sub>O<sub>3</sub> for most specimens.

I-W. Chen—contributing editor

Manuscript No. 196697. Received May 20, 1991; approved September 26, 1991.

Supported by the U.S. Air Force Office of Scientific Research under Contract No. F49620-89-C-0031. The colloidal science research on short-range repulsive potentials that led to the method for forming the layered structure was supported at the University of California, Santa Barbara, by the Office of Naval Research under Contract No. N00014-90-J-1141.

\*Member, American Ceramic Society.



Fig. 1. Optical micrographs showing isolated layers of  $\text{Al}_2\text{O}_3/\text{Ce-ZrO}_2$  (darker regions) with thicknesses of approximately 10, 35, and 70  $\mu\text{m}$  in a matrix of Ce-TZP.

Optical micrographs of typical layers of  $\text{Al}_2\text{O}_3/\text{Ce-ZrO}_2$  within a matrix of Ce-TZP are shown in Fig. 1. Reasonably uniform layers with thicknesses in the range 10 to 100  $\mu\text{m}$  were readily formed. A multilayered structure of alternating Ce-TZP and  $\text{Al}_2\text{O}_3/\text{Ce-ZrO}_2$  layers of thickness 35  $\mu\text{m}$  is shown in Fig. 7.

### III. Mechanical Properties

#### (1) The Role of Isolated Layers

The influence of individual layers of  $\text{Al}_2\text{O}_3$  or 50%  $\text{Al}_2\text{O}_3/\text{Ce-ZrO}_2$  on crack growth and transformation zones in

Ce-TZP was investigated by fabricating composites containing widely spaced layers. Measurements were obtained from controlled crack growth in notched beams, fracture of smooth bars, and indentation experiments using a Vickers indenter.

Crack growth experiments with notched beams were done in two steps, using two different loading fixtures, which operated on the stage of an optical microscope and allowed high-magnification observation of the side of the beam during loading. All experiments were done in a dry nitrogen atmosphere. The dimensions of the beams were approximately 28 mm  $\times$  6 mm  $\times$  1 mm, with the initial notch of 170- $\mu\text{m}$  width and approximately 2-mm depth. First, a stable crack was initiated from the root of the notch under monotonic loading, using the fixture illustrated in Fig. 2(a). The WC/Co flexure beams in series with the test specimen make the loading system extremely stiff and thereby allow stable crack growth. The beams are equivalent to very stiff springs in parallel with the specimen and thus act as a crack arrester, as described for different geometrical arrangements by Mai and Atkins<sup>15</sup> and Sakai and Inagaki.<sup>16</sup> This initial crack growth was induced without use of a load cell, in order to stiffen the loading system further. After thus growing the crack for  $\sim 500 \mu\text{m}$ , the loading system was changed to include a load cell with conventional four-point loading through rollers (Fig. 2(b)) in order to allow measurement of the fracture toughness (or crack growth resistance). The stress intensity factor was evaluated from the measured loads and crack lengths (obtained from optical micrographs) using the expression from Ref. 17.

Results that were obtained from a specimen containing three layers of  $\text{Al}_2\text{O}_3-\text{Ce-ZrO}_2$  widely spaced ahead of the notch are shown in Fig. 3. After initiating stably in the immediate vicinity of the notch, the crack grew unstably when the loading system was changed to include the load cell, and arrested approximately 20  $\mu\text{m}$  before the first layer of  $\text{Al}_2\text{O}_3/\text{ZrO}_2$  (which had a thickness of  $\sim 35 \mu\text{m}$ ). The width of the transformation zone over the wake of the crack, as determined by Nomarski interference, was approximately 15  $\mu\text{m}$ . However, near the tip of the arrested crack, the transformation zone extended adjacent to the  $\text{Al}_2\text{O}_3/\text{ZrO}_2$  layer for distances of more than 150  $\mu\text{m}$  each side of the crack, as shown schematically in Fig. 3(b). Some transformation also occurred on the opposite side of the  $\text{Al}_2\text{O}_3/\text{ZrO}_2$  layer, also for a distance of 150  $\mu\text{m}$  both sides of the crack plane.

After further loading, the crack grew unstably through the  $\text{Al}_2\text{O}_3/\text{ZrO}_2$  layer, into the Ce-TZP on the opposite side, and arrested again  $\sim 40 \mu\text{m}$  before the second layer (which had a thickness of 70  $\mu\text{m}$ ). The shape of the transformation zone

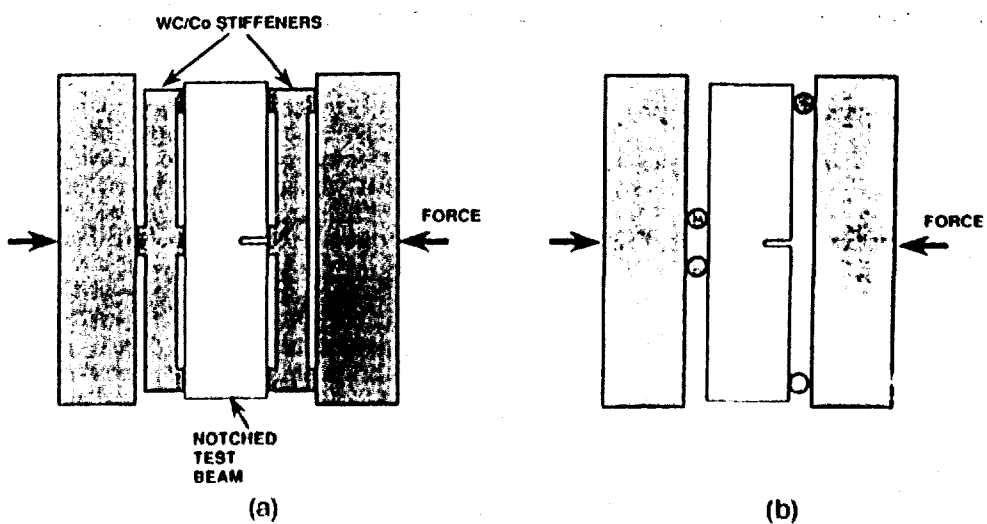


Fig. 2. Loading fixtures for notched beam fracture testing: (a) high-stiffness system used for crack initiation; (b) conventional system used for stress intensity factor measurements.

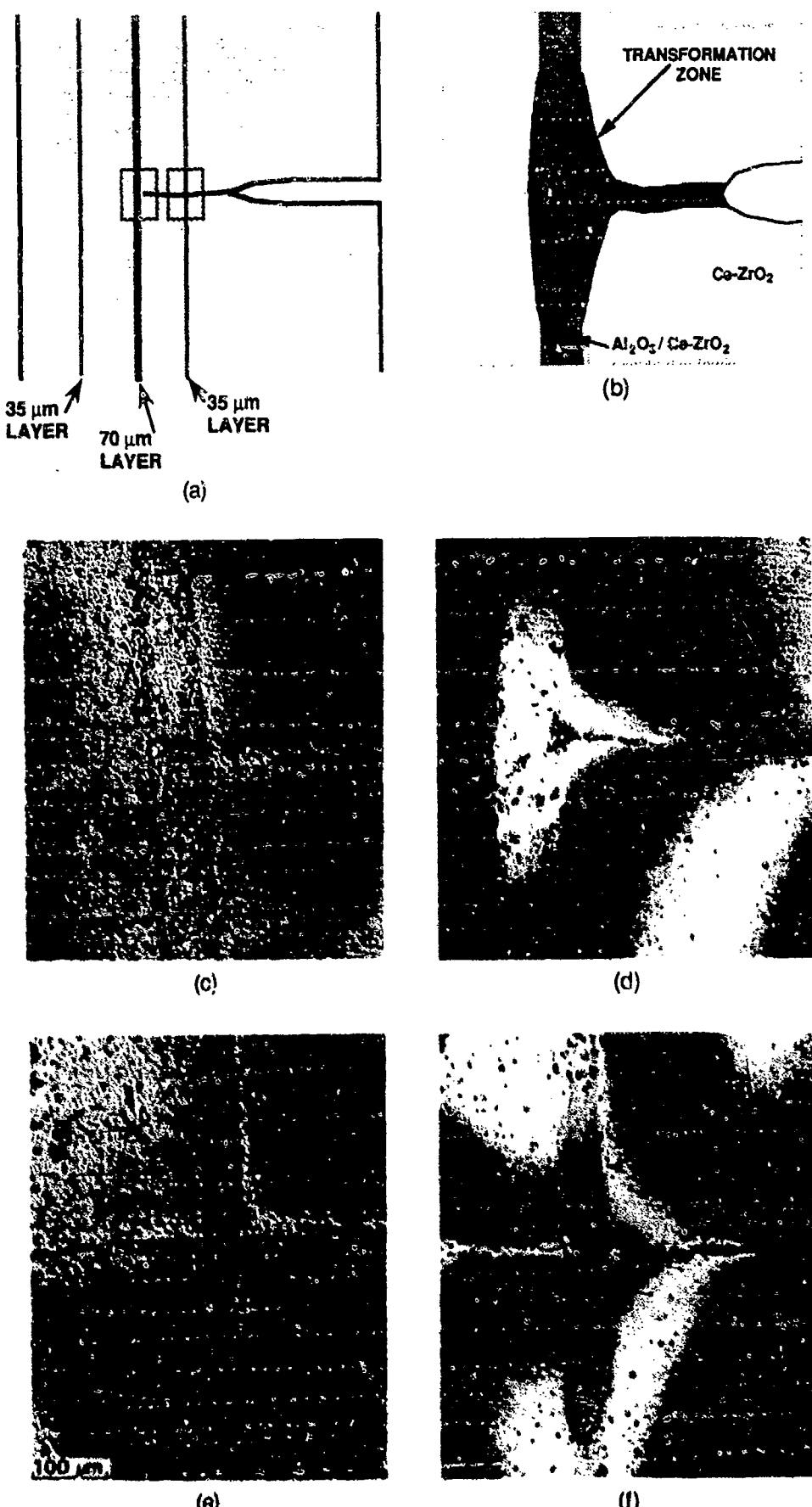


Fig. 3. Schematic of notched beam of Ce-TZP containing three layers of  $\text{Al}_2\text{O}_3/\text{Ce-ZrO}_2$ . (b) Schematic diagram of arrested crack near  $\text{Al}_2\text{O}_3/\text{Ce-ZrO}_2$  layer, showing shape of enlarged transformation zone adjacent to the layer. (c) Nomarski interference micrograph showing arrested crack tip near  $\text{Al}_2\text{O}_3/\text{Ce-ZrO}_2$  layer (area indicated in (a)) with widened transformation zone adjacent to layer. (d) Two-beam interference micrograph of area in (b). Reference mirror is parallel to surface remote from crack, so that fringes represent contours of constant surface uplift (due to transformation strains). (e, f) Micrographs taken as in (c) and (d), on the region in the crack wake near the first  $\text{Al}_2\text{O}_3/\text{Ce-ZrO}_2$  layer, as indicated in (a).

along the layer near the crack tip was similar to that at the first arrest position. Nomarski interference and two-beam interference micrographs of regions around the first and second layers, with the crack tip at this position, are shown in Figs. 3(e) to (f). These results indicate that the  $\text{Al}_2\text{O}_3/\text{ZrO}_2$  barrier layers have a much larger effect than simply arresting the growth of a transformation zone ahead of a crack; they also promote expansion of the zone to the side of the crack, which is the location that gives rise to crack tip shielding and hence toughening.<sup>18-20</sup>

The applied stress intensity factors were calculated at various stages of crack growth, using the measured loads and crack lengths. The fracture toughness of the Ce-ZrO<sub>2</sub> matrix was  $\approx 5 \text{ MPa}\cdot\text{m}^{1/2}$ , whereas the stress intensity factor had to be raised to  $\approx 10 \text{ MPa}\cdot\text{m}^{1/2}$  to drive the crack across each layer. After the crack tip passed each layer, the unstable crack growth prevented continued measurement of the stress intensity factor until the crack arrested again. However, when the crack had arrested the applied stress intensity factor had decreased to  $\sim 5 \text{ MPa}\cdot\text{m}^{1/2}$ , indicating that the toughening effect of each layer decreased as it moved further into the wake of the crack. Similar results were obtained from specimens containing layers of 100%  $\text{Al}_2\text{O}_3$  in the same Ce-TZP matrix.

Smooth beams of the same composite as in Fig. 3 were broken in bending in the two orientations shown in Figs. 4(a) and (b). In the orientation of Fig. 4(a), which is the same as that of the notched beam, failure occurred unstably at a critical load. The polished side surfaces of the beams exhibited similar evidence for widening of the transformation zone near the

$\text{Al}_2\text{O}_3/\text{ZrO}_2$  layers as in Figs. 3(b) to (f). Therefore, this beneficial interaction occurs for fast-moving as well as stable cracks. In the orientation of Fig. 4(b), fracture also initiated unstably from the tensile surface at a critical load. However, the crack arrested before it reached the opposite side, leaving the beam intact (Fig. 4(c)). The effectiveness of the  $\text{Al}_2\text{O}_3/\text{ZrO}_2$  layers in arresting this crack is especially noteworthy since there were only two layers in the beam, accounting for 2% of its volume. On the surface that had been loaded in tension, there were several narrow bands of transformed material in addition to the crack that caused the sudden load drop, similar to observations in the literature.<sup>21,22</sup> However, some of the transformation bands were arrested at the  $\text{Al}_2\text{O}_3/\text{ZrO}_2$  layers. There is also evidence that the crack itself arrested at the  $\text{Al}_2\text{O}_3/\text{ZrO}_2$  layer before joining with a second crack to cause failure.

Vickers indentations in the Ce-TZP were surrounded by large zones of transformed material, which caused uplift of the surface adjacent to the indentations. Micrographs, obtained using both Nomarski interference and two-beam interference, of several such zones in the vicinities of  $\text{Al}_2\text{O}_3/\text{ZrO}_2$  layers are shown in Fig. 5. At indentation loads up to 300 N, there was no cracking caused by the indentations. The presence of a nearby  $\text{Al}_2\text{O}_3/\text{ZrO}_2$  layer within the transformation zone caused spreading of the zone in the region adjacent to the layer, in a pattern that is similar to the crack tip zone spreading of Fig. 3. There was also transformed material on the side opposite the indentation. The surface uplift, measured from the optical interference micrograph of Fig. 5(b), is plotted in

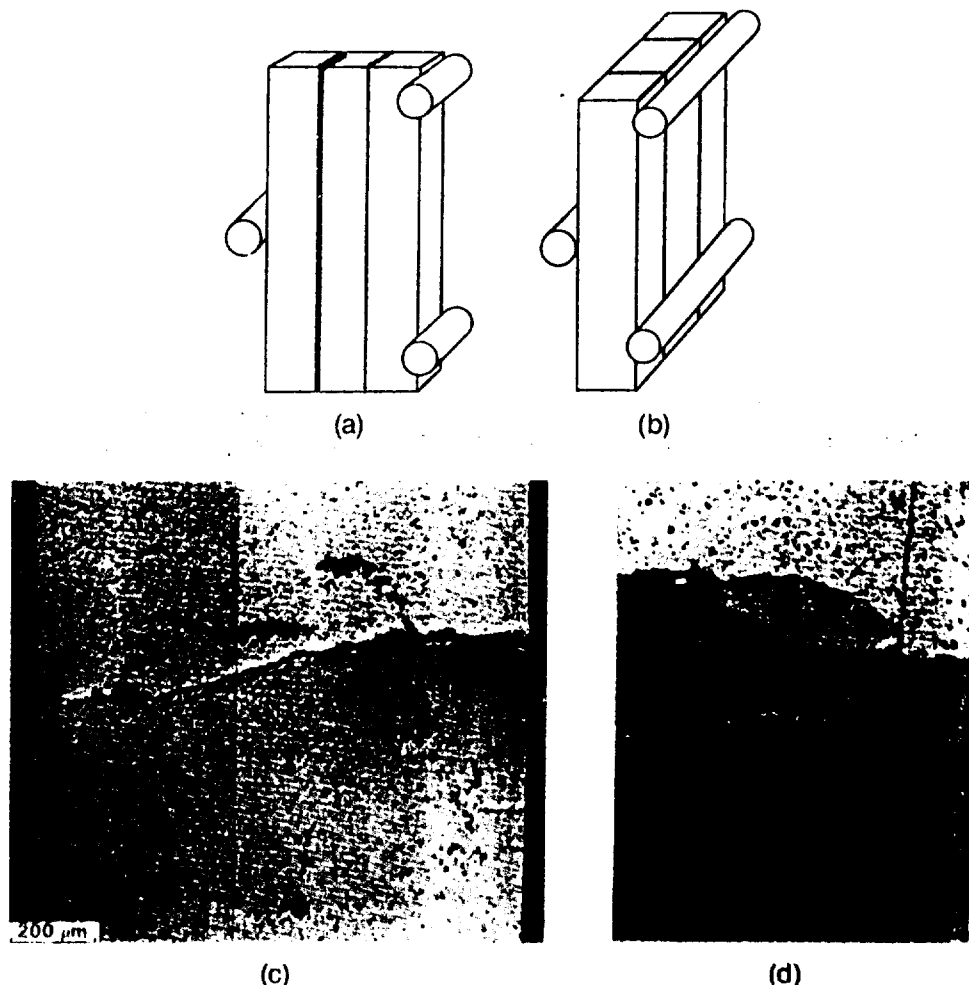


Fig. 4. (a, b) Bending test geometry showing orientations of  $\text{Al}_2\text{O}_3/\text{ZrO}_2$  layers relative to bending direction. (c) Side view of crack in specimen oriented as in (b), showing crack arrest before complete failure. (d) Tensile surface of specimen from (c) showing crack arrest at  $\text{Al}_2\text{O}_3/\text{ZrO}_2$  layer and arrest of transformation bands at the  $\text{Al}_2\text{O}_3/\text{ZrO}_2$  layer (note the transformation band can also be seen on the side surface in (c)).



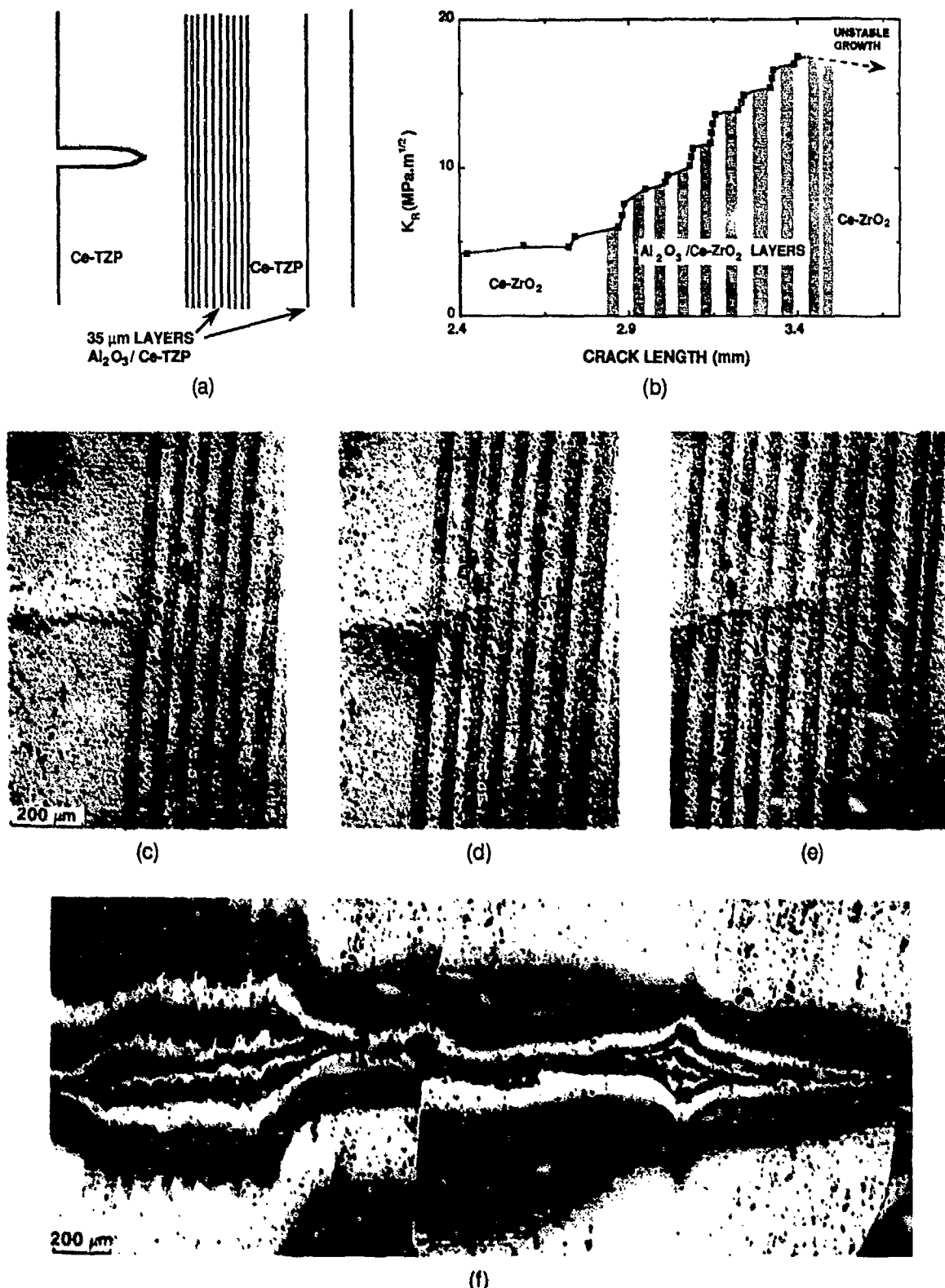


Fig. 7. (a) Multilayered region embedded within a matrix of Ce-TZP. (b) Critical applied stress intensity factor for crack growth up to and through the multilayered region of (a). (c-e) In situ optical micrographs (Nomarski interference) showing crack tip at several stages of growth through the multilayered region. (f) Optical interference micrographs of specimen in (a) to (c) after the crack had grown past the isolated layer. Reference mirror is parallel to undistorted specimen surface, so that fringes represent contours of out-of-plane surface displacements (the discontinuity in the lower central region is due to the joining of two micrographs with imperfect matching of the reference mirror positions).

through the multiple layers. However, as the crack approached the last of the layers, it extended unstably for 1.5 mm and arrested at a position 400  $\mu\text{m}$  past the isolated layer.

The applied stress intensity factor,  $K_R$ , needed to extend the crack up to and through the multiple layers is shown in Fig. 7(b), and micrographs showing the crack tip at several

positions within the layers are shown in Figs. 7(c) to (e). The critical stress intensity factor increased from approximately 5 MPa $\cdot\text{m}^{1/2}$  in the Ce-TZP to 17.5 MPa $\cdot\text{m}^{1/2}$  as the crack approached the end of the layered region. A corresponding increase in the size of the transformation zone surrounding the crack tip is evident in the micrographs of Figs. 7(c) to (e).

Surface distortions due to the volume strain associated with the transformation can be detected as far as 300  $\mu\text{m}$  from the crack plane, whereas the zone width in the single phase Ce-TZP is only  $\sim 15 \mu\text{m}$ .

The increased width of the transformation zone within the layered region is more clearly evident in the optical interference micrograph of Fig. 7(f), in which the fringes represent contours of surface uplift adjacent to the crack. This micrograph was obtained after the load was removed at the conclusion of the experiment. The surface uplift adjacent to the crack is also larger (by a factor of about 2) within the layered region than in the single-phase Ce-TZP, even though the uplift is constrained by the higher-stiffness Al<sub>2</sub>O<sub>3</sub>/ZrO<sub>2</sub> layers, and the average volume fraction of the Ce-ZrO<sub>2</sub> is lower in the layered region. Both the zone width and the magnitude of the surface uplift adjacent to the crack decreased where the crack grew unstably out of the multilayered region into the single-phase Ce-ZrO<sub>2</sub>, and increased again as the crack passed through the isolated Al<sub>2</sub>O<sub>3</sub>/ZrO<sub>2</sub> layer.

The response of cracks oriented parallel to the layers was assessed by loading a double cantilever beam using another fixture on the stage of the optical microscope. The cantilever beam was cut, as shown in Fig. 8(a), from a region of the specimen that contained a conveniently located large processing flaw, which served as an initial sharp crack (a flat nonsintered region  $\sim 1 \text{ mm}$  in diameter at the edge of the multilayered area). Micrographs obtained at two stages during loading are shown in Figs. 8(b) and (c). As the load was increased initially, a zone of material within the single-phase Ce-TZP ahead and to one side of the crack tip transformed before the crack began to grow. With further load increase, the crack grew but was forced to cross the first layer of Al<sub>2</sub>O<sub>3</sub>/ZrO<sub>2</sub>, presumably because of the compressive stresses due to the transformation zone on one side of the crack. The crack then grew along the first layer of Ce-ZrO<sub>2</sub> within the multilayered region, causing transformation in an increasingly wide zone of adjacent layers. The stress intensity factor was not evaluated during this test because the ends of the beam were glued into the loading fixture rather than being loaded through

pins. Nevertheless, it is clear that the layers caused an enhancement of the width of the transformation zone, and hence the toughness, in this orientation as well as in the normal orientation.

#### IV. Discussion

The results in the previous section show that the presence of layers of Al<sub>2</sub>O<sub>3</sub> or Al<sub>2</sub>O<sub>3</sub>/ZrO<sub>2</sub> in Ce-TZP can dramatically modify the sizes and shapes of the transformation zones around cracks. Two effects have been identified. One is the anticipated truncation of the elongated frontal zone, as discussed in the Introduction, which can increase the toughening due to crack shielding by a factor of approximately 2. The other, unexpected effect is the spreading of the transformation zones along the regions adjacent to the layers.

The zone spreading must be driven by the modification of the stress field outside the transformation zone resulting from the nontransformable nature of the layers and/or their higher elastic stiffness. Residual stress due to the difference in thermal expansion coefficients of the Ce-TZP and the Al<sub>2</sub>O<sub>3</sub>-containing layers could potentially influence zone spreading in multilayered composites, where, for example, the magnitude of the stress would be as high as  $\sim 100 \text{ MPa}$  if the layer thicknesses were equal. However, in the present experiments, the zone spreading was observed around cracks and indentations near isolated layers, which represented less than 1% of the total specimen volume. In this case the residual stress in the Ce-TZP was negligibly small and therefore was not a significant influence on the spreading of the transformation zones. This conclusion is further supported by observations that layers containing 50% Al<sub>2</sub>O<sub>3</sub> or 100% Al<sub>2</sub>O<sub>3</sub> (for which the thermal expansion mismatches with the Ce-TZP differ) caused the same degree of zone spreading (e.g., Figs. 5(b) and (c)).

The combined effects of the zone spreading and truncation caused an increase in the fracture toughness of the layered material by a factor of 3.5 (from 5 to  $17.5 \text{ MPa}\cdot\text{m}^{1/2}$ ). Noting that the measured toughnesses are given by the sum of the

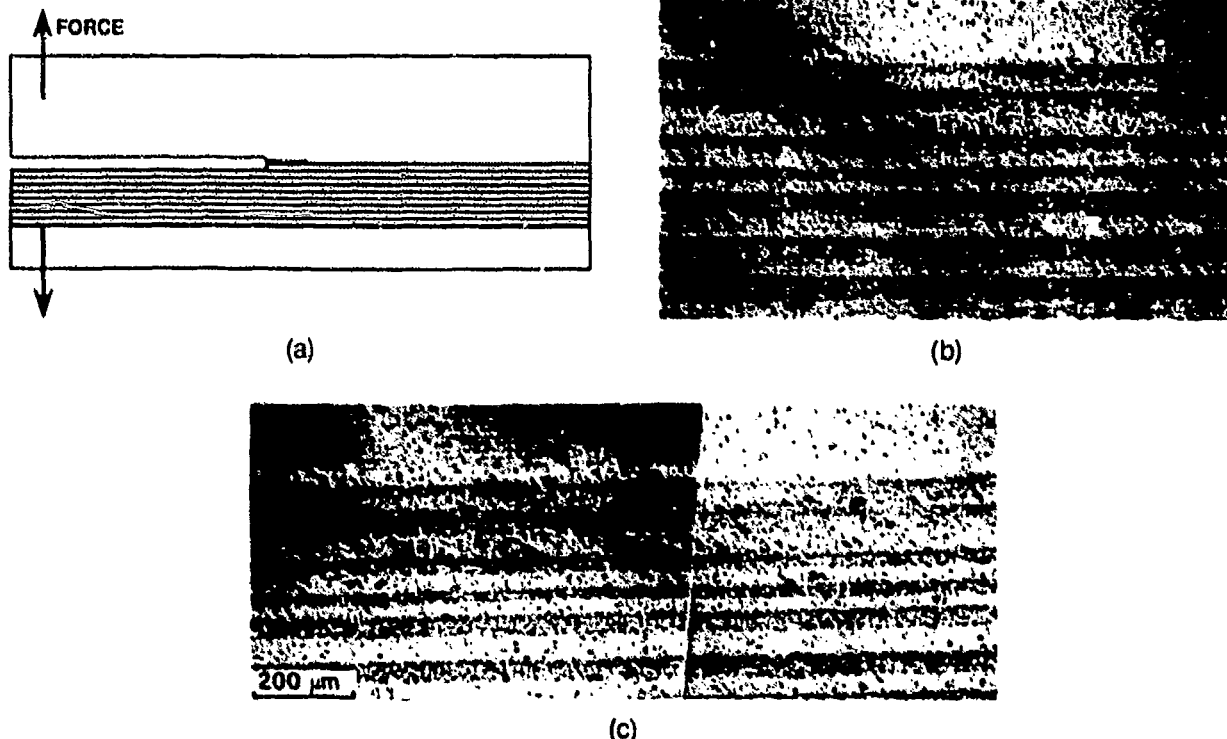


Fig. 8. (a) Schematic diagram of double cantilever beam cut from same composite as in Fig. 7. (b, c) In situ optical micrographs (Nomarski interference) showing crack and surrounding transformation zone at several stages of growth along the layers.

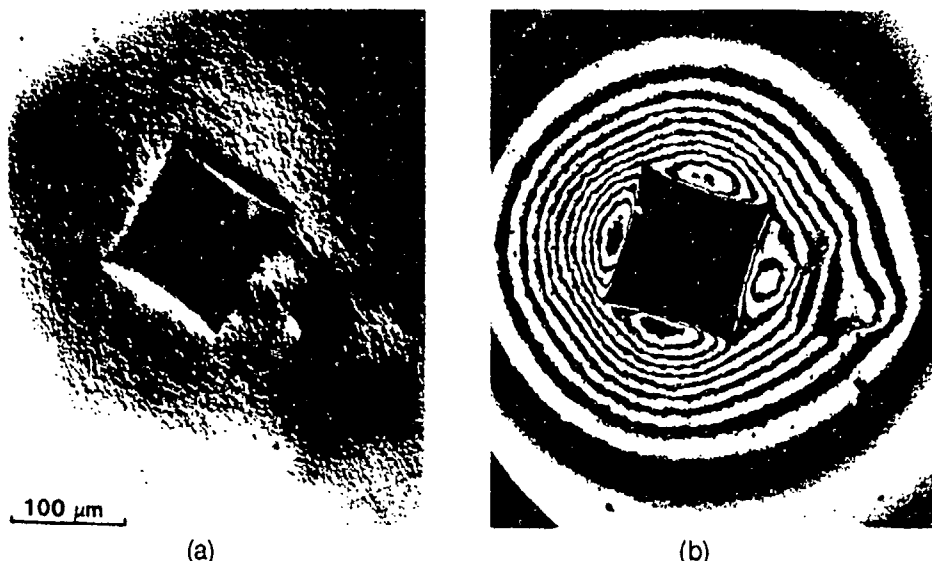


Fig. 9. Vickers indentation (200-N load) near sapphire fiber in Ce-TZP matrix, showing interaction of fiber with transformation zone: (a) Nomarski interference, (b) two-beam interference with reference mirror parallel to specimen surface remote from indentation.

intrinsic toughness of the Ce-TZP without any transformation zone and the crack tip shielding component,  $K_s$ , due to the transformation zone, the observed toughness increase corresponds to an increase in  $K_s$  by a factor of 5.

The Ce-ZrO<sub>2</sub> material used in this preliminary study exhibited a fracture toughness of  $\sim 5 \text{ MPa} \cdot \text{m}^{1/2}$  and a transformation zone size of  $\sim 15 \mu\text{m}$  (Figs. 7(b) and (c)). These values are substantially smaller than the toughnesses and zone sizes reported in more transformable Ce-ZrO<sub>2</sub> materials<sup>1-8</sup> ( $K_R \approx 14 \text{ MPa} \cdot \text{m}^{1/2}$  and zone sizes of several hundred micrometers). However, despite this relatively low starting toughness, the multilayered microstructure was characterized by a crack resistance curve that went as high as  $17.5 \text{ MPa} \cdot \text{m}^{1/2}$ , and which had not begun to saturate to a steady-state value when the crack encountered the end of the layered microstructure. This peak value of  $K_R$  is one of the highest toughnesses recorded in a ceramic material, being surpassed only by weakly bonded fiber-reinforced composites,<sup>21</sup> weakly bonded laminar composites,<sup>22</sup> and by some Mg-PSZ materials immediately after heat treatment<sup>23,24</sup> (the high-toughness Mg-PSZ materials age and lose some of their toughening at room temperature). There is clearly a potential for substantially higher fracture toughnesses in layered microstructures fabricated with the higher-toughness Ce-TZP starting materials. Fabrication of such materials is under way.

The mechanisms of toughening enhancement observed here should not be restricted to the laminar geometry used in this study. Similar effects may be expected for any high-modulus, nontransforming microstructural unit, such as continuous or chopped fibers or platelets, distributed over a similar spatial scale as the layers. An example of the interaction of a transformation zone around an indentation with an isolated sapphire fiber in the Ce-TZP matrix is shown in Fig. 9. By direct analogy with the effect of the Al<sub>2</sub>O<sub>3</sub> layers, the sapphire fiber caused spreading of the transformation zone and a larger overall surface uplift in the vicinity of the fiber.

## V. Conclusions

Laminar composites containing alternating layers of Ce-TZP and a mixture of Al<sub>2</sub>O<sub>3</sub> and Ce-ZrO<sub>2</sub> have been fabricated using a colloidal technique. In situ observations during controlled crack growth experiments in these microcomposites have yielded the following results:

(1) The layers interacted strongly with the transformation zones surrounding cracks and indentations, causing the zones

to spread along the regions adjacent to the layers and leading to enhanced fracture toughness.

(2) Multilayered microstructures exhibited R-curve behavior for cracks oriented normal to the layers, with the critical stress intensity factor increasing by a factor of 3.5 from the starting toughness of the Ce-TZP ( $\sim 5 \text{ MPa} \cdot \text{m}^{1/2}$ ) to a value of at least  $17.5 \text{ MPa} \cdot \text{m}^{1/2}$ . (This peak value had not saturated to a steady state, but instead was limited by the crack having reached the end of the multilayered region.)

(3) Zone spreading and toughening effects were observed for cracks growing parallel to the layers as well as for those oriented normal to the layers.

## References

- M. V. Swain, R. H. J. Hannink, and J. Drennan, "Some Interfacial Related Properties of Transformation-Toughened Ceramics," p. 819 in *Ceramic Microstructures '86: Role of Interfaces*, Edited by J. A. Pask and A. G. Evans, Plenum, New York, 1987.
- R. H. J. Hannink and M. V. Swain, "Metastability of Martensitic Transformation in a 12 mol% Ceria-Zirconia Alloy: Deformation and Fracture Observations," *J Am Ceram Soc.*, **72** [1] 90-98 (1989).
- L. R. F. Rose and M. V. Swain, "Transformation Zone Shape in Ceria-Partially-Stabilized Zirconia," *Acta Metall.*, **36** [4] 955-62 (1988).
- C.-S. Yu and D. K. Shetty, "Transformation Zone Shape, Size, and Crack-Growth-Resistance (R-Curve) Behavior of Ceria-Partially-Stabilized Zirconia Polycrystals," *J Am Ceram Soc.*, **72** [6] 921-28 (1989).
- P. E. Reyes-Morel and I.-W. Chen, "Transformation Plasticity of CeO<sub>2</sub>-Stabilized Tetragonal Zirconia Polycrystals. I. Stress Assistance and Auto-catalysis," *J Am Ceram Soc.*, **72** [5] 543-53 (1988).
- P. E. Reyes-Morel, J.-S. Chering, and I.-W. Chen, "Transformation Plasticity of CeO<sub>2</sub>-Stabilized Tetragonal Zirconia Polycrystals. II. Pseudoelasticity and Shape Memory Effects," *J Am Ceram Soc.*, **71** [8] 648-57 (1988).
- K. E. Tsukuma and M. Shimada, "Strength, Fracture Toughness, and Vickers Hardness of CeO<sub>2</sub>-Stabilized Tetragonal Zirconia Polycrystals (Ce-TZP)," *J Mater Sci.*, **20** [4] 1178-84 (1985).
- T. Sato, T. Endo, and M. Shimada, "Post-sintering Hot Isostatic Pressing of Ceria-Doped Tetragonal Zirconia/Alumina Composites in an Argon-Oxygen Gas Atmosphere," *J Am Ceram Soc.*, **72** [5] 761-64 (1989).
- D. B. Marshall, "Crack Shielding in Ceria-Partially-Stabilized Zirconia," *J Am Ceram Soc.*, **73** [10] 3119-21 (1990).
- D. B. Marshall, M. C. Shaw, R. H. Dauskardt, R. O. Ritchie, M. Readey, and A. H. Heuer, "Crack Tip Transformation Zones in Toughened Zirconia," *J Am Ceram Soc.*, **73** [9] 2659-66 (1990).
- A. H. Heuer, M. Rühle, and D. B. Marshall, "On the Thermoelastic Transformation in Tetragonal ZrO<sub>2</sub>," *J Am Ceram Soc.*, **73** [4] 1084-93 (1990).
- R. H. J. Hannink and M. V. Swain, "Magnesia-Partially-Stabilized Zirconia: The Influence of Heat Treatment on Thermomechanical Properties," *J Aust Ceram Soc.*, **18** [2] 53-62 (1982).
- B. V. Velamakanni, J. C. Chang, F. F. Lange, and D. S. Pearson, "New Method for Efficient Colloidal Particle Packing via Modulation of Repulsive Lubricating Hydration Forces," *Langmuir*, **6**, 1323-25 (1990).
- J. C. Chang, B. V. Velamakanni, F. F. Lange, and D. S. Pearson, "Centrifugal Consolidation of Al<sub>2</sub>O<sub>3</sub> and Al<sub>2</sub>O<sub>3</sub>/ZrO<sub>2</sub> Composite Slurries vs

Interparticle Potentials: Particle Packing and Mass Segregation," *J. Am. Ceram. Soc.*, 74 [9] 2201-204 (1991).

<sup>15</sup>Y. W. Mai and A. G. Atkins, "Crack Stability in Fracture Toughness Testing," *J. Strain Anal.*, 15 [2] 63-74 (1980).

<sup>16</sup>M. Sakai and M. Inagaki, "Dimensionless Load-Displacement Relation and Its Application to Crack Propagation Problems," *J. Am. Ceram. Soc.*, 72 [3] 388-94 (1989).

<sup>17</sup>H. Tada, *The Stress Analysis of Cracks Handbook*, 2nd ed. Paris Productions Inc., St. Louis, MO, 1985.

<sup>18</sup>R. M. McMeeking and A. G. Evans, "Mechanics of Transformation Toughening in Brittle Materials," *J. Am. Ceram. Soc.*, 65 [5] 242-46 (1982).

<sup>19</sup>D. B. Marshall, A. G. Evans, and M. Drory, "Transformation Toughening in Ceramics"; p. 289 in *Fracture Mechanics and Ceramics*, Vol. 6. Edited by R. C. Bradt, A. G. Evans, D. P. H. Hasselman, and F. F. Lange. Plenum Press, New York, 1983.

<sup>20</sup>A. G. Evans and R. M. Cannon, "Toughening of Brittle Solids by Martensitic Transformations," *Acta Metall.*, 34 [5] 651-800 (1986).

<sup>21</sup>A. G. Evans and D. B. Marshall, "The Mechanical Behavior of Ceramic Matrix Composites," *Acta Metall.*, 37 [10] 2607-83 (1989).

<sup>22</sup>W. J. Clegg, K. Kendall, N. McN. Alford, T. W. Button, and J. D. Birchall, "A Simple Way to Make Tough Ceramics," *Nature (London)*, 347, 455-57 (1990).

<sup>23</sup>A. H. Heuer, M. J. Readey, and R. Steinbrech, "Resistance Curve Behavior of Supertough  $MgO$ -Partially-Stabilized  $ZrO_2$ ," *Mater. Sci. Eng.*, A105/106, 83-89 (1988).

<sup>24</sup>M. J. Readey and A. H. Heuer, "Annealing of Test Specimens of High-Toughness Magnesia-Partially-Stabilized Zirconia," *J. Am. Ceram. Soc.*, 71 [1] C-2-C-6 (1988). □



**Rockwell International**  
**Science Center**

**SC71002.FR**

### **3.2 THE DESIGN OF HIGH TOUGHNESS LAMINAR ZIRCONIA COMPOSITES**

to be published in Bull. Amer. Ceram. Soc.

# THE DESIGN OF HIGH TOUGHNESS LAMINAR ZIRCONIA COMPOSITES

D.B. Marshall

Rockwell International Science Center  
1049 Camino Dos Rios  
Thousand Oaks, CA 91360

## ABSTRACT

The development of new layered microcomposites of Ce-ZrO<sub>2</sub> and Al<sub>2</sub>O<sub>3</sub> which exhibit enhanced transformation toughening is described. The layered microstructures were designed on the basis of transformation zone measurements and calculations of the influence of zone shape on toughening in Ce-ZrO<sub>2</sub> and Mg-ZrO<sub>2</sub>.

## 1. INTRODUCTION

Since the discovery of transformation toughening in ZrO<sub>2</sub> in 1975,<sup>1</sup> a variety of toughened ZrO<sub>2</sub>-based materials have been developed. Magnesia-partially-stabilized zirconia (Mg-PSZ) and ceria-zirconia tetragonal polycrystalline materials (Ce-TZP) can now be fabricated with toughesses in the range 10-20 MPa·m<sup>1/2</sup>.<sup>2-7</sup>

The optimization of the microstructures of these materials has occurred together with advances in our understanding of the micromechanics of toughening and with development of techniques that allow direct measurement of transformation zone characteristics. In this paper, some recent direct measurements of transformation zones in Ce-TZP and Mg-PSZ will be described, along with calculations of the effect of zone shape on toughening, which have led to the development of new layered composites with dramatically increased toughness. These materials may herald a new class of dual scale microstructures in ZrO<sub>2</sub>-toughened ceramics.

## 2. TRANSFORMATION ZONES IN Ce-TZP AND Mg-PSZ

### 2.1 Transformation Zones and Toughening

Toughening of  $ZrO_2$  ceramics is caused by a martensitic tetragonal-to-monoclinic transformation, which is induced by crack tip stresses within a limited zone surrounding the crack. The transforming particles (usually grains or precipitates) undergo a shape change which comprises dilatation of ~ 4% and shear strain of ~ 7% at the unit cell level, although the shear component of the overall particle shape change can be partly or fully eliminated by twinning or variant formation.<sup>8</sup> The toughening can be understood either in terms of the direct reduction of crack tip stresses caused by the shape change, or from an energy balance analysis of crack growth, in which the toughening is associated with the energy required to cause the transformation.<sup>8-11</sup>

The degree of toughening is dependent upon the distribution of transformation strains around the crack. Although the influences of microstructural parameters, such as particle size and stabilizer content, on increasing or decreasing zone size are known qualitatively, quantitative predictions of the strain distribution are not presently possible because neither the critical stress/strain condition for transformation nor the degree of shear strain accommodation is known. However, if the distribution is specified, the toughening can be evaluated using either the stress intensity or the energy balance approaches (which are rigorously equivalent<sup>11</sup>). Thus, if a uniform volume fraction,  $f$ , of particles transform with net dilatation,  $e^T$ , within a zone of arbitrary shape, the toughness increase (shielding stress intensity factor) is

$$K_S = A E e^T f \sqrt{w} \quad (1)$$

where  $E$  is the Youngs modulus,  $A$  is a dimensionless constant dependent on the zone

shape, and  $w$  is a characteristic zone width. The shape parameter,  $A$ , can be readily evaluated for any specified zone shape using the weight function method of McMeeking and Evans.<sup>10</sup> If the volume fraction,  $f$ , is not uniform within the zone, the result is more complicated, although for the case where  $e^T$  is dilatation and contours of constant  $f$  are geometrically similar, Eq. (1) holds with the product  $f\sqrt{w}$  simply replaced by an integral.<sup>12</sup>

## 2.2 Direct Zone Measurements

Several techniques have been used to characterize transformation zones in  $\text{ZrO}_2$  materials, and thus provide critical testing of the transformation toughening theory. Initially, x-ray measurements confirmed the presence of monoclinic phase on fracture surfaces, although the spatial resolution is not sufficient to measure zone shapes near crack tips. Such crack-tip zone measurements have been obtained using several methods that examine a specimen surface normal to the crack plane; optical interference microscopy (Nomarski or Tolanski), which detects out-of-plane distortions caused by transformation strains near the crack (Fig. 1(a))<sup>12</sup>; moiré interferometry and high resolution differential strain mapping, which detect in-plane transformation strains (Fig. 1(b))<sup>13</sup>; and Raman microprobe spectroscopy,<sup>12,14</sup> which provides measurements of the relative volume fractions of monoclinic and tetragonal phases with spatial resolution of several microns (Fig. 1(c)).

Examples of such measurements in Mg-PSZ are shown in Fig. 1. Raman measurements (Fig. 1(c)), obtained by scanning along lines around the crack, indicate that the volume fraction of transformed monoclinic phase decreases continuously with distance from the crack and that the zone shape near the crack tip is approximately semicircular. Optical interference micrographs (Fig. 1(a)) provide a convenient

indication of the approximate zone size and shape, although direct quantitative deduction of zone characteristics is not simple because the out-of-plane surface distortions extend beyond the transformation zone. Nevertheless, the results suggest an almost semicircular zone ahead of the crack tip, consistent with the Raman measurements. Moiré interferometry (Fig. 1(b)) and high resolution differential strain mapping provide direct measurements of the strains normal to the crack plane, which are directly responsible for shielding the crack tip, although even in this case account must be taken of the distortion of the free surface. Calculation of these surface strains from the Raman measurements of the distribution of transformed material (using FEM to account for surface relaxation effects) yielded results that were consistent with the direct strain measurements (Fig. 1(b)).

Both the Raman results and the in-plane strain measurements can be used to calculate the shielding stress intensity factor. Such measurements in Mg-PSZ materials that had been heat treated to yield different steady state fracture toughnesses ( $16 \text{ MPa}\cdot\text{m}^{1/2}$  and  $12 \text{ MPa}\cdot\text{m}^{1/2}$ ) indicated that large fractions of the measured toughnesses ( $8 \text{ MPa}\cdot\text{m}^{1/2}$  and  $4 \text{ MPa}\cdot\text{m}^{1/2}$ ) were due directly to the dilatation associated with the tetragonal to monoclinic transformation.<sup>12</sup>

The shapes of transformation zones observed in high-toughness Ce-ZrO<sub>2</sub> ceramics differ substantially from those in Mg-ZrO<sub>2</sub> (Fig. 2). The zones in Ce-ZrO<sub>2</sub> are very elongated, extending ahead of the crack a distance of ~ 10 to 20 times the zone width.<sup>5,6</sup> Calculations of the shielding stress intensity factors using Eq. (1) with measured zone shapes and distributions of transformed material have indicated that, as in Mg-PSZ, most of the toughening may be accounted for by shielding due to the dilatational transformation strain.<sup>15</sup>

### 2.3 Relations Between Zone Shape and Toughening

Calculations of the influence of zone shape on toughening have shown that dilatational transformation of particles located within an angular range of  $\pm 60^\circ$  ahead of the crack tip causes an increase in the crack tip stresses, and thus detracts from toughening.<sup>10,11</sup> (The net toughening arises from the dominant effect of particles outside this range.) Therefore, the elongated frontal zone in Ce-TZP (Fig. 2) is detrimental to toughening by crack tip shielding. Calculations of the shielding stress intensity factors for zones with various ratios of frontal length to width (Fig. 3) indicate that the net toughening due to the zone in Fig. 2 is more than a factor of 2 smaller than it would be if the frontal zone was semicircular.<sup>15</sup> Therefore there would be substantial benefit if the elongated frontal zone in Ce-TZP could be eliminated.

### 2.4 Modification of Zone Shape

The elongated frontal zone in Ce-TZP is thought to result from autocatalytic transformation, i.e., sequential triggering of transformation in a grain by transformation strains in an adjacent grain. Autocatalytic effects have also been observed in other experiments; sudden bursts of transformation that occur upon cooling through the  $M_s$  temperature (the temperature at which spontaneous transformation occurs), and load drops during tensile loading, which coincide with the formation of narrow, well-defined bands of transformed material which extend completely through the specimen in an orientation normal to the applied tension.<sup>16,17</sup>

An approach for modifying the crack tip zone shape is suggested by comparing the transformation responses and microstructures of Ce-TZP and Mg-PSZ. The microstructure of Mg-PSZ may be thought of as dual scale; the individual precipitates that transform from tetragonal to monoclinic phase are lenticular in shape (~ 300 nm

diameter) and are contained within grains that are larger by about 2 orders of magnitude. Autocatalytic transformation also occurs in Mg-PSZ, as evidenced by the formation of well-defined shear bands on the surfaces of specimens loaded in tension or compression (Fig. 4).<sup>18</sup> However, the transformation bands are arrested at the grain boundaries rather than extending completely through the specimen. Separate initiation of transformation is thus necessary in each grain, resulting in a smoothly increasing stress strain curve, progressive transformation when cooling through the  $M_s$  temperature, and, presumably, a modified shape of the transformation zone ahead of a crack tip. In Ce-TZP, which comprises a polycrystalline array of uniform tetragonal grains, each of several microns diameter, there is no such large scale barrier to arrest a developing transformation band; in this case the transforming particles are the individual grains and there is no larger microstructural unit. The presence of second phase grains in  $Al_2O_3$ /Ce-ZrO<sub>2</sub> particulate composites has been shown to prevent autocatalytic transformation,<sup>17</sup> but it also leads to reduced zone width and thus reduced toughness. The analogy with Mg-PSZ suggests that the frontal zone may be eliminated while maintaining the large zone width over the crack wake, if a dual scale microstructure could be created in Ce-ZrO<sub>2</sub>, with barriers distributed on a scale substantially larger than the grain size, but smaller than the transformation zone width.

In the following section an approach for introducing such large-scale microstructural units into Ce-ZrO<sub>2</sub> in the form of layers of either  $Al_2O_3$  or a mixture of  $Al_2O_3$  and Ce-ZrO<sub>2</sub> is described. Based on the preceding discussion, the optimum spacing of the layers would be ~ 20 to 100  $\mu m$ .

### 3. LAYERED MICROCOMPOSITES

Multilayered composites with alternating layers of Ce-TZP and  $Al_2O_3$ /Ce-

$\text{ZrO}_2$  have been fabricated using a colloidal technique for consolidation.<sup>19</sup> The technique involved sequential centrifuging of solutions containing suspended particles to form the green body, followed by drying and sintering. The barrier layers were composed of 50% by volume of  $\text{Al}_2\text{O}_3$  and  $\text{Ce-ZrO}_2$  rather than pure  $\text{Al}_2\text{O}_3$ , in order to minimize differential shrinkage during sintering. Reasonably uniform layers with thicknesses in the range 10 to 100  $\mu\text{m}$  were readily formed using this technique.

Controlled crack growth experiments using notched beams with regions of multilayered material (or isolated layers) embedded in a matrix of  $\text{Ce-ZrO}_2$  allowed the influence of the layers to be identified. In addition to the anticipated truncation of the elongated frontal zone, an unforeseen spreading of the transformation zone along the  $\text{Al}_2\text{O}_3/\text{ZrO}_2$  layers normal to the crack plane was observed (Fig. 5). The extra transformation in this location causes additional shielding of the crack and hence toughening.

The applied stress intensity factor,  $K_R$ , needed to extend a crack stably up to and through a multilayered region, comprising layers of 35  $\mu\text{m}$  thickness, is shown in Fig. 6(a). In this test, the crack grew under steady state conditions, at  $K_R = 5 \text{ MPa}$ , in the Ce-TZP before reaching the multilayered region. The value of  $K_R$  then increased almost linearly with crack extension as the crack grew through the layers, reaching a value of  $17.5 \text{ MPa}\cdot\text{m}^{1/2}$  as the crack approached the end of the layered region, whereupon the crack extended unstably into the Ce-TZP on the other side. A corresponding increase in the size of the transformation zone surrounding the crack tip was observed (Fig. 6(b)).

Similar results have been obtained using specimens with layers of different thickness and with Ce-TZP materials of different starting toughness (the toughness of the  $\text{Ce-ZrO}_2$  used for the data of Fig. 6,  $K_R = 5 \text{ MPa}\cdot\text{m}^{1/2}$ , was relatively low). In all

cases the R-curves increased as the cracks grew through the layered regions (all of width  $\leq 1$  mm) without any sign of saturation, and with maximum measured values of  $K_R$  being limited by unstable growth when the crack encountered the end of the layered region. The transformation zone in one of these specimens containing  $\text{Ce-ZrO}_2$  of high initial toughness ( $K_R = 10 \text{ MPa}\cdot\text{m}^{1/2}$ ) is shown in Fig. 7: the zone spreading was much more extensive. The frontal zone penetrated past the end of the layered region, with subsequent unstable crack growth, after the crack had penetrated only half of the layers (at  $K_R = 15 \text{ MPa}\cdot\text{m}^{1/2}$ ).<sup>20</sup>

## CONCLUSIONS

Microlaminates of  $\text{Ce-ZrO}_2$  with  $\text{Al}_2\text{O}_3/\text{ZrO}_2$  layers exhibit dramatically increased fracture resistance. Development of these composites was motivated by results of micromechanics analysis combined with direct observations of zone characteristics in Mg-PSZ and Ce-TZP, which indicated that substantial toughening would result from modifying shape of the transformation zone in Ce-TZP. Two effects that enhance the transformation toughening in the layered structures have been identified. One is the truncation of the elongated frontal zone that forms in single phase  $\text{Ce-ZrO}_2$  and the other is the spreading of the transformation zone along the layers.

The toughening enhancement should not be limited to planar layered microstructures with cracks normal to the layers. Evidence has been presented elsewhere<sup>18</sup> for enhanced toughening for cracks growing parallel to the layers and for spreading of the transformation zone near  $\text{Al}_2\text{O}_3$  fibers embedded in a Ce-TZP matrix. Thus, many other three-dimensional dual scale microstructures that enhance toughening may be envisioned using fibers, platelets or nonplanar  $\text{Al}_2\text{O}_3/\text{ZrO}_2$  layers as barriers to autocatalytic transformation.

### Acknowledgments

The work summarized here was done in collaboration with M. Shaw, B. Cox, M. Dadkhah, W.L. Morris, J. Ratto, F. Lange and R. Cutler. Funding for the work was provided by the U.S. Air Force Office of Scientific Research under Contract No. F49620-89-C-0031.

### References

1. R.S. Garvie, R.H.J. Hannink, and R.T. Pascoe, "Ceramic Steel?" *Nature (London)*, 258, 703-705 (1975).
2. K.E. Tsukuma and M. Shimada, "Strength, Fracture Toughness, and Vickers Hardness of CeO<sub>2</sub>-Stabilized Tetragonal Zirconia Polycrystals (Ce-TZP)," *J. Mat. Sci.* 20[4] 1178-84 (1985).
3. T. Sato, T. Endo, and M. Shimada, "Postsintering Hot Isostatic Pressing of Ceria-Doped Tetragonal Zirconia/Alumina Composites in an Argon-Oxygen Gas Atmosphere," *J. Am. Ceram. Soc.* 72[5] 761-64 (1989).
4. R.H.J. Hannink and M.V. Swain, "Metastability of Martensitic Transformation in a 12 mol.% Ceria-Zirconia Alloy: Deformation and Fracture Observations," *J. Am. Ceram. Soc.* 72[1] 90-98 (1989).

5. L.R.F. Rose and M.V. Swain, "Transformation Zone Shape in Ceria-Partially-Stabilized Zirconia," *Acta Metall.* 36[4] 955-962 (1988).
6. C-S Yu and D.K. Shetty, "Transformation Zone, Shape, Size and Crack-Growth-Resistance (R-curve) Behavior of Ceria-Partially Stabilized Zirconia Polycrystals," *J. Am. Ceram. Soc.* 72[6] 921-28 (1989).
7. A.H. Heuer, M.J. Readey and R. Steinbrech, "Resistance Curve Behavior of Supertough MgO-Partially-Stabilized ZrO<sub>2</sub>," *Mater. Sci. Eng.* A105/106 83-89 (1988).
8. A.G. Evans and R.M. Cannon, "Toughening of Brittle Solids by Martensitic Transformations," *Acta Metall.* 34[5] 651-800 (1986).
9. A.G. Evans and A.H. Heuer, "Review - Transformation Toughening in Ceramics: Martensitic Transformation in Crack-Tip Stress Fields," *J. Am. Ceram. Soc.* 63, 241 (1980).
10. R.M. McMeeking and A.G. Evans, "Mechanics of Transformation Toughening in Brittle Materials," *J. Am. Ceram. Soc.* 65[5] 242-46 (1982).
11. D.B. Marshall, A.G. Evans and M. Drory, "Transformation Toughening in Ceramics," p. 289 in Fracture Mechanics of Ceramics, Vol. 6, edited by R.C. Bradt, A.G. Evans, D.P.H. Hasselman and F.F. Lange, Plenum Press, New York (1983).

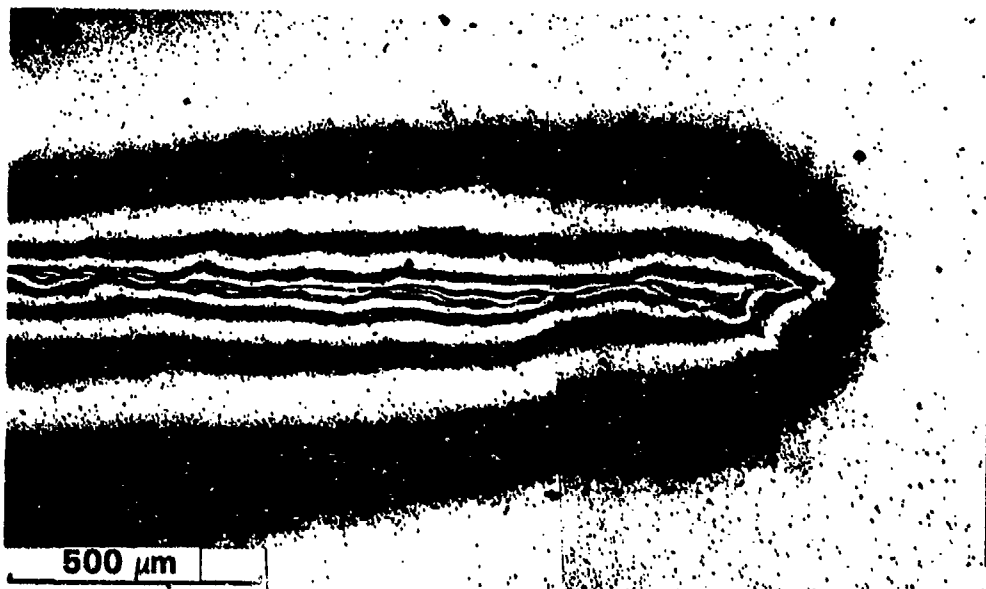
12. D.B. Marshall, M.C. Shaw, R.H. Dauskardt, R.O. Ritchie, M. Readey and A.H. Heuer, "Crack Tip Transformation Zones in Toughened Zirconia," *J. Am. Ceram. Soc.*, 73[9] 2659-66 (1990).
13. M.S. Dadkhah, D.B. Marshall, W.L. Morris and B.N. Cox, "Direct Measurement of Transformation Zone Strains in Toughened Zirconia," *J. Am. Ceram. Soc.* 74[3], 584-92 (1991).
14. D.R. Clarke and F. Adar, "Measurement of the Crystallographically Transformed Zone Produced by Fracture in Ceramics Containing Tetragonal Zirconia," *J. Am. Ceram. Soc.* 65[6], 284-88 (1982).
15. D.B. Marshall, "Crack Shielding in Ceria-Partially-Stabilized Zirconia," *J. Am. Ceram. Soc.* 73[10] 3119-21 (1990).
16. P.E. Reyes-Morel and I-W Chen, "Transformation Plasticity of  $\text{CeO}_2$ -stabilized Tetragonal Zirconia Polycrystals and I Stress Assistance and Autocatalysis," *J. Am. Ceram. Soc.* 72[5] 343-53 (1988).
17. J.F. Tsai, C-S Yu and D.K. Shetty, "Autocatalytic Transformation and Zone Shape in Ceria-Partially-Stabilized Zirconia (Ce-TZP)," unpublished work.
18. A.H. Heuer, M. Rühle and D.B. Marshall, "On the Thermoelastic Transformation in Tetragonal  $\text{ZrO}_2$ ," *J. Am. Ceram. Soc.* 73[4] 1084-93 (1990).

19. D.B. Marshall, J.J. Ratto and F.F. Lange, "Enhanced Fracture Toughness in Layered Microcomposites of Ce-ZrO<sub>2</sub> and Al<sub>2</sub>O<sub>3</sub>," J. Am. Ceram. Soc., in press.
20. D.B. Marshall, J.J. Ratto and R.A. Cutler, unpublished work.

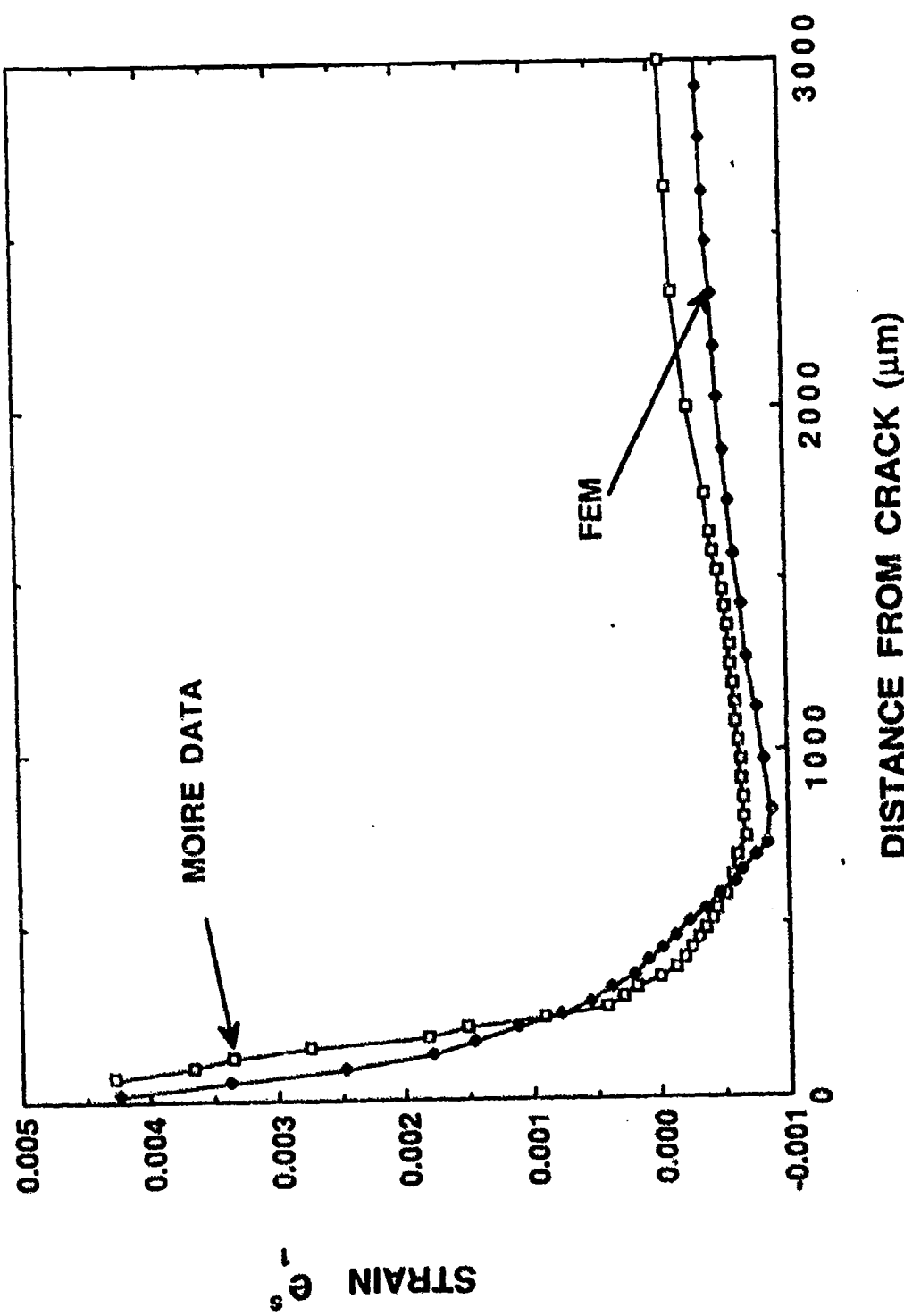
Figure Captions

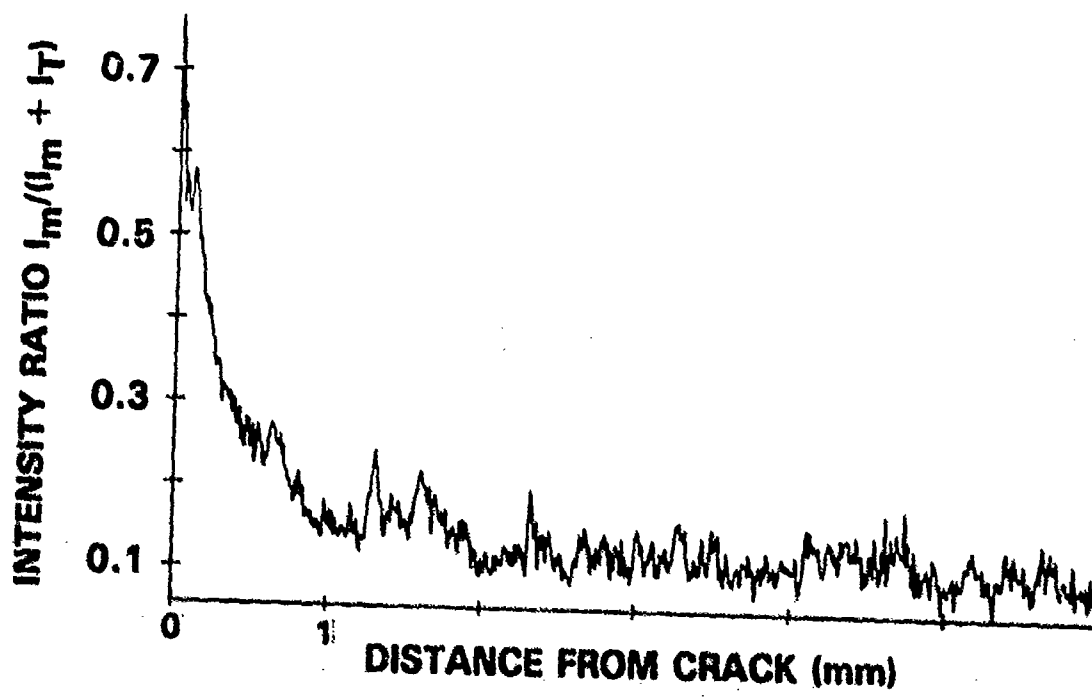
1. (a) Optical interference micrograph showing out-of-plane surface distortion due to transformation zone surrounding crack in Mg-PSZ. Fringes represent contours of constant displacement.  
(b) Residual transformation strains in wake of crack in Mg-PSZ in the direction normal to the crack plane. Data from moiré interference. Finite element calculations using Raman measurements of volume fraction of transformed phase, assuming dilatational transformation.  
(c) Fraction monoclinic phase in wake of crack in Mg-PSZ, measured by Raman spectroscopy.
2. Nomarski interference micrograph showing crack in Ce-TZP (specimen supplied by Dr. D. Shetty).
3. Crack tip shielding stress intensity factor for steady-state cracks with various frontal zone shapes.
4. Nomarski interference micrograph of surface of Mg-PSZ loaded in compression, showing transformation bands.
5. Arrested crack near  $\text{Al}_2\text{O}_3/\text{ZrO}_2$  layer (darker region) in Ce-TZP showing spreading of the transformation zone adjacent to the layer.

- 6. (a) Critical stress intensity factor for crack growth through multilayered region of Ce-TZP/(Al<sub>2</sub>O<sub>3</sub>-ZrO<sub>2</sub>) composite.  
(b) Nomarski interference micrograph showing enlargement of transformation zone (outlined by broken line) during crack growth through multilayered region of (a).
- 7. Nomarski interference micrograph showing enlargement of transformation zone caused by multilayered region of composite with high toughness Ce-TZP matrix.

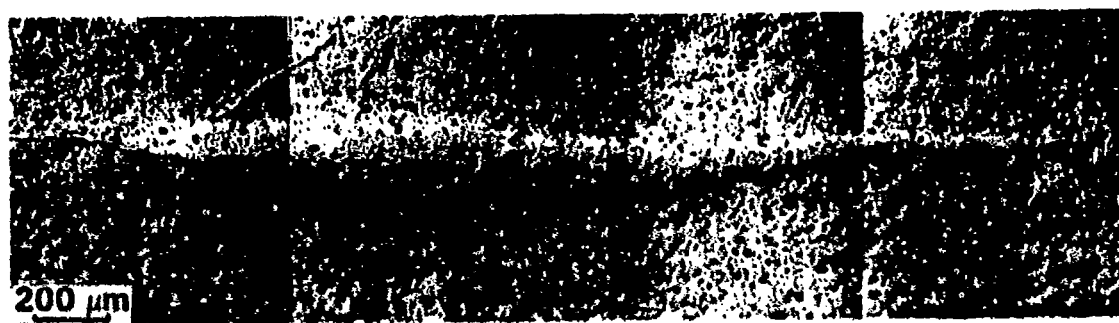


1(a)





1(c)



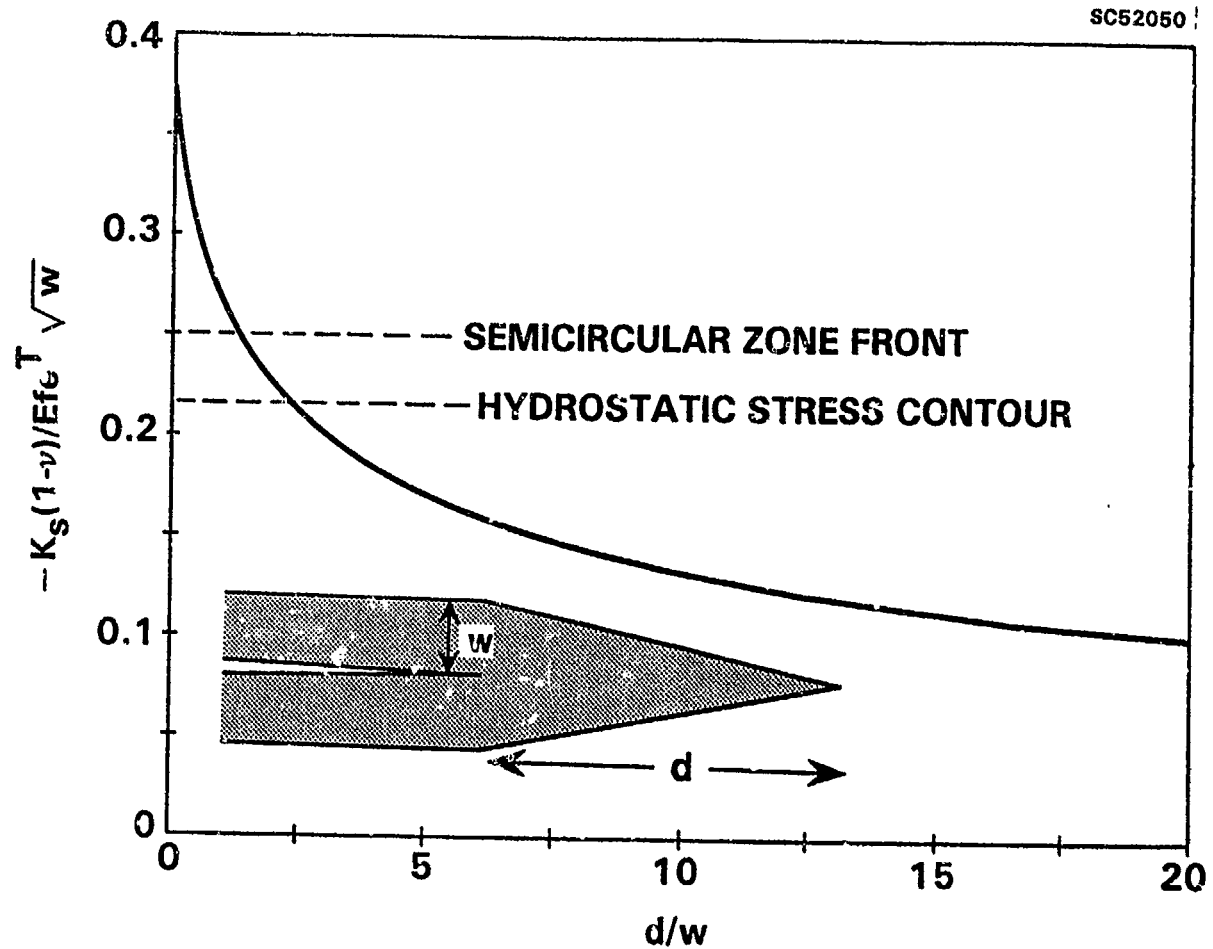
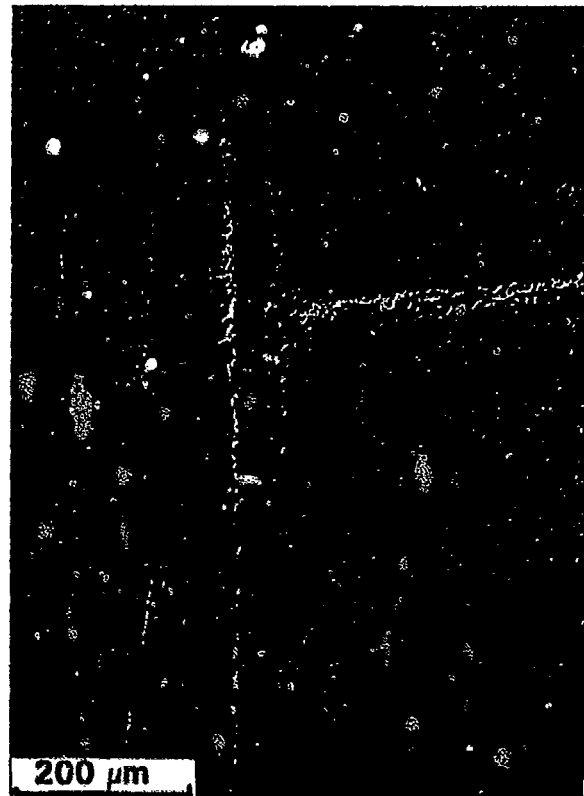




Fig. 4



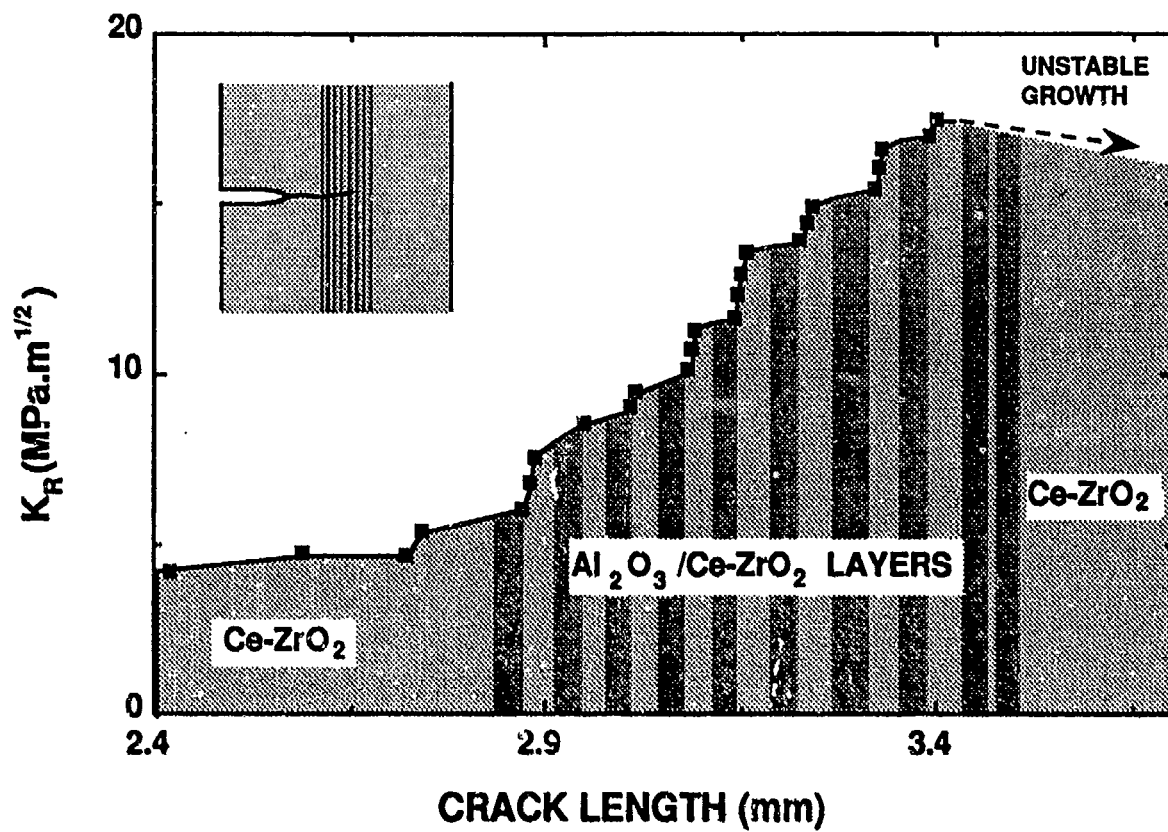
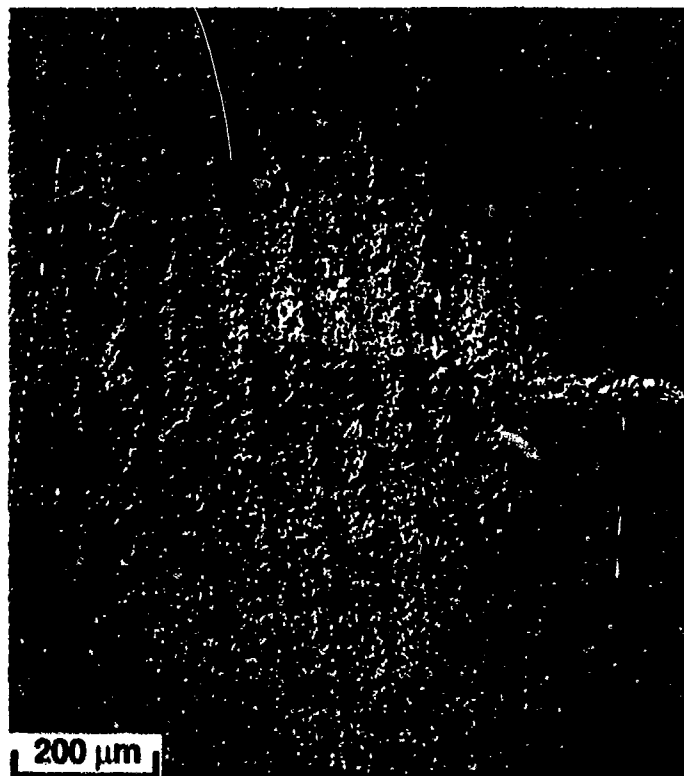
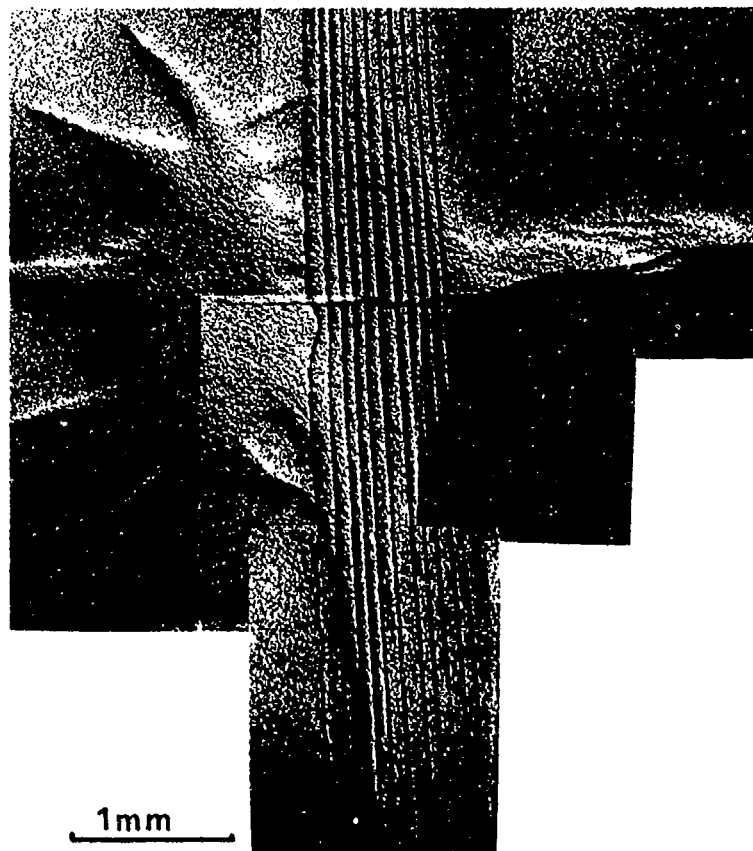


Fig. 6(a)



6/16





Rockwell Internatio  
Science Center

SC71002.FR

### 3.3 CRACK RESISTANCE CURVES IN LAYERED ZIRCONIA CERAMICS

to be published in J. Am. Ceram. Soc.

# CRACK RESISTANCE CURVES IN LAYERED Ce-ZrO<sub>2</sub>/Al<sub>2</sub>O<sub>3</sub> CERAMICS

D.B. Marshall, J.J. Ratto and F.F. Lange

Rockwell International Science Center  
1049 Camino Dos Rios  
Thousand Oaks, CA 91360

## ABSTRACT

Crack resistance curves have been measured in layered Ce-ZrO<sub>2</sub>/Al<sub>2</sub>O<sub>3</sub> composites with various layer thicknesses and with Ce-ZrO<sub>2</sub> materials of two different initial fracture toughnesses. Increasing the transformability of the Ce-ZrO<sub>2</sub> phase shifts the R-curves to higher values of stress intensity factor. However, the slopes of the R-curves were relatively insensitive to layer thickness over the range examined.

### 1. Introduction

A recent study has shown a strong enhancement of transformation toughening in Ce-ZrO<sub>2</sub> materials containing layers of either Al<sub>2</sub>O<sub>3</sub> or a mixture of Al<sub>2</sub>O<sub>3</sub> and ZrO<sub>2</sub>.<sup>1</sup> The presence of these layers modified the shape and size of the crack tip transformation zone in two ways, both of which increased the degree of crack shielding: the transformation zone spread along the region adjacent to the layers, thus increasing the zone width of a normally incident crack by up to a factor of 10, and the elongated portion of the transformation zone that forms ahead of a crack in uniform Ce-ZrO<sub>2</sub> was truncated by the layers. The toughening was evaluated using controlled crack growth experiments in composites containing multilayered regions embedded within uniform Ce-ZrO<sub>2</sub>. The critical stress intensity factor needed to grow a crack was found to increase from ~ 5 MPa·m<sup>1/2</sup> within the Ce-ZrO<sub>2</sub>, to more than 18 MPa·m<sup>1/2</sup> after growing through ~ 18 layers of 30  $\mu$ m thickness.

In this paper, we investigate the effects of varying the dimensions of the layered regions, increasing the number of layers, and increasing the starting fracture toughness of the Ce-ZrO<sub>2</sub> material.

## 2. Experiments

Composites of Ce-ZrO<sub>2</sub>, with layers containing a mixture of 50% by volume of Al<sub>2</sub>O<sub>3</sub> and Ce-ZrO<sub>2</sub>, were fabricated using a colloidal technique as described previously.<sup>1</sup> The technique involved sequential centrifuging of solutions containing suspended particles to form the layered green body, followed by drying and sintering at 1600°C for 3 h. Use was made of a technique described recently by Velamakanni et al.,<sup>3</sup> and Chang et al.,<sup>4</sup> in which an aqueous electrolyte (NH<sub>4</sub>NO<sub>3</sub>) was used to produce short range repulsive hydration forces and to reduce the magnitudes of the longer range electrostatic forces between the suspended particles. Such conditions produce a weakly attractive network of particles which prevents mass segregation during centrifugation, but, because of the lubricating action of the short range repulsive forces, allows the particles to pack to high green density. Two ZrO<sub>2</sub> powders containing 12 mole% CeO<sub>2</sub> were used, one from Tosoh (TZ12Ce) and the other an experimental powder from Ceramatec. The Ceramatec powder was chosen because other studies have shown that high toughness (~ 14 MPa<sup>1/2</sup>) can be achieved. In our previous work with the Tosoh powder, the fracture toughness of the Ce-ZrO<sub>2</sub> was ~ 5 MPa<sup>1/2</sup>. The alumina powder was from Sumitomo (AKP30). The composites contained multilayered regions sandwiched between regions of uniform Ce-ZrO<sub>2</sub> as illustrated in Fig. 1, in order to allow continuous measurement of crack growth, first through the Ce-ZrO<sub>2</sub> then through the layered region.

Crack growth experiments with notched beams were done in two steps, using two different loading fixtures, which operated on the stage of an optical microscope and allowed high magnification observation of the side of the beam during loading.<sup>1</sup> All experiments were done in a dry nitrogen atmosphere. The dimensions of the beams were approximately 28 x 6 x 1 mm, with

the initial notch of 170  $\mu\text{m}$  width and approximately 2 mm depth. First, a stable crack was initiated from the root of the notch under monotonic loading, using a very stiff fixture that made use of WC/Cu flexure beams in series with the test specimen.<sup>1</sup> The beams were equivalent to very stiff springs in parallel with the specimen and thus acted as a crack arrester. The initial crack growth was induced without use of a load cell, in order to stiffen the loading system further. After thus growing the crack for  $\sim 500 \mu\text{m}$ , the loading system was changed to include a load cell with conventional four-point loading through rollers in order to allow measurement of the fracture toughness (or crack growth resistance). As the cracks grew stably through the layered composites, the stress intensity factors were evaluated from the measured loads and crack lengths (obtained from optical micrographs) using the expression from Ref. 5.

### 3. Results

Composites were fabricated using the Tosoh powder with the layer arrangement of Fig. 1 with four different layer thicknesses, as shown in Fig. 2. The critical stress intensity factor,  $K_R$ , measured as a function of crack growth up to and through the layered regions are shown in Fig. 3, with the crack position being measured relative to the beginning of the layers to allow direct comparison of the responses of the different layer thicknesses (crack growth in the Ce-ZrO<sub>2</sub> up to the layers thus corresponds to negative position in this plot). Three of the specimens contained 20 layers and one contained 40 layers. In all cases,  $K_R$  increased almost linearly as the cracks grew through the layers. The peak value of  $K_R$  coincided with the onset of unstable growth as the crack approached the end of the layered region and the transformation zone penetrated the Ce-ZrO<sub>2</sub> beyond. Therefore, since there is no indication in these data of  $K_R$  saturating to a constant value, the maximum toughnesses are limited by the finite extent of the layered regions. The slopes of the R-curves are all similar, although there is an indication that the slope is maximum at a layer thickness of  $\sim 35 \mu\text{m}$ .

The cracks used for the quasi-static resistance curve measurements of Fig. 3 were all surrounded by transformation zones that increased in width from  $\sim 15 \mu\text{m}$  in the Ce-ZrO<sub>2</sub> to  $\sim 200 \mu\text{m}$  at the end of the layered region. These transformation zones were observed by optical interference microscopy, which detects out-of-plane surface distortions due to the transformation strain. Increasing zone widths have also been observed for cracks that were growing unstably through the layers. An example is shown in Fig. 4 for a crack that grew unstably during initiation from the initial notch and arrested after penetrating the first three layers of Al<sub>2</sub>O<sub>3</sub>/ZrO<sub>2</sub> (the fringes in this micrograph correspond to contours of constant surface uplift).

Resistance curves from two composites fabricated with Ceramatec powder are shown in Fig. 5. One of these composites was sintered almost to full density and contained 21 layers, whereas the other contained 10% porosity and 41 layers. In both composites,  $K_R$  increased almost linearly, with similar slope, as the cracks grew through the layers. However, in the fully dense composite, the R-curve was displaced to larger values of  $K_R$  by an amount ( $\sim 4 \text{ MPa}\cdot\text{m}^{1/2}$ ) equal to the difference in fracture toughnesses of the Ce-ZrO<sub>2</sub> materials ( $\sim 5-6 \text{ MPa}\cdot\text{m}^{1/2}$  in the low density material, c.f.,  $9-10 \text{ MPa}\cdot\text{m}^{1/2}$  in the higher density material). The peak values of  $K_R$  were limited by unstable crack growth as the cracks approached the ends of the layered regions and transformation zones penetrated the uniform Ce-ZrO<sub>2</sub>.

The widths of the transformation zones in the composite containing the higher toughness Ceramatec Ce-ZrO<sub>2</sub> were much larger than in the other materials. The initial zone width within the Ce-ZrO<sub>2</sub> was  $\sim 200 \mu\text{m}$  (Fig. 6(a), c.f.,  $\sim 15 \mu\text{m}$  in the Tosoh material). After the crack had penetrated  $\sim 10$  of the layers, the transformation zone had spread to a width of  $\sim 3 \text{ mm}$  (Fig. 6(b)). At this stage, the front of the zone penetrated the uniform Ce-ZrO<sub>2</sub> beyond the layered region. The crack then grew unstably and arrested after extending  $\sim 1 \text{ mm}$  into the Ce-ZrO<sub>2</sub>. The zone width within the Ce-ZrO<sub>2</sub> beyond the layered region (Fig. 6(c)) was much larger ( $\sim 1.5 \text{ mm}$ ) than the steady-state zone width for a crack grown in this Ce-ZrO<sub>2</sub> material (such as in front of the layers, where the zone width is  $\sim 200 \mu\text{m}$ ), but smaller than the zone width within the layers. This result

suggests that the zone width of the unstable crack as it exits the layered region is determined by the applied stress intensity factor, as it would be for a quasi-statically growing crack (zone width approximately proportional to  $K^2$ ). The measured increase in zone width from 200  $\mu\text{m}$  to 1.5 mm would correspond to an increase in  $K$  by a factor of approximately 2.7, roughly consistent with the observed increase in  $K$  at the point of instability.

#### **4. Discussion**

All of the composites tested exhibited crack resistance curves that increased almost linearly as the cracks grew through the layered regions. The slopes of the R-curves were similar in composites with various layer thicknesses, although the slope of the R-curve from the composite with intermediate thickness layer (35  $\mu\text{m}$ ) was significantly higher than the others. Although the range of layer thicknesses tested was not large (~ 25  $\mu\text{m}$  to 70  $\mu\text{m}$ ), these results do show that the previously observed toughening effect is not limited to a narrow range of layer thicknesses. The peak toughnesses measured were in the range 14-18  $\text{MPa}\cdot\text{m}^{1/2}$ , limited in all cases by the finite extent of the layered regions (there was no evidence of an approach to steady state in the R-curves).

The large transformation zones observed in the composite with the higher toughness Ceramatec  $\text{ZrO}_2$  suggest that very high fracture toughnesses could be achieved in a composite containing more layers. With the observed zone width (which had not saturated) of 3 mm and the relation  $K_S \propto \sqrt{w}$ ,<sup>6,7</sup> where  $K_S$  is the steady-state shielding stress intensity factor and  $w$  is the zone width, a fracture toughness of more than 30  $\text{MPa}\cdot\text{m}^{1/2}$  would be predicted.

#### **5. Acknowledgement**

Funding for this work was provided by the U.S. Air Force Office of Scientific Research under Contract No. F49620-89-C-0031. The colloidal science research on short range repulsive potentials that led to the method for forming the layered structure was supported at UCSB by the

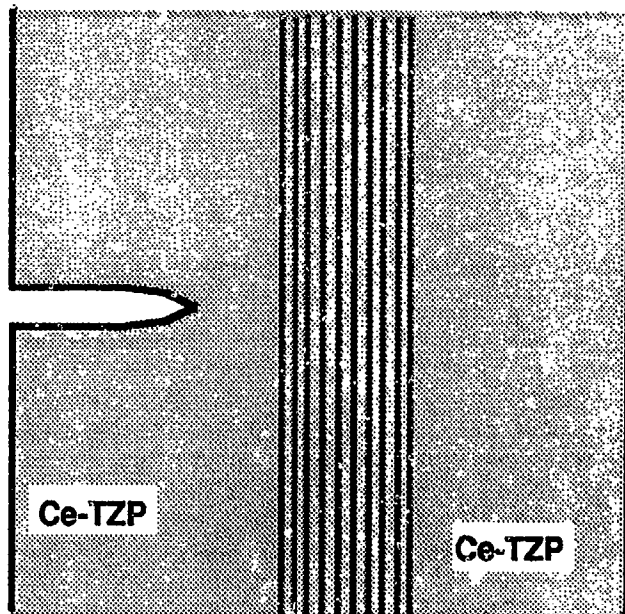
Office of Naval Research under Contract No. N00014-90-J-1141. The authors are grateful to R. Cutler of Ceramatec for supplying the Ce-ZrO<sub>2</sub> powder used to fabricate the highly transformable material.

### References

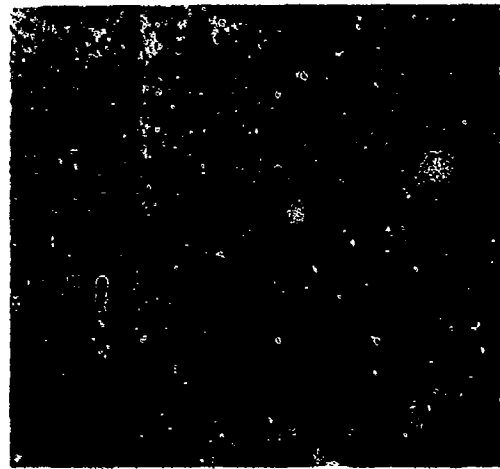
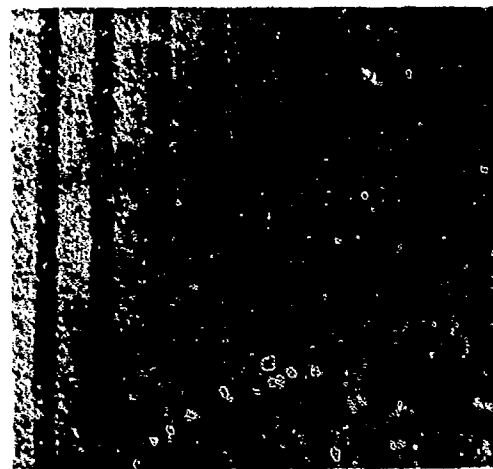
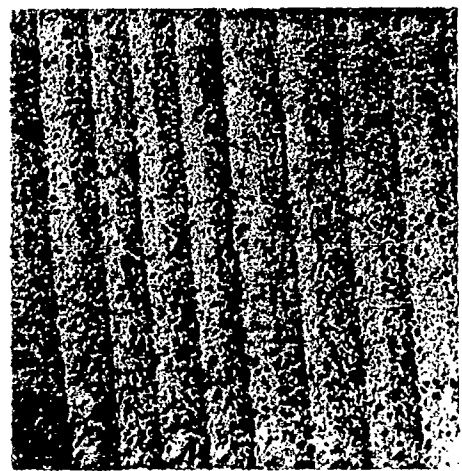
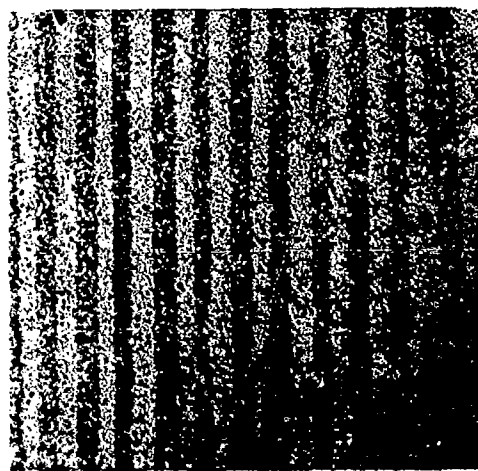
1. D.B. Marshall, J.J. Ratto and F.F. Lange, "Enhanced Fracture Toughness in Layered Microcomposites of Ce-ZrO<sub>2</sub> and Al<sub>2</sub>O<sub>3</sub>," *J. Am. Ceram. Soc.* 74[12] 2979-87 (1991).
2. D.B. Marshall, "The Design of High Toughness Laminar Zirconia Composites," *Bull. Amer. Ceramic Soc.*, in press.
3. B.V. Velamakanni, J.C. Chang, F.F. Lange and D.S. Pearson, "New Method for Efficient Colloidal Particle Packing Via Modulation of Repulsive Lubricating Hydration Forces," *Langmuir* 6, 1323-25 (1990).
4. J.C. Chang, F.F. Lange and D.S. Pearson, "Centrifugal Consolidation of Al<sub>2</sub>O<sub>3</sub> and Al<sub>2</sub>O<sub>3</sub>/ZrO<sub>2</sub> Composite Slurries vs Interparticle Potentials: Particle Packing and Mass Segregation," *J. Am. Ceram. Soc.*, in press.
5. H. Tada, The Stress Analysis of Cracks Handbook, 2nd Edition, Paris Prod. Inc., St. Louis (1985).
6. R.M. McMeeking and A.G. Evans, "Mechanics of Transformation Toughening in Brittle Materials," *J. Am. Ceram. Soc.* 65[5] 242-46 (1982).
7. D.B. Marshall, A.G. Evans and M. Drory, "Transformation Toughening in Ceramics," p. 289 in Fracture Mechanics of Ceramics, Vol. 6, edited by R.C. Bradt, A.G. Evans, D.P.H. Hasselman and F.F. Lange, Plenum Press, New York (1983).

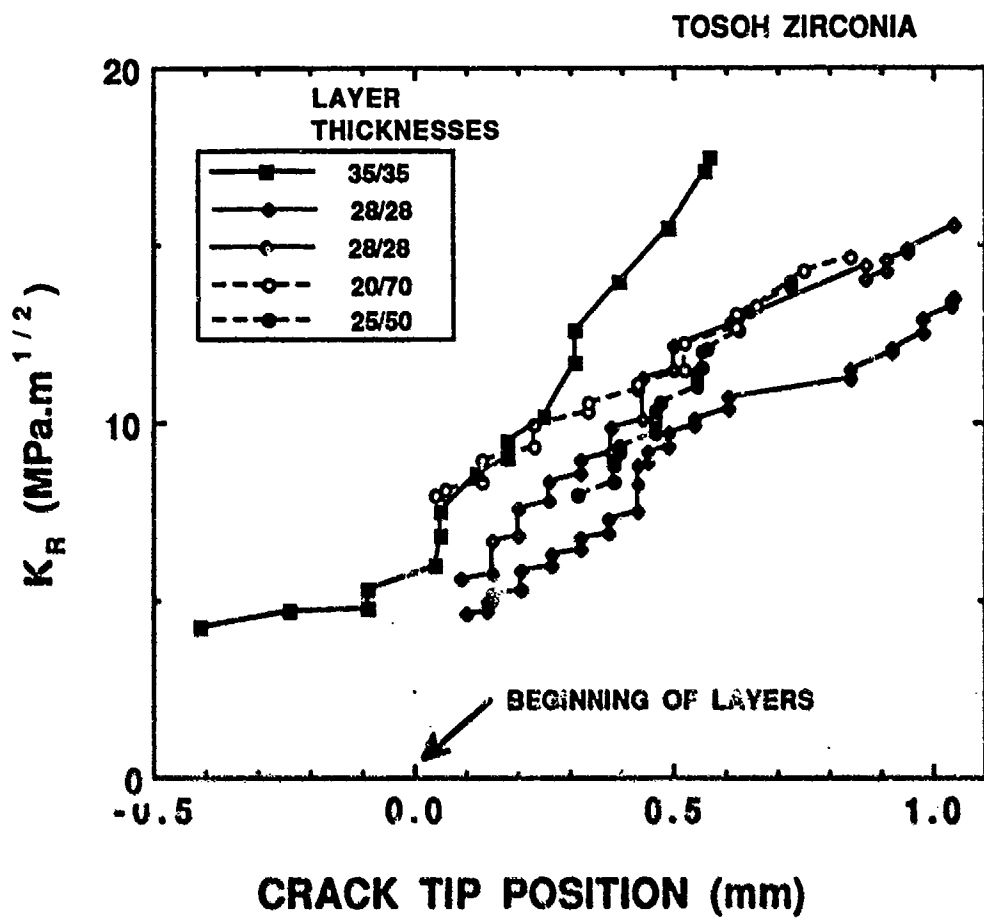
## FIGURE CAPTIONS

1. Layered composite test specimen.
2. Optical micrographs of multilayered composites fabricated with Tosoh powder: darker phase is  $\text{Al}_2\text{O}_3$ , lighter phase is  $\text{Ce-ZrO}_2$ .
3. Crack resistance curves from the composites shown in Fig. 2. Data labeled by layer thicknesses of  $\text{Al}_2\text{O}_3/\text{ZrO}_2$  in microns.
4. Optical interference micrograph showing transformation zone around crack that initiated unstably in the  $\text{Ce-ZrO}_2$  and arrested in the layered region.
5. Crack resistance curves for multilayered composites fabricated from Ceramatec  $\text{Ce-ZrO}_2$  powder. Data labeled by  $\text{Al}_2\text{O}_3/\text{ZrO}_2$  layer thickness in microns.
6. In situ optical micrographs (Nomarski interference) from specimen of Fig. 5 (25  $\mu\text{m}$   $\text{Al}_2\text{O}_3/\text{ZrO}_2$  layer thickness, 50  $\mu\text{m}$   $\text{Ce-ZrO}_2$ ) at several stages of crack growth:
  - (a) crack within uniform  $\text{Ce-ZrO}_2$ ,
  - (b) crack extended partly through multilayered region, and
  - (c) after crack grew unstably out of multilayered region.



**LAYERS**  
 $\text{Al}_2\text{O}_3$  / Ce-TZP



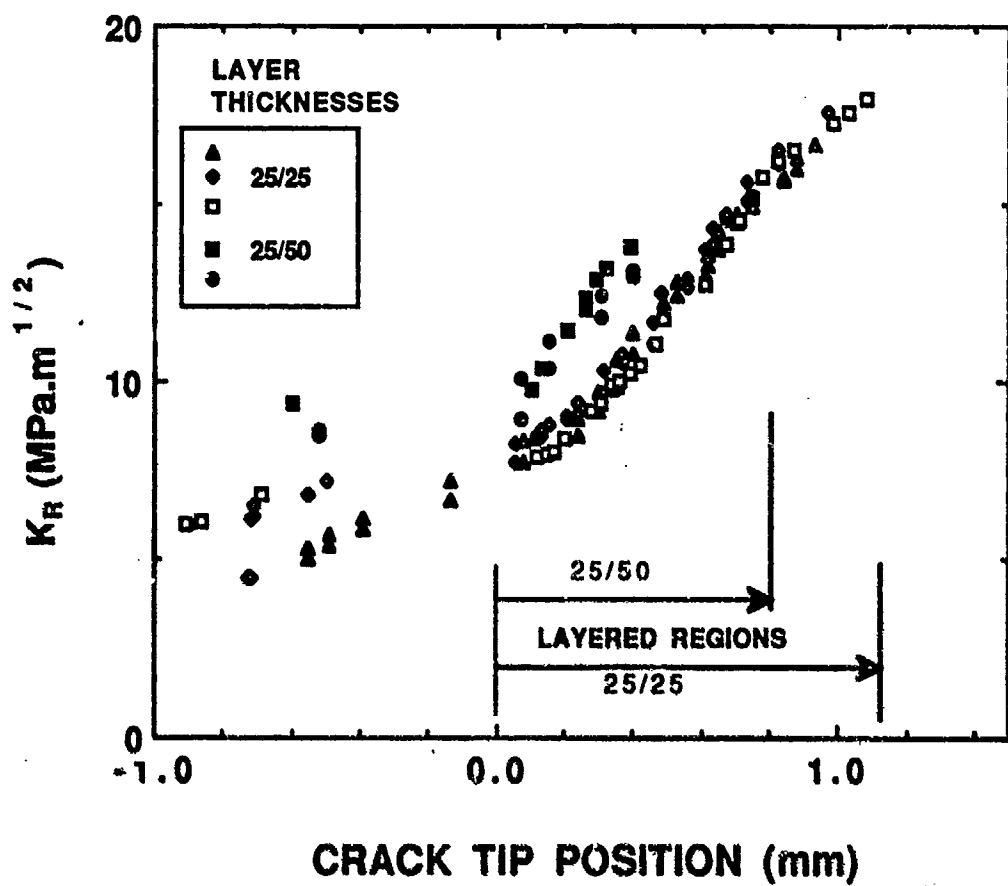


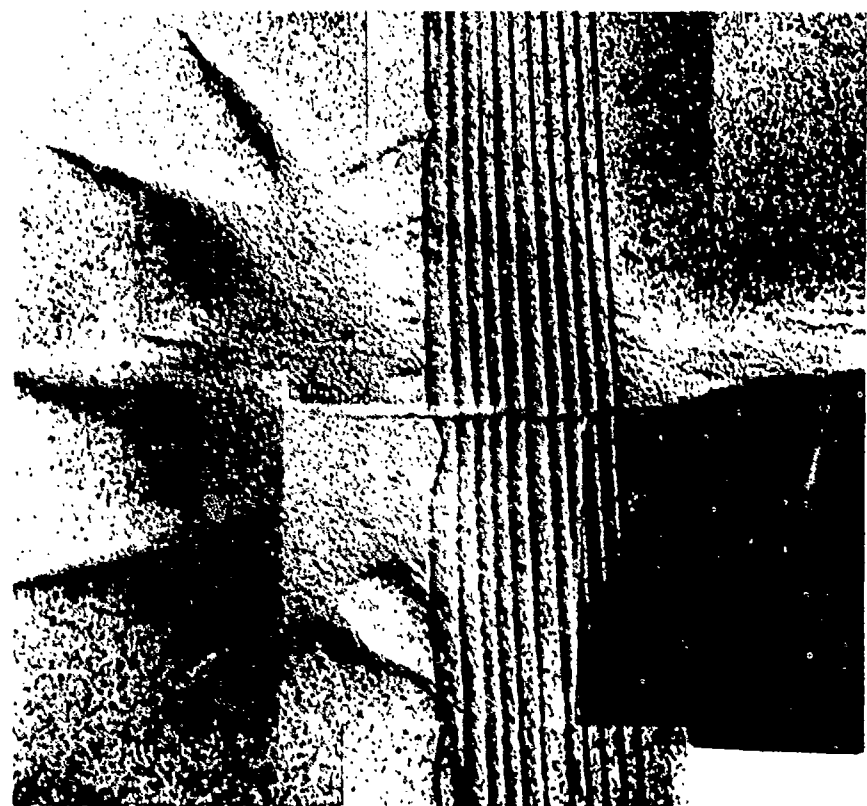
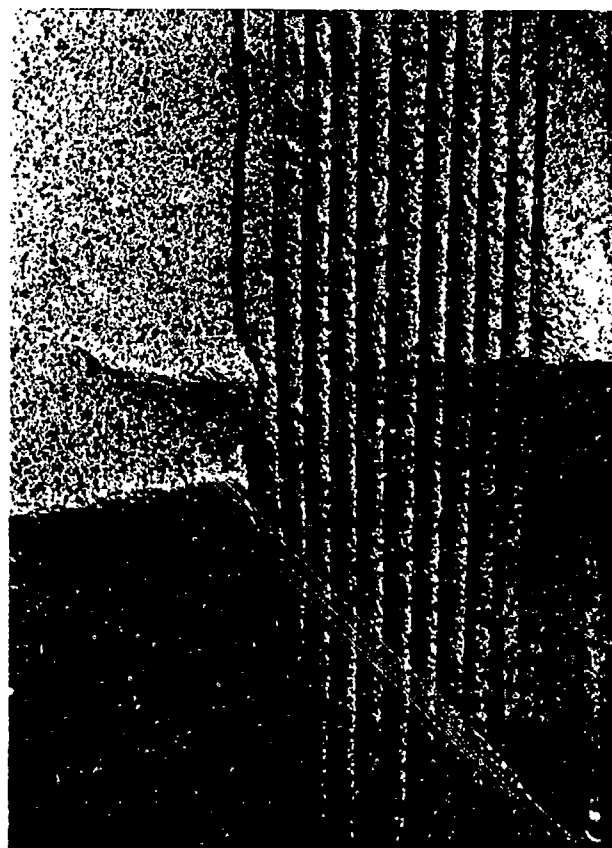
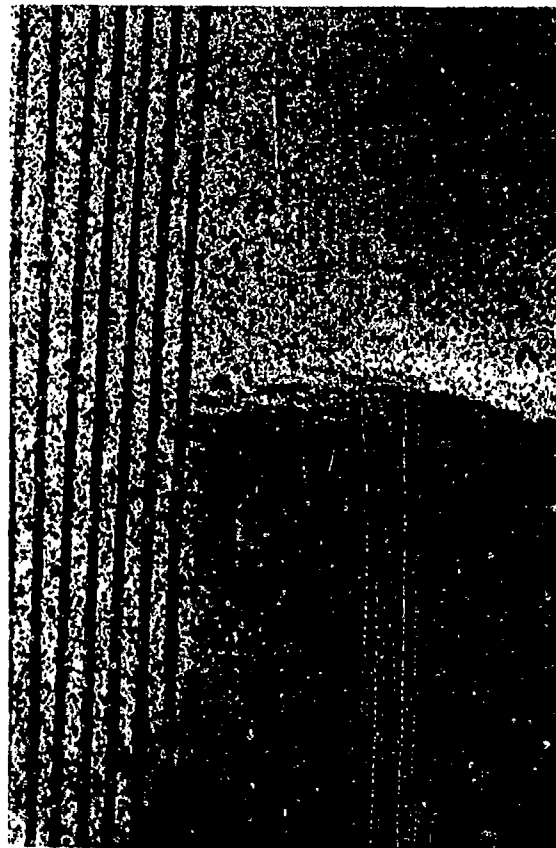


Ce-ZrO<sub>2</sub>  $\nearrow$  Al<sub>2</sub>O<sub>3</sub> / Ce-ZrO<sub>2</sub>

25  $\mu\text{m}$

50  $\mu\text{m}$







Rockwell International

Science Center

SC71002.FR

#### 4.0 ANALYSIS OF CRACK SHIELDING AND ZONE SHAPE EFFECTS



**Rockwell Internatio**  
Science Center  
SC71002.FR

**4.1 TRANSFORMATION ZONE SHAPE EFFECTS IN CRACK SHIELDING  
IN CERIA-PARTIALLY STABILIZED ZIRCONIA (Ce-TZP)-ALUMINA  
COMPOSITES**

to be published in J. Am. Ceram. Soc.

# TRANSFORMATION ZONE SHAPE EFFECTS ON CRACK SHIELDING IN CERIA-PARTIALLY-STABILIZED ZIRCONIA (Ce-TZP)-ALUMINA COMPOSITES

Cheng-Sheng Yu and Dinesh Shetty

Department of Materials Science and Engineering  
University of Utah  
Salt Lake City, UT 84112

Michael C. Shaw and David B. Marshall

Rockwell International Science Center  
1049 Camino Dos Rios  
Thousand Oaks, CA 91360

## ABSTRACT

Crack tip shielding is evaluated for observed transformation zones in Ce-TZP/Al<sub>2</sub>O<sub>3</sub> composites, in which the transformation zone sizes were changed significantly by varying the sintering temperature to control the transformation yield stress. The calculated shielding effects are consistent with an observed insensitivity of crack resistance curves to transformation zone size; smaller zones in materials with higher yield stress were associated with larger ratios of wake length to zone width and correspondingly higher normalized shielding stress intensity factor. Shielding due to the dilatational component of the transformation strain accounted for most of the toughening observed in these materials.

## 1. INTRODUCTION

In a recent study, Yu and Shetty<sup>1</sup> measured crack resistance curves (R-curves) in a series of Ce-TZP/Al<sub>2</sub>O<sub>3</sub> materials that had been sintered at various temperatures to vary the transformation yield stress within the range 190-390 MPa. The specimen geometry used for these measurements allowed stable crack growth for the initial, rising part of the resistance curve

(typically for crack extensions of 1 to 2 mm). However, unstable crack growth occurred before reaching a steady-state toughness. The widths of the transformation zones at the instability points varied from  $\sim 30 \mu\text{m}$  in the material with the highest yield stress to  $300 \mu\text{m}$  in the material with the lowest yield stress. Despite this large variation in zone size, the R-curves were almost the same in all of the materials, with instability occurring at an applied stress intensity factor of  $\sim 15 \text{ MPa}\cdot\text{m}^{1/2}$ .

Calculations of the crack tip shielding due the observed transformation zones in the material with the lowest yield stress have shown that the measured stress intensity factors were consistent with most of the toughening being due to shielding associated with the dilatational component of the transformation zone.<sup>2</sup> In this paper we present more extensive calculations to investigate whether the measured R-curves for these materials are consistent with shielding, and especially to rationalize the observed insensitivity of the R-curves to the transformation yield stress.

## 2. MATERIALS AND TEST PROCEDURES

The processing, microstructures, and mechanical properties of the Ce-TZP/Al<sub>2</sub>O<sub>3</sub> materials used in this study are described elsewhere.<sup>1,3</sup> The nominal compositions were 12 mole % CeO<sub>2</sub>-ZrO<sub>2</sub> + 10 weight % Al<sub>2</sub>O<sub>3</sub> + 2 weight % proprietary dopant. The same notation as in a previous paper is used to identify materials fabricated from two powder batches (I and II) and sintered at 1500, 1475 and 1450°C (A, B and C) (Table 1).

R-curves were measured using single-edge-notched bend specimens as described elsewhere.<sup>1</sup> In all cases the specimens were precracked under monotonic loading and then annealed to eliminate the transformation zone. The R-curves were then evaluated using incremental loading, with unloading at various stages to allow measurement of the transformation zone.

The transformation zone dimensions were measured from optical Nomarski interference micrographs which highlight surface uplift caused by dilatation within the zone. The relative concentrations of monoclinic and tetragonal phases adjacent to the cracks were measured by x-ray diffraction from the fracture surfaces.<sup>4</sup> In a material made from a third batch of powder and annealed at 1500°C (i.e., type IIIA), Raman spectroscopy was used to measure the relative distributions of monoclinic and tetragonal phases within transformation zones. These measurements were obtained using a microprobe system (~ 2  $\mu\text{m}$  lateral resolution) which was scanned along several lines traversing transformation zones that were formed during interrupted R-curve tests.

### 3. ZONE SHAPES AND R-CURVES

The large differences in sizes of the crack tip transformation zones in the various Ce-TZP/Al<sub>2</sub>O<sub>3</sub> materials at given applied stress intensity factor,  $K_a$ , are shown in Fig. 1. For the purpose of the shielding calculations in the following section, the zone shapes can be approximated as shown in Fig. 1(e), with triangular shapes ahead of and behind the crack tip. The zone size is then characterized by the width  $w$ , and the shape by the normalized lengths  $l/w$  and  $d/w$ .

The measured R-curves for these four materials are shown in Fig. 2(a), and the corresponding zone dimensions are shown in Figs. 2(b)-(d). Despite the large differences in zone width at given  $K_a$ , all of the R-curves are almost the same. The parameter  $l/w$ , which defines the frontal zone, is roughly constant during crack growth and is the same for all materials, most values falling within the range 9 to 13. The wake zone parameter  $w/d$  decreases with crack extension for a given material and increases with decreasing yield stress at given crack extension.

The variation of the volume fraction of monoclinic phase with distance from the crack, as measured by Raman spectroscopy, is shown in Fig. 3. A continuous decrease in  $f$  with distance is evident, similar to that reported in  $\text{MgO-ZrO}_2$  materials,<sup>5</sup> with a significant amount of transformed material lying outside the zone boundary that was inferred from the Nomarski interference image. This difference arises because the contrast in Nomarski interference is caused by changes in inclination of the surface rather than absolute surface displacement; the highest contrast occurs where  $f$  changes most rapidly. X-ray measurements from the fracture surfaces of the specimens used for Figs. 1 and 2 (Table 1) suggest that the fraction of monoclinic phase adjacent to the crack decreases slightly with increasing yield stress. However, these measurements represent values averaged over the penetration depth of the x-rays ( $\sim 20 \mu\text{m}$ ). For the material with the lowest yield stress, the gradient in  $f$  is not significant. However, for the other materials, with smaller zone widths, a significant decrease in  $f$  occurs within the penetration depth (assuming that the zone profile of Fig. 3 scales with the zone width). With this spatial variation in  $f$  accounted for, the x-ray results would indicate that the value of  $f$  at the fracture surface is approximately the same for all of the materials ( $f \approx 0.8$ ).

#### 4. CRACK SHIELDING CALCULATIONS

For a transformation zone with the shape depicted in Fig. 1(e), containing a uniform volume fraction,  $f$ , of transformed material with a net hydrostatic transformation strain,  $\epsilon^T$ , the shielding stress intensity factor,  $K_s$ , can be written

$$\frac{K_s(1-v)}{\epsilon^T E f w} = \kappa \left( \frac{w}{l}, \frac{w}{d} \right) \quad (1)$$

where  $v$  is the Poisson's ratio,  $E$  is Young's modulus, and  $\kappa$  is a function of the zone shape parameters.<sup>5</sup> The function  $\kappa$  can be evaluated using the weight function method of McMeeking and Evans,<sup>6</sup> as described for zones of similar shape in Ref. 2. This expression can be readily modified to account for nonuniform  $f$  within the zone, if contours of constant  $f$  are geometrically similar. In that case,  $fw$  in Eq. (1) is replaced by

$$fw \rightarrow \int_0^w \frac{f(x)}{2\sqrt{x}} dx \equiv f_0 w \int_0^w \frac{g(x/w)}{2\sqrt{x/w}} d(x/w) \quad (2)$$

where  $f(x)$  is the volume fraction of transformed material as a function of distance,  $x$ , from the crack. In the normalized expression on the right side of Eq. (2),  $f_0$  is the value of  $f(x)$  adjacent to the crack ( $x = 0$ ),  $g(x/w)$  is the normalized function  $f(x)/f_0$ , and  $w$  is a length scale that can be chosen arbitrarily. For the following calculations we take  $w$  as the zone width measured by Nomarski interference (as indicated in Fig. 3), and assume that  $g(x/w)$  is given by Fig. 3 for all of the materials. Then, evaluation of the integral in Eq. (2) gives

---

<sup>5</sup> For the zone shape of Fig. 1(e),  $\kappa$  is not strictly independent of  $v$  as it is for the zones analyzed by McMeeking and Evans. However, the variation with  $v$  is very weak (< 2% for  $v = 0.2$  to 0.3).

$$\int_0^1 \frac{g(x/w)}{2\sqrt{x/w}} d(x/w) = 0.9. \quad (3)$$

With  $f_0 = 0.8$  from the x-ray measurements, Eqs. (1), (2) and (3) give

$$K_s = \frac{e^T E f w}{1-v} \kappa \left( \frac{w}{l}, \frac{w}{d} \right) \quad (4)$$

where  $f = 0.7$ .

The shielding stress intensity factors evaluated from Eq. (4) using the measured values of zone parameters  $w$ ,  $w/d$  and  $l/w$  (Figs. 2(b) to (d)), with  $E = 200$  GPa,  $v = 0.3$  and  $e^T = 0.04$ , are compared with the measured R-curve data in Fig. 4(a). The values of  $K_s$  fall on a curve with shape that is similar to that of the R-curve but displaced by a constant amount to smaller values of  $K$ . The differences,  $K_R - K_s$ , for all of the data are plotted in Fig. 4(b). The difference is approximately constant, most values falling within the range 4 to 5 MPa·m<sup>1/2</sup>.

## S. DISCUSSION

The crack resistance,  $K_R$ , at any point on the R-curve is given by the sum of the following contributions: the toughness,  $K_0$ , of the transformed  $ZrO_2$ ; the shielding stress intensity factor,  $K_s$ , due to the dilatational component of the transformation strain; shielding due to the shear component of the transformation strain; and contributions from other toughening mechanisms. The value of  $K_0$  would be expected to be  $\sim 3$  MPa·m<sup>1/2</sup>. Therefore, since the results in Fig. 4 show that  $K_R - K_s \sim 4$  to 6 MPa·m<sup>1/2</sup>, it is evident that the measured values of  $K_R$  are almost fully accounted for by the sum of  $K_0$  and  $K_s$ . The results also indicate that the observed

insensitivity of the R-curves to the transformation yield stress (i.e., transformation zone size) is consistent with the values of  $K_s$  calculated with the observed zone sizes and shapes.

The insensitivity of  $K_R$  to transformation yield stress warrants further examination. During initial loading in these experiments, the transformation zone extends behind the crack tip a distance  $d_0$  before the crack begins to grow, as indicated in Fig. 1(e). After the crack extends by  $\Delta a$ , the wake zone length,  $d$ , is

$$d = d_0 + \Delta a \quad (5)$$

where the values of  $d_0$  range from 80 to 150  $\mu\text{m}$  (but not systematically with yield stress). Thus, if we take  $d_0$  as approximately constant (valid for sufficiently large crack extensions), the value of  $d$  at given crack extension is approximately the same for all materials. Moreover the values of  $l/w$  are approximately the same for all of the zones measured in this study (Fig. 2). Therefore, the relative zone shapes in different materials at given crack extension are roughly as shown schematically in Fig. 5. The tendency for  $K_s$  to increase with increasing zone size ( $K_s \propto \sqrt{w}$ , Eq. (1)) is thus cancelled by the effect of changing zone shape, which causes  $\kappa$  in Eq. (1) to decrease (as the zone gets larger in changing to materials with lower yield stress, the frontal shape remains constant, but the relative extent of the wake zone ( $d/w$ ) decreases (Fig. 2)). The combined effect of these two changes is conveniently assessed by rewriting Eq. (4) as

$$K_s = \frac{E^T E f' \sqrt{d}}{(1-v)} \left[ 1/\sqrt{\frac{w}{d}} - \kappa \left( \frac{w}{d}, \frac{w}{l} \right) \right], \quad (6)$$

so that  $K_s$  is proportional to the term in square brackets at given  $\Delta a$  (i.e., given  $d$ ). This term is plotted in Fig. 5 as a function of  $w/d$  for fixed  $l/w = 13$ . Over the ranges of  $w/d$  observed in the

four materials of this study (as marked in Fig. 5), this term varies slowly, thus explaining the observed insensitivity of  $K_s$  to the value of w/d.

With the value of  $\left[ \sqrt{\frac{w}{d}} \kappa \left( \frac{w}{d}, \frac{w}{l} \right) \right]$  given by Fig. 5, Eqs. (5) and (6) provide an approximate expression for the R-curve:

$$K_s = \left[ \frac{e^T E f}{(1-v)} \left[ \sqrt{\frac{w}{d}} \kappa \left( \frac{w}{d}, \frac{w}{l} \right) \right] \right] \sqrt{d + \Delta a} \quad (7)$$

The edges of the shaded regions in Fig. 4(a) are defined by Eq. (5), evaluated using values of  $e^T$ ,  $E$ ,  $v$ , and  $f$  as defined earlier, and with  $\left[ \sqrt{\frac{w}{d}} \kappa \left( \frac{w}{d}, \frac{w}{l} \right) \right] = 0.022$  and  $0.035$ , representing the approximate extremes within the ranges of w/d indicated in Fig. 5.

Materials with w/d far out of the range of the present experiments would not exhibit the insensitivity of the R-curve to yield stress, since the curve in Fig. 5 decreases rapidly with changing w/d outside this range. Moreover, since the slope of the R-curve is proportional to  $\left[ \sqrt{\frac{w}{d}} \kappa \left( \frac{w}{d}, \frac{w}{l} \right) \right]$ , materials with w/d out of the range of the present experiments would also have R-curves of lower slope. Finally, we emphasize that all of the results discussed here pertain to the initial, rising part of the R-curve, where the zone shapes are approximately as depicted in Fig. 1(c). At larger crack extensions, the R-curves would be expected to diverge and approach steady state values, corresponding to transformation zones with uniform widths over the crack wakes. The steady state values of  $K_R$  would be expected to increase with increasing zone size.

## 6. CONCLUSIONS

1. The insensitivity of measured initial rising portions of R-curves in Ce-TZP/Al<sub>2</sub>O<sub>3</sub> materials to variations in transformation zone size is consistent with the calculated effect of zone shape on

crack shielding. The smaller zones were more efficient in shielding the crack tip because of their larger ratio of wake length to zone width.

2. Most of the measured toughening in Ce-TZP/Al<sub>2</sub>O<sub>3</sub> can be accounted for by crack tip shielding due to the dilatational component of the martensitic tetragonal-to-monoclinic transformation.

#### ACKNOWLEDGEMENT

This research was supported at the University of Utah by the Army Research Office under Contract No. DAAL03-87-0060 and at Rockwell Science Center by the U.S. Air Force Office of Scientific Research under Contract No. F49620-89-C-0031.

#### REFERENCES

1. C.S. Yu and D.K. Shetty, "Transformation Yielding, Plasticity and Crack-Growth-Resistance (R-Curve) Behavior of CeO<sub>2</sub>-TZP," *J. of Mater. Sci.*, **25**, 2025-2035 (1990).
2. D.B. Marshall, "Crack Shielding in Ceria-Partially-Stabilized Zirconia," *J. Am. Ceram. Soc.*, **73** [10] 3119-21 (1990).
3. J.F. Tsai, C.S. Yu and D.K. Shetty, "Fatigue Crack Propagation in Ceria-Partially-Stabilized Zirconia (Ce-TZP)-Alumina Composites," *J. Am. Ceram. Soc.* **73** [10] 2992-3001 (1990).

4. H. Toraya, M. Yoshimura and S. Somiya, "Calibration Curve for Quantitative Analysis of the Monoclinic-Tetragonal  $ZrO_2$  System by X-Ray Diffraction," *J. Am. Ceram. Soc.*, **71** [5] 343-53 (1988).
5. D.B. Marshall, M.C. Shaw, R.H. Dauskardt, R.O. Ritchie, M.J. Radey and A.H. Heuer, "Crack-Tip Transformation Zones in Toughened Zirconia," *J. Am. Ceram. Soc.*, **73** [9] 2659-66 (1990).
6. R.M. McMeeking and A.G. Evans, "Mechanics of Transformation-Toughening in Brittle Materials," *J. Am. Ceram. Soc.*, **65** [5] 242-46 (1982).

**Table 1**  
**Ce-TZP/Al<sub>2</sub>O<sub>3</sub> Composites**

Composite Type	Sintering Temperature (°C)	Yield Stress (MPa)	f*
IA	1500	190 ± 5	0.85
IIA	1500	236 ± 13	0.82
IIB	1475	280 ± 6	0.81
IIC	1450	326 ± 9	0.78

\*Volume fraction of monotonic phase on the fracture surface, determined from x-ray diffraction analysis.

## Figure Captions

1. Nomarski interference micrographs showing crack tip transformation zones in SENB specimens of four types of Ce-TZP/Al<sub>2</sub>O<sub>3</sub> composites, at applied stress intensity factor of 10 MPa·m<sup>1/2</sup>: (a) type IA, (b) type IIA, (c) type IIB, (d) type IIC, (e) schematic of zone shape.
2. (a) Crack resistance curves for the materials of Fig. 1, measured using single-edge-notched-beam specimens. (b), (c) and (d) transformation zone dimensions (as defined in Fig. 1(e)) corresponding to the data of (a).
3. (a) Variation of volume fraction of monoclinic phase adjacent to crack in type IIIA Ce-TZP/Al<sub>2</sub>O<sub>3</sub> composite, measured by Raman spectroscopy. (b) Crack tip transformation zone used for (a) showing scan line.
4. (a) Comparison of resistance curve data from Fig. 2(a) and calculated shielding stress intensity factors. Shaded bands are representations of Eq. 5. (b) Differences between measured applied stress intensity factors and the calculated shielding stress intensity factor.
5. Variation of shielding stress intensity factor with zone shape parameter, w/d. Inset shows relative zone sizes and shapes at given crack extension in Ce-TZP/Al<sub>2</sub>O<sub>3</sub> materials of different yield stress.

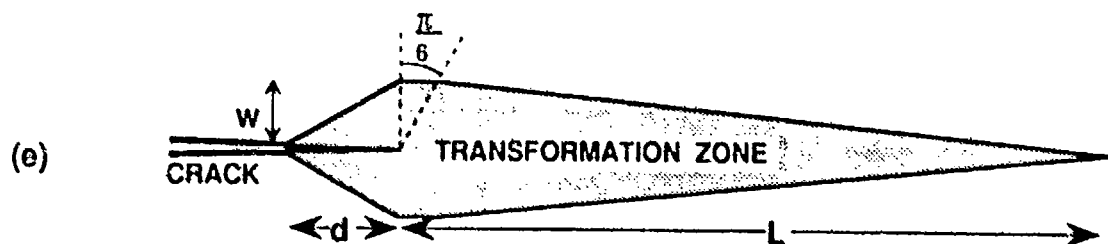
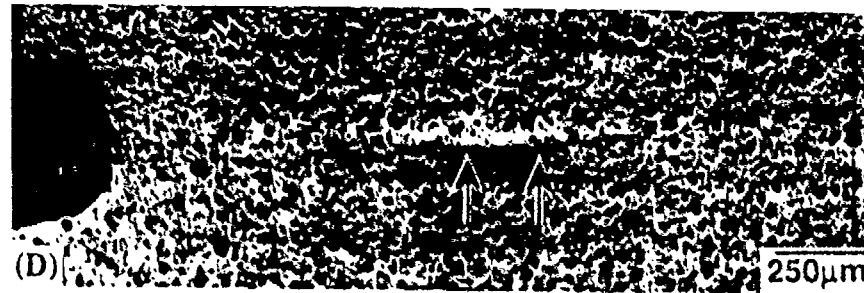
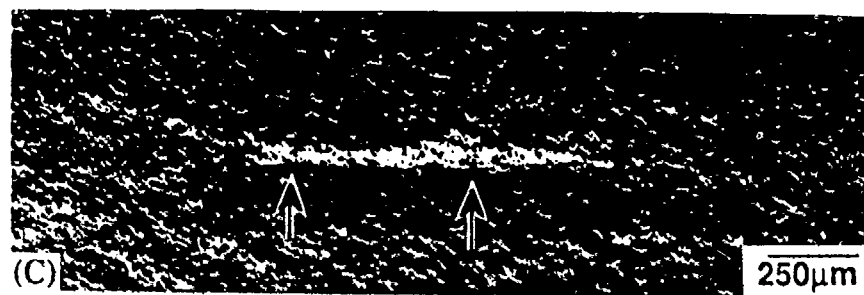
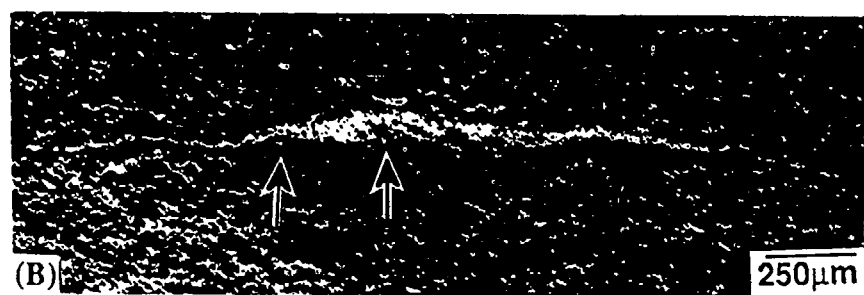
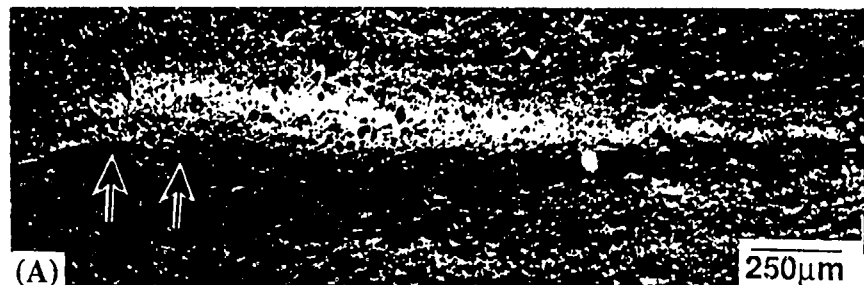


Fig. 1

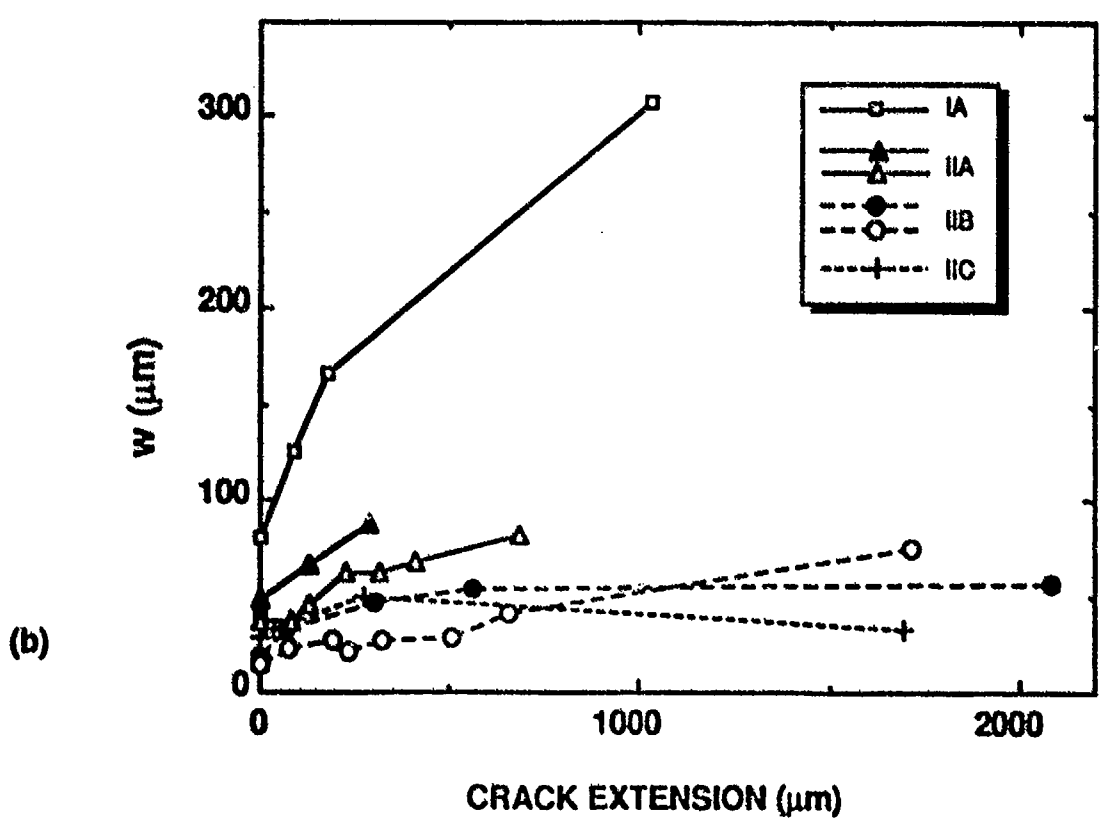
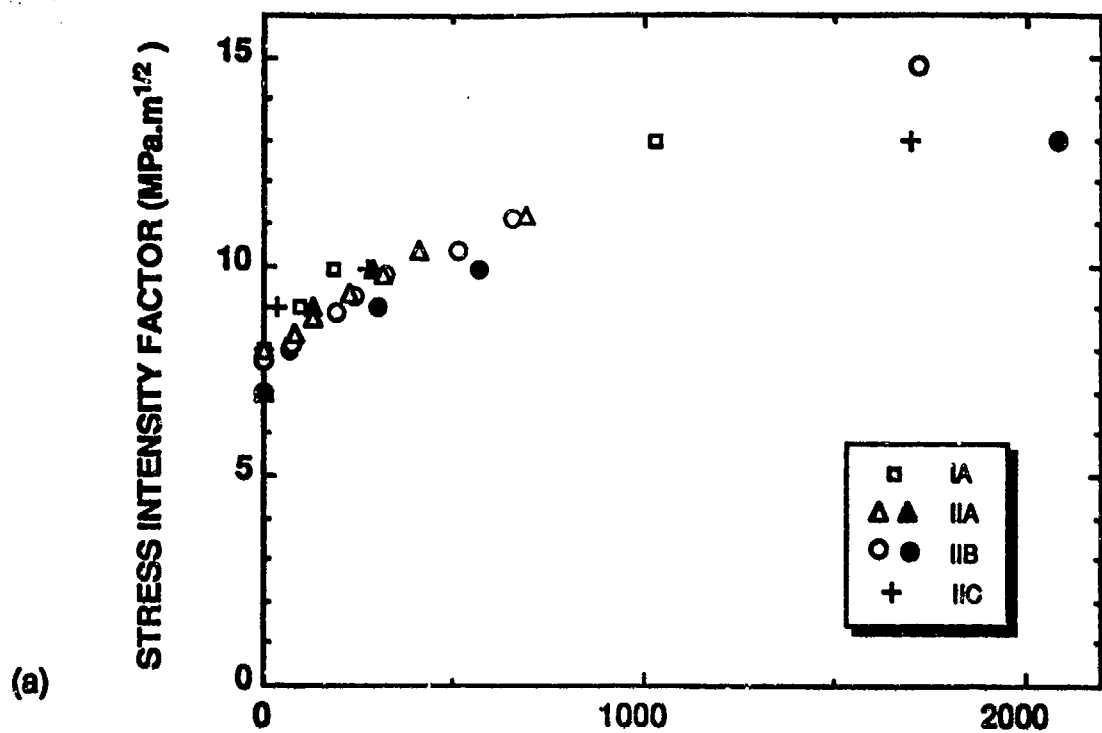


Fig.2

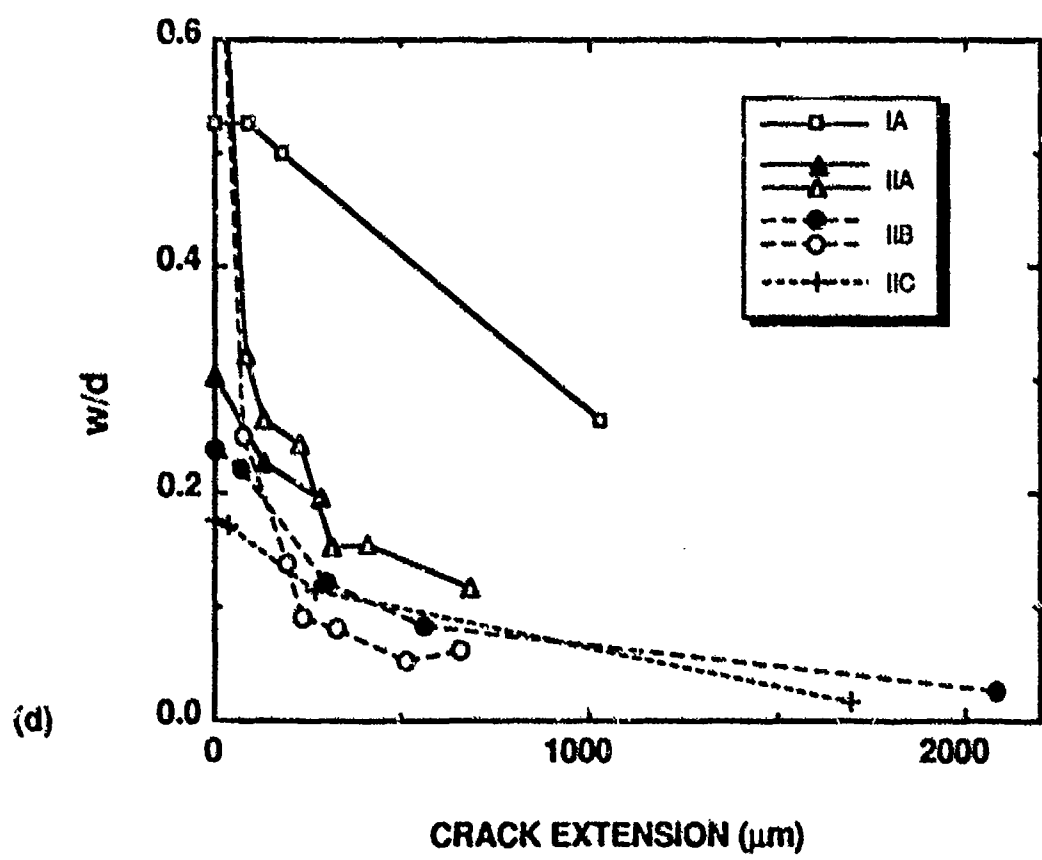
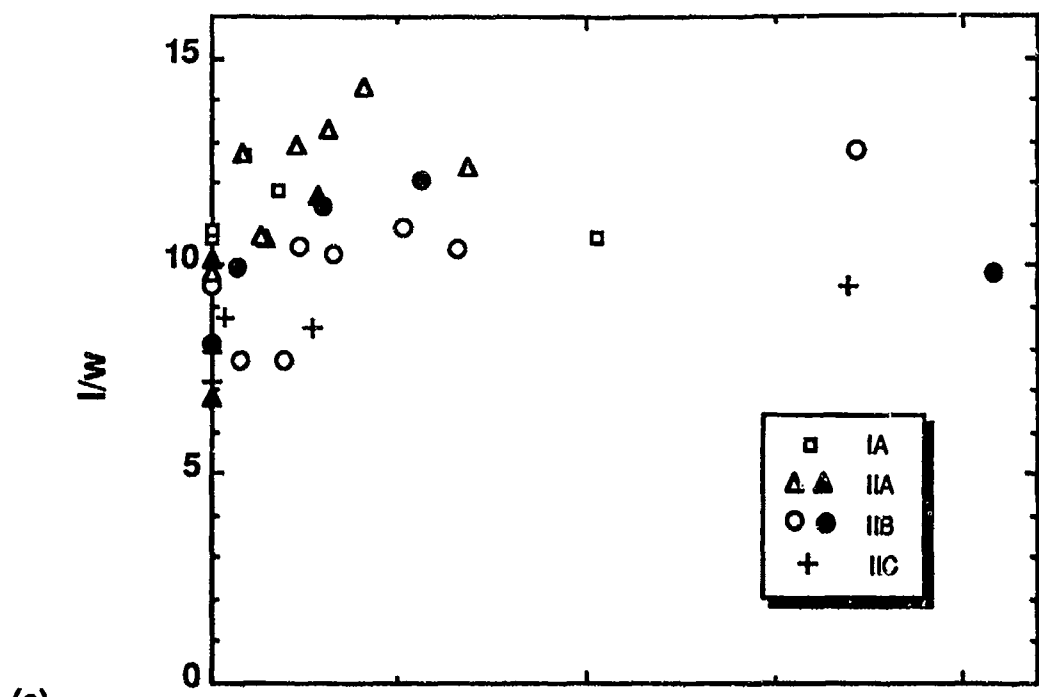


Fig. 2

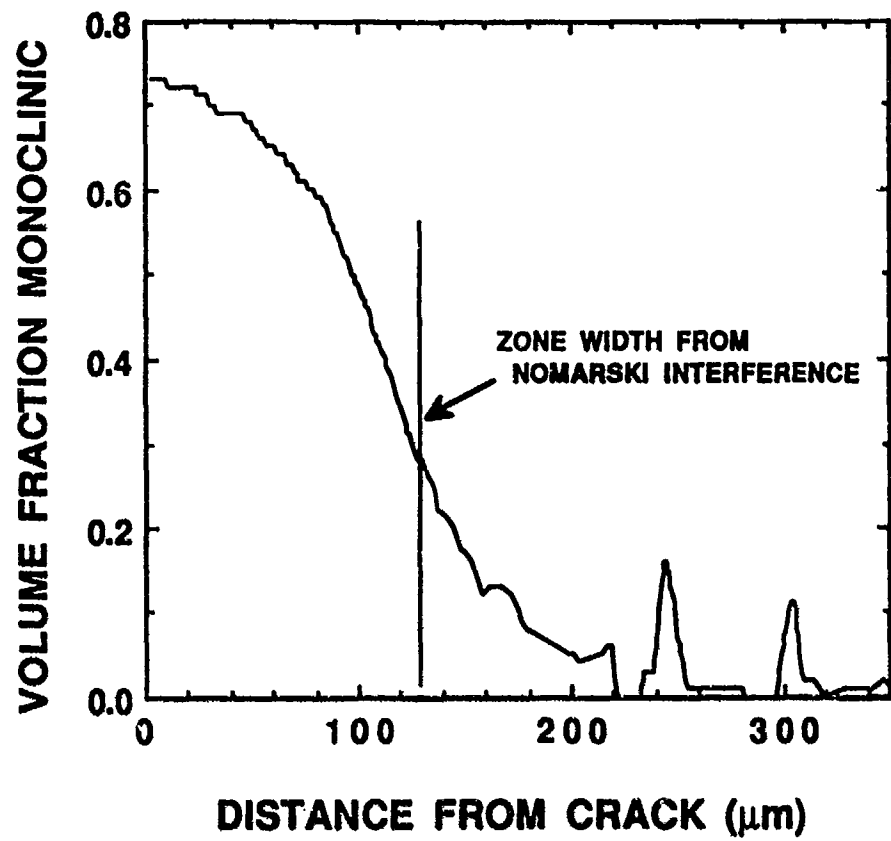


Fig. 3

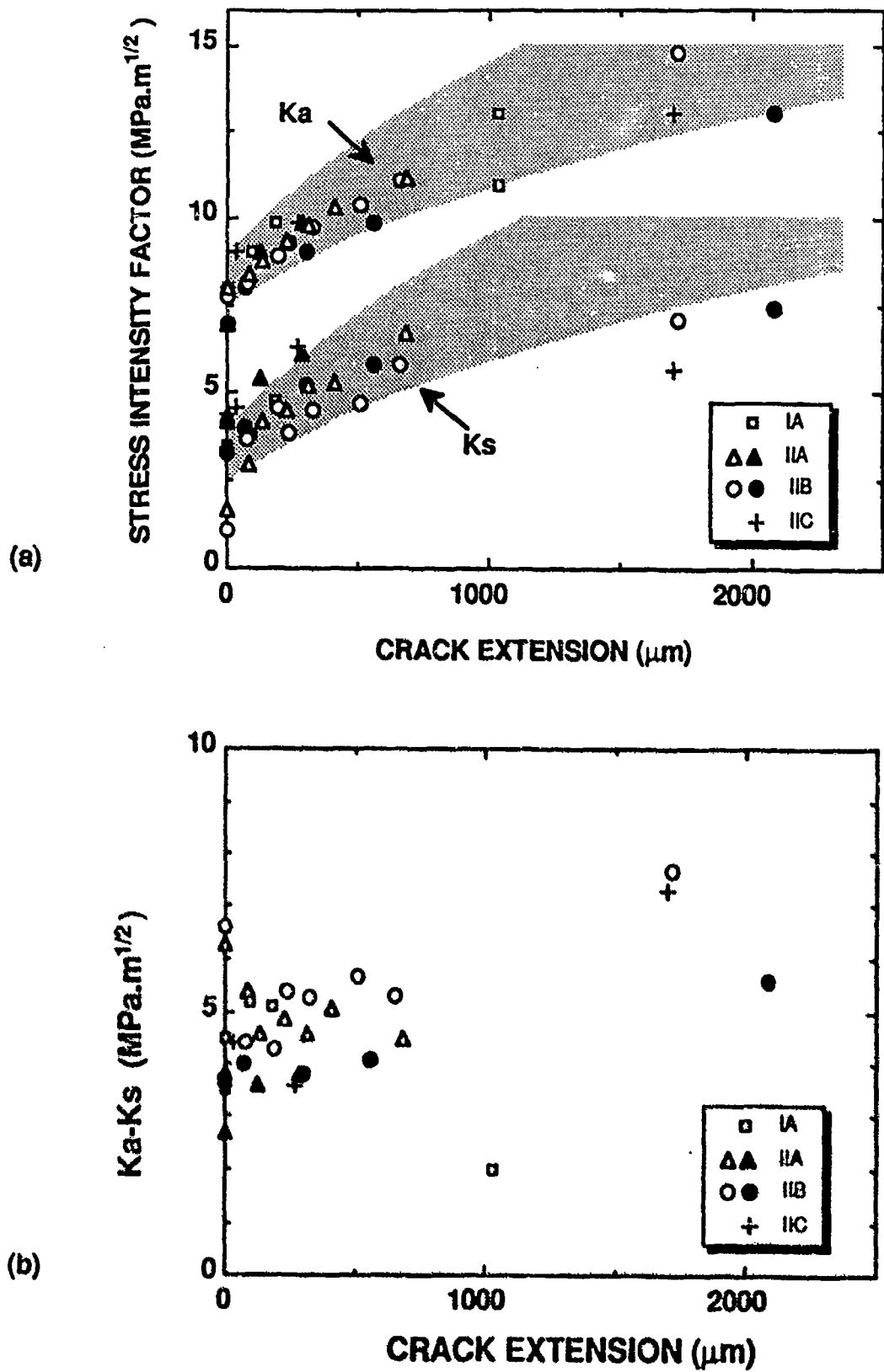


FIG.4

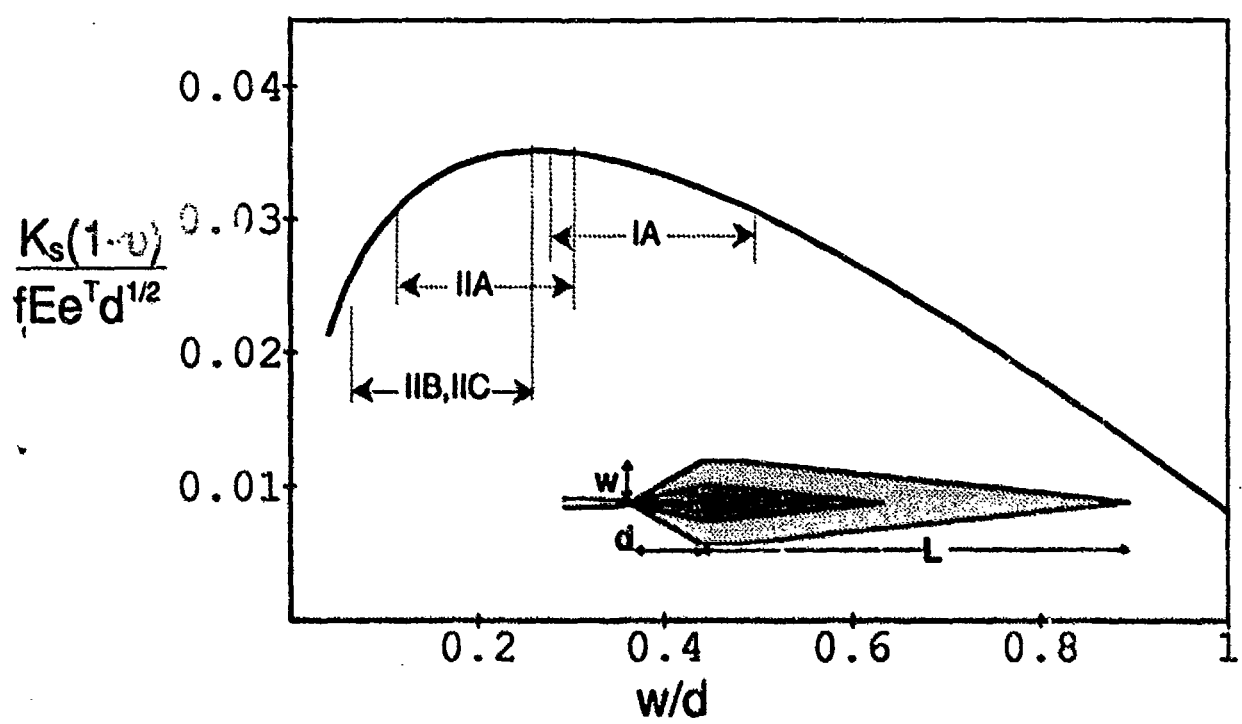


Fig. 5



Rockwell International  
Science Center  
SC71002.FR

## 4.2 CRACK SHIELDING IN CERIA-PARTIALLY STABILIZED ZIRCONIA

published in J. Am. Ceram. Soc.

## Crack Shielding In Ceria-Partially-Stabilized Zirconia

David B. Marshall\*

Rockwell International Science Center, Thousand Oaks, California 91360

The crack tip shielding stress intensity factor has been calculated for several elongated transformation zone shapes observed in high-toughness ceria-zirconia ceramics. The results show that the measured increases in fracture toughness of these materials are consistent with the crack tip shielding mechanism, to which the toughening of other zirconia ceramics has been attributed. Moreover, the presence of a very elongated zone ahead of a steady-state crack is shown to decrease the degree of shielding compared with that of a zone with semicircular frontal shape and equivalent width by a factor of about 2. [Key words: fracture toughness, tetragonal zirconia polycrystals, cerium, shielding, transformations.]

## I. Introduction

SEVERAL recent studies have demonstrated that high fracture toughnesses, in the range 12 to 20 MPa·m<sup>1/2</sup>, can be achieved in ceria-partially-stabilized zirconia (Ce-TZP) ceramics that readily undergo martensitic transformation from tetragonal to monoclinic phase.<sup>1-7</sup> However, the shapes of the transformation zones surrounding cracks in these materials are very different from those in other zirconia materials of comparable toughness; in magnesia-partially-stabilized zirconia (Mg-PSZ) the zone extends approximately equal distances ahead and to the side of the crack,<sup>7</sup> whereas the zone in Ce-TZP is very elongated, extending ahead of the crack a distance ~10 to 20 times the zone width (Fig. 1).<sup>1-4</sup> This appearance of a slitlike zone ahead of the crack has prompted several analyses of crack growth and toughening in terms of a Dugdale zone model.<sup>1,4</sup> Moreover, in one of these studies<sup>4</sup> it was specifically suggested that the crack tip shielding mechanism, which is generally accepted as the source of toughening in other toughened zirconia materials, is not applicable for Ce-TZP.

Calculations of the crack tip shielding due to transformation zones with the shapes observed in Ce-TZP are presented here, with two purposes in mind. One is to determine whether such shielding is indeed consistent with the measured fracture toughness. The other is to assess whether a substantial increase in toughness might be possible by modifying the microstructure to eliminate or reduce the extended frontal zone. The large frontal zone is detrimental to toughening by crack tip shielding, since dilatational transformation of material located within an angular range of  $\pm 60^\circ$  ahead of the crack causes an increase in crack tip stresses.<sup>12,13</sup>

## II. Analysis

Crack tip shielding occurs when the transformation strains within the zone surrounding the crack act to reduce the

I-W. Chen—contributing editor

Manuscript No. 197553. Received May 24, 1990; approved August 1, 1990. Sponsored by the U.S. Air Force Office of Scientific Research under Contract No. F49620-89-C-0031.

\*Member, American Ceramic Society.

stress intensity factor near the crack tip, as characterized by

$$K_{ip} = K_c + K_s \quad (1)$$

where  $K_c$  is the applied stress intensity factor and  $K_s$  is the shielding stress intensity factor due to the zone. The condition for crack growth is taken as  $K_{ip} = K_0$ , the fracture toughness of the fully transformed material, whereupon  $-K_s$  is the increase in fracture toughness due to the transformation zone. The magnitude of  $K_s$  can be calculated following the method of McMeeking and Evans,<sup>10</sup> by applying imaginary surface tractions to the boundary of the transformation zone to restore the original shape that it had before transformation, and applying a weight function method to compute the stress intensity factor due to the body forces,  $T$ , needed to cancel these tractions:

$$K_s = \int_{\Gamma} T \cdot h \, ds \quad (2)$$

where  $ds$  is an element of the zone boundary  $\Gamma$ ,  $\nu$  is Poisson's ratio, and  $h$  is the weight function, given, for mode I loading in an isotropic homogeneous body in plane strain, by<sup>10</sup>

$$\begin{aligned} \left\{ \begin{array}{l} h_1 \\ h_2 \end{array} \right\} = & \frac{1}{2\sqrt{2\pi(1-\nu)\sqrt{r}}} \\ & \times \left\{ \begin{array}{l} \cos(\theta/2)[2\nu - 1 + \sin\theta/2 \sin 3\theta/2] \\ \sin(\theta/2)[2 - 2\nu - \cos\theta/2 \cos 3\theta/2] \end{array} \right\} \end{aligned} \quad (3)$$

where  $r$  and  $\theta$  are position coordinates relative to the crack tip.

To assess the role of the extended frontal zone on crack tip shielding, Eq. (2) was evaluated for the steady-state (i.e., constant zone width in wake of crack) zones shown in Fig. 1, as depicted by Rose and Swain.<sup>3</sup> The net transformation strain within the zone was taken to be hydrostatic dilatation, so that the tractions  $T$  consist of outward acting pressure  $P$  normal to the zone boundary (including the crack surfaces) as shown in Fig. 1(B). The pressure is related to the unconstrained trans-

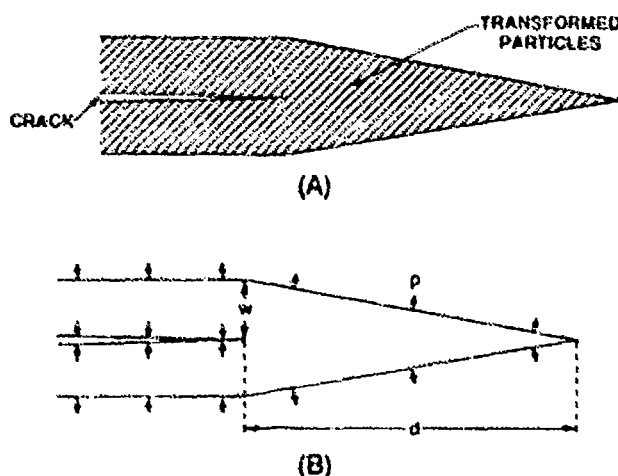


Fig. 1. (A) Steady-state transformation zone shape in Ce-TZP (from Ref. 3). (B) Zone boundary and traction use for shielding calculations of Fig. 2.

formation strain  $e^T$  and the volume fraction,  $f$ , of material transformed within the zone by<sup>10</sup>

$$p = fe^T E/3(1 - 2\nu) \quad (4)$$

where  $E$  is Young's modulus. Evaluation of Eq. (2) for the zone configuration of Fig. 1(B), with various ratios of length,  $d$ , to width,  $w$ , gives the result

$$K_s(1 - \nu)/e^T Ef \sqrt{w} = \kappa(d/w) \quad (5)$$

where the function  $\kappa(d/w)$  is plotted in Fig. 2. At  $d/w = 0$  (i.e., no frontal zone) the value  $\kappa(d/w) = -0.37$  is the same as the corresponding result given by McMeeking and Evans<sup>10</sup> as an upper bound for the toughening. As the frontal zone gets very large ( $d/w \rightarrow \infty$ )  $K_s$  approaches zero, but it does so very slowly ( $\kappa = -0.033$  at  $d/w = 1000$  and  $\kappa = -0.0033$  at  $d/w = 10^5$ ).

Also shown in Fig. 2 are results from McMeeking and Evans<sup>10</sup> for steady-state zones with two other frontal zone shapes, one defined by a semicircle centered on the crack tip and the other defined by a contour of constant hydrostatic stress in the prior elastic crack-tip field. The semicircular shape is characteristic of zones in high-toughness Mg-PSZ materials.<sup>9</sup> The results in Fig. 2 indicate that replacement of the long frontal zone with  $d/w \sim 20$  in Ce-TZP by a semicircular frontal zone would more than double the toughening due to transformation shielding.

To ascertain whether the measured fracture toughness of Ce-TZP is consistent with a shielding mechanism,  $K_s$ , was calculated for two transformation zones from the paper by Yu and Shetty,<sup>4</sup> who also measured the parameters needed to calculate the shielding. The zone boundaries, corresponding to two stages of growth of a crack which initially did not have a zone, are shown in Fig. 3(A): the zone that developed after 180  $\mu\text{m}$  of crack extension, at  $K_s = 9.9 \text{ MPa} \cdot \text{m}^{1/2}$ , was traced directly from Fig. 2 of Ref. 4, whereas the zone corresponding to 1.3 mm of crack extension (broken lines) at  $K_s = 14.5 \text{ MPa} \cdot \text{m}^{1/2}$  was drawn to be consistent with the dimensions  $w = 340 \mu\text{m}$  and  $d/w = 13$  given in Ref. 4. An estimate of the shielding stress intensity factor for the larger zone, using the result from McMeeking and Evans<sup>10</sup> for a steady-state crack with a frontal zone defined by a hydrostatic stress contour (i.e.,  $\kappa = 0.22$  in Eq. (5)), gave  $K_s = 45 \text{ MPa} \cdot \text{m}^{1/2}$ , much larger than the measured fracture toughness.<sup>4</sup> However, the observed zone shapes of Fig. 3(A) differ from the shape corresponding to this result, both in their

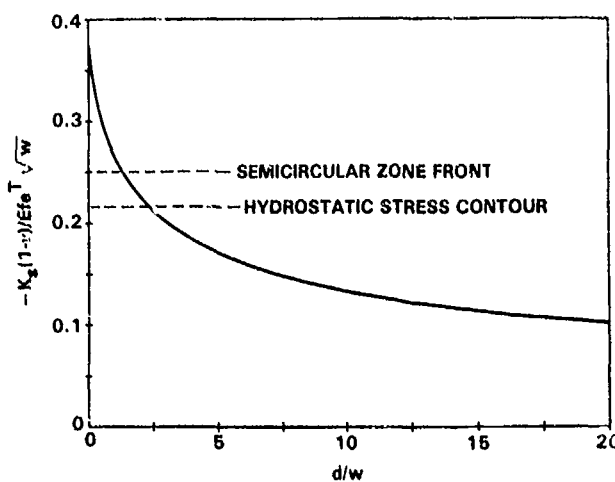


Fig. 2. Crack tip shielding stress intensity factors for steady-state cracks. Solid curve refers to zones with the shape depicted in Fig. 1(B) with various relative zone dimensions,  $d/w$ , ahead of the crack. Results for zones defined ahead of the crack by a semicircle and by a contour of constant hydrostatic stress in an elastic crack tip field are also shown.

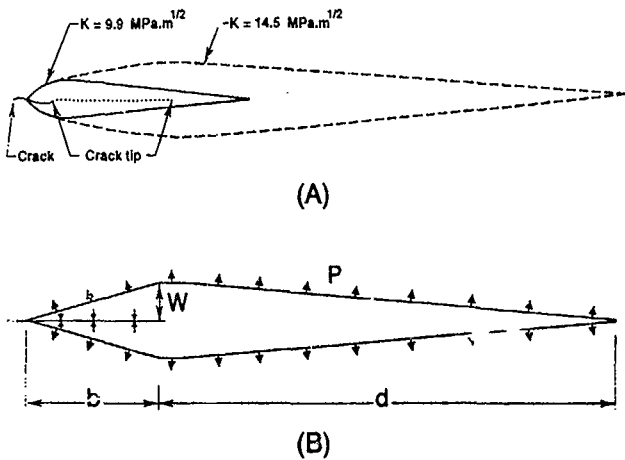


Fig. 3. (A) Transformation zone boundaries corresponding to two stages of crack growth (from data in Ref. 4): solid lines at crack extension of 180  $\mu\text{m}$ , broken lines at crack extension of 1.3 mm. (B) Zone shape and tractions used to calculate  $K_s$  for the zones of (A).

form ahead of the crack tip and in the absence of fully developed steady-state wake regions. To evaluate  $K_s$  for the zones of Fig. 3(A), the shapes were approximated as in Fig. 3(B), with  $b/w = 2$  for the smaller zone and  $b/w = 4$  for the larger zone. The net transformation strain was assumed to be hydrostatic dilation. With these assumptions, the boundary tractions are defined by Eq. (4), as in the above calculation, and evaluation of Eq. (2) gives  $\kappa = -0.043$  and  $\kappa = -0.070$  for the smaller and larger zones. The corresponding values of  $K_s$  (with  $f = 0.8$  from Ref. 4,  $E = 200 \text{ GPa}$ ,  $\nu = 0.25$ , and  $e^T = 0.04$ ) are  $-4.7 \text{ MPa} \cdot \text{m}^{1/2}$  for the smaller zone ( $w = 166 \mu\text{m}$ ) and  $-11 \text{ MPa} \cdot \text{m}^{1/2}$  for the larger zone ( $w = 340 \mu\text{m}$ ). These values of  $K_s$  should be regarded only as estimates, since the value of  $f$  was obtained by X-ray diffraction from the fracture surface and was assumed to be constant throughout the zone, whereas the fraction of material transformed usually decreases with distance from the crack.<sup>9</sup> Also, possible effects of a net shear component in the transformation zone or of microcracks that have been observed within the zone<sup>3</sup> have not been considered. Nevertheless, the values of  $K_s$  are consistent with the measured values of  $K_s$  (9.9 and  $14.5 \text{ MPa} \cdot \text{m}^{1/2}$ ), in the sense that the magnitude of  $K_s$  is smaller than, but a substantial fraction of,  $K_s$ : Eq. (1) with these two values of  $K_s$  gives  $K_0 = 5.2$  and  $3.5 \text{ MPa} \cdot \text{m}^{1/2}$  for the toughness of the fully transformed material.

In view of these results, it is worthwhile contemplating microstructural changes that might lead to a reduced frontal zone and consequential increase in toughness. The reason for the formation of the elongated frontal zone is not known, but it is thought to be associated with a strong tendency to autocatalytic transformation. Effects of autocatalytic transformation in Ce-TZP have been observed in many other experiments. These include sudden bursts of transformation that occur upon cooling through the  $M_1$  temperature, as well as load drops that occur during tensile loading experiments, coinciding with the formation of narrow, well-defined bands of transformed material oriented normal to the applied tension.<sup>5</sup>

A possible approach for controlling the autocatalytic transformation may be suggested by comparing the behaviors and microstructures of Ce-TZP and high-toughness Mg-PSZ. In Mg-PSZ the transformation zone ahead of a crack is approximately semicircular.<sup>9</sup> Mg-PSZ also undergoes autocatalytic transformation, as seen by well-defined bands on the surfaces of specimens loaded in either tension or compression.<sup>12,13</sup> However, rather than extending completely through the specimen, the bands arrest at grain boundaries. Because the bands are arrested, separate initiation of the transformation

at multiple locations is necessary, resulting in a smoothly increasing stress-strain curve and progressive transformation when cooling through the  $M_s$  temperature. Such arrest of transformation bands presumably also modifies the shape of the transformation zone ahead of a crack tip. The essential microstructural difference between the magnesia- and ceria-doped materials is that the Mg-PSZ contains a dual-scale microstructure, with small tetragonal precipitates (lens-shaped with largest diameter  $\sim 300$  nm) within large grains ( $\sim 50$   $\mu\text{m}$  in diameter) of cubic phase, whereas the Ce-TZP consists simply of a polycrystalline array of tetragonal grains of uniform size (several micrometers) without any barriers to arrest a band of autocatalytically transforming grains once it forms. Tsai<sup>1</sup>, Yu, and Shetty<sup>14</sup> have shown that the presence of second-phase  $\text{Al}_2\text{O}_3$  grains of similar size and spacing as the  $\text{ZrO}_2$  grains is effective in preventing the autocatalytic transformation and in modifying the shape of the zone, but also leads to reduced zone width. By analogy with Mg-PSZ, if a dual-scale microstructure could be created in Ce-TZP, with barriers distributed on a scale substantially larger than the grain size, it may be possible to eliminate the large crack tip frontal zone while maintaining the width of the wake zone and thereby increase the fracture toughness by approximately a factor of 2. Several approaches are being pursued to test this hypothesis, including introduction of large platelets of  $\text{Al}_2\text{O}_3$  and fabrication of layered structures.

### III. Conclusion

In conclusion, the calculated shielding stress intensity factors confirm that the measured fracture toughness in Ce-TZP is consistent with the toughening being due to crack shielding from the observed transformation zones. Although this does not rule out the possibility of a Dugdale zone model as proposed in Refs. 3 and 4, we note that the shielding mechanism is also consistent with the reported<sup>4</sup> linear dependence of the zone width on the square of the applied stress intensity factor.<sup>9</sup> According to the crack shielding model, microstruc-

tural modifications that decrease the elongation of the zone ahead of the crack could increase the toughness by a factor of approximately 2.

### References

- 1M.V. Swain, R. H. J. Hannink, and J. Drennan, "Some Interfacial Related Properties of Transformation-Toughened Ceramics"; p. 819 in Ceramic Microstructures '86, Role of Interfaces. Edited by J. A. Pask and A. G. Evans. Plenum Press, New York, 1987.
- 2R. H. J. Hannink and M. V. Swain, "Metastability of Martensitic Transformation in a 12 mol% Ceria-Zirconia Alloy: I, Deformation and Fracture Observations," *J. Am. Ceram. Soc.*, **72** [1] 90-98 (1989).
- 3L. R. F. Rose and M. V. Swain, "Transformation Zone Shape in Ceria-Partially-Stabilized Zirconia," *Acta Metall.*, **36** [4] 955-62 (1988).
- 4C.-S. Yu and D. K. Shetty, "Transformation Zone Shape, Size, and Crack-Growth-Resistance (R-curve) Behavior of Ceria-Partially Stabilized Zirconia Polycrystals," *J. Am. Ceram. Soc.*, **72** [6] 921-28 (1989).
- 5P. E. Reyes-Morel and I.-W. Chen, "Transformation Plasticity of  $\text{CeO}_2$ -Stabilized Tetragonal Zirconia Polycrystals: I, Stress Assistance and Autocatalysis," *J. Am. Ceram. Soc.*, **72** [5] 343-53 (1988).
- 6P. E. Reyes-Morel, J.-S. Cherng, and I.-W. Chen, "Transformation Plasticity of  $\text{CeO}_2$ -Stabilized Tetragonal Zirconia Polycrystals: II, Pseudoelasticity and Shape Memory Effect," *J. Am. Ceram. Soc.*, **71** [8] 648-57 (1988).
- 7K. E. Tsukuma and M. Shimada, "Strength, Fracture Toughness, and Vickers Hardness of  $\text{CeO}_2$ -Stabilized Tetragonal Zirconia Polycrystals (Ce-TZP)," *J. Mater. Sci.*, **20** [4] 1178-84 (1985).
- 8T. Sato, T. Endo, and M. Shimada, "Post-sintering Hot Isostatic Pressing of Ceria-Doped Tetragonal Zirconia/Alumina Composites in an Argon-Oxygen Gas Atmosphere," *J. Am. Ceram. Soc.*, **72** [5] 761-64 (1989).
- 9D. B. Marshall, M. C. Shaw, R. H. Dauskardt, R. O. Ritchie, M. Readey, and A. H. Heuer, "Crack-Tip Transformation Zones in Toughened Zirconia," *J. Am. Ceram. Soc.*, **73** [9] 2659-66 (1990).
- 10R. M. McMeeking and A. G. Evans, "Mechanics of Transformation Toughening in Brittle Materials," *J. Am. Ceram. Soc.*, **65** [5] 242-46 (1982).
- 11D. B. Marshall, A. G. Evans, and M. Drory, "Transformation Toughening in Ceramics"; p. 289 in Fracture Mechanics of Ceramics, Vol. 6. Edited by R. C. Bradt, A. G. Evans, D. P. H. Hasselman, and F. F. Lange. Plenum Press, New York, 1983.
- 12D. B. Marshall and M. V. Swain, "Crack Resistance Curves in Magnesia-Partially-Stabilized Zirconia," *J. Am. Ceram. Soc.*, **71** [6] 399-407 (1988).
- 13A. H. Heuer, M. Rühle, and D. B. Marshall, "On the Thermoelastic Martensitic Transformation in Tetragonal  $\text{ZrO}_2$ ," *J. Am. Ceram. Soc.*, **73** [4] 1084-93 (1990).
- 14J.-F. Tsai, C.-S. Yu, and D. K. Shetty, "Autocatalytic Transformation and the Zone Shape in Ceria-Partially-Stabilized Zirconia (Ce-TZP)"; unpublished work.  $\square$



Rockwell International  
Science Center

SC71002.FR

## 5.0 DIRECT MEASUREMENTS OF TRANSFORMATION ZONE CHARACTERISTICS



Rockwell International  
Science Center

SC71002.FR

## 5.1 DIRECT MEASUREMENT OF TRANSFORMATION ZONE STRAINS IN TOUGHENED ZIRCONIA

published in J. Am. Ceram. Soc.

# Direct Measurement of Transformation Zone Strains in Toughened Zirconia

Mahyar S. Dadkhah,\* David B. Marshall,\* Winfred L. Morris, and Brian N. Cox\*

Rockwell Science Center, Thousand Oaks, California 91360

Residual strains responsible for crack tip shielding have been measured within transformation zones surrounding cracks in Mg-PSZ. Two techniques were used for strain measurement: moiré interferometry and high-resolution image matching. Both methods provide maps of differential in-plane displacements within the specimen surface intersected by the crack, the latter method with the higher resolution. The results are compared with finite-element analysis to assess surface relaxation effects, and the measured strains are used to evaluate the crack tip shielding stress intensity factor. Calculations based on the assumption that the unconstrained transformation strain is hydrostatic dilatation yielded results that were significantly smaller than the measured toughness increases. [Key words: partially stabilized zirconia, transformation toughening, crack tip, shielding, finite-element analysis.]

## I. Introduction

THE high fracture toughness of certain zirconia-containing ceramics has been attributed to shielding of crack tips by transformation strains.<sup>1-10</sup> The strains result from shape changes associated with the martensitic tetragonal-to-monoclinic transformation within limited zones surrounding the cracks. The existence of such zones has been detected by several techniques: X-ray diffraction,<sup>6,11-14</sup> transmission electron microscopy,<sup>6,15,16</sup> and Raman spectroscopy,<sup>17-21</sup> all of which detect the presence of the monoclinic transformation product.

If the net transformation strain were known unambiguously, these zone measurements would allow calculation of the degree of crack tip shielding, and hence a direct comparison of transformation toughening theory and experimental toughness measurements.<sup>10,22-27</sup> The transformation strain is composed of both shear (16%) and dilatational (4%) components.<sup>2,8,10</sup> However, the long-range shear component can be partly, or completely, relieved by twinning in the monoclinic product, thus introducing an uncertainty of approximately a factor of 2 in calculating the toughening.<sup>10</sup> Elimination of this uncertainty requires direct measurement of transformation strains within the crack zone. Indirect measurements of the strains have been obtained from optical interference measurements of out-of-plane surface distortions due to the transformation strains.<sup>21,28-31</sup> In this paper, we present measurements by high-resolution displacement mapping and moiré interferometry of transformation strains normal to the crack plane within the wake of the crack. This technique could potentially

D. K. Shetty—contributing editor

Manuscript No. 197504. Received June 13, 1990; approved November 20, 1990.

Presented at the 92nd Annual Meeting of the American Ceramic Society, Dallas, TX, April 24, 1990 (Engineering Ceramics Division, Paper No. 59-C-90).

Supported by the U.S. Air Force Office of Scientific Research under Contract No. F49620-82-C-0031.

\*Member, American Ceramic Society.

be used, in conjunction with out-of-plane displacement measurements and finite-element modeling, to deduce the net transformation strain directly. In the present work, preliminary measurements and finite-element analysis are used to evaluate the crack tip shielding, assuming purely dilatational strain.

## II. Experimental Procedure

### (1) Materials and Crack Growth Experiments

The test material was a partially stabilized zirconia\* containing 9 mol% MgO (Mg-PSZ), as used in previous studies.<sup>20,21</sup> Fabrication, heat treatment, and microstructure are described by Hannink<sup>32</sup> and Hannink and Swain.<sup>7</sup> Two final heat treatments, which involved subeutectoid annealing at 1100°C, were used to make materials with steady-state fracture toughnesses of 11 and 16 MPa·m<sup>1/2</sup>. The microstructures were composed of cubic ZrO<sub>2</sub> grains of ~50 μm diameter, containing lens-shaped tetragonal and monoclinic precipitates (~40% by volume) with largest dimension ~300 nm. Recent study has shown that the subeutectoid heat treatment used to manipulate the stability of the tetragonal precipitates (and hence the toughness) also causes formation of a large amount of the δ-phase, Mg<sub>2</sub>Zr<sub>5</sub>O<sub>12</sub>, both at the precipitate boundaries and throughout the matrix.<sup>33,34</sup>

Cracks were grown stably under measured loading conditions in compact tension fracture mechanics specimens of dimension 25 mm × 30 mm × 2 mm. A loading fixture that could attach to the stage of an optical microscope was used, to allow in situ observation of the crack tip and wake zones by several techniques.

### (2) Out-of-Plane Displacement Measurements

Out-of-plane displacements of the specimen surface adjacent to the crack ( $u_2$  in Fig. 1) were measured by optical interference microscopy. The interference measurements were obtained from the surface of the compact tension specimen which had been polished flat before introduction of the crack.

### (3) In-Plane Strain Measurements

Transformation strains,  $e_1^S$ , normal to the crack plane (Fig. 1) were measured by two techniques (the superscript S denoting strains measured at the specimen surface). One technique was moiré interferometry,<sup>35</sup> which involved gluing a diffraction grid to the surface of the compact tension specimen before growing the crack, and then, during loading to extend the crack, illuminating the surface with a He-Ne laser (wavelength 632 nm) in the configuration of Fig. 2. In this setup, half of the incident beam impinged directly onto the specimen surface, while the other half, after reflection from a plane mirror, was incident in a symmetrical direction to produce a virtual reference grating. The combination of this reference grating and the diffraction grating bonded to the specimen produced the moiré pattern, which was recorded photographically. The moiré pattern consists of a set of

\*Nilcor Ceramics, Elmhurst, IL.

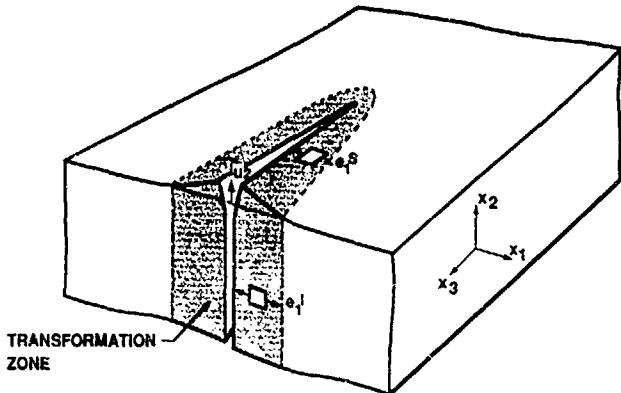


Fig. 1. Schematic of crack surrounded by dilatational transformation zone.

fringes, which represent contours of constant displacement in the  $x_1$  direction, the increment between adjacent fringes being equal to the period of the reference grating ( $0.417 \mu\text{m}$ ). In the present experiments, this technique allowed strain resolution of  $10^{-3}$  over gauge lengths as small as  $40 \mu\text{m}$ .

The second technique of in-plane strain measurement entailed digital image matching of high-magnification optical micrographs, taken from the surface of the compact tension specimen before and after passage of the crack. The image matching provides maps of relative displacements of corresponding features within the "before" and "after" images. This technique (referred to as HASMAP) has been described more fully in Ref. 36. In the present experiments, the specimen surface, which had been highly polished after heat treatment, was coated with a thin ( $\sim 100 \text{ \AA}$ ) layer of gold then decorated with submicrometer MgO crystallites (from smoke of burning Mg), which provided the reference features for image matching. Then a set of optical micrographs were obtained from the regions ahead of the notch while the specimen was in the loading fixture, before the load was applied. After the load was applied and a crack of sufficient length to reach steady state (in toughness and transformation zone size) had grown, another set of micrographs, which exactly matched the first set in position and imaging conditions, was

obtained. Analysis of these micrographs provided  $x_1$ - $x_3$  displacement maps with relative displacement resolution of  $\sim 100 \text{ \AA}$  (substantially smaller than the point-to-point image resolution). The usable gauge length for strain measurement was as small as  $10 \mu\text{m}$ , substantially smaller than that achievable by moiré interferometry.

### III. Experimental Results

#### (1) Moiré Interferometry

Moiré interference micrographs from a compact tension specimen containing a steady-state crack are shown in Figs. 3(A) and (B). The crack was grown stably from the notch a distance of 5 mm, unloaded (Fig. 3(A)), then reloaded and extended a further 1.7 mm (Fig. 3(B)). The steady-state fracture toughness was  $16 \text{ MPa} \cdot \text{m}^{1/2}$ . In other specimens that were subjected to the same heat treatment in an earlier study,<sup>21</sup> increasing crack resistance curves for the initial 1 to 2 mm of crack extension and transformation zones of  $\sim 1 \text{ mm}$  in width (from Raman spectroscopy) were reported.

The fringes in Figs. 3(A) and (B) represent contours of constant displacement in the direction  $x_1$  normal to the crack. Therefore, in these micrographs, an area of constant normal strain,  $e_1^s$ , in the  $x_1$  direction would give rise to equally spaced horizontal fringes; an area of pure rotation or shear,  $e_2^s$ , would cause equally spaced vertical fringes; and areas of mixed normal strain  $e_1^s$  and either rotation or shear would give inclined fringes. (To distinguish rotation and shear a second moiré image would be needed with the plane of incidence of the laser rotated by  $90^\circ$ .) Several zones surrounding the crack in Fig. 3 can be identified. Behind the crack tip and far from the crack plane (top left and bottom left of the micrographs), nearly pure rotation (or shear strain) is evident, whereas adjacent to the crack plane in the wake region, there is mixed rotation and normal strain, with the normal strain component  $e_1^s$  being tensile. Surrounding the tensile region is a zone in which  $e_1^s$  is compressive. The compressive strains are caused by Poisson's contraction, associated with out-of-plane displacements of material outside the transformation zone (see Section IV). The difference in fringe spacing in Figs. 3(A) and (B) gives a measure of the difference in crack opening in the loaded (Fig. 3(B)) and unloaded (Fig. 3(A)) states.

The out-of-plane displacements were measured from optical interference micrographs (Fig. 4(A)) obtained from the wake region of the crack in Fig. 3. The fringes in Fig. 4(A) represent contours of constant separation of the specimen surface and an inclined reference mirror: equally spaced horizontal fringes represent a flat specimen surface, whereas the fringe deflections toward the bottom of the micrograph indicate surface uplift. The narrow region ( $\sim 20\text{-}\mu\text{m}$  width) immediately adjacent to the crack in Fig. 4(A), where the fringes deflect in the opposite direction, toward the top of the micrograph, is due to deformation of the moiré grid and glue, and corresponds to the region in Figs. 3(A) and (B) near the crack where the moiré fringes become indistinct.

The residual in-plane and out-of-plane displacements,  $u_1$  and  $u_2$ , obtained from the steady-state wake region of Figs. 3(B) and 4(A), are compared in Fig. 4(B); the distances from the crack plane over which  $u_1$  and  $u_2$  are nonzero are similar. The corresponding variation of the normal strain  $e_1^s$  with distance from the crack is shown in Fig. 4(C). Also plotted in Fig. 4(C) is the result of a finite-element calculation that takes into account the effects of surface relaxation on the strains  $e_1^s$  (see Section IV).

#### (2) High-Resolution Displacement Field Mapping

The image matching technique was used for generating in-plane displacement maps for the lower-toughness material; because of the smaller transformation zone, the higher resolution of this method was needed to obtain information from

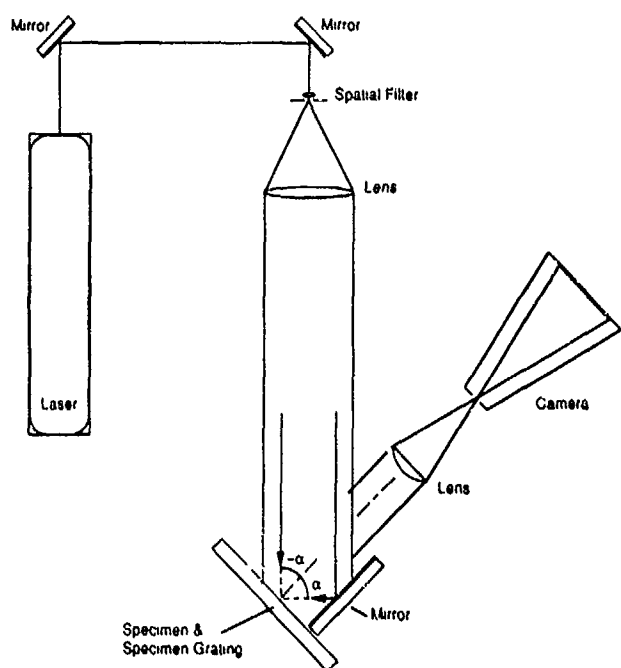


Fig. 2. Setup for moiré interferometry.

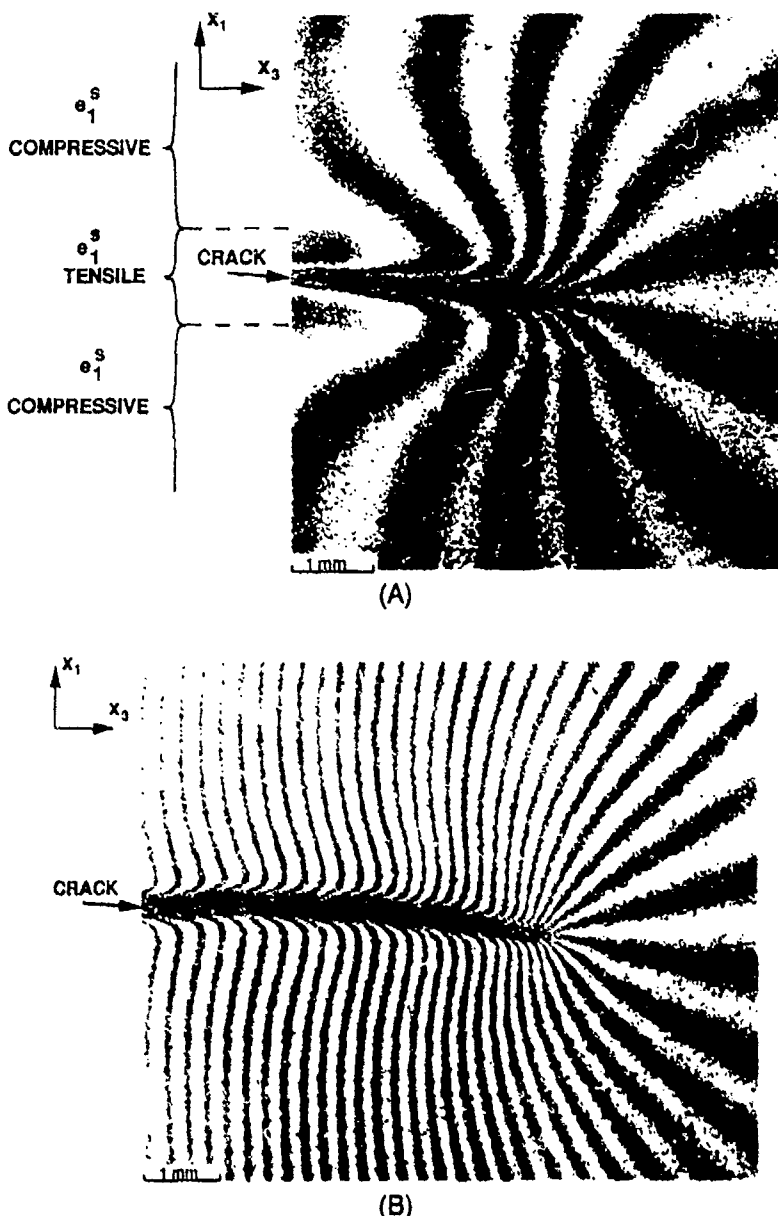


Fig. 3. Moiré interference micrographs from high-toughness Mg-PSZ compact tension specimen: (A) crack grown 5 mm from notch then applied load removed; (B) crack extended further 1.7 mm and applied load held constant while micrograph recorded.

within the zone. Optical interference micrographs from the steady-state crack used for analysis are shown in Figs. 5(A) and (B); these micrographs were obtained with the reference mirror parallel to the undistorted specimen surface, so that the fringes represent contours of constant out-of-plane displacement, at increments of  $\Delta u_2 = 270$  nm. The degree of uplift in the uniform wake zone (approximately  $0.8 \mu\text{m}$  adjacent to the crack) and the measured steady-state fracture toughness,  $K_C = 12 \text{ MPa}\cdot\text{m}^{1/2}$ , are the same as in nominally identical materials used in two previous studies,<sup>20,21</sup> and referred to therein as "mid-toughened." Rows of indentations visible in Figs. 5(A) and (B) near the crack were introduced using a Vickers indenter at 2-N load, to provide references for precise alignment of the micrographs taken before and after crack growth.

Results of the displacement analysis from the region adjacent to the crack in Fig. 5(B) are shown in Fig. 5(C). The strains  $\epsilon_1^s$  normal to the crack are plotted on the vertical axis, and the  $x_1-x_3$  plane corresponds to the area marked on Fig. 5(B). The actual micrographs used for analysis (not shown) were obtained at a magnification of  $280\times$  using a  $\times 25$  objective lens with numerical aperture 0.45. The residual

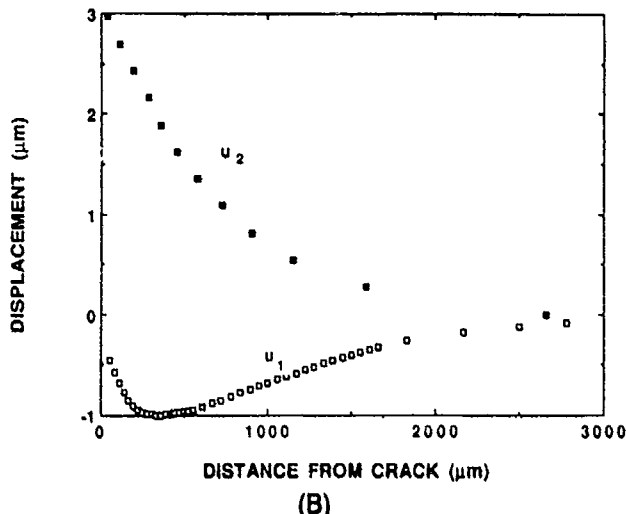
strain  $\epsilon_1^s$  is tensile within approximately  $50 \mu\text{m}$  of the crack and compressive beyond. The strain distribution is qualitatively similar to the result from moiré interferometry from the higher-toughness material, but the zone width is smaller.

The magnitude of the strain adjacent to the crack is quite variable at different locations along the wake. The amplitudes of the variations are about an order of magnitude larger than the sensitivity of the measurements. Moreover, there is a one-to-one correspondence between the nonuniformity of the strain  $\epsilon_1^s$  and areas in Fig. 5(B) where the out-of-plane displacements are larger than average (as indicated by the bulges in the interference fringes adjacent to the crack). These variations in out-of-plane displacements along the line of the crack are also evident in Nomarski interference (which highlights changes in angle of the specimen surface) when the direction of apparent illumination is along the crack (Fig. 6). These correlations provide confidence that the nonuniformity of  $\epsilon_1^s$  in Fig. 5(C) is not an artifact due to an unidentified error in measurement.

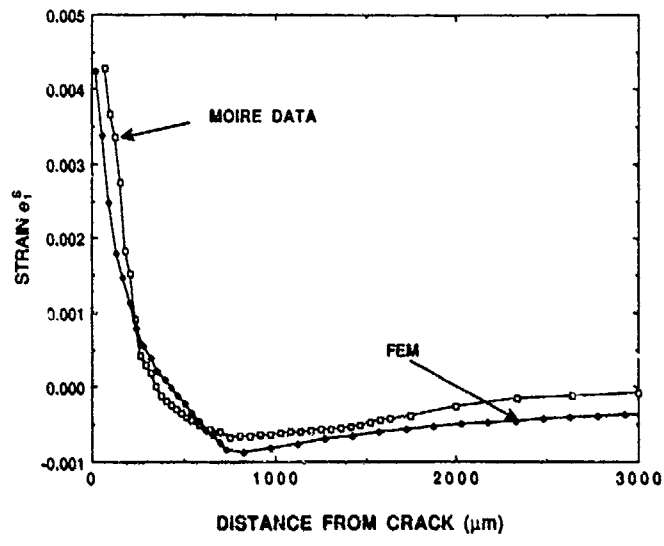
The displacements corresponding to Fig. 5(C), measured along a set of 12 equally spaced lines normal to the crack, are shown in Fig. 7(A). The average in-plane displacements from



(A)



(B)



(C)

Fig. 4. (A) Two-beam optical interference micrograph (wavelength 540 nm) of surface in Fig. 3 after crack was grown entirely through specimen. Reference mirror tilted so that downward deflection of fringes results from surface uplift. (B) In-plane and out-of-plane displacements from Figs. 3(B) and 4(A). (C) Normal strains  $\epsilon_1^S$  from data of (B) and finite-element results from Fig. 8(A) (see Section IV).

Fig. 7(A) at each distance from the crack are compared with the average out-of-plane displacements from Fig. 5(B) in Fig. 7(B). The results are qualitatively similar to those in Fig. 4(B) for the higher-toughness material, but the width of the zone of residual displacements is smaller. The average in-plane strains  $\epsilon_1^S$  are shown in Fig. 7(C), along with a finite-element calculation taking into account free surface relaxation (see Section IV).

#### IV. Analysis of Surface Displacements and Strains

The shielding of the crack tip by a transformation zone has been expressed in terms of the unconstrained transformation strains within the zone (see Section V). In the interior of the specimen, where uniaxial strain conditions exist within a steady-state wake zone formed by hydrostatic dilatational transformation, the unconstrained transformation strains are related straightforwardly to the residual strain in the wake. For transformation with hydrostatic dilatation  $\epsilon^T$ , the residual strain normal to the crack plane is (Appendix)

$$\epsilon_1^S = \left( \frac{1 + \nu}{1 - \nu} \right) \epsilon^T \quad (1)$$

where  $\nu$  is Poisson's ratio and the superscript S denotes a position adjacent to the crack plane in the interior of the specimen. However, experimental strain measurements by techniques reported here are restricted to the specimen surface and are influenced by surface relaxation, as indicated schematically in Fig. 1. At the edge of the crack, uniaxial stress conditions exist and, for the dilatational transforma-

tion, the residual strain normal to the crack is (Appendix)

$$\epsilon_1^S = (1 + \nu) \epsilon^T / 3 \quad (2)$$

Further from the crack, analytical solutions relating the surface strains to  $\epsilon^T$  are not available. Therefore, to evaluate the effect of surface relaxation in this region, finite-element calculations were done (using the program ABAQUS) for the geometry shown in Fig. 8(A) (inset), which simulates a transformation zone of width  $w$ , within which the unconstrained transformation strain  $\epsilon^T(x_1)$  is a function of distance  $x_1$  from the crack plane, but is uniform in the directions  $x_2$  and  $x_3$  over the wake of the crack. The following boundary conditions were imposed: normal displacements  $u_3 = 0$  everywhere, normal displacements  $u_1$  and  $u_2$  zero along the right and bottom edges, respectively, and normal stresses zero along the crack and specimen surfaces. Elements within a distance  $w$  of the crack plane were given a hydrostatic dilatational transformation strain (some results for nonhydrostatic strain are given in the Appendix) with magnitude unity adjacent to the crack and decreasing to zero at  $x_1/w = 1$ , as shown in Fig. 8(C). The function in Fig. 8(C) was obtained by assuming that  $\epsilon^T(x_1)$  is proportional to the volume fraction of material transformed at  $x_1$ , as measured by Raman microprobe spectroscopy on similar materials.<sup>21</sup> Alternatively, we could have taken various trial functions for  $\epsilon^T(x_1)$  and chosen the function that gave closest agreement between calculated and measured values of  $\epsilon_1^S(x_1)$ , as described in Ref. 31. Then, comparison of the optimum function with the Raman measurements would provide an independent experimental verification of the consistency of the strain and Raman measurements and the assumption that the transformation strain is



(A)



(B)

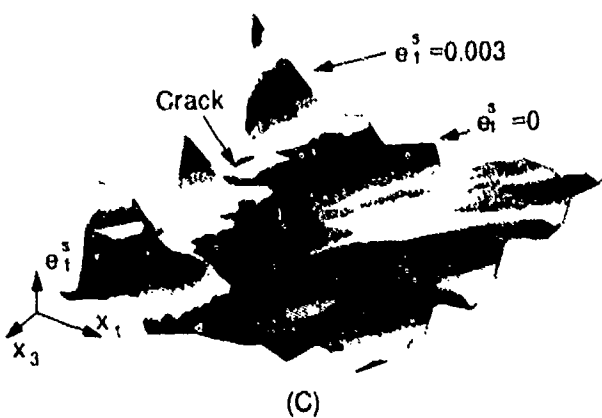


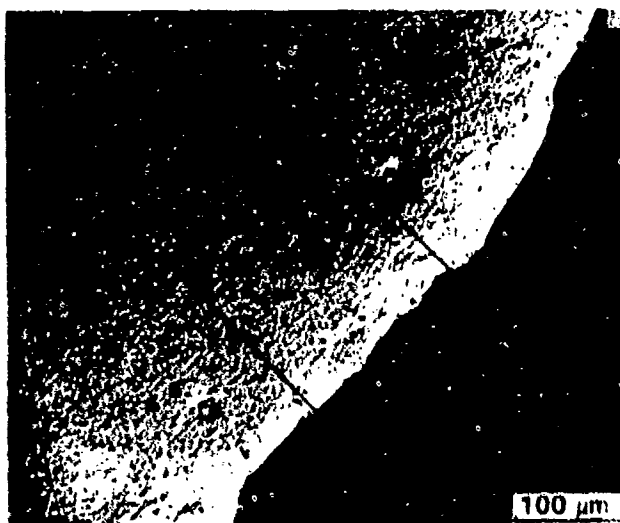
Fig. 5. (A) Optical interference micrograph of midtoughness Mg-PSZ compact tension specimen containing a crack grown stably under monotonically increasing displacement. Reference mirror parallel to specimen surface so that fringes represent contours of out-of-plane displacement (uplift). (B) Higher magnification from (A) showing area analyzed by HASMAP (using other, higher-magnification optical micrographs). (C) Residual strains normal to the crack plane within the area outlined in (B).

proportional to the volume traction of material transformed. With the procedure used here, comparison of the calculated and measured strains  $e_1^s(x_1)$  affords a similar verification.

Computed displacements and strains are shown in Figs. 8(A) and (B) for  $\nu = 0.3$ . The in-plane and out-of-plane displacements,  $u_1^s$  and  $u_2^s$ , are qualitatively similar to the ex-



(A)

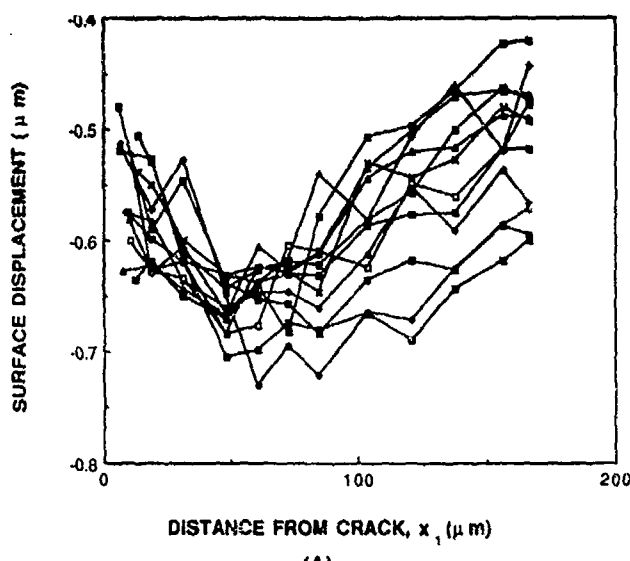


(B)

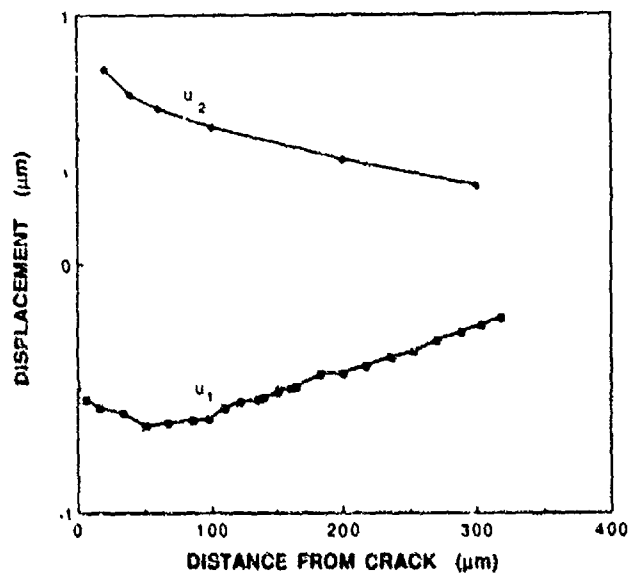
Fig. 6. Nomarski interference micrographs from the area of Fig. 5(B) at two different specimen orientations.

perimental results of Figs. 4(B) and 7(B). The strain  $e_1$  adjacent to the crack plane (i.e., at  $x_1 = 0$ ) is consistent with Eq. (1) at the interior and Eq. (2) at the top corner. The magnitude of the strain  $e_1^s$  in the interior decreases with distance from the crack plane, to zero at the edge of the zone. However, the strain  $e_1^s$  at the surface decreases to zero, and becomes compressive within the zone, with the maximum compressive strain occurring close to the edge of the zone ( $x/w = 1$ ). Therefore, the experimentally observed compressive residual strains outside the region of residual tensile strains are accounted for by surface relaxation. It is also noteworthy that the surface relaxations are such that the net displacement of the edge of the crack is negative (i.e., increased separation of the crack surfaces), whereas in the interior of the specimen, the net displacement is, of course, positive (i.e., closure).

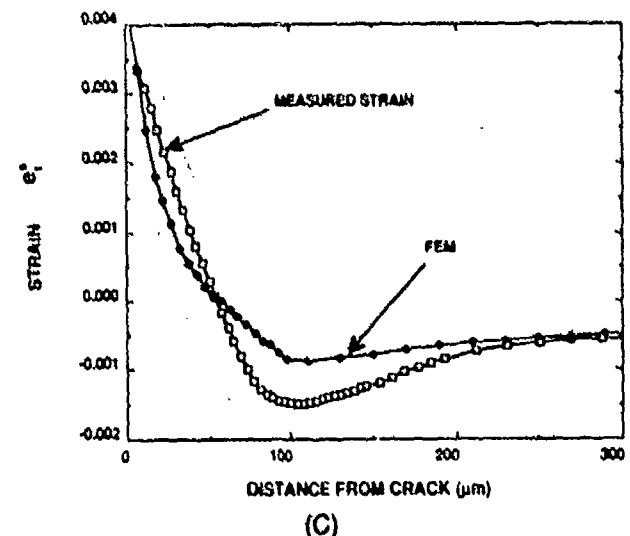
The computed strain distributions  $e_1^s(x_1)$  are compared quantitatively with the experimental measurements in Figs. 4(C) and 7(C), with the values of zone width,  $w$ , and transformation strain,  $e^T(0)$ , adjacent to the crack chosen to give the best fit to the data. For the moiré results from the higher toughness material of Fig. 4(C), the parameters were  $w = 750 \mu\text{m}$  and  $e^T(0) = 0.01$ . With the dilatational component of the transformation strain in the individual transform



(A)

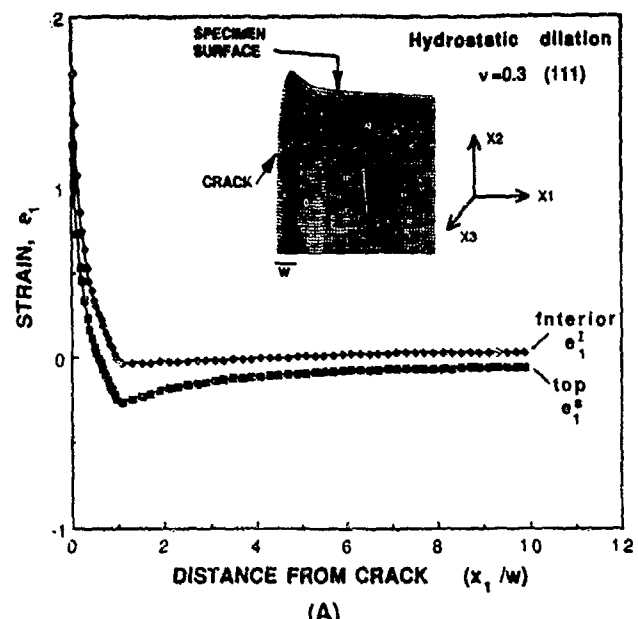


(B)

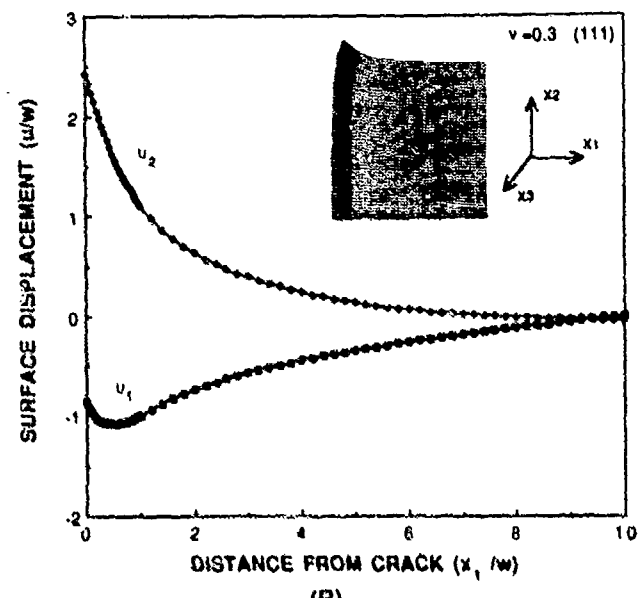


(C)

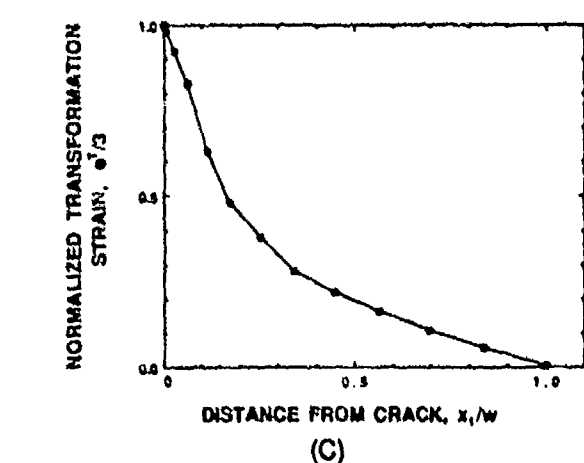
Fig. 7. (A) Residual displacements from Fig. 5(C), measured along a set of 12 equally spaced lines normal to the crack. (B) Average surface displacements adjacent to the crack in Fig. 5(B): out-of-plane displacements,  $u_2$ , from interference micrographs, in-plane displacements from the data used for Figs. 5(C) and 7(A). (C) Average in-plane strains  $\epsilon_1^*$  from data in Fig. 5(C). Shaded band represents range within which 90% of data fall. Finite-element results from Fig. 8(A) (see Section IV).



(A)



(B)



(C)

Fig. 8. Finite-element calculations of (A) residual strain normal to crack at the specimen surface ( $\epsilon_1^*$ ) and in the interior of the specimen ( $\epsilon_1$ ). (B) Residual in-plane and out-of-plane displacements at the specimen surface. (C) Variation of transformation strain with distance from crack (from Raman microprobe measurements of Ref. 21).

ing particles being  $e_0^T = 0.04$ , this value of  $e^T(0)$  corresponds to a volume fraction of transformed phase of  $f = e^T(0)/e_0^T = 0.25$ . For the strain mapping measurements from the lower-toughness material of Fig. 7(C), the fitted parameters were  $w = 100 \mu\text{m}$  and  $e^T(0) = 0.01$ . In both cases, the computed and measured strain distributions show reasonable agreement. Moreover, the fitted parameters are consistent with values obtained from the above-mentioned Raman measurements from similar materials in Ref. 21:  $w = 900 \mu\text{m}$ ,  $f = 0.22$  for the higher-toughness material and  $w = 200 \mu\text{m}$ ,  $f = 0.19$  for the lower-toughness material.

## V. Crack Tip Shielding

The measured residual strains within the transformation zone can be used directly to calculate the reduction of crack tip stresses due to the transformations and, hence, the toughness increase. The reduction in stress at the crack tip is expressed in terms of a shielding stress intensity factor,  $K_s$ :<sup>22</sup>

$$K_{tip} = K_s - K, \quad (3)$$

where  $K_{tip}$  is the local stress intensity factor at the crack tip and  $K_s$  is the applied stress intensity factor. The criterion for crack growth under monotonic loading is taken as a critical value of  $K_{tip}$  (i.e.,  $K_{tip} = K_0$ , where  $K_0$  is the fracture toughness in the absence of transformation shielding). The corresponding value of  $K_s$  ( $K_s = K_c = K_0 + K_t$ ) is the fracture toughness measured in the presence of shielding, and  $K_t$  is the toughness increase.

For a steady-state crack (i.e., crack growth at constant  $K_s$ ), with a wake zone of constant width,  $w$ , containing a uniform volume fraction,  $f$ , of transformed particles, the shielding stress intensity factor under plane strain conditions is<sup>22,23,24</sup>

$$K_s = \frac{AEe^T\sqrt{w}}{1 - \nu} \quad (4)$$

where  $E$  is Young's modulus,  $e^T$  is the unconstrained transformation strain of the entire zone ( $e^T = fe_0^T$  where  $e_0^T$  is the unconstrained transformation strain of the individual transforming particles within the zone), and the constant  $A$  is dependent upon the shape of the zone ahead of the crack tip, as well as the nature of the transformation strain. If  $e^T$  is isotropic dilatational strain and the frontal zone is defined by a contour of hydrostatic tension in the elastic crack-tip field, then  $A = 0.22$ . However, if the frontal zone is semicircular, as suggested by several observations in Mg-PSZ (Fig. 5(A) and Ref. 21), then  $A = 0.25$ .

Previous studies of Mg-PSZ<sup>20,21</sup> (see Fig. 8(C)) have shown that the fraction of particles transformed within the zone decreases continuously with increasing distance from the crack (corresponding to a subcritical transformation in the notation of Ref. 24). In this case, the transformation strain  $e^T$  is not uniform. However, provided all the contours of constant  $e^T$  around the crack tip and wake are geometrically similar and the net transformation strain is isotropic dilatation, the shielding stress intensity factor can be obtained by integration of Eq. (4):<sup>21,23,24</sup>

$$K_s = \frac{AE}{1 - \nu} \int_0^w e^T(x_1) d\sqrt{x_1} \quad (5)$$

where  $x_1$  is the distance from the crack plane. With Eq. (1) this result can be expressed alternatively in terms of the residual strain  $e_1^T$  in the steady-state wake of the crack

$$K_s = \frac{3AE}{1 + \nu} \int_0^w e_1^T(x_1) d\sqrt{x_1} \quad (6)$$

With the finite-element results of Fig. 8(A) being used to relate the strains  $e^T(x_1)$  and  $e_1^T(x_1)$ , the integral in Eq. (6) was

evaluated from the experimentally measured surface strains  $e_1^T(x_1)$  of Figs. 4(C) and 7(C). These results, along with the parameters  $A = 0.25$  for the semicircular zone front,  $E = 200 \text{ GPa}$ , and  $\nu = 0.25$  give  $K_s = 9 \text{ MPa} \cdot \text{m}^{1/2}$  for the moiré results from the high-toughness material and  $K_s = 3 \text{ MPa} \cdot \text{m}^{1/2}$  for the strain mapping measurements in the lower-toughness material. These results are similar to the values 8.8 and  $3.9 \text{ MPa} \cdot \text{m}^{1/2}$  deduced directly from Raman measurements (also with the assumption of hydrostatic dilatational strain) from nominally identical materials in Ref. 21.

## VI. Discussion

The results described in the previous sections provide direct measurements of transformation strains that are a source of toughening in Mg-PSZ. With the assumption that the net unconstrained transformation strain is hydrostatic dilatation (i.e., long-range shear strains are relieved by twinning), we have used the measured residual strain components normal to the crack plane in two materials of different toughness to calculate the crack tip shielding stress intensity factors. The results agree closely with values obtained from similar materials using Raman microprobe measurements of the distributions of transformed monoclinic phase within the transformation zones, with the same assumption of a hydrostatic transformation strain.<sup>21</sup> Both of these calculations also implicitly assumed that the distribution of monoclinic phase within the transformation zone was the same in the plane strain crack tip region in the interior of the specimen as in the near-surface crack tip region where plane stress conditions are approached. Some preliminary Raman microprobe measurements have been done to test this approximation.<sup>25</sup> This entailed growing a crack completely through a compact tension specimen, preparing a polished section normal to both the crack plane and the original surface of the specimen, and measuring the volume fraction of monoclinic phase along scan lines normal to the crack at various depths below the original surface. The results of these scans were not significantly different from those on the original surface.

The assumption of hydrostatic dilatational transformation strain in this and other studies is rationalized mainly on the observation by transmission electron microscopy of extensive twinning in the transformed monoclinic particles within transformation zones.<sup>4,13,17</sup> However, possible thin-foil relaxation effects cast some doubt as to whether such observations are representative of the behavior in bulk material. Moreover, the magnitude of  $K_s$  obtained with this assumption, here and in other studies, does not appear to account fully for the observed toughening: with the values of  $K_s$  from Section V (3 and  $9 \text{ MPa} \cdot \text{m}^{1/2}$ ) and the measured fracture toughnesses (11 and  $16 \text{ MPa} \cdot \text{m}^{1/2}$ ), Eq. (3) gives  $K_0 = 7$  and  $8 \text{ MPa} \cdot \text{m}^{1/2}$ . These values of  $K_0$  are substantially larger than expected for the fracture toughness of the material without any toughening. One possible source of this discrepancy is the existence of nonhydrostatic and nonuniform strains in the transformation zone,<sup>20,24</sup> although other toughening mechanisms, such as twin boundary movement as the particles move through the crack tip stress field, crack deflection, or microcracking, are also possible. Experimental methods are needed to distinguish these possibilities.

The techniques used here could potentially be used to determine the deviatoric components of transformation strain within the zone. In-plane residual shear strains  $e_{11}$  can be obtained directly from the image matching data that were used to generate the results in Figs. 5 and 7, or from moiré images obtained with two-dimensional gratings. Short-range, nonuniformly distributed shear strains  $e_{11}$  were observed from the strain mapping data, but their magnitudes were smaller than  $6 \times 10^{-4}$ , an order of magnitude lower than the strains  $e_1^T$  adjacent to the crack. With the transformation of two sets of orthogonally oriented precipitates, an elongation due to shear

strain components that is equivalent to plastic deformation on two slip systems is possible, without giving a long-range shear strain  $e_{13}$ . In this case, the relative magnitudes of the strain components ( $e_1^T, e_2^T, e_3^T$ ) of the unconstrained transformation could be determined from comparison of the in-plane and out-of-plane displacements  $u_1$  and  $u_2$ . This would involve measurement of  $u_1$  and  $u_2$  as in Figs. 4(B) and 7(B), measurement of the distribution,  $f(x)$ , of transformed material within the zone by Raman microprobe spectroscopy, and superposition of the finite-element solutions of Fig. A1 with the relative magnitudes of  $e_1^T, e_2^T$ , and  $e_3^T$  adjusted so as to build up a zone consistent with both the Raman results and the measured values of  $u_1$  and  $u_2$ . Such an analysis was not attempted here because of the variability in the amount of transformation at different positions along the crack wake (Fig. 7(A)). However, materials with more uniform zones may be amenable to analysis.

## VII. Conclusions

Moiré interferometry and high-resolution strain mapping by image correlation have been used to measure directly the residual transformation strains that exist adjacent to cracks, and are responsible for toughening, in two Mg-PSZ materials. The residual strains were consistent with Raman microprobe measurements of the volume fraction of material transformed. Substantial variability in the residual strains along the crack path was detected. The average strains were used to calculate directly the crack tip shielding stress intensity factor, with the assumption that the unconstrained transformation strain is hydrostatic dilatation. The results are consistent with other equivalent calculations based on Raman microprobe measurements of the distribution of transformed monoclinic phase, which also assumed that only the hydrostatic component of the transformation strain contributes. However, the calculated shielding is significantly smaller than the measured toughness increase, suggesting that either non-hydrostatic components of the transformation strain are significant or other toughening mechanisms operate. An approach was suggested for resolving this issue using the strain measurement methods described herein.

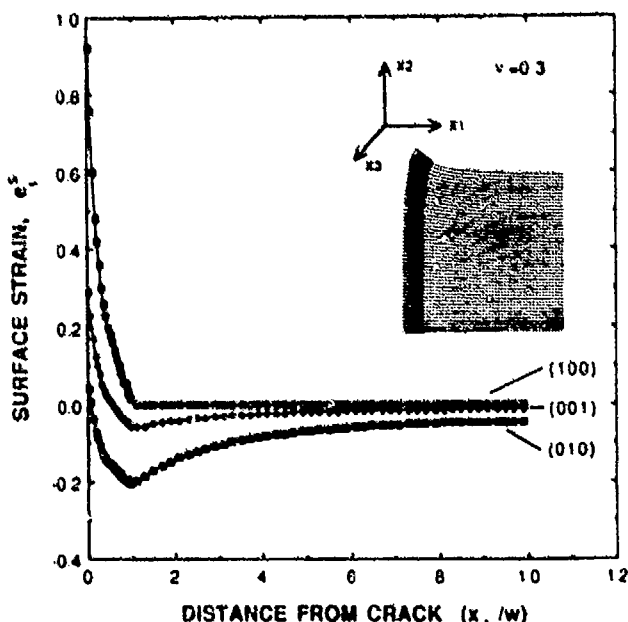


Fig. A1. Finite-element calculations of residual strains at the specimen surface resulting from uniaxial unconstrained transformation strains in the three directions  $x_1, x_2, x_3$ .

## APPENDIX

### Residual Transformation Strains

Consider a slab of material adjacent to a crack, as in Fig. 8, which undergoes uniform transformation with unconstrained normal strains ( $e_1^T, e_2^T, e_3^T$ ). At positions near the crack but far from the specimen surface, the following conditions exist:

$$e_2^T = e_3^T = 0, \quad \sigma_1 = 0 \quad (A-1)$$

where  $e^T$  is measured relative to the untransformed state. Therefore, the elastic strains  $e_2$  and  $e_3$  are equal to  $-e_2^T$  and  $-e_3^T$ , respectively, and Hooke's law results in

$$Ee_1 = -\nu\sigma_2 - \nu\sigma_3 \quad (A-2)$$

$$Ee_2 = \sigma_2 - \nu\sigma_3 \quad (A-3)$$

$$Ee_3 = -\nu\sigma_2 + \sigma_3 \quad (A-4)$$

Addition of Eqs. (A-3) and (A-4) and substitution into Eq. (A-2) gives

$$e_1 = \left( \frac{\nu}{1-\nu} \right) (e_2^T + e_3^T) \quad (A-5)$$

for the elastic strain. The total strain  $e^T$  is the sum of this and the transformation strain:

$$e^T = e_1^T + \left( \frac{\nu}{1-\nu} \right) (e_2^T + e_3^T) \quad (A-6)$$

For hydrostatic dilatation of magnitude  $e^T = 3e_1^T$ , with  $e_1^T = e_2^T = e_3^T$ , Eq. (A-6) becomes

$$e^T = \left( \frac{1+\nu}{1-\nu} \right) \frac{e_1^T}{3} \quad (A-7)$$

At the edge of the specimen surface and the crack, the following uniaxial stress conditions exist:

$$\sigma_1 = \sigma_2 = 0, \quad e_3^T = 0 \quad (A-8)$$

In this case, application of Hooke's law gives

$$e_3^T = e_1^T + \nu e_2^T$$

which, for hydrostatic dilatation becomes

$$e_3^T = (1+\nu)e_1^T/3 \quad (A-9)$$

Results of finite-element computations of the strain  $e_1^T$  at the specimen surface as a function of distance from the crack plane are shown in Fig. A1 for the three stress-free transformation strains (1, 0, 0), (0, 0, 1), and (0, 1, 0). The results for the more general transformation strain ( $e_1^T, e_2^T, e_3^T$ ) can be obtained by superposition.

### References

- 'R. S. Garvie, R. H. J. Hannink, and R. T. Pascoe, "Ceramic Steel?," *Nature* (London), **238**, 703-705 (1975).
- 'D. L. Porter and A. H. Heuer, "Mechanisms of Toughening Partially Stabilized Zirconia," *J. Am. Ceram. Soc.*, **60** [3-4] 183-84 (1977).
- 'F. F. Lange, "Transformation Toughening: Part 5. Effect of Temperature and Alloy on Fracture Toughness," *J. Mater. Sci.*, **17**, 253-63 (1982).
- 'F. F. Lange, "Transformation Toughening: Part 4. Fabrication, Fracture Toughness and Strength of  $\text{Al}_2\text{O}_3$ - $\text{ZrO}_2$  Composites," *J. Mater. Sci.*, **17**, 247-54 (1982).
- 'N. Clausen and M. Rühle, "Design of Transformation-Toughened Ceramics," pp. 137-63 in *Advances in Ceramics, Vol. 3, Science and Technology of Zirconia*. Edited by A. H. Heuer and L. W. Hobbs. American Ceramic Society, Columbus, OH, 1981.
- 'M. V. Swain, R. H. J. Hannink, and R. C. Garvie, pp. 339-54 in *Fracture Mechanics of Ceramics, Vol. 6*. Edited by R. C. Bied, A. G. Evans, D. P. H. Hasselman, and F. F. Lange. Plenum Press, New York, 1983.
- 'R. H. J. Hannink and M. V. Swain, "Magnesia-Partially Stabilized Zirconia: The Influence of Heat Treatment on Thermomechanical Properties," *J. Aust. Ceram. Soc.*, **10** [2] 53-62 (1982).
- 'A. H. Heuer, "Transformation Toughening in  $\text{ZrO}_2$ -Containing Ceramics," *J. Am. Ceram. Soc.*, **70** [10] 689-98 (1987).

<sup>9</sup>A. H. Heuer, M. J. Readey, and R. Steinbrech, "Resistance Curve Behavior of Supertough MgO-Partially-Stabilized  $ZrO_2$ ," *Mater. Sci. Eng.*, **A105/106**, 83-89 (1988).

<sup>10</sup>A. G. Evans and R. M. Cannon, "Toughening of Brittle Solids by Martensitic Transformations," *Acta Metall.*, **34** [5] 761-800 (1986).

<sup>11</sup>K. D. Keefer and T. A. Michalske, "Determination of Phase Transformation Depth Profiles with Synchrotron Radiation," *J. Am. Ceram. Soc.*, **70** [4] 227-31 (1987).

<sup>12</sup>R. C. Garvie, R. H. T. Hannink, and M. V. Swain, "X-Ray Analysis of the Transformed Zone in Partially Stabilized Zirconia (PSZ)," *J. Mater. Sci. Lett.*, **1**, 437-40 (1982).

<sup>13</sup>T. Kosmac, R. Wagner, and N. Claussen, "X-ray Determination of Transformation Depths in Ceramics Containing Tetragonal  $ZrO_2$ ," *J. Am. Ceram. Soc.*, **64** [4] C-72-C-73 (1981).

<sup>14</sup>Y. Mori, Y. Kitano, and A. Ishitani, "X-ray Determination of Transformation Zone Size in Toughened Zirconia Ceramics," *J. Am. Ceram. Soc.*, **71** [7] C-322-C-324 (1988).

<sup>15</sup>L. H. Schoenlein and A. H. Heuer; pp. 309-26 in *Fracture Mechanics of Ceramics*, Vol. 6. Edited by R. C. Bradt, A. G. Evans, D. P. H. Hasselman, and F. F. Lange. Plenum Press, New York, 1983.

<sup>16</sup>L. H. Schoenlein, M. Rühle, and A. H. Heuer, "In Situ Straining Experiments of Mg-PSZ Single Crystals"; pp. 275-82 in *Advances in Ceramics*, Vol. 12, *Science and Technology of Zirconia II*. Edited by N. Claussen, M. Rühle, and A. H. Heuer. American Ceramic Society, Columbus, OH, 1984.

<sup>17</sup>D. R. Clarke and F. Adar, "Measurement of the Crystallographically Transformed Zone Produced by Fracture in Ceramics Containing Tetragonal Zirconia," *J. Am. Ceram. Soc.*, **65** [6] 284-88 (1982).

<sup>18</sup>R. H. Dauskardt, D. K. Veirs, and R. O. Ritchie, "Spatially Resolved Raman Spectroscopy of Transformed Zones in MgO-Partially-Stabilized Zirconia," *J. Am. Ceram. Soc.*, **72** [7] 1124-30 (1989).

<sup>19</sup>G. Katagiri, H. Ishida, A. Ishitani, and T. Masaki, "Direct Determination of Transformation Zone Size in  $Y_2O_3$  Containing Tetragonal  $ZrO_2$  Polycrystals"; pp. 537-44 in *Advances in Ceramics*, Vol. 24A, *Science and Technology of Zirconia III*. Edited by S. Sōmiya, N. Yamamoto, and H. Hanagida. American Ceramic Society, Westerville, OH, 1988.

<sup>20</sup>R. H. Dauskardt, D. B. Marshall, and R. O. Ritchie, "Cyclic Fatigue-Crack Propagation in Magnesia-Partially-Stabilized Zirconia Ceramics," *J. Am. Ceram. Soc.*, **73** [4] 893-903 (1990).

<sup>21</sup>D. B. Marshall, M. C. Shaw, R. H. Dauskardt, R. O. Ritchie, M. Readey, and A. H. Heuer, "Crack-Tip Transformation Zones in Toughened Zirconia," *J. Am. Ceram. Soc.*, **73** [9] 2659-66 (1990).

<sup>22</sup>R. M. McMeeking and A. G. Evans, "Mechanics of Transformation Toughening in Brittle Materials," *J. Am. Ceram. Soc.*, **65** [5] 242-46 (1982).

<sup>23</sup>D. B. Marshall, M. Drory, and A. G. Evans, "Transformation Toughening in Ceramics"; pp. 289-307 in *Fracture Mechanics of Ceramics*, Vol. 6. Edited by R. C. Bradt, A. G. Evans, D. P. H. Hasselman, and F. F. Lange. Plenum Press, New York, 1983.

<sup>24</sup>B. Budiansky, J. W. Hutchinson, and J. C. Lambropoulos, "Continuum Theory of Dilatant Transformation Toughening in Ceramics," *Int. J. Solids Struct.*, **19**, 337 (1983).

<sup>25</sup>D. M. Stump and B. Budiansky, "Crack Growth Resistance in Transformation-Toughened Ceramics," *Int. J. Solids Struct.*, **25** [6] 635-46 (1989).

<sup>26</sup>J. C. Lambropoulos, "Shear, Shape and Orientation Effects in Transformation Toughening," *Int. J. Solids Struct.*, **22**, 1083-106 (1986).

<sup>27</sup>L. R. F. Rose, "Kinematical Model for Stress-Induced Transformation around Cracks," *J. Am. Ceram. Soc.*, **69** [3] 208-12 (1986).

<sup>28</sup>M. V. Swain and R. H. J. Hannink, "R-Curve Behavior in Zirconia Ceramics"; pp. 225-39 in *Advances in Ceramics*, Vol. 12, *Science and Technology of Zirconia II*. Edited by N. Claussen, M. Rühle, and A. H. Heuer. American Ceramic Society, Columbus, OH, 1984.

<sup>29</sup>D. B. Marshall, "Strength Characteristics of Transformation-Toughened Zirconia," *J. Am. Ceram. Soc.*, **69** [3] 173-80 (1986).

<sup>30</sup>D. B. Marshall and M. V. Swain, "Crack Resistance Curves in Magnesia-Partially-Stabilized Zirconia," *J. Am. Ceram. Soc.*, **71** [6] 399-407 (1988).

<sup>31</sup>B. N. Cox, D. B. Marshall, D. Kouris, and T. Mura, "Surface Displacement Analysis of the Transformed Zone in Magnesia Partially Stabilized Zirconia," *J. Eng. Mater. Technol.*, **110** [2] 105-109 (1988).

<sup>32</sup>R. H. J. Hannink, "Microstructural Development of Subeutectoid-Aged  $ZrO_2$  Alloys," *J. Mater. Sci.*, **18** [2] 457-70 (1983).

<sup>33</sup>R. H. J. Hannink, C. J. Howard, E. H. Kisi, and M. V. Swain, "Relationship Between Fracture Toughness and Phase Assemblage in Mg-PSZ"; unpublished work.

<sup>34</sup>R. J. Hill and B. E. Reichert, "Measurement of Phase Abundance in Magnesia-Partially-Stabilized Zirconia by Rietveld Analysis of X-ray Diffraction Data," *J. Am. Ceram. Soc.*, **73** [10] 2822-27 (1990).

<sup>35</sup>D. Post, "Moiré Interferometry"; Ch. 7 in *Handbook on Experimental Mechanics*. Edited by A. S. Kobayashi. Prentice-Hall, Englewood Cliffs, NJ, 1987.

<sup>36</sup>M. R. James, W. L. Morris, and B. N. Cox, "A High Accuracy Automated Strain Field Mapper," *Exp. Mech.*, **30**, 60-68 (1990).

<sup>37</sup>A. G. Evans, D. B. Marshall, and N. H. Burlingame, "Transformation Toughening in Ceramics"; pp. 202-16 in *Advances in Ceramics*, Vol. 3, *Science and Technology of Zirconia*. Edited by A. H. Heuer and L. W. Hobbs. American Ceramic Society, Columbus, OH, 1981.

<sup>38</sup>C. H. Hsueh and P. F. Becker, "Some Considerations of Nonideal Transformation-Zone Profile," *J. Am. Ceram. Soc.*, **71** [6] 494-97 (1988).

<sup>39</sup>D. B. Marshall and M. C. Shaw; in preparation. □



Rockwell International  
Science Center

SC71002.FR

## 5.2 CRACK-TIP TRANSFORMATION ZONES IN TOUGHENED ZIRCONIA

published in J. Am. Ceram. Soc.

## Crack-Tip Transformation Zones in Toughened Zirconia

David B. Marshall\* and Michael C. Shaw\*

Rockwell International Science Center, Thousand Oaks, California 91360

Reinhold H. Dauskardt\* and Robert O. Ritchie

Center for Advanced Materials, Lawrence Berkeley Laboratory, University of California, Berkeley, California 94720

Michael J. Readey\* and Arthur H. Heuer\*

Department of Materials Science and Engineering, Case Western Reserve University, Cleveland, Ohio 44106

Transformation zones surrounding cracks in several toughened magnesia-partially-stabilized zirconia ceramics are characterized by optical interference measurements of surface uplift and by Raman microprobe spectroscopy. The measurements demonstrate that the volume fraction of transformation is nonuniform within the zone and that the extent of the frontal zone is approximately the same as that of the wake. Results are used to evaluate the crack-tip shielding stress intensity factor and to compare with the measured fracture toughness. [Key words: crack tip, partially stabilized zirconia, Raman spectroscopy, transformations, toughness.]

## I. Introduction

The fracture toughness of  $ZrO_3$ -based ceramics can be increased by an order of magnitude (from ~2 to 20 MPa·m<sup>1/2</sup>) by manipulating their microstructures to change the stability of the retained tetragonal phase.<sup>1-9</sup> It is reasonably well established that at least a substantial portion of this toughening results from shielding of crack tips from the applied load by the strains resulting from a martensitic transformation from tetragonal to monoclinic symmetry within limited zones surrounding the cracks.<sup>7-10</sup> Such zones have been detected by several techniques: X-ray diffraction,<sup>4,11-13</sup> transmission electron microscopy (TEM),<sup>6,16,17</sup> Raman spectroscopy,<sup>18-20</sup> and observations by optical interference methods of surface distortions due to the transformation strains.<sup>21-23</sup> However, these methods have not yet been used to provide sufficiently quantitative measurements of transformation zone parameters (i.e., distributions of the transformation products, net transformation strain) for a complete calculation of the toughening due to shielding.

In this paper, we present detailed measurements of distributions of transformation products within zones around cracks that were grown under controlled and known stress intensity factors, and preliminary correlations of the amount of shielding with fracture mechanics predictions. Previous attempts at such correlations have been at best order-of-magnitude esti-

mates because of the difficulty of measuring zone parameters: most have used X-ray measurements from fracture surfaces of broken test pieces to estimate the zone size, assuming a steady-state crack with a constant amount of transformation inside the zone and none outside.<sup>4,10,12,13</sup> We will show that, for MgO-partially-stabilized zirconia materials, the distribution of monoclinic phase is not well approximated by a step function. Moreover, unless the fracture surface is formed by crack growth at constant applied stress intensity factor, zone width measurements from a large area of the fracture surface (as is the case for X-ray measurements) may be misleading.

## II. Shielding Crack Tips by Transformation Zones

Rigorous fracture mechanics analyses have been derived to relate the toughness increase due to a crack-tip transformation zone to the zone parameters.<sup>10,23-30</sup> Two equivalent approaches have been used, one being based on an energy-balance analysis and the other involving calculation of the reduction in crack-tip stresses by the transformation strains. In the latter formulation, the shielding effect of the transformation zone is defined by a stress intensity factor,  $K_s$ , such that the crack-tip stress intensity factor,  $K_{tip}$ , is given by

$$K_{tip} = K_s - K_a \quad (1)$$

where  $K_a$  is the applied stress intensity factor. The criterion for crack growth under quasi-static, monotonic loading is taken as  $K_{tip} = K_0$ , where  $K_0$  is the fracture toughness in the absence of shielding. The corresponding value of  $K_s$  ( $K_s = K_0 + K_a$ ) is the fracture toughness measured in the presence of shielding.

For a steady-state crack (i.e., crack growth at constant  $K_a$ ), with a zone containing a uniform volume fraction,  $f$ , of transformation product over a distance  $w$  from the crack surface, the shielding stress intensity factor is<sup>23,25</sup>

$$K_s = \frac{A/\sqrt{E}e^{\gamma} \sqrt{w}}{1 - \nu} \quad (2)$$

where  $E$  is Young's modulus,  $\nu$  is Poisson's ratio,  $e^{\gamma}$  is the transformation strain, and the constant  $A$  is dependent upon the shape of the zone ahead of the crack tip, as well as the nature of transformation strain. If  $e^{\gamma}$  is an isotropic dilatational strain (i.e., all long-range shear strains relieved by twinning) and the frontal zone is defined by a contour of constant hydrostatic tension in the elastic crack-tip field, then  $A = 0.22$ .<sup>23</sup> If the amount of transformation is not uniform, but contours of constant  $f$  in the wake and around the crack tip are all geo-

D. Clarke—contributing editor

Manuscript No. 19793. Received November 21, 1989, approved May 11, 1990.

Funding for this work was supplied at Rockwell by the U.S. Air Force Office of Scientific Research under Contract No. F49620-89-C-0031, at I.B.I. by the U.S. Department of Energy under Contract No. DE-AC03-76SF00098, and at Case Western Reserve University by the National Science Foundation under Grant No. DMR87-15623.

\*Member, American Ceramic Society.

metrically similar (and the net transformation stress is dilatational), then  $K_c$  can be evaluated by integration of Eq. (2):<sup>10,25,31,32</sup>

$$K_c = \frac{AEe^T}{1-\nu} \int_0^{w_0} \frac{f(x)}{2\sqrt{x}} dx \quad (3)$$

where  $f(x)$  is the function representing the variation of the volume fraction of transformed product with distance  $x$  from the crack surface and  $w_0$  is the distance from the crack at which no transformation occurs. It is important to note that Eqs. (2) and (3) are restricted to steady-state cracks, with wake zones of constant width. In general, initial growth of a crack in these materials is dictated by an  $R$ -curve, with increasing zone width as the crack grows.<sup>21-23,33</sup> Calculations of these  $R$ -curves indicate that the steady-state zone width is achieved after the crack grows a distance several times the width of the steady-state zone.<sup>25,26,28</sup> It is also noteworthy that, while the fracture mechanics analyses are available to relate toughness to zone parameters, predictions of the zone parameters such as  $f(x)$ , the frontal shape, and the net transformation strain are presently not available. These parameters are determined by the initiation condition for transformation and the degree of relaxation of shear strains by twinning and variant formation.

Since the stresses outside the transformation zone are dominated by the applied stress intensity factor,  $K_a$ , the size of the transformation zone in a given material is dependent upon  $K_a$ . Therefore, the degree of shielding is diminished if crack growth occurs at  $K_a < K_c$  (e.g., slow crack growth induced by cyclic loading or reactive environment), or enhanced if growth occurs at  $K_a > K_c$  (unstable crack growth, if dynamic effects do not reduce the zone width). The dependence of  $K_c$  on  $K_a$  can be estimated by assuming that transformation initiates at a position corresponding to a critical stress  $\sigma_c$  in the elastic field defined by  $K_a$ . Then the zone width is  $\sqrt{w} \propto K_a/\sigma_c$ , and the shielding stress intensity factor (Eq. (2) or (3)) becomes

$$K_c = \beta K_a \quad (4)$$

where  $\beta$  is a constant for a given material (i.e., for given  $\sigma_c$ ,  $e^T$ ,  $E$ ).

### III. Experiments

Partially stabilized zirconia containing 9 mol% MgO (Mg-PSZ) was chosen as the test material because the fracture toughness (and amount of shielding) can be varied over a wide range by subeutectoid heat treatment. Fabrication, heat treatment, and microstructures have been described by Hannink<sup>24</sup> and Hannink and Swain;<sup>7</sup> the microstructures are composed of cubic  $ZrO_3$  grains  $\sim 50 \mu\text{m}$  in diameter containing lens-shaped tetragonal precipitates ( $\sim 40 \text{ vol\%}$ ) with largest dimension  $\sim 300 \text{ nm}$ . The subeutectoid heat treatment does not significantly alter the microstructural dimensions, but it is known to cause a decomposition reaction resulting in growth of an intermediate ( $\delta$ ) phase,  $\text{Mg}_2\text{Zr}_2\text{O}_5$ , at the precipitate-matrix boundaries, which is thought to destabilize the tetragonal phase.

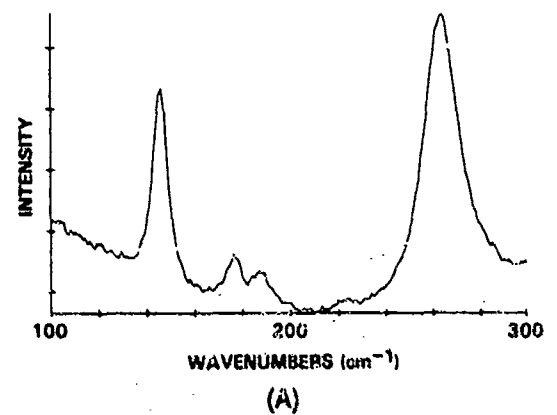
Transformation zones surrounding cracks grown under known loading conditions (both cyclic and monotonic) in compact tension fracture mechanics specimens were characterized by two methods: interference microscopy and Raman spectroscopy. The optical interference measurements were obtained from the faces of the compact tension specimens which had been polished prior to introduction of the cracks. The out-of-plane surface displacements detected by this technique provide an indication of the transformation strains. The Raman spectra from the same surface provide direct measurements of the fractions of tetragonal and monoclinic phases.<sup>14</sup>

Two optical interference methods were used: Nomarski interference and conventional interference. Nomarski interference provides a qualitative indication of changes in the

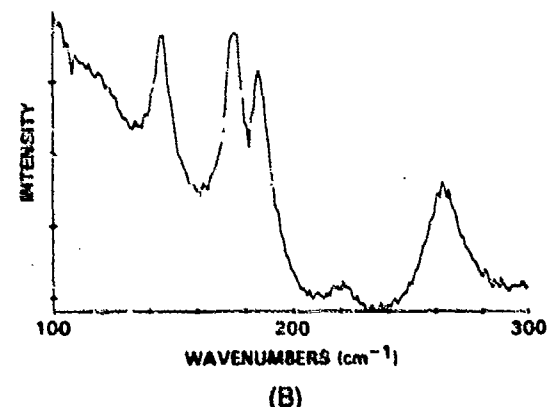
inclination of the surface, whereas the conventional interference provides a direct quantitative measure of the normal surface displacement.\*

Raman measurements were obtained using a microprobe system with lateral and depth resolution of  $\sim 2 \mu\text{m}$ . Typical Raman spectra from regions adjacent to a crack and remote from the crack in a material of high toughness ( $K_c = 16 \text{ MPa}\cdot\text{m}^{1/2}$ ) are shown in Fig. 1. In most experiments, the specimens

\*Interference microscopy uses a Michelson interferometer to form an image by interference of light from the specimen surface and a flat reference mirror. Variations in the distance between the specimen surface and reference mirror then show up as fringes corresponding to contours of constant separation, with increments of half of the wavelength of the light.



(A)



(B)

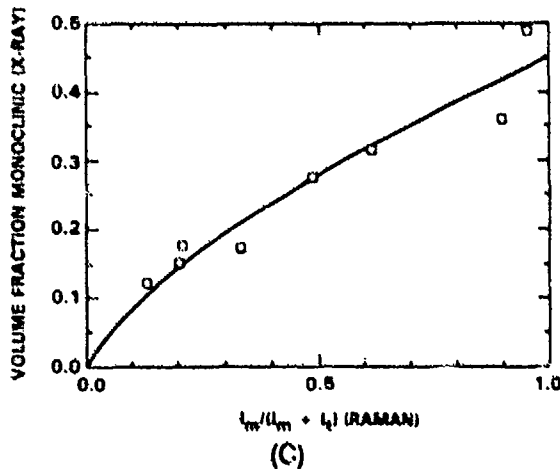


Fig. 1. Raman spectra from Mg-PSZ with (A) mostly tetragonal (remote from crack) and (B) mostly monoclinic (adjacent to crack) precipitates. (C) Comparison of Raman intensity ratios with the fraction of monoclinic phase evaluated from X-ray measurements.

were scanned using a motorized stage, with the intensities of the monoclinic and tetragonal peaks being measured as a function of distance from the crack, along lines normal to the crack, on the polished surface. The fraction of monoclinic phase was calculated from intensity ratios, using a calibration with X-ray measurements.<sup>12</sup> The calibration was done by comparing X-ray and Raman measurements from a series of specimens that were heat-treated (1100°C) for various times to change the amount of tetragonal-to-monoclinic transformation throughout the bulk.<sup>7</sup>

#### IV. Results

##### (1) Raman Calibration

The volume fractions of monoclinic phase in the series of heat-treated specimens were evaluated from the integrated X-ray intensities from the monoclinic (111) and (111) and the tetragonal/cubic (111) peaks. The integrated intensities were derived from area measurements obtained by subtracting the background and fitting Pearson VII functions.<sup>35</sup> These results are compared with intensity ratios for the monoclinic (179 cm<sup>-1</sup>) and tetragonal (145 cm<sup>-1</sup>) Raman peaks in Fig. 1(C). Similar calibration curves were obtained from the area ratios using the combined peaks 179, 189 cm<sup>-1</sup> for the monoclinic phase and 145, 265 cm<sup>-1</sup> for the tetragonal phase. In all cases the calibration curves were nonlinear. In previous studies that used Raman measurements to evaluate the volume fraction of transformation in ZrO<sub>2</sub>, a linear relation was assumed.

##### (2) Crack-Tip Zone Shape

Nomarski and conventional interference micrographs of the crack-tip region in a high-toughness ( $K_c = 16 \text{ MPa} \cdot \text{m}^{1/2}$ ) material are compared in Figs. 2(A) and (B). The conventional interference micrograph was obtained with the reference mirror set parallel to the undistorted surface, so that the fringes represent contours of constant out-of-plane surface displacement, separated by half of the wavelength of the monochromatic illumination ( $\lambda/2 = 2700 \text{ \AA}$ ). Surface uplift is detected to a distance of ~1.5 mm from the crack plane, and the contours ahead of the crack appear to be approximately semicircular in shape. These out-of-plane displacements give an approximate idea of the transformation zone dimensions. However, the contours do not provide a one-to-one correspondence, because the transformation strains cause elastic surface uplift outside the zone. Moreover, the displacements are influenced by constraint conditions, which differ near the crack tip and in the wake. Therefore, the width of the uplifted region is larger than the actual transformation zone, and the uplift adjacent to the crack is smaller near its tip than further behind the tip (Figs. 2(A) and 3(A)).

In the Nomarski interference micrograph (Fig. 2(B)), the same general surface uplift is evident adjacent to the crack, but the extent of uplift is not resolved as sensitively as in conventional interference. In addition, there is a general appearance in Nomarski interference of small transformation bands oriented at an angle of ~45° to the direction of crack growth, suggestive of a frontal zone defined by shear stress contours. These small transformation bands are also visible in Fig. 2(A), as jagged outlines of the contours which would otherwise be smooth. It is clear from this micrograph that the bands are only a small perturbation on the overall displacements due to the transformation zone.

A more definitive determination of the frontal zone shape is obtained from Raman microprobe measurements along scans ahead of, and beside, the crack (Fig. 3(B)). These results indicate that the decrease in volume fraction of transformed monoclinic phase with distance from the crack is approximately the same ahead of the crack tip as in the crack wake. Therefore, the zone shape (as defined by any contour of constant  $f$ ) is approximately semicircular ahead of the crack tip. This shape differs significantly from that of a hydro-

static stress contour, which is often assumed, and which would extend further ahead of the crack than to the side by a factor of 1.5.<sup>26</sup>

##### (3) Initial Zone Development

The crack shown in Fig. 2 was grown initially from a saw notch with a monotonically increasing stress intensity factor, following the resistance curve shown in Fig. 4: the critical applied stress intensity factor increased from an initial value of ~7 MPa · m<sup>1/2</sup> to a steady-state value of ~16 MPa · m<sup>1/2</sup> over a crack extension of ~4 mm (with 90% of the increase occurring within the first 2 mm). The corresponding increase in size of the transformation zone is clearly evident in the interference micrograph of Fig. 2(A): the outer limit of detectable surface displacement increased from an initial value of ~50 μm from the crack plane to ~1.5 mm over the same region of crack growth. The out-of-plane surface displacements, obtained from Fig. 2(A) at several positions along the crack, both within the region of initial growth and within the steady-state region, are plotted as a function of distance from the crack in Fig. 3(A). Corresponding Raman measurements of the volume fractions of monoclinic phase are shown in Fig. 3(B). The increasing size of the transformation zone with initial crack growth is reflected in both measurements.

##### (4) Steady-State Transformation Zone

Transformation zones were characterized in regions adjacent to cracks that had been grown under steady-state conditions in two materials, one with a steady-state toughness of 10 MPa · m<sup>1/2</sup> and the other with toughness of 16 MPa · m<sup>1/2</sup>. Both monotonic and cyclic loading conditions were used in order to allow comparison of zones developed under different values of  $K_c$  in a given material. Details of the cyclic loading experiments and fatigue crack growth characteristics are described in Ref. 36. For monotonically loaded cracks, measurements were obtained from regions where the cracks had grown at constant  $K_c$  for distances larger than 5 times the transformation zone width. Under cyclic loading, the cracks were grown at constant velocity over a similar distance, with  $K_c$  varying between fixed values  $K_{c,\text{ax}}$  and  $K_{c,\text{min}}$ , with  $K_{c,\text{min}}/K_{c,\text{ax}} = 0.1$ . Under such conditions, fatigue crack growth occurs for  $K_{c,\text{ax}} \geq K_c/2$  in these materials.<sup>36</sup>

Interference micrographs are shown in Figs. 5(A) and (B) for steady-state cracks that were grown under monotonic loading. These micrographs were obtained with the reference mirror tilted so that the undistorted flat surface appears as parallel equally spaced fringes normal to the crack, and out-of-plane surface displacements appear as displacement of the fringes in a direction parallel to the crack. The areas shown were well behind the crack tip, where the displacements were not influenced by the near-tip constraint mentioned above. The displacements measured from Figs. 5(A) and (B), as well as from steady-state cracks grown under cyclic loading, are plotted in Fig. 5(C). Large differences are evident in both the magnitude of the displacement at the crack plane and in the extent of the displacement field from the crack.

Corresponding Raman measurements of the fraction of transformed precipitates as a function of distance from the crack plane are shown in Figs. 6 and 7; intensity measurements (with background subtracted) from a single scan from the higher-toughness material are shown in Figs. 6(A) and (B), whereas averaged data from several scans, converted to fraction transformed, are plotted as a function of  $\sqrt{x}$  in Fig. 7. The shielding contributions to the fracture toughnesses (Eq. (3)) are proportional to the areas beneath the curves in Fig. 7. Several results from these figures are noteworthy:

(1) The minor peaks in the individual scans of Figs. 6(A) and (B) are genuine variations in the fraction of monoclinic and tetragonal phases, both within the transformation zone and remote from the crack. (Statistical fluctuations in the Raman intensities are smaller than these variations by a factor of approximately 5.) The spatial scale of the variations

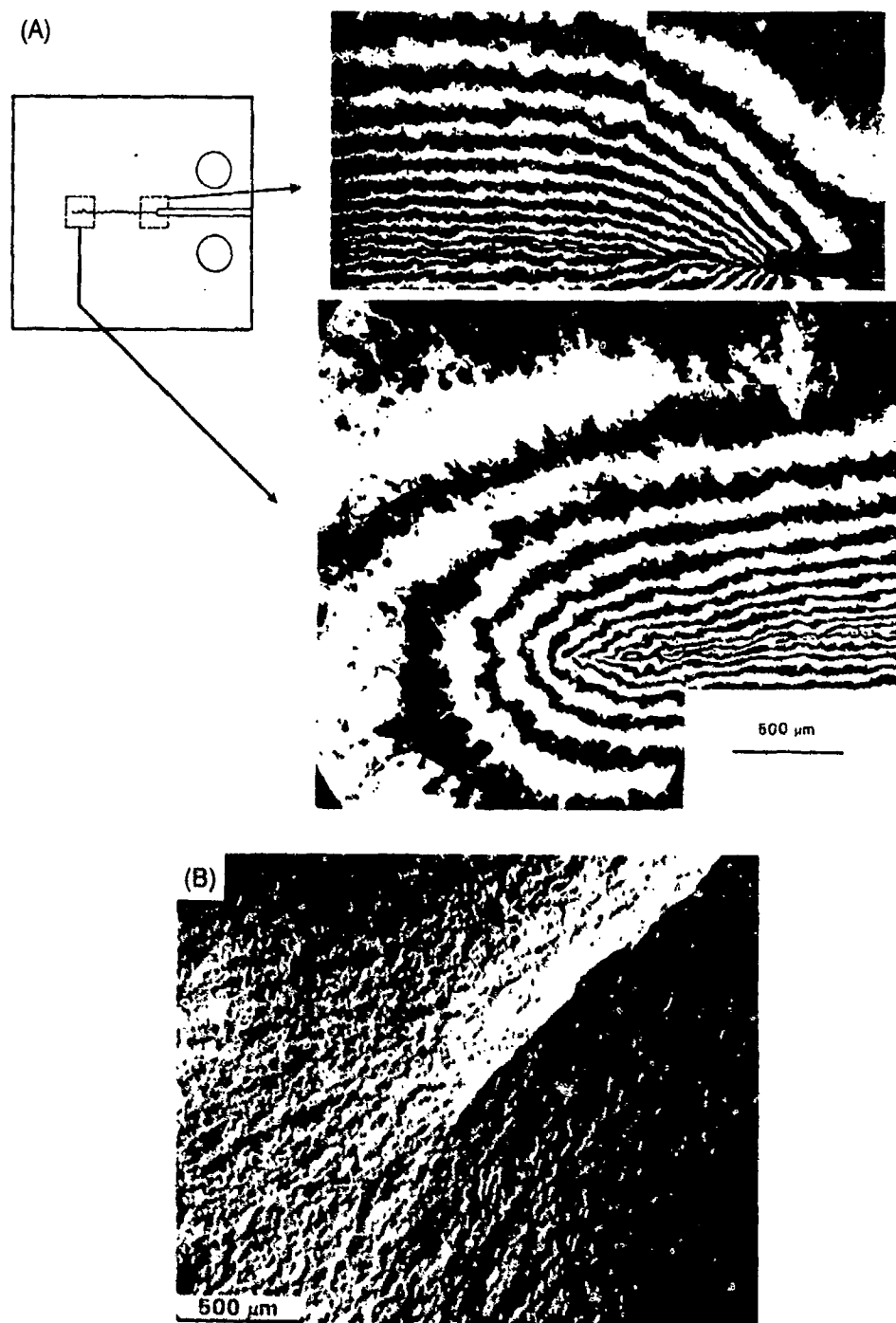


Fig. 2. (A) Optical interference micrographs ( $\lambda = 5400 \text{ \AA}$ ) of crack-tip region and region of initial crack growth in high-toughness Mg-PSZ ( $K_c = 16 \text{ MPa} \cdot \text{m}^{1/2}$ ). Reference mirror parallel to undistorted surface. (B) Nomarski interference micrograph of crack tip in (A).

is approximately equal to the grain size (as are the widths of the irregularities in surface distortions observed by interference microscopy), suggesting that the crystallographic orientation relative to the crack-tip stress field affects the amount of transformation.

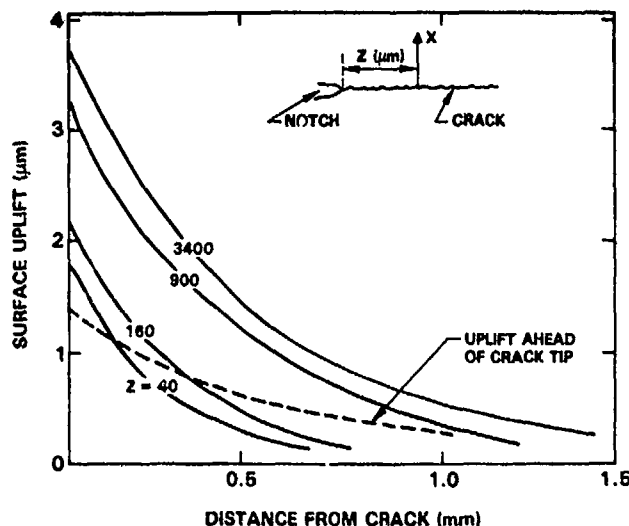
(2) Complete transformation of the available tetragonal phase was never observed in regions adjacent to the crack; the maximum intensity ratio  $I_m/(I_m + I_t) \approx 0.8$  observed for the high-toughness material corresponds to a volume fraction of  $\sim 0.35$ , whereas the total fraction of tetragonal and monoclinic phases is  $\sim 0.45$ . Moreover, with the background (preexisting) monoclinic content subtracted, the largest volume fraction of transformation induced by the crack is only  $f_0 = 0.25$ .

(3) Both the fraction of transformed monoclinic phase adjacent to the crack and the width of the transformation zone

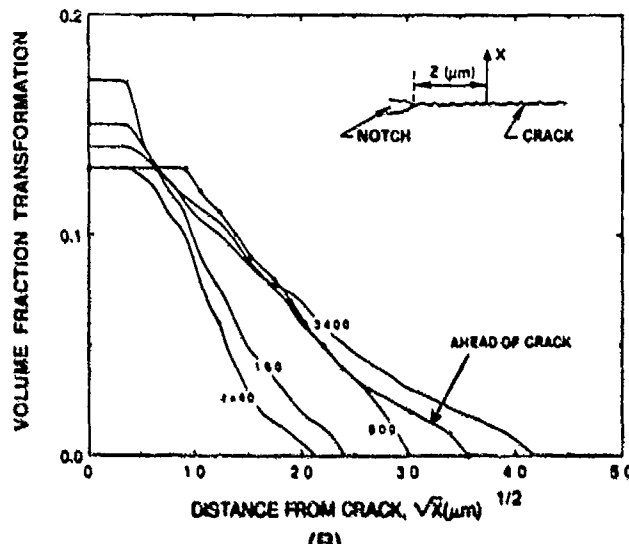
are larger in the higher-toughness material than in the lower-toughness material, and larger under monotonic loading than under cyclic loading in a given material (note that crack growth under monotonic loading involves a larger applied stress intensity factor than under cyclic loading).

## V. Discussion

Previous calculations of crack-tip shielding have assumed that the amount of transformed monoclinic phase adjacent to the crack is equal to the fraction of tetragonal precipitates in the original material ( $\sim 0.45$ ).<sup>6,10,12</sup> This was based on transmission electron microscopy observations which showed all precipitates transformed near the crack.<sup>6,14,17</sup> The results in Section IV(4) indicate that the fraction transformed is al-



(A)



(B)

Fig. 3. (A) Normal surface displacements adjacent to crack in Fig. 2(A) at several positions along the region of initial growth and within steady-state region. Crack tip is at  $z = 6$  mm. Displacements ahead of crack are measured along a line parallel to the crack plane, ahead of the tip. All other measurements taken along lines normal to crack plane at locations indicated. (B) Fraction of material transformed from tetragonal to monoclinic phase by the crack at positions in (A).

ways less than this (maximum 0.25), thus suggesting that the reduced constraint of a thin TEM foil allows additional transformation. These results indicate that calculation of transformation zone sizes based on X-ray measurements, with the assumption of complete transformation (or even uniform volume fraction of transformed phase) within the zone, would give substantial underestimates. Moreover, since the zone sizes evident in Figs. 3(B) and 7 are much larger than the penetration depths of X-rays,<sup>11</sup> the zone depths could not be characterized by X-ray measurements from fracture surfaces, regardless of whether or not any assumptions were made about the zone profile.

The shape of the zone ahead of the crack has been predicted to have a large effect on the degree of shielding.<sup>10,20</sup> For example, with a given zone width in the wake of the crack, a frontal zone defined by a contour of constant maximum crack-tip shear stress ( $A = 0.38$  in Eq. (2)) results in a calculated toughness increase larger by a factor of 1.7 than that due to a frontal zone defined by a contour of constant hydrostatic stress ( $A = 0.22$ ).<sup>10</sup> The results of Fig. 2 suggest

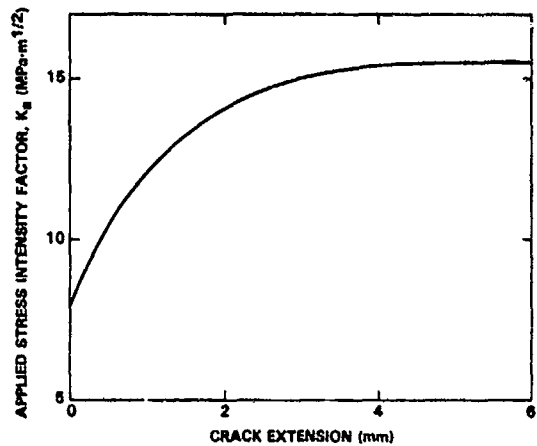


Fig. 4. Crack growth resistance curve for initial growth of crack in Fig. 2.

that in Mg-PSZ the zone shape is approximately semicircular ahead of the crack tip. Local bands of transformation within the zone show strong contrast in Nomarski interference because of large local changes in slope of the surface. Such observations could be taken to suggest a zone defined by a shear stress contour. However, both the surface displacement and Raman measurements indicate that these bands are only a small fluctuation within the overall transformation zone (although it is noted that they may be a critical step in the mechanism for determining the total size of the zone). Evaluation of  $K_t$  for a dilatational transformation strain within a zone of constant width in the wake of the crack and semicircular shape ahead of the crack tip yields  $A = 0.25$  in Eqs. (2) and (3).<sup>21</sup>

The results in Fig. 7 can be used with Eq. (3) to evaluate the shielding stress intensity factors, if we assume that the net transformation strain is purely dilatational ( $\epsilon^t = 0.04$ ) and take the frontal zone to be semicircular. The calculated values of  $K_t$  (using  $E = 200$  GPa for Mg-PSZ) for the four sets of data in Fig. 7 are plotted as a function of the maximum applied stress intensity factor ( $K_t$  for monotonic loading,  $K_{t,0}$  for cyclic loading) in Fig. 8.

In both materials the dependence of the calculated values of  $K_t$  on  $K_{t,0}$  for cracks grown under monotonic and cyclic loading, is consistent with Eq. (4). This correlation implies that, provided the assumed transformation strains are the same in both loading conditions, the shielding from the transformation zone is dictated by the maximum value of  $K_t$  and is not influenced by the cyclic nature of the load. Therefore, the fatigue crack growth mechanism must involve reduction of the intrinsic toughness,  $K_0$ , rather than degradation of the transformation toughening. This conclusion is supported independently by crack growth data which have been shown to exhibit a velocity that is determined uniquely by the crack-tip stress intensity factor range  $\Delta K_{t,0} = K_{t,0} - K_t$  in these two materials, as well as in several others that were heat-treated to give different degrees of toughening.<sup>22</sup>

The transformation strains in monotonic and cyclic loading can be compared by combining the Raman and surface uplift measurements of Figs. 5(C) and 7. Qualitatively similar differences between the four sets of data within each of these figures are evident. Direct comparison of the displacement,  $u_0$ , adjacent to the cracks, with values of  $K_t$  calculated from the Raman measurements is shown in Fig. 9. Both  $u_0$  and  $K_t$  must be monotonically increasing functions of  $f$  and zone width, as measured from the Raman data. However, the measured values of  $u_0$  are influenced also by the actual transformation strains,  $\epsilon^t$ , whereas the calculated values of  $K_t$  are not affected by  $\epsilon^t$  because a constant value was assumed in calculating  $K_t$  from the Raman data. Therefore, if the transformation strains differed in monotonic and cyclic loading (e.g., different

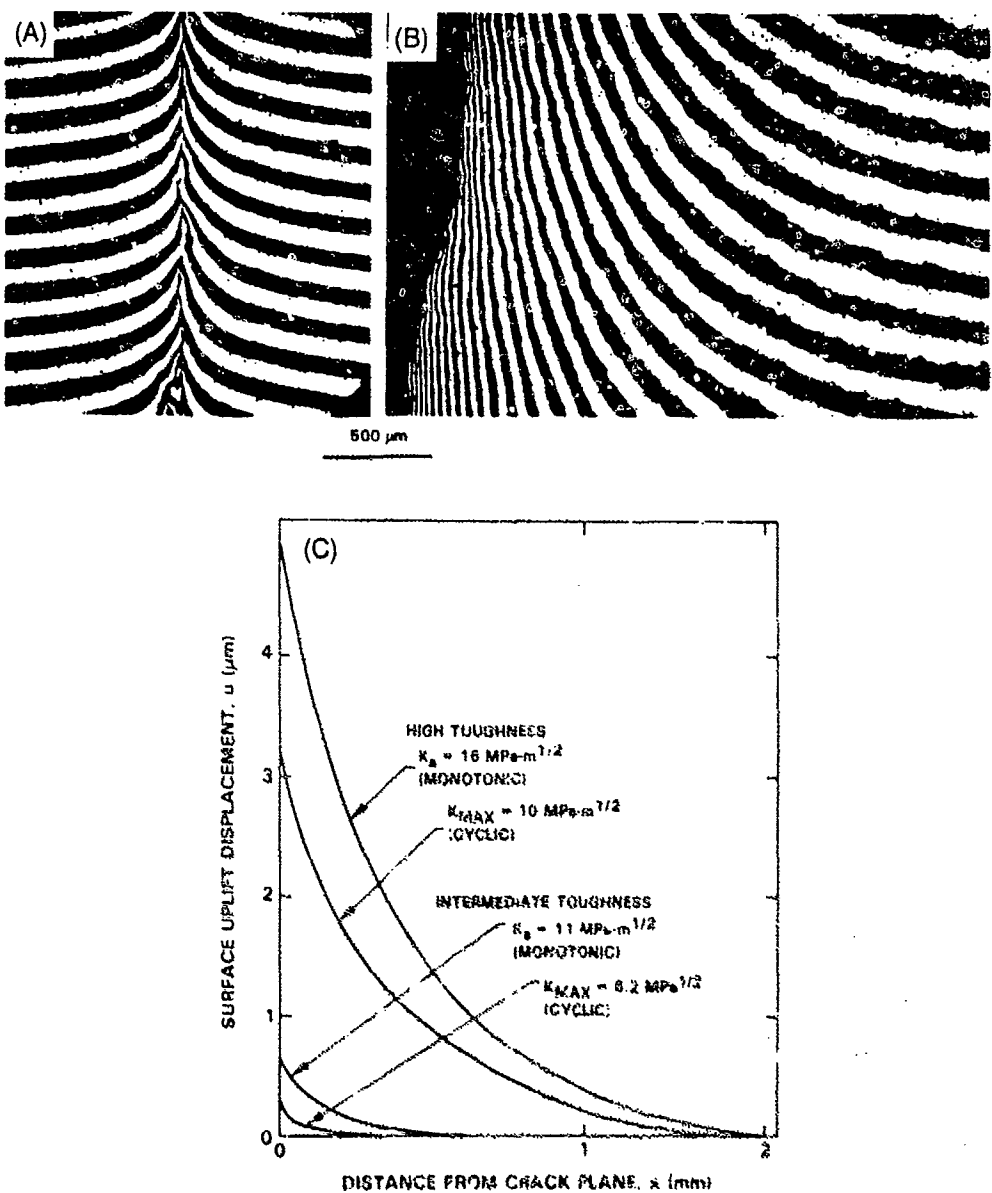


Fig. 5. Optical interference micrographs from regions adjacent to steady-state cracks in Mg-PSZ with (A) intermediate and (B) high toughness (one side of crack only). Reference mirror tilted so as to give parallel equally spaced fringes from the undistorted specimen surfaces. Fringe deflections toward the top of the micrographs within the regions adjacent to the cracks correspond to uplift of the surface. (C) Normal surface displacement adjacent to steady-state cracks (measured from optical interference micrographs such as (A) and (B))

amounts of twinning resulting in different shear components in  $\epsilon'$ ), the data in Fig. 9 would fall on two separate curves for monotonic and cyclic loading. Since all of the data fall on a single curve within the measurement accuracy, it is concluded that the transformation strains in cyclic and monotonic loading do not differ significantly.

The magnitudes of the shielding stress intensity factors may be compared with the measured toughness using Eq. (1): fitting this equation to the data for monotonic loading (broken curve in Fig. 8) gives  $K_0 = 7 \text{ MPa}\cdot\text{m}^{1/2}$ . This is larger than the value  $K_0 = 3 \text{ MPa}\cdot\text{m}^{1/2}$  measured from overaged material in which transformation toughening is eliminated, implying that the calculated values of  $K_0$  do not fully account for the measured toughness increases. Several possible causes of this discrepancy are (1) partial reversibility in the transformation, (2) a shear component in the net transformation strain (i.e., transformation shear strain not fully relieved by twinning), and (3) contributions from other toughening mechanisms. Whether or not there is a shear component in the transformation strain can in principle be determined by

comparison of measured surface displacement profiles such as Fig. 5 with displacements calculated using various trial combinations of dilation and shear in the strain  $\epsilon'$  and the fraction of transformation,  $f(x)$ , measured by Raman spectroscopy. Preliminary calculations with  $\epsilon'$  assumed to be purely dilational suggested that a component of shear may exist, especially in the region close to the crack;<sup>24</sup> further calculations with a shear component added to  $\epsilon'$  are needed to resolve this issue. Other *in situ* zone measurements during loading and unloading are also needed to determine whether there are any changes in zone shape during unloading.

Finally, it is noteworthy that the interference measurements of surface uplift such as in Fig. 5 are a very sensitive indicator of changes in zone size and toughness. The relative increases in the uplift,  $\Delta u$ , at the crack and in the width,  $w_0$ , of the zone are both larger than the relative toughness increase between the two materials. Since  $\Delta u$  scales with  $f w_0$  and, from Eq. (1),  $K$  scales with  $f \sqrt{w}$ , both  $\Delta u$  and  $w$  should scale approximately with  $(\Delta K)^2$  (since the variation in  $f$  is relatively small). This is consistent with the results in Fig. 5.

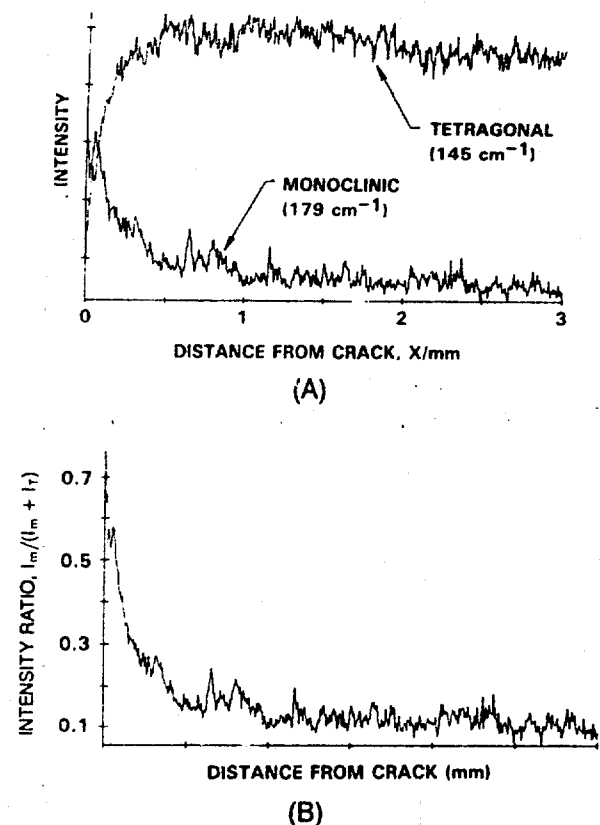


Fig. 6. (A) Intensities of monoclinic and tetragonal Raman peaks as a function of distance from the crack in the high-toughness material of Fig. 5. (B) Intensity ratios from (A):  $I_m$  and  $I_r$  are the intensities of the monoclinic and tetragonal peaks.

## VI. Conclusions

Characterization of transformation zones around cracks in several toughened Mg-PSZ ceramics by optical interference measurements of surface displacements and by Raman microprobe spectroscopy has provided the following results:

- (1) The shape of the transformation zone ahead of the crack tip is approximately semicircular.
- (2) The volume fraction of stress-induced transformation from tetragonal to monoclinic symmetry is not uniform within the transformation zone.
- (3) Transformation of *all* of the tetragonal phase was never observed by Raman spectroscopy in regions adjacent to

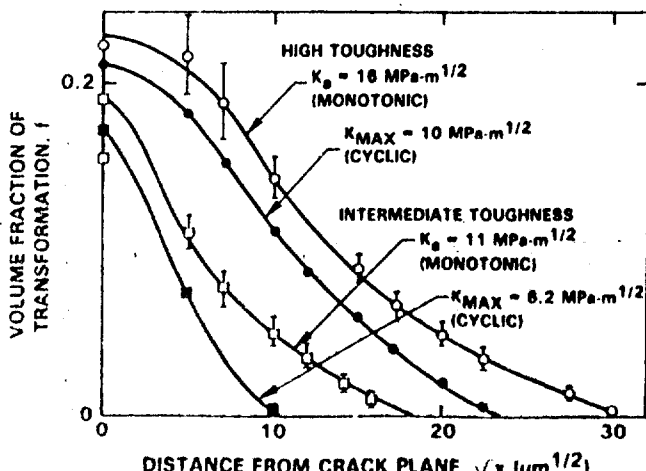


Fig. 7. Fraction of material transformed from tetragonal to monoclinic phase by the steady-state cracks of Fig. 5(C), as a function of distance from the cracks.

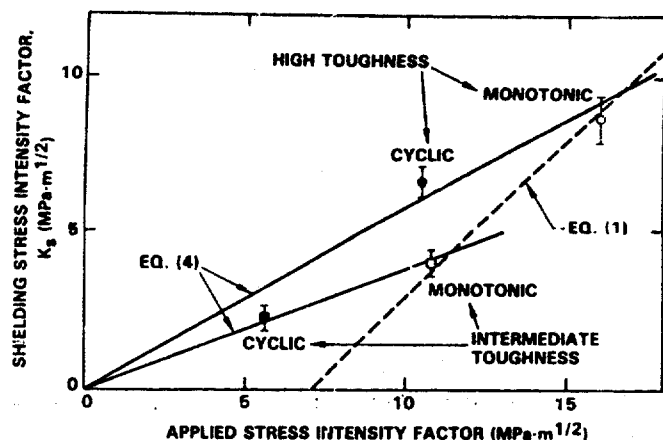


Fig. 8. Shielding stress intensity factors calculated using the measurements of Fig. 7 for steady-state cracks, plotted as a function of the applied stress intensity factor ( $K_a$  for monotonic loading,  $K_{\text{MAX}}$  for cyclic loading).

cracks, contrary to TEM observations (the maximum amount transformed was approximately 80% of the original tetragonal phase).

(4) The reductions in crack-tip stress intensity factor ( $K_a$ ) due to shielding from the transformation zone were calculated from the Raman measurements of the zone profile, assuming that only the dilation component of the transformation remains (i.e., that the shear component is relieved by twinning). The values of  $K_a$  were significantly smaller than the measured toughness increases. This result implies that either there are other toughening mechanisms operating or there is a significant component of transformation shear strain that is not relieved by twinning.

(5) In cyclic loading, the size of the transformation zone is determined by the maximum stress intensity factor and the crack-tip shielding is not influenced by the cyclic nature of the load.

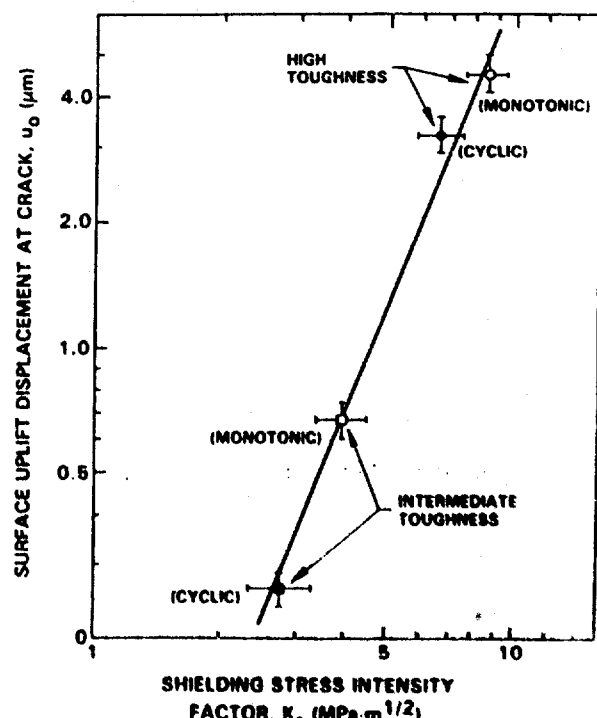


Fig. 9. Comparison of surface uplift adjacent to cracks (from Fig. 5(C)) with shielding stress intensity factors (from Fig. 8).

**Acknowledgments:** We are grateful to Dr. M. R. James for providing X-ray measurements used to calibrate the Raman data.

## References

- 1 R. S. Garvie, R. H. J. Hannink, and R. T. Pascoe, "Ceramic Steel?," *Nature (London)*, **258**, 703–705 (1975).
- 2 D. L. Porter and A. H. Heuer, "Mechanisms of Toughening Partially Stabilized Zirconia," *J. Am. Ceram. Soc.*, **60** [3–4] 183–84 (1977).
- 3 F. F. Lange, "Transformation Toughening: Part 5. Effect of Temperature and Alloy on Fracture Toughness," *J. Mater. Sci.*, **17**, 255–63 (1982).
- 4 F. F. Lange, "Transformation Toughening: Part 4. Fabrication, Fracture Toughness and Strength of  $Al_2O_3-ZrO_2$  Composites," *J. Mater. Sci.*, **17**, 247–54 (1982).
- 5 N. Claussen and M. Rühle, "Design of Transformation-Toughened Ceramics," pp. 137–63 in *Advances in Ceramics, Vol. 3, Science and Technology of Zirconia*. Edited by A. H. Heuer and L. W. Hobbs. American Ceramic Society, Columbus, OH, 1981.
- 6 M. V. Swain, R. H. J. Hannink, and R. C. Garvie; pp. 339–54 in *Fracture Mechanics of Ceramics, Vol. 6*. Edited by R. C. Bradt, A. G. Evans, D. P. H. Hasselman, and F. F. Lange. Plenum Press, New York, 1983.
- 7 R. H. J. Hannink and M. V. Swain, "Magnesia-Partially Stabilized Zirconia: The Influence of Heat Treatment on Thermomechanical Properties," *J. Aust. Ceram. Soc.*, **18** [2] 53–62 (1982).
- 8 A. H. Heuer, "Transformation Toughening in  $ZrO_2$ -Containing Ceramics," *J. Am. Ceram. Soc.*, **70** [10] 689–98 (1987).
- 9 A. H. Heuer, M. J. Readey, and R. Steinbrech, "Resistance Curve Behavior of Supertough  $MgO$ -Partially-Stabilized  $ZrO_2$ ," *Mater. Sci. Eng.*, **A105/106**, 83–89 (1988).
- 10 A. G. Evans and R. M. Cannon, "Toughening of Brittle Solids by Martensitic Transformations," *Acta Metall.*, **34** [5] 761–800 (1986).
- 11 K. D. Keefer and T. A. Michalske, "Determination of Phase Transformation Depth Profiles with Synchrotron Radiation," *J. Am. Ceram. Soc.*, **70** [4] 227–31 (1987).
- 12 R. C. Garvie, R. H. J. Hannink, and M. V. Swain, "X-Ray Analysis of the Transformed Zone in Partially Stabilized Zirconia (PSZ)," *J. Mater. Sci. Lett.*, **1**, 437–40 (1982).
- 13 T. Kosmac, R. Wagner, and N. Claussen, "X-ray Determination of Transformation Depths in Ceramics Containing Tetragonal  $ZrO_2$ ," *J. Am. Ceram. Soc.*, **64** [4] C-72–C-73 (1981).
- 14 Y. Mori, Y. Kitano, and A. Ishitani, "X-ray Determination of Transformation Zone Size in Toughened Zirconia Ceramics," *J. Am. Ceram. Soc.*, **71** [7] C-322–C-324 (1988).
- 15 M. V. Swain, "Inelastic Deformation of Mg-PSZ and Its Significance for Strength-Toughness Relationship of Zirconia Toughened Ceramics," *Acta Metall.*, **33** [11] 2083–91 (1985).
- 16 L. H. Schoenlein and A. H. Heuer; pp. 369–26 in *Fracture Mechanics of Ceramics, Vol. 6*. Edited by R. C. Bradt, A. G. Evans, D. P. H. Hasselman, and F. F. Lange. Plenum Press, New York, 1983.
- 17 L. H. Schoenlein, M. Rühle, and A. H. Heuer, "In Situ Straining Experiments of Mg-PSZ Single Crystals," pp. 275–82 in *Advances in Ceramics, Vol. 12, Science and Technology of Zirconia II*. Edited by N. Claussen, M. Rühle, and A. H. Heuer. American Ceramic Society, Columbus, OH, 1984.
- 18 D. R. Clarke and F. Adler, "Measurement of the Crystallographically Transformed Zone Produced by Fracture in Ceramics Containing Tetragonal Zirconia," *J. Am. Ceram. Soc.*, **65** [6] 284–88 (1982).
- 19 R. H. Dauskardt, D. K. Veirs, and R. O. Ritchie, "Spatially Resolved Raman Spectroscopy of Transformed Zones in  $MgO$ -Partially-Stabilized Zirconia," *J. Am. Ceram. Soc.*, **72** [7] 1124–30 (1989).
- 20 G. Katagiri, H. Ishii, A. Ishitani, and T. Masaki, "Direct Determination by a Raman Microprobe of the Transformation Zone Size in  $Y_2O_3$  Containing Tetragonal  $ZrO_2$  Polycrystals," pp. 537–44 in *Advances in Ceramics, Vol. 24A, Science and Technology of Zirconia III*. Edited by S. Somiya, N. Yamamoto, and H. Hanagida. American Ceramic Society, Westerville, OH, 1988.
- 21 M. V. Swain and R. H. J. Hannink, "R-Curve Behavior in Zirconia Ceramics," pp. 225–39 in *Advances in Ceramics, Vol. 12, Science and Technology of Zirconia II*. Edited by N. Claussen, M. Rühle, and A. H. Heuer. American Ceramic Society, Columbus, OH, 1984.
- 22 D. B. Marshall, "Strength Characteristics of Transformation-Toughened Zirconia," *J. Am. Ceram. Soc.*, **69** [3] 173–80 (1986).
- 23 D. B. Marshall and M. V. Swain, "Crack Resistance Curves in Magnesia-Partially-Stabilized Zirconia," *J. Am. Ceram. Soc.*, **71** [6] 399–407 (1988).
- 24 B. N. Cox, D. B. Marshall, D. Kouris, and T. Mura, "Surface Displacement Analysis of the Transformed Zone in Magnesia Partially Stabilized Zirconia," *J. Eng. Mater. Technol.*, **110** [2] 105–109 (1988).
- 25 R. M. McMeeking and A. G. Evans, "Mechanics of Transformation Toughening in Brittle Materials," *J. Am. Ceram. Soc.*, **65** [5] 242–46 (1982).
- 26 D. B. Marshall, M. Drory, and A. G. Evans, "Transformation Toughening in Ceramics," pp. 289–307 in *Fracture Mechanics of Ceramics, Vol. 6*. Edited by R. C. Bradt, A. G. Evans, D. P. H. Hasselman, and F. F. Lange. Plenum Press, New York, 1983.
- 27 B. Budiansky, J. W. Hutchinson, and J. C. Lambropoulos, "Continuum Theory of Dilatant Transformation Toughening in Ceramics," *Int. J. Solids Struct.*, **19**, 337 (1983).
- 28 D. M. Stump and B. Budiansky, "Crack Growth Resistance in Transformation Toughened Ceramics," *Int. J. Solids Struct.*, **25** [6] 635–46 (1989).
- 29 J. C. Lambropoulos, "Shear, Shape and Orientation Effects in Transformation Toughening," *Int. J. Solids Struct.*, **22**, 1083–106 (1986).
- 30 L. R. F. Rose, "Kinematical Model for Stress-Induced Transformation around Cracks," *J. Am. Ceram. Soc.*, **69** [3] 208–12 (1986).
- 31 A. G. Evans, D. B. Marshall, and N. H. Burlingame, "Transformation Toughening in Ceramics," pp. 202–16 in *Advances in Ceramics, Vol. 3, Science and Technology of Zirconia*. Edited by A. H. Heuer and L. W. Hobbs. American Ceramic Society, Columbus, OH, 1981.
- 32 C.-H. Hsueh and P. F. Becker, "Some Considerations of Nonideal Transformation-Zone Profile," *J. Am. Ceram. Soc.*, **71** [6] 494–97 (1988).
- 33 M. V. Swain, "R-Curve Behaviour of Magnesia Partially Stabilized Zirconia and Its Significance to Thermal Shock," pp. 355–69 in *Fracture Mechanics of Ceramics, Vol. 6*. Edited by R. C. Bradt, D. P. H. Hasselman, and F. F. Lange. Plenum Press, New York, 1983.
- 34 R. H. J. Hannink, "Microstructural Development of Subeutectoid-Aged  $ZrO_2$  Alloys," *J. Mater. Sci.*, **18** [2] 457–70 (1983).
- 35 S. V. Naiden and C. R. Hause, "Profile Separation in Complex Powder Patterns," *J. Appl. Crystallogr.*, **15** [2] 190–96 (1982).
- 36 R. H. Dauskardt, D. B. Marshall, and R. O. Ritchie, "Cyclic Fatigue-Crack Propagation in Magnesia-Partially-Stabilized Zirconia Ceramics," *J. Am. Ceram. Soc.*, **73** [4] 893–903 (1990). □



**Rockwell International**  
**Science Center**  
**SC71002.FR**

### **5.3 CYCLIC FATIGUE-CRACK PROPAGATION IN Mg-PSZ CERAMICS**

published in J. Am. Ceram. Soc.

# Cyclic Fatigue-Crack Propagation in Magnesia-Partially-Stabilized Zirconia Ceramics

Reinhold H. Dauskardt,<sup>\*†</sup> David B. Marshall,<sup>†‡</sup> and Robert O. Ritchie<sup>\*</sup>

Department of Materials Science and Mineral Engineering,

University of California, Berkeley, California 94720;

Center for Advanced Materials, Materials and Chemical Sciences Division,

Lawrence Berkeley Laboratory, Berkeley, California 94720;

and Rockwell International Science Center, Thousand Oaks, California 91360

The subcritical growth of fatigue cracks under (tension-tension) cyclic loading is demonstrated for ceramic materials, based on experiments using compact C(T) specimens of a MgO-partially-stabilized zirconia (PSZ), heat-treated to vary the fracture toughness  $K_c$  from  $\sim 3$  to  $16 \text{ MPa}\cdot\text{m}^{1/2}$  and tested in inert and moist environments. Analogous to behavior in metals, cyclic fatigue-crack rates (over the range  $10^{-11}$  to  $10^{-3} \text{ m/cycle}$ ) are found to be a function of the stress-intensity range, environment, fracture toughness, and load ratio, and to show evidence of fatigue crack closure. Unlike toughness behavior, growth rates are not dependent on through-thickness constraint. Under variable-amplitude cyclic loading, crack-growth rates show transient accelerations following low-high block overloads and transient retardations following high-low block overloads or single tensile overloads, again analogous to behavior commonly observed in ductile metals. Cyclic crack-growth rates are observed at stress intensities as low as 50% of  $K_c$ , and are typically some 7 orders of magnitude faster than corresponding stress-corrosion crack-growth rates under sustained-loading conditions. Possible mechanisms for cyclic crack advance in ceramic materials are examined, and the practical implications of such "ceramic fatigue" are briefly discussed. [Key words: mechanical properties, zirconia: partially stabilized, magnesia, cracks, fatigue.]

## I. Introduction

The projected use of ceramics rather than metallic materials for structural applications has been motivated in part by the prospect that they may be insensitive to degradation from cyclic fatigue.<sup>1,2</sup> However, several investigations<sup>3-15</sup> using smooth specimens, sometimes containing indentation flaws, tested under rotating bending, four-point bending, or by repeated thermal stressing, have shown reduced lifetimes for alumina, zirconia-alumina, TZP, and silicon nitride under cyclic, as opposed to static, loading conditions. Moreover, subcritical cracking has been reported for several monolithic and composite ceramics containing notches and tested under

far-field cyclic compressive loads.<sup>16-21</sup> Here, limited crack extension occurs from a notch due to residual tensile stresses; mechanistically, it is still uncertain whether this process is similar to crack growth under applied tensile loads. However, there are few direct observations of fatigue crack growth in cyclic tension-tension loading in ceramics.

The refuted existence of true cyclic fatigue has been based primarily on the absence of crack-tip plasticity. However, other inelastic deformation mechanisms such as microcracking, martensitic transformation, or frictional sliding between a reinforcement phase and the matrix may exist in the vicinity of a crack tip. Direct evidence of cyclic fatigue-crack growth under tension-tension loads was first reported<sup>22</sup> in MgO-partially-stabilized zirconia (Mg-PSZ) that had been toughened slightly by martensitic transformation (fracture toughness,  $K_c = 5.5 \text{ MPa}\cdot\text{m}^{1/2}$ ). Crack-growth rates were found to follow a power-law function of the stress-intensity range (with exponent  $\sim 24$ ), were sensitive to frequency and load ratio, and exhibited crack closure, analogous to that in metals.<sup>23</sup> The existence of fatigue cracking under tension-tension loads was confirmed in Mg-PSZ<sup>2</sup> with higher toughness,<sup>22,24</sup> cyclic crack growth rates as a function of  $\Delta K$  have also been reported for alumina under tension-compression loading.<sup>25</sup> Moreover, limited cyclic fatigue-crack growth data have been recently reported for several other ceramics, including alumina,<sup>22,26</sup>  $\text{Si}_3\text{N}_4$ ,<sup>27</sup> SiC-reinforced alumina<sup>22,28</sup> and Y-TZP/ $\text{Al}_2\text{O}_3$ <sup>29</sup> composites, and pyrolytic carbon/graphite.<sup>30</sup>

In the present study, a more extensive examination of cyclic fatigue-crack growth in Mg-PSZ ceramics is undertaken to investigate the dependence of growth rate on (i) fracture toughness, (ii) the environment, (iii) through-thickness constraint, and (iv) variable-amplitude cyclic loading sequences (i.e., post-overload behavior). The results are compared with direct measurements of transformation zone characteristics in order to provide some elucidation of the mechanisms of cyclic fatigue.

## II. Experimental Procedure

### (I) Material

Precipitated, partially stabilized zirconia, containing 9 mol% magnesia (Mg-PSZ), was selected as the test material for its well-characterized and controllable transformation-toughening behavior.<sup>31-34</sup> The microstructure consists of cubic  $\text{ZrO}_2$  grains,  $\sim 50 \mu\text{m}$  in diameter, with approximately 40 vol% lens-shaped tetragonal precipitates of maximum size 300 nm. The tetragonal phase undergoes a stress-induced martensitic transformation to a monoclinic phase in the presence of the high stress field near a crack tip. The resulting dilatant transformation zone in the wake of the crack exerts

A. Evans — contributing editor

Manuscript No. 198319. Received March 28, 1989; approved September 21, 1989.

Supported by the Office of Energy Research, Office of Basic Energy Sciences, Materials Sciences Division of the U.S. Department of Energy, under Contract No. DE-AC03-76F00094 at LBL, and by the U.S. Air Force Office of Scientific Research under Contract No. F49620-89-C-0031 at Rockwell.

<sup>\*</sup>Member, American Ceramic Society.

<sup>†</sup>University of California and Lawrence Berkeley Laboratory.

<sup>‡</sup>Rockwell International Science Center, Thousand Oaks, CA.

<sup>1</sup>Although a redundant expression in metallurgical terminology, the term "cyclic fatigue" is used here to distinguish from other phenomena traditionally referred to in the ceramics literature as fatigue, i.e., static fatigue and dynamic fatigue.

4MS-grade Mg-PSZ, Nitro Ceramics, Elmhurst, IL.

compressive tractions on the crack surfaces and hence shields<sup>3</sup> the crack tip from the applied (far-field) stresses.<sup>36</sup> The reduction in crack-tip stress-intensity factor,  $K_t$ , is dependent upon the volume fraction,  $f$ , of the transforming phase within the zone, the width  $w$  of the zone, and the dilatational component of the transformation strain  $\epsilon^T$ .<sup>36-40</sup>

$$K_{tip} = K - K_t \quad (1a)$$

where  $K_{tip}$  and  $K$  are the local (near-tip) and applied (far-field) stress-intensity factors, and

$$K_t \propto E' \epsilon^T f w^{1/2} \quad (1b)$$

with  $E' = E/(1 - \nu)$ ,  $E$  being Young's modulus and  $\nu$  Poisson's ratio.

The Mg-PSZ was examined in four microstructural conditions, achieved by subeutectoid aging at 1100°C to vary the fracture toughness from 2.9 MPa·m<sup>0.5</sup> in the overaged (non-transformation-toughened) condition to 16 MPa·m<sup>0.5</sup> in the peak-toughened (TS) condition. The heat treatments, together with ambient-temperature mechanical properties, are listed in Table I. Further details of the microstructures and mechanical properties of these materials are described elsewhere.<sup>12-15</sup>

## (2) Test Methods

(A) *Cyclic Fatigue:* Cyclic fatigue-crack propagation was measured using compact C(T) specimens, containing long (>3 mm) through-thickness cracks, in general accordance with the ASTM Standard E 647-86a for measurement of fatigue-crack growth rates in metallic materials.<sup>41</sup> Most test pieces were 3 mm in thickness, although thicknesses of 1.5 and 7.8 mm were also tested to examine the role of through-thickness constraint. Specimens were cyclically loaded at a load ratio (ratio of minimum to maximum loads) of 0.1 and a frequency of 50 Hz (sine wave) in high-resolution, computer-controlled electro-servo-hydraulic testing machines, operating under closed-loop displacement or stress-intensity control. Testing was performed in controlled room air (22°C, 45% rh), dehumidified gaseous nitrogen, and distilled water environments.

Electrical potential measurements across ~0.1-μm NiCr foils, evaporated onto the specimen surface, were used in situ to monitor crack lengths to a resolution better than ±2 μm.<sup>32,33</sup> Unloading compliance measurements using back-face gauges were also used to assess the extent of fatigue crack closure in terms of the far-field stress intensity,  $K_a$ , at first contact of the fracture surfaces during the unloading cycle.<sup>42</sup> The  $K_a$  value is calculated from the highest load where the elastic unloading compliance line deviates from linearity. However, it should be noted that for a transforming material such as PSZ, a local measure of the closure stress intensity will differ from the measured (far-field) value by an amount equal to the shielding stress intensity (Eq. (1a)). The test setup is illustrated in Fig. 1.

<sup>36</sup>Crack-tip shielding mechanisms act to impede crack advance by lowering the local "crack driving force" experienced in the vicinity of the crack tip (e.g., Ref. 23). Examples include transformation and microcrack toughening in ceramics (Refs. 31, 41), crack bridging in composites (Ref. 42) and crack closure during fatigue-crack growth (Ref. 43).

Crack-growth rates,  $da/dN$ , were determined over the range ~10<sup>-11</sup> to 10<sup>-5</sup> m/cycle under computer-controlled  $K$ -decreasing and  $K$ -increasing conditions. Data are presented in terms of the applied stress-intensity range ( $\Delta K = K_{max} - K_{min}$ , where  $K_{max}$  and  $K_{min}$  are the maximum and minimum stress intensities in the fatigue cycle). By considering the effect of crack closure, an effective (near-tip) stress-intensity range can also be estimated as  $\Delta K_{eff} = K_{max} - K_a$ .

A fatigue threshold stress-intensity range,  $\Delta K_{th}$ , below which crack growth is presumed dormant,<sup>43</sup> was defined as the maximum value of  $\Delta K$  at which growth rates did not exceed 10<sup>-10</sup> m/cycle, consistent with the more conservative ASTM E 647 procedure.<sup>44</sup> Thresholds were approached by varying the applied loads so that the instantaneous values of crack length,  $a$ , and stress intensity range,  $\Delta K$ , changed according to the equation<sup>44</sup>

$$\Delta K = \Delta K_0 \exp(C^*(a - a_0)) \quad (2)$$

where  $a_0$  and  $\Delta K_0$  are the initial values of  $a$  and  $\Delta K$ , and  $C^*$  is the normalized  $K$ -gradient ( $(1/K)(dK/da)$ ) which was set to ±0.08 mm<sup>-1</sup>. For the C(T) geometry, stress intensities were computed from handbook solutions, in terms of the applied load  $P$ , crack length  $a$ , test-piece thickness  $B$ , and width  $W$ , as<sup>33,34</sup>

$$K = (P/3W^{1/2})g(a/W)$$

where

$$g(a/W) = \{[2 + (a/W)][0.886 + 4.64(a/W) - 13.32(a/W)^2 + 14.72(a/W)^3 - 5.6(a/W)^4]/[1 - (a/W)]\}^{1/2} \quad (3)$$

Owing to the brittleness of the materials, initiation of the precrack was one of the most critical procedures in the test. In the current work, as previously,<sup>12,13</sup> this was achieved by machining a wedge-shaped starter notch and carefully growing the crack roughly 2 mm out of this region by fatigue under displacement control. Thus, all measurements reported here involved cracks that had built up a wake of transformed material.

(B) *Fracture Toughness:* Following completion of the fatigue crack-growth tests, fracture toughnesses were determined by loading monotonically (with displacement control) to generate a resistance curve,  $K_r(a)$ . Procedures essentially conform to ASTM Standard E 399-87 for the measurement of the toughness at crack initiation,  $K_i$ .<sup>45</sup> In addition, a maximum toughness,  $K_{max}$ , was measured at the steady-state plateau or peak of the  $R$ -curve. Since these tests all involve sharp cracks, the measured toughnesses may be smaller than values obtained from other methods that rely on a machined notch as the initial crack.<sup>46</sup> On the other hand, test specimens that lead to instability of the crack in the rising part of the  $R$ -curve would give lower apparent toughnesses than those reported here.

## III. Results and Discussion

### (1) Role of Fracture Toughness

(A) *Growth-Rate Behavior:* Resistance curves for the four microstructures are illustrated in Fig. 2. The overaged material contains only transformed monoclinic precipitates and

Table I. Heat Treatments and Tensile Properties of Mg-PSZ

Condition (grade)	Heat treatment	Young's modulus, $E$ (GPa)	Approx. tensile strength (MPa)	Fracture toughness (MPa·m <sup>0.5</sup> ) <sup>a</sup>	$K_i$	$K_{max}$
Overaged	24 h at 1100°C	<200	300	2.5	2.9	
Low toughness (AF)	As received	208	300	3.0	5.5	
Mid toughness (MS)	3 h at 1100°C	208	600	3.0	11.5	
Peak toughness (TS)	7 h at 1100°C	208	400	3.5	16.0	

<sup>a</sup> $K_i$  and  $K_{max}$  are the initiation (from Ref. 35) and plateau toughness values from the  $R$  curve.

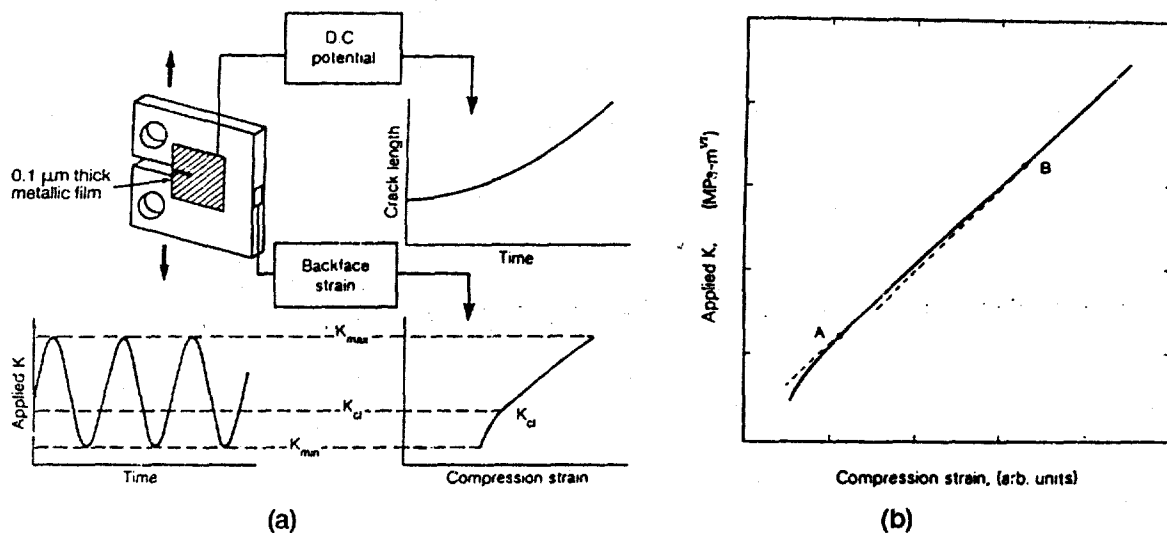


Fig. 1. Experimental techniques used to monitor continuously crack length and the stress intensity,  $K_d$  at crack closure during cyclic fatigue-crack propagation tests are schematically illustrated in (a). Actual back-face strain data indicating points of marked (point A) and marginal (point B) deviations in linearity of the compliance curve are shown in (b).

shows only a very shallow  $R$ -curve with  $K_c = 2.9 \text{ MPa} \cdot \text{m}^{1/2}$ . The other materials exhibit various degrees of transformation toughening, with toughnesses (plateau  $K_c$ ) of 5.5 to  $16 \text{ MPa} \cdot \text{m}^{1/2}$ . Note that the results in Fig. 2 do not represent the entire  $R$ -curves, since measurements were obtained directly after fatigue testing, with the first measurement being taken at the  $K_{\max}$  of the previous fatigue loading cycle.

Cyclic fatigue-crack propagation data are plotted in Fig. 3 as a function of the stress-intensity range  $\Delta K$ , for a controlled room-air environment. As in metallic materials, growth rates can be fitted to a conventional Paris law relationship:<sup>33</sup>

$$da/dN = C(\Delta K)^m \quad (4)$$

However, the exponent  $m$  is considerably larger than reported for metals, i.e., in the range 21 to 42 (as opposed to 2 to 4 for metals), and the constant  $C$  scales inversely with the fracture toughness. It is especially noteworthy that the overaged material, in which the nonlinear deformation behavior associated with transformation plasticity has been removed, displays extensive cyclic fatigue-crack propagation, with a power-law dependence on the stress-intensity range similar to

that of the toughened materials. Moreover, the present data indicate that the overaged material exhibits fatigue-crack growth at stress intensities below that required for crack initiation under monotonic loading on the  $R$ -curve ( $K_i$  values from Ref. 35 in Table I). In fact, each set of data shows an apparent threshold below which crack growth is presumed dormant (i.e.,  $<10^{-10} \text{ m/cycle}$ ) at a value,  $\Delta K_{TH}$ , approximately 50% of  $K_c$ . Values of  $C$ ,  $m$ , and  $\Delta K_{TH}$  for each microstructure are listed in Table II. These results show that resistance to cyclic fatigue-crack growth in Mg-PSZ is enhanced with increasing fracture toughness.

The data in Fig. 3 for the low-toughness (AF) material were shown previously<sup>22</sup> to be a true cyclic fatigue phenomenon, with growth rates proportional to the range of stress intensity, rather than subcritical cracking at maximum load. These tests involved monitoring crack growth rates at constant  $K_{\max}$ , with (i) the load cycled between  $K_{\max}$  and  $K_{\min}$  ( $R = 0.1$ ) compared to being held constant at  $K_{\max}$  (Fig. 4(a)), and (ii) the value of  $K_{\min}$  being varied (Fig. 4(b)).

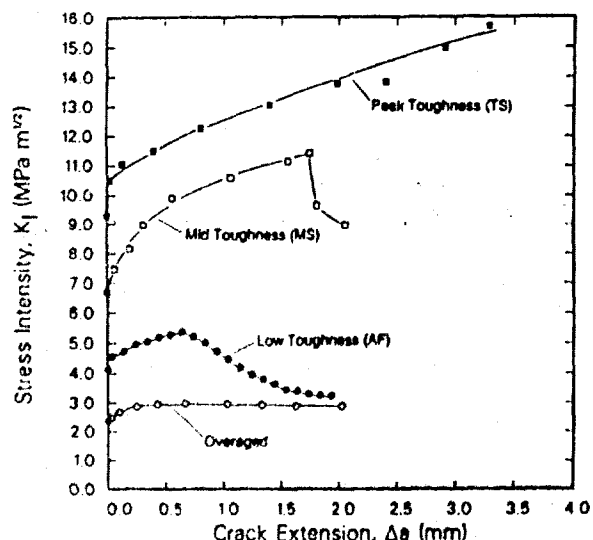


Fig. 2. Fracture-toughness behavior of Mg-PSZ, subeutectoid aged to a range of  $K_c$  values from 2.9 to  $15.5 \text{ MPa} \cdot \text{m}^{1/2}$ , showing  $K_c(\Delta a)$  resistance curves.

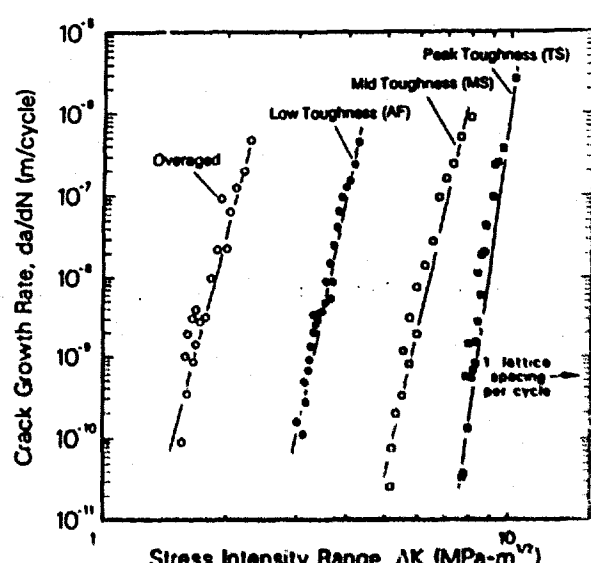


Fig. 3. Cyclic fatigue-crack growth behavior, in terms of growth rates per cycle,  $da/dN$ , as a function of the stress-intensity range,  $\Delta K$ , for Mg-PSZ, subeutectoid aged to a range of  $K_c$  toughnesses from 2.9 to  $15.5 \text{ MPa} \cdot \text{m}^{1/2}$ . Data were obtained on C(T) samples in a room-air environment at 50 Hz frequency with a load ratio ( $R = K_{\min}/K_{\max}$ ) of 0.1.

Table II. Values of  $C$  and  $m$  (in Eq. (4)) and the Threshold  $\Delta K_{TH}$  in Mg-PSZ

	$K_c$ (MPa $\cdot$ m $^{1/2}$ )	$C$ (m/cycle (MPa $\cdot$ m $^{1/2}$ ) $^{-m}$ )	$m$	$\Delta K_{TH}^*$ (MPa $\cdot$ m $^{1/2}$ )
Overaged	2.9	$2.00 \times 10^{-14}$	21	1.6
Low toughness (AF)	5.5	$4.89 \times 10^{-22}$	24	3.0
Mid toughness (MS)	11.5	$5.70 \times 10^{-28}$	24	5.2
Peak toughness (TS)	16.0	$1.70 \times 10^{-48}$	42	7.7

\* $\Delta K_{TH}$  defined at a maximum growth rate less than  $10^{-10}$  m/cycle.<sup>47</sup>

(B) *Fractography*: The transgranular nature of crack paths was clearly evident from optical microscopy of etched surfaces (Fig. 5) in which grain boundaries were decorated with monoclinic zirconia phase. Crack paths additionally show evidence of frequent crack deflection, branching, and uncracked ligament bridging behind the crack tip. The degree of crack tortuosity, however, appears progressively diminished with decreasing toughness, as evidenced by the comparatively flat crack path in the overaged microstructure (Fig. 5(b)). Corresponding scanning electron micrographs (Fig. 6) indicate that the fracture-surface appearance under cyclic loading is nominally identical to that under monotonic loading; moreover, unlike many metals and polymers, no evidence of fatigue striations or crack arrest markings are apparent on the fatigue fracture surfaces.<sup>48</sup>

(C) *Fatigue Crack Closure*: In addition to possible crack-tip shielding from crack deflection and bridging noted above, fatigue-crack growth in PSZ ceramics shows evidence of crack closure, analogous to behavior in metals.<sup>23,43,54</sup> Such closure involves premature contact between the crack surfaces during the unloading cycle, which raises the effective  $K_{min}$  ( $\equiv K_{cl}$ ), thereby lowering the effective  $\Delta K$ .<sup>54</sup> Global (far-field)  $K_{cl}$  values, calculated from the highest load at the onset of marked deviation from linearity of the back-face strain compliance measurements (point (A) in Fig. 1(b)), show increasing  $K_{cl}/K_{max}$  ratios as the threshold  $\Delta K_{TH}$  is approached (Fig. 7), characteristic of (contact) shielding by wedging (which is enhanced at smaller crack opening displacements). In view of the deflected nature of the crack paths, it is suggested that such closure results primarily from the wedging action of fracture-surface asperities (roughness-induced crack closure).<sup>55-57</sup> This would also be consistent with the progressively higher levels

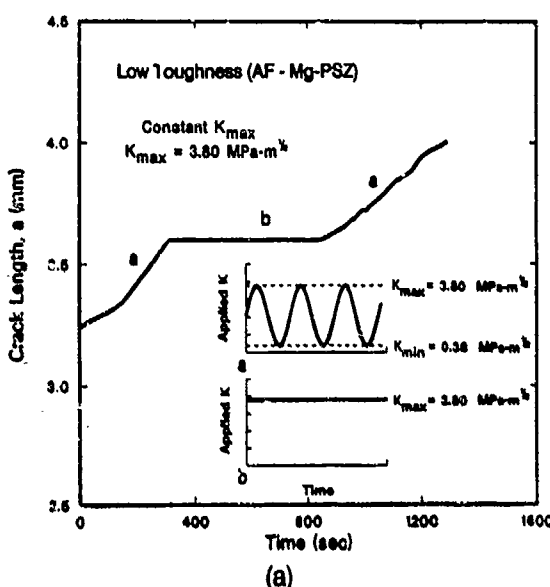
of crack closure seen in the higher toughness microstructures, which exhibit the roughest crack paths. Moreover, the increasingly dilatant transformation zones in the tougher materials act to reduce the crack opening displacements, which further encourages premature crack-surface contact on unloading.

(D) *Observation of Transformation Zones*: The influence of transformation-zone shielding on fatigue cracking was investigated by comparing wake zones in the mid- and peak-toughened materials. Two techniques were used to characterize the zones: interference microscopy and Raman spectroscopy. The Raman spectroscopy provides a direct measure of the fraction of tetragonal and monoclinic phases within the zone, with a spatial resolution of  $\sim 2 \mu\text{m}$  (using a microprobe system).<sup>58-60</sup> The optical interference measurements from the polished face of the compact tension specimens provide a measure of normal surface displacements due to the transformation within the zone. The displacements are dependent on both the fraction of transformation and the net transformation strain.<sup>59,61</sup>

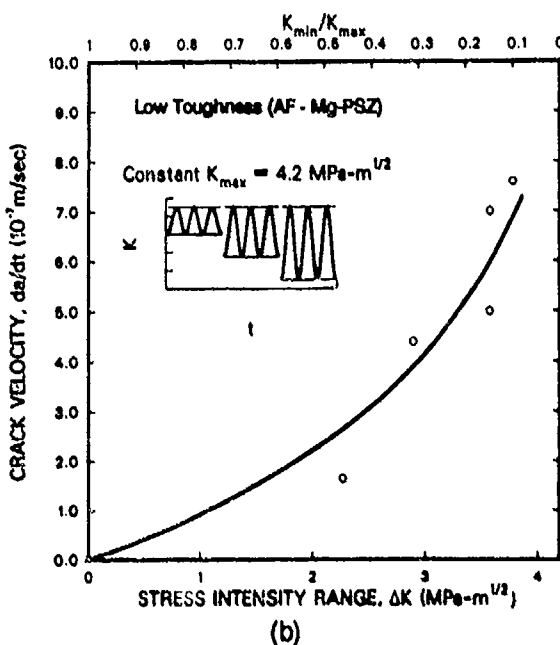
Raman measurements of the volume fraction of material transformed to the monoclinic phase, within zones adjacent to cracks that had been grown under cyclic loading at constant  $\Delta K$  or under steady-state, monotonic loading (i.e., at  $K = K_c$ ), are shown in Fig. 8. The results indicate that the fraction of transformed material is in all cases nonuniform and smaller than the total available fraction of tetragonal phase ( $\sim 0.4$ ), even adjacent to the fracture surface.

The shielding stress-intensity factors,  $K_s$ , corresponding to the data of Fig. 8 can be calculated by integration of Eq. (1b) (which is valid for a step-function zone profile).<sup>62</sup>

<sup>48</sup>Integration of Eq. (1b) to obtain Eq. (5) requires that all contours of constant  $f$  in the wake and around the tip of the crack be geometrically similar. Other Raman measurements confirm that this requirement is satisfied.<sup>58,60</sup>



(a)



(b)

Fig. 4. Effect in low-toughness Mg-PSZ (AF) microstructure of (a) sustained and cyclic loading conditions on the crack velocity,  $da/dt$ , at constant  $K_{max}$  ( $\equiv 3.8 \text{ MPa} \cdot \text{m}^{1/2}$ ), and (b) varying applied stress-intensity range  $\Delta K$  on crack velocity at constant  $K_{max}$  ( $\equiv 4.2 \text{ MPa} \cdot \text{m}^{1/2}$ ) [after Ref. 22].

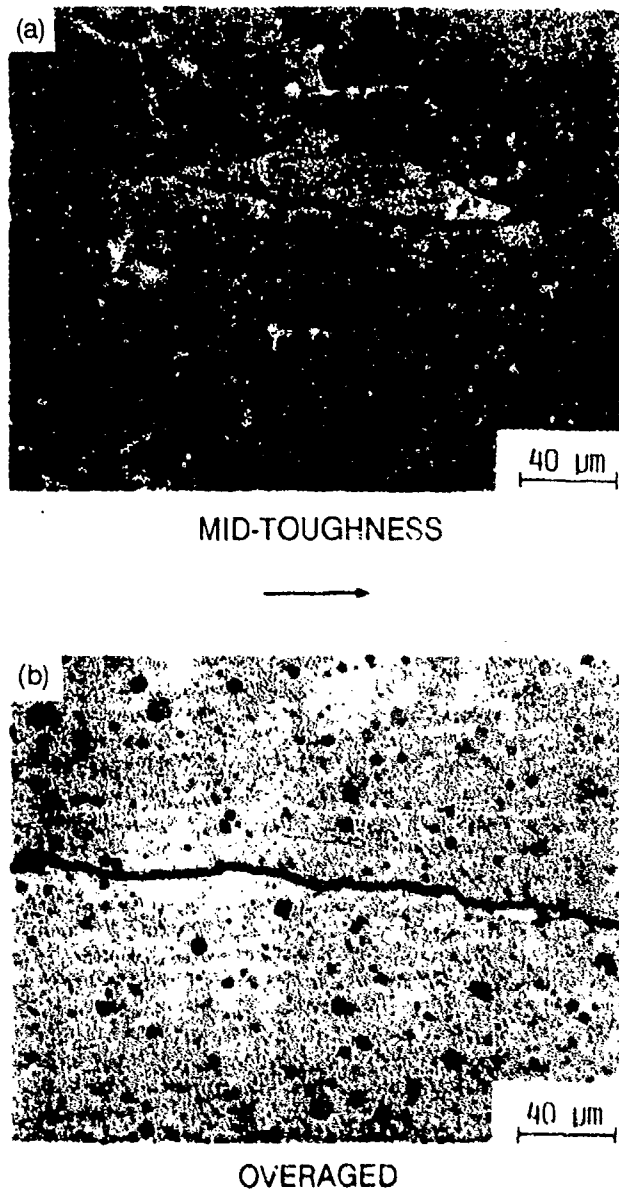


Fig. 5. Optical micrographs of the morphology of cyclic fatigue-crack paths in Mg-PSZ, showing (a) an increasingly deflected crack path in the mid-toughened (MS) microstructure at  $\Delta K = 6 \text{ MPa} \cdot \text{m}^{1/2}$  compared to (b) an essentially linear crack path in the overaged material at  $\Delta K = 2 \text{ MPa} \cdot \text{m}^{1/2}$ . Note the transgranular fracture morphology and evidence of crack branching in the MS microstructure. Arrow indicates general direction of crack growth.

$$K_t = AE\epsilon^f \int_0^f \frac{f}{2\sqrt{t}} dt \quad (5)$$

where the constant  $A$  is dependent upon the shape of the zone ahead of the crack tip as well as the transformation strain  $\epsilon^f$ .<sup>14</sup> For a purely dilatational transformation strain (i.e., all long-range shear strains relieved by twinning) and a frontal zone defined by a contour of constant hydrostatic stress in the crack-tip field,  $A$  is equal to 0.22.<sup>15</sup> The values of  $K_t$  evaluated from the four sets of data in Fig. 8, using Eq. (5) with  $E = E/(1 - \nu) = 272 \text{ MPa}$  and  $\epsilon^f = 0.04$ , are compared by plotting  $K_t$  as a function of the maximum applied stress intensity factor,  $K$  ( $K_{\text{cyclic}}$  for cyclic loading,  $K$  for monotonic loading), in Fig. 9. For each material, the values of  $K_t$  under monotonic and cyclic loading conditions are consistent with the relation

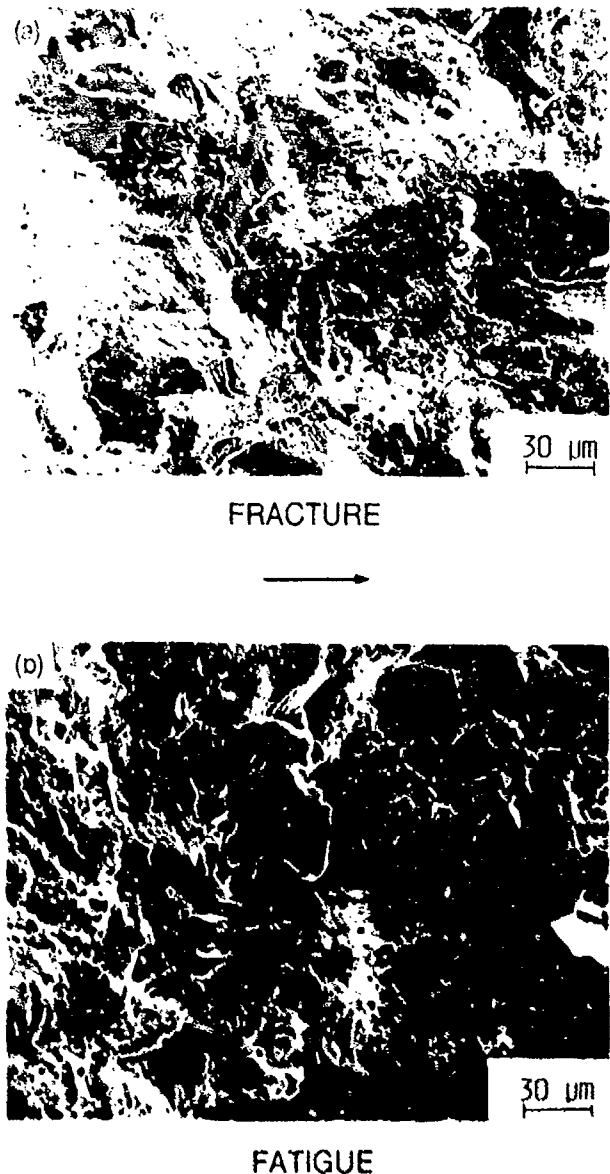


Fig. 6. Representative scanning electron micrographs of the nominally identical fracture surface morphologies obtained in Mg-PSZ (MS grade) for (a) overload fracture under monotonic loads at  $\Delta K = 11.5 \text{ MPa} \cdot \text{m}^{1/2}$ , and (b) fatigue fracture under cyclic loads at  $\Delta K = 6 \text{ MPa} \cdot \text{m}^{1/2}$ . Note, in contrast to metals, the absence of striations or crack-arrest markings on the fatigue fracture surface. Arrow indicates general direction of crack growth.

$K_t \propto K$  expected from Eq. (1b).<sup>11</sup> Therefore, if the frontal zone shapes and the transformation strains  $\epsilon^f$  are the same in cyclic and monotonic loading, the micromechanisms of fatigue-crack advance clearly do not involve a reduction in transformation-zone shielding.

A comparative assessment of the transformation strains in monotonic and fatigue loading can be obtained from optical interference measurements of the surface uplift at the locations from which the Raman data of Fig. 8 were obtained. The results plotted in Fig. 10 show differences between the four locations qualitatively similar to those of the Raman data. Comparison of the measured displacement,  $u_0$ , adjacent to the cracks with the values of  $K_t$  calculated from the Raman data, is shown in Fig. 11. Both  $u_0$  and  $K_t$  must increase with increasing  $f$  and zone width. However, the measured values of  $u_0$  are dependent on the transformation strains,  $\epsilon^f$ , whereas a constant value of  $\epsilon^f$  was assumed in calculating  $K_t$ . Therefore, the data in Fig. 11 would fall on different curves for cyclic and monotonic loading if the transformation strains differed for these two loading conditions (e.g., different amounts

<sup>11</sup>Stresses outside the transformation zone are defined approximately by the applied stress intensity factor,  $\sigma_c + Kt$ . Therefore, if the transformation occurs at a critical stress  $\sigma_c$  in a given material, then the zone width is  $w = K^2$  and Eq. (1b) becomes  $K_t = K$  (Ref. 6).

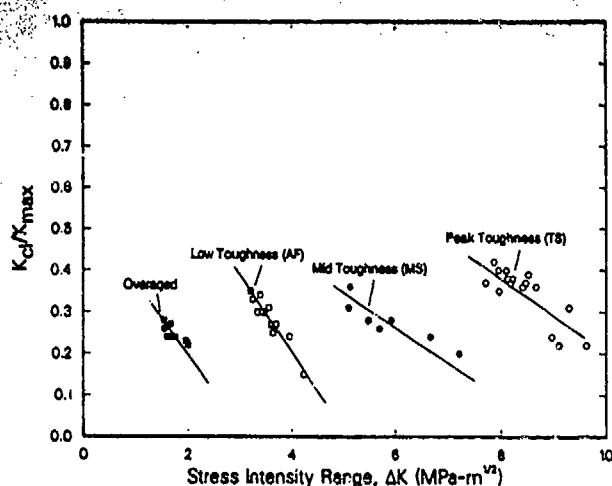


Fig. 7. Experimentally measured variation in fatigue crack closure corresponding to cyclic crack-growth rate data at  $R = 0.1$ , for the Mg-PSZ microstructures plotted in Fig. 3. Results, based on back-face strain compliance measurements, show the ratio  $K_c/K_{\max}$  as a function of the applied stress-intensity range,  $\Delta K$ .

of twinning resulting in different shear components in  $\epsilon^T$ ). Since all of the data fall on a single curve within the measurement accuracy, it is concluded that the *transformation strains*, in cyclic and monotonic loading *do not differ significantly*.

## (2) Role of Environment

It has been suggested that cyclic fatigue effects in ceramics may be the result of stress-corrosion cracking.<sup>43,44</sup> To examine this hypothesis, cyclic crack-growth rates in the low-toughness AF material were measured in inert (dehumidified nitrogen gas) and corrosive (distilled water) environments; results are plotted as a function of  $\Delta K$  in Fig. 12. Growth rates are faster in moist room air and water than in inert nitrogen, indicating a marked corrosion-fatigue effect which presumably involves the weakening of atomic bonds at the crack tip by the adsorption of water molecules. However, crack growth is observed in the inert atmosphere, implying that, analogous to behavior in metals and consistent with the observations cited above, *cyclic fatigue in the ceramic is a mechanically induced cyclic process which may be accelerated by the environment*.

Another comparison of the effects of mechanical load cycling and environmentally assisted crack growth is illustrated

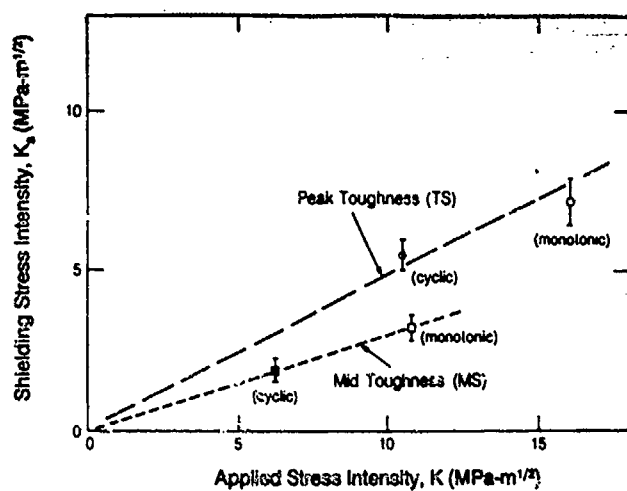


Fig. 9. Estimates of the shielding stress-intensity factor,  $K_s$ , calculated from Eq. (5) for the transformation zones presented in Fig. 6, as a function of the applied stress-intensity factor,  $K$ . Values of  $K_s$  under both monotonic and cyclic loading are consistent with the relation  $K_s = \beta K$ , where the slope of the curve  $\beta$  is dependent on the material.

in Fig. 13 for the MS material tested in moist air. Cyclic crack velocities, expressed in terms of time ( $da/dt$ ), are compared with corresponding stress-corrosion crack velocities measured under sustained loads; at equivalent  $K$  levels at this frequency, cyclic crack-growth rates are up to 7 orders of magnitude faster (or at equivalent velocities,  $K_{\max}$  is smaller by about 40% for cyclic loading).

It would thus appear that nonconservative estimates of the subcritical advance of incipient cracks, and serious overestimates of lifetimes, may result if defect-tolerant predictions are based solely on sustained-load (stress-corrosion) and fracture-toughness data and do not consider a cyclic fatigue effect.

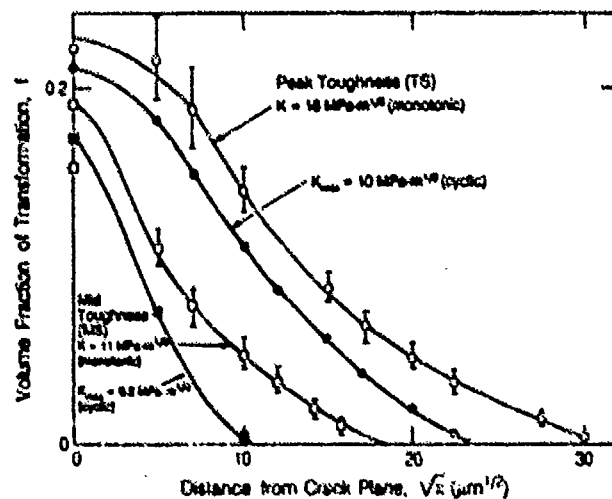


Fig. 8. Raman measurements of volume of material transformed from tetragonal to monoclinic phase in zones adjacent to cracks grown under both monotonic and cyclic loading conditions in the mid- (MS) and peak- (TS) toughened materials, as a function of distance  $x$  from the crack plane.

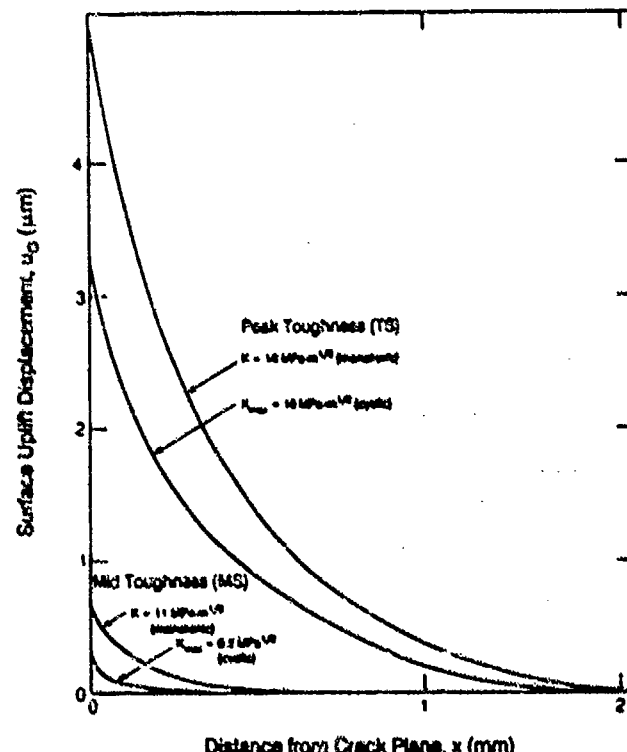


Fig. 10. Variation in surface uplift displacement,  $u_s$ , adjacent to cracks as calculated from optical/interference measurements, showing qualitatively similar differences between the four locations assessed using Raman spectroscopy shown in Fig. 8.

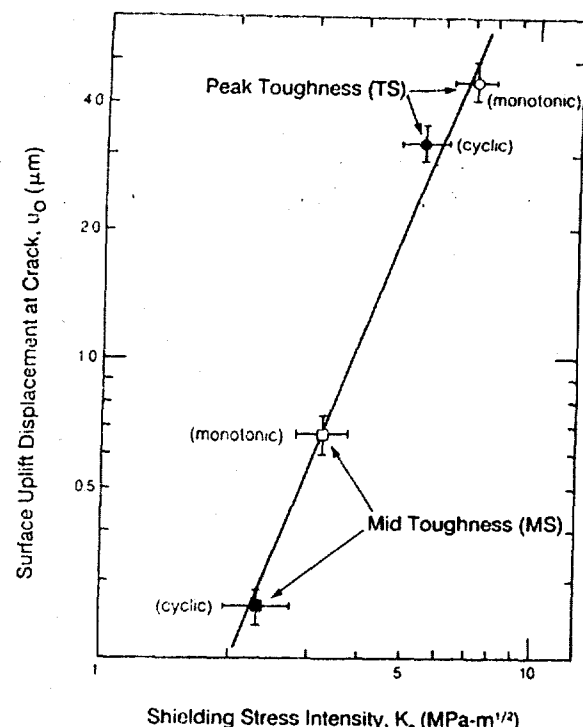


Fig. 11. Comparison of the surface uplift displacements,  $u_0$ , immediately adjacent cracks, with the values of  $K_s$  calculated from the Raman data, for cracks grown under monotonic and cyclic loading conditions. The resulting linear relationship implies that the transformation strains under cyclic and monotonic loading do not differ significantly.

### (3) Role of Through-Thickness Constraint

Recent work<sup>65</sup> on  $R$ -curve behavior in Mg-PSZ has indicated an important effect of test-piece thickness on the fracture toughness. Specifically, the plateau toughness was 22% higher and the slope of the  $R$ -curve steeper in samples with a thickness of 4 mm compared to 1 mm. This trend is opposite to that accompanying the transition from plane stress to plane strain in metals, where the toughness decreases with in-

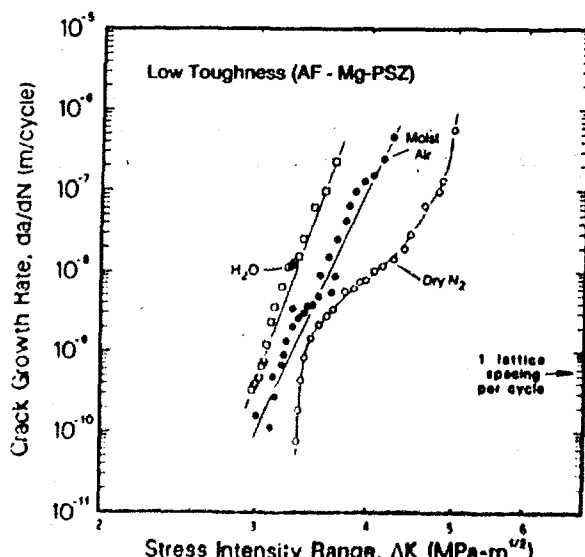


Fig. 12. Cyclic fatigue-crack growth rates,  $da/dN$ , as a function of the applied stress-intensity range,  $\Delta K$ , in low-toughness (AF) Mg-PSZ, in dry nitrogen gas, room air, and distilled water environments, showing an acceleration in growth rates due to water vapor. (CT) tests were performed at a crack velocity of  $10^{-4} \text{ m/sec}$ .

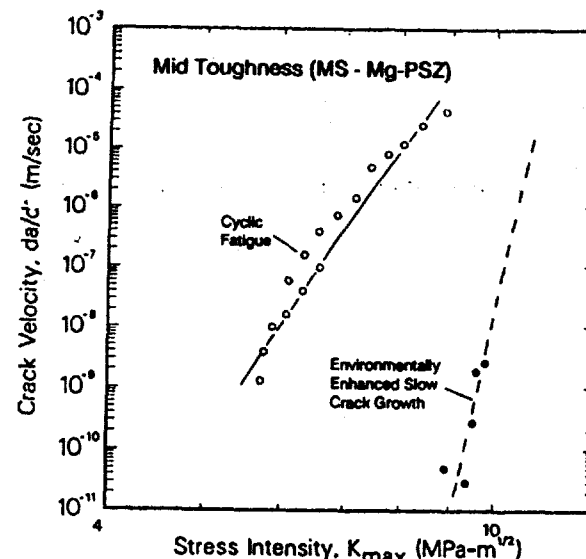


Fig. 13. Subcritical crack-growth behavior in mid-toughness (MS) Mg-PSZ, showing a comparison of crack velocities  $da/dt$ , as a function of  $K_{\max}$ , measured under monotonic and cyclic loading conditions in a moist air environment. Note how the cyclic crack velocities are up to 7 orders of magnitude faster at equivalent stress-intensity levels.

creasing thickness, but is consistent with expectations for shielding due to transformation.

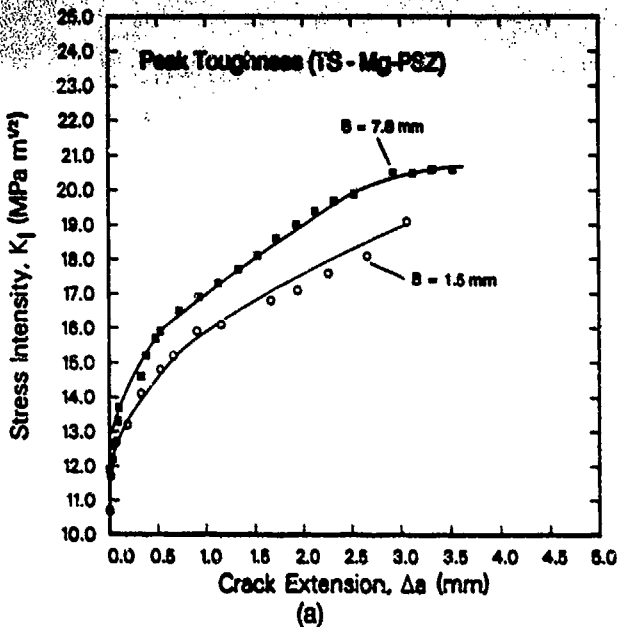
To examine whether such through-thickness constraint effects are important in influencing fatigue behavior, cyclic fatigue-crack growth rates and  $R$ -curves were measured using C(T) specimens of the TS-grade material<sup>64</sup> with thicknesses of 1.5 and 7.8 mm (Fig. 14). The  $K_c$  fracture-toughness values are larger in the thicker specimens by approximately 9% (Fig. 14(a)). However, no significant difference in the corresponding fatigue-crack propagation rates was detected (Fig. 14(b)).

### (4) Role of Variable-Amplitude Loading

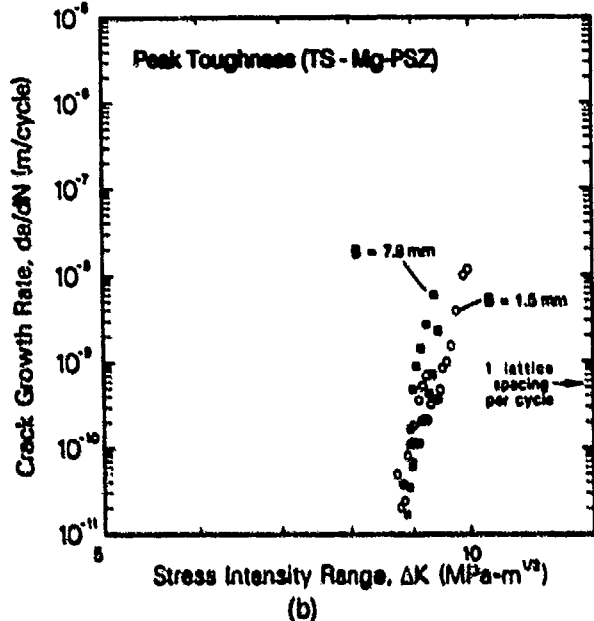
The results described above pertain to constant-amplitude cyclic loading; to examine the influence of variable-amplitude loading, single and block overload sequences were applied during steady-state fatigue-crack growth in the MS- and TS-grade materials. Results for high-low and low-high block overloads in mid-toughness (MS) material are shown in Fig. 15. Over the first  $\sim 2.5$  mm of crack advance, the crack-growth rate remains approximately constant at constant  $\Delta K (= 5.48 \text{ MPa} \cdot \text{m}^{1/2})$ . On reducing the cyclic loads so that  $\Delta K = 5.30 \text{ MPa} \cdot \text{m}^{1/2}$  (high-low block overload), a transient retardation is seen followed by a gradual increase in growth rates until the (new) steady-state velocity is achieved. Similarly, by subsequently increasing the cyclic loads so that  $\Delta K = 5.60 \text{ MPa} \cdot \text{m}^{1/2}$  (low-high block overload), growth rates show a transient acceleration before decaying to the steady-state velocity. Such behavior is analogous to that widely observed in metals,<sup>66</sup> where to the first order the crack-growth increment affected by the overload is comparable with the extent of the overload plastic zone. In the present experiments, the affected crack-growth increments are  $\sim 500 \mu\text{m}$ , approximately 5 times the measured<sup>59,60</sup> transformed zone width of  $\sim 85$  to  $108 \mu\text{m}$ . This is consistent with zone-shielding calculations in which the maximum steady-state shielding is achieved after crack extensions of approximately 5 times the zone width.<sup>36,37</sup>

Similar crack-growth retardation following a high-low block overload ( $\Delta K = 9.5$  to  $8.5 \text{ MPa} \cdot \text{m}^{1/2}$ ) is shown for

<sup>64</sup>As TS grade materials are prone to age at room temperature, resulting in lower toughness, tests on these two thicknesses were conducted at a nominally fixed time of time (approximately 1 month) following heat treatment.



(a)



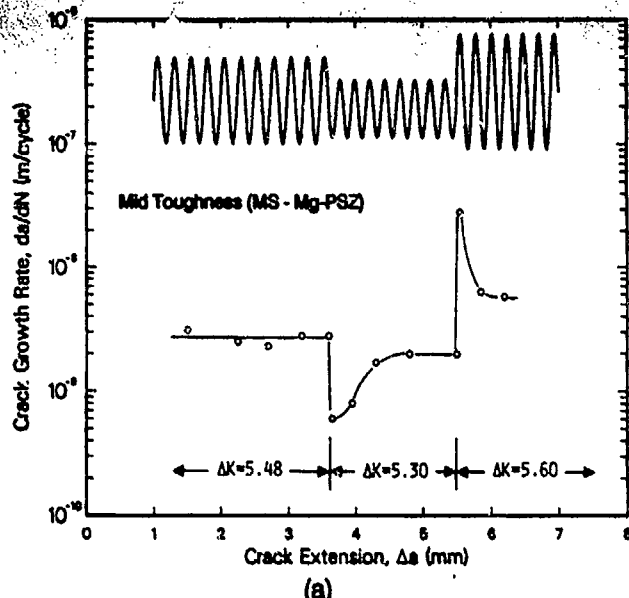
(b)

Fig. 14. Effect of through-thickness constraint on (a)  $K_I(\Delta a)$  fracture-toughness resistance curves and (b) cyclic fatigue-crack propagation behavior in high-toughness (TS) Mg-PSZ, tested in a room-air environment. Note the higher toughness, yet relatively unaffected crack-growth rates, in the 7.8-mm-thick C(T) sample, compared to the 1.5-mm-thick sample.

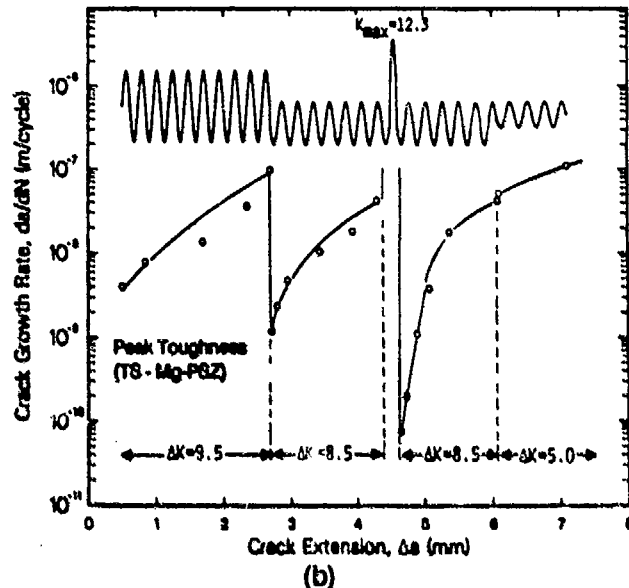
peak-toughness Mg-PSZ in Fig. 15(b); in addition, significant retardation can be seen following a single tensile overload to a  $K_{max}$  of 12.3 MPa·m<sup>1/2</sup>. Such results can be rationalized in terms of changes in crack-tip shielding from the transformation zone.<sup>47</sup>

#### IV. Mechanisms of Cyclic Fatigue

Mechanisms of fatigue crack growth may be conveniently classified into two categories; *intrinsic* mechanisms where the unloading portion of the cycle results in enhanced microstructural "damage" ahead of the crack tip (as in metals), and *extrinsic* mechanisms where the unloading acts to diminish the effect of a crack-tip shielding process, thereby increasing the near-tip stress intensity compared to equivalent monotonic loading conditions. In transforming ceramics, such an extrinsic mechanism could result from a reduction of the degree of transformation toughening under cyclic loading, re-



(a)



(b)

Fig. 15. Transient fatigue-crack growth behavior in (a) mid-toughness (MS) and (b) peak-toughness (TS) Mg-PSZ due to variable-amplitude cyclic loads, showing immediate crack-growth retardations following high-low block overloads, immediate accelerations following low-high block overloads, and delayed retardations following a single tensile overload.

sulting from changes in the process-zone morphology, cyclic accommodation of the transformation strains (related to the type of martensitic twin variants that form), or changes in the degree of reversibility of the transformation. Alternatively, if bridging by frictional/geometrical interlocking of microstructurally rough fracture surfaces<sup>48,49</sup> contributes significantly to the toughness, cyclic loading may result in progressive degradation of the bridging zone.

In the present study, however, several observations argue against such mechanisms, and suggest instead that an intrinsic mechanism is responsible for fatigue-crack growth in Mg-PSZ. The most compelling evidence is that crack growth under cyclic loading is exhibited by the overaged material in which stress-induced transformation cannot occur. Moreover, the crack-growth rates in all the materials can be shown to be uniquely related to the local (near-tip) stress-intensity range,  $\Delta K_{1c}$ , regardless of the degree of transformation toughening. Evaluation of  $\Delta K_{1c}$  must include the effects of both zone shielding and premature crack closure due to contact of

asperities.<sup>11</sup> The maximum and minimum near-tip stress-intensity factors are related to the corresponding far-field applied (measured) values,  $K_{max}$  and  $K_d$  (using Eq. (1a)):

$$(K_{tip})_{max} = K_{max} - K, \quad (6)$$

$$(K_{tip})_{min} = K_d - K, \quad (7)$$

$K_d$  is assumed to remain constant during unloading and was shown in Section III(1) to be given by

$$K_d = \beta K_{max} \quad (8)$$

where  $\beta$  is a constant for a given material.

Equation (7) requires  $K_d \geq K$ , that is, in the absence of roughness-induced closure, the transformation shielding causes crack-tip closure at  $K_d = K$ , whereas the presence of sufficiently large roughness effects could cause contact behind the crack tip at larger values of  $K_d$ . However, the closure stress intensity factors from Fig. 7 (measured from point (A) of the compliance curve of Fig. 1(b)) are smaller than the corresponding values of  $K$ , in Fig. 9. This suggests that the values in Fig. 7 represent roughness-induced contact well behind the crack tip, at a lower applied load than that which allows initial, near-tip closure. Closer examination of the present unloading compliance curves reveals a marginal change in linearity after unloading ~20% to 30% from the maximum load (point (B) in Fig. 1(b)). Such behavior is consistent with the notion that, during unloading, crack-surface contact occurs first over a short distance (of the order of micrometers) behind the crack tip,<sup>11</sup> before roughness-induced crack contact over the remaining crack surfaces. Estimation of the closure stress intensities from these higher closure loads yields  $K_d$  values within 5% of  $K$ . Therefore, it appears that initial tip closure occurs at  $K_d = K$ , and the tip-stress intensity range is given by

$$\Delta K_{tip} = K_{max} - K, \quad (9)$$

The crack-growth rates for all materials are plotted in Fig. 16(a) in terms of  $\Delta K_{tip}$  evaluated from Eq. (9), with  $K$ , obtained from Eq. (8). All data fall close to a universal curve of the form

$$da/dN = A(\Delta K_{tip})^n \quad (10)$$

where  $n = 22$  and  $A = 3.5 \times 10^{-13} \text{ m}^{(1-n/2)} \cdot \text{cycle}^{-1} \cdot \text{MPa}^{-n}$ .

The growth-rate data may be normalized equivalently in terms of the steady-state toughness,  $K_c$ . This may be readily demonstrated by noting that  $K_c = K_0 + K$ , where  $K_0$  is the intrinsic toughness (without transformation shielding), from which  $K_c = K_0/(1 - \beta)$  from Eq. (8). With this result, Eq. (9) can be written

$$\Delta K_{tip} = K_0 \left( \frac{K_{max}}{K_c} \right) \quad (11a)$$

or

$$\Delta K_{tip} = \frac{K_0}{(1 - R)} \left( \frac{\Delta K}{K_c} \right) \quad (11b)$$

where  $\Delta K = K_{max}(1 - R)$ , and Eq. (11) becomes

$$\frac{da}{dN} = A \frac{K_0}{(1 - R)^n} \left( \frac{\Delta K}{K_c} \right)^n \quad (12)$$

According to Eq. (12), a universal curve is obtained by shifting the data for each material in Fig. 3 along the  $\Delta K$  axis by a constant multiplying factor,  $K_0/[K_c(1 - R)]$ . The result of

<sup>11</sup>Where the near-tip stress-intensity range is estimated by considering the effect of crack closure only,  $\Delta K_{tip}$  is commonly referred to in the fatigue literature as  $\Delta K_{eff}$ , as defined in Section II.

<sup>12</sup>Note that macroscopic back-face strain compliance techniques for detecting crack closure are global in nature and are not particularly sensitive to local crack-surface contact occurring near the crack tip.

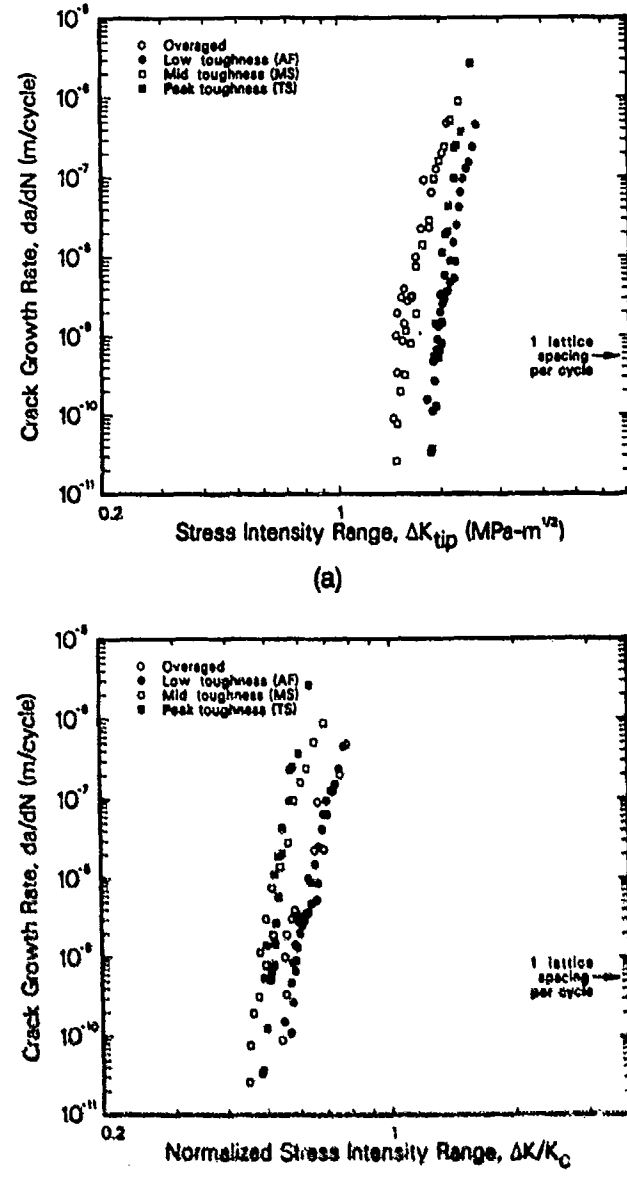


Fig. 16. Cyclic fatigue-crack growth rates for Mg-PSZ in the four toughness conditions plotted as a function of (a)  $\Delta K_{tip}$  from Eq. (10), and (b) the normalized stress-intensity range,  $\Delta K/K_c$ .

normalizing the data in this manner is shown in Fig. 16(b). An analogous result for environmentally assisted crack growth has been discussed by Lawn.<sup>12</sup>

The Raman and surface-uplift measurements of Section III further support the contention that transformation-zone shielding is not affected by the cyclic nature of the loading. Specifically, the results in Figs. 9 and 11 indicate that for steady-state crack growth under cyclic or monotonic loading,  $K$  is determined by the maximum applied stress-intensity factor (Eq. (7)). Although these results pertain only to the contribution to  $K$  from the wake region of the zone (detailed comparisons of frontal zones have not yet been completed), preliminary estimates indicate that the frontal zone in fatigue loading would need to be enlarged by a factor of 4 compared with that in monotonic loading in order to make a significant difference to the above conclusions.

Potential intrinsic mechanisms of fatigue include accumulated damage in material ahead of the crack tip in the form of localized microplasticity, or microcracking, particularly in grain boundary and precipitate/matrix interface regions. Matrix microcracking associated with the formation of transformation shear bands has also been suggested.<sup>12</sup> Such

microcracking could be enhanced by the cyclic movement of twin boundaries in transformed monoclinic particles in response to cyclic loading. In fact, cyclic stress vs strain (hysteresis) behavior has been demonstrated for several transforming zirconia materials.<sup>21</sup> Other mechanisms may include Mode II and III cracking, due either to the wedging action of crack-surface asperities on unloading or to changes in the local stress state induced by Mode I opening on the loading cycle. In addition, crack extension during loading may permit relaxation of residual stresses in specifically orientated grains, with subsequent development of additional tensile and shear stresses upon unloading because of the inability of the relaxed grains to be accommodated in their original positions.<sup>4,7</sup> These effects are likely to be a strong function of residual stress states arising from thermal expansion anisotropy (in noncubic systems),<sup>4</sup> elastic anisotropies of the grains,<sup>72</sup> and the nature of cyclic accommodation of the transformation strains when these are present in the material.

### V. Implications for Design

The results of this work provide evidence of the premature failure of zirconia materials under tension-tension cyclic loading. In engineering design with ceramics, however, such cyclic fatigue phenomena have been rarely considered. With the damage-tolerant approach, for example, component lifetimes are predicted on the basis of fracture-toughness and subcritical crack-growth behavior (i.e., stress-corrosion and creep data) determined under monotonic loads. In view of the high cyclic crack velocities observed, far in excess of those under sustained loads at equivalent stress-intensity levels, and the occurrence of fatigue-crack growth at stress intensities as low as 50% of  $K_c$ , the results of the present study imply that ignoring cyclic fatigue in design and life prediction may have dire consequences.

For design procedures based on crack propagation, as in many safety-critical applications involving metallic components, allowance for the cyclic fatigue effect can be achieved by estimating the time to grow preexisting defects to critical size through integration of the cyclic fatigue-crack growth relationship (e.g., Eq. (4)). However, with the very high exponents ( $m$ ) and resultant extreme sensitivity of the projected lifetime to the applied stresses (albeit over only a narrow range of stress), this may not be a sensible approach. Moreover, the transient effects demonstrated in Fig. 15 imply that Eq. (4) is adequate only for constant  $\Delta K$  loading: In general, the fatigue-crack growth relationship (and hence lifetime) is dependent upon loading history as well as the instantaneous  $\Delta K$ . A more practicable approach may be to base design on crack initiation, with allowance being made for the existence of a cyclic fatigue threshold for crack growth as low as ~50% of the fracture toughness. However, it must be noted that, in ceramic components, subcritical crack growth and subsequent instability may involve very small cracks. Since it is well-known for metallic materials that such "small" ( $\leq 500 \mu\text{m}$ ) cracks may propagate at rates significantly faster than those of "long" cracks (e.g., Refs. 46 and 73), it is vital that future studies on ceramics address the role of crack size in influencing cyclic behavior.

### VI. Conclusions

Based on a study of the growth of fatigue cracks in Mg-PSZ under tension-tension cyclic loads, the following conclusions can be drawn:

Fatigue-crack growth in overaged and partially stabilized (transformation-toughened) zirconia is unequivocally demonstrated to be a mechanically induced cyclic process, which is accelerated in moist air and distilled water environments. Growth rates ( $da/dN$ ) can be described in terms of a power-law function of the stress-intensity range ( $\Delta K$ ), with an exponent  $m$  in the range of 21 to 42.

(2) Resistance to cyclic crack-growth increases when the fracture toughness ( $K_c$ ) of Mg-PSZ is increased; the apparent threshold for fatigue-crack growth ( $\Delta K_{th}$ ), below which cracks are presumed dormant, is approximately 50% of  $K_c$ .

(3) Cyclic crack growth in ceramics shows evidence of crack closure in addition to other crack-tip shielding mechanisms (crack deflection, uncracked ligament bridging, transformation toughening). Moreover, when subjected to variable-amplitude cyclic loading, fatigue cracks in Mg-PSZ experience transient crack-growth retardation immediately following high-low block overloads, transient acceleration immediately following low-high block overloads, and delayed retardation following single tensile overloads. Such behavior is analogous to that commonly reported for metallic materials and consistent with expectations of crack-tip shielding due to transformation.

(4) Cyclic crack velocities in Mg-PSZ are found to be up to 7 orders of magnitude faster, and threshold stress intensities almost 40% lower, than stress-corrosion crack velocities measured in identical environments under sustained-loading conditions. Such observations may have serious implications for defect-tolerant life predictions in zirconia ceramics.

(5) Although the detailed mechanism of cyclic fatigue-crack growth has not been identified, an intrinsic mechanism is implicated by several observations; that is, the mechanism does not appear to involve cyclic reduction in the degree of transformation toughening.

**Acknowledgments:** The authors thank Drs. R. M. Cannon, M.V. Swain, and W. Yu for invaluable discussions, Dr. D.K. Veirs and M. Shaw for assistance with the Raman studies, and Madeline Penton for her help in preparing the manuscript.

### References

- A.G. Evans, "Fatigue in Ceramics," *Int. J. Fract.*, 16 [6] 485-98 (1980).
- A.G. Evans and M. Linzer, "High Frequency Cyclic Crack Propagation in Ceramic Materials," *Int. J. Fract.*, 12 [2] 217-22 (1976).
- F. Gulu, "Cyclic Fatigue of Polycrystalline Alumina in Direct Push-Pull," *J. Mater. Sci. Lett.*, 13 [6] 1357-61 (1978).
- D. Lewis, "Cyclic Mechanical Fatigue in Ceramic-Ceramic Composites — An Update," *Ceram. Eng. Sci. Proc.*, 4 [9-10] 874-81 (1983).
- R.W. Rice, "Capabilities and Design Issues for Emerging Tough Ceramics," *Am. Ceram. Soc. Bull.*, 63 [2] 256-62.
- H.N. Ko, "Fatigue Strength of Sintered  $\text{Al}_2\text{O}_3$  under Rotary Bending," *J. Mater. Sci. Lett.*, 5 [4] 464-66 (1986).
- T. Kawakubo and K. Komeya, "Static and Cyclic Fatigue Behavior of a Sintered Silicon Nitride at Room Temperature," *J. Am. Ceram. Soc.*, 70 [6] 400-05 (1987).
- I. Oda, M. Matsui, and T. Soma, "Dynamic Fatigue of Sintered  $\text{Si}_3\text{N}_4$ ," pp. 1149-54 in Proceedings of 1987 Tokyo Int'l. Gas Turbine Congress, 1987.
- M.V. Swain and V. Zelisko, "Comparison of Static and Cyclic Fatigue on Mg-PSZ Alloys," pp. 595-606 in *Advances in Ceramics, Vol. 24, Science and Technology of Zirconia III*. Edited by S. Sano, N. Yamamoto, and H. Yanagida. American Ceramic Society, Westerville, OH, 1988.
- T. Kawakubo, "Static and Cyclic Fatigue in Ceramics," in *Structural Ceramics/Fracture Mechanics, Proceedings of the MRS International Meeting on Advanced Materials, Vol. 5*, Tokyo, Japan, June, 1988. Edited by Y. Hamano, O. Kamigaito, T. Kishi, and M. Sakai. Materials Research Society, Pittsburgh, PA, 1989.
- K. Ohya, K. Ogura, M. Takatsu, and H. Kamiya, "Cyclic Fatigue Test of PSZ Using a Piezoelectric Bimorph Actuator — Effect of Stress Amplitude and Frequency," in *Structural Ceramics/Fracture Mechanics, Proceedings of the MRS International Meeting on Advanced Materials, Vol. 5*, Tokyo, Japan, June, 1988. Edited by Y. Hamano, O. Kamigaito, T. Kishi, and M. Sakai. Materials Research Society, Pittsburgh, PA, 1989.
- M.V. Swain, V. Zelisko, S. Lam, and M. Marmach, "Comparison of the Static and Cyclic Fatigue Behaviour of Mg-PSZ and Alumina in Ringer's Solution," to be published in *Biomaterials, Proceedings of the MRS International Meeting on Advanced Materials, Vol. 1*, Tokyo, Japan, June, 1988. Materials Research Society, Pittsburgh, PA, 1989.
- T. Soma, M. Matsuda, M. Matsui, and I. Oda, "Cyclic Fatigue Testing of Ceramic Materials," to be published in *Proceedings of Conference on Mechanical Testing of Engineering Ceramics at High Temperatures*, London, U.K., 1988.
- S. Horibe, "Cyclic Fatigue Crack Growth from Indentation Flaw in  $\text{Si}_3\text{N}_4$ ," *J. Mater. Sci. Lett.*, 7 [7] 725-27 (1988).
- M. Matsuda, T. Soma, M. Matsui, and I. Oda, "Fatigue of Ceramics (Part 1) — Fatigue Behavior of Sintered  $\text{Si}_3\text{N}_4$  under Tension-Compression Cyclic Stress," *J. Ceram. Soc. Jpn. Inter. Ed.*, 96, 275-80 (1988).
- L. Ewart and S. Sureab, "Dynamic Fatigue Crack Growth in Polycrystalline Alumina under Cyclic Compression," *J. Mater. Sci. Lett.*, 5 [4] 774-78 (1986).

<sup>18</sup>S. Suresh, L. X. Han, and J. P. Petrovic, "Fracture of  $\text{Si}_3\text{N}_4$ - $\text{SiC}$  Composites under Cyclic Loads," *J. Am. Ceram. Soc.*, 71 [3] C-158-C-161 (1988).

<sup>19</sup>L. Ewart and S. Suresh, "Crack Propagation in Ceramics under Cyclic Loads," *J. Mater. Sci.*, 22 [4] 1173-92 (1987).

<sup>20</sup>J. R. Brockenbrough and S. Suresh, "Constitutive Behavior of a Micro-cracking Brittle Solid in Cyclic Compression," *J. Mech. Phys. Solids*, 35 [6] 721-42 (1987).

<sup>21</sup>S. Suresh and J. R. Brockenbrough, "Theory and Experiments of Fracture in Cyclic Compression: Single-Phase Ceramics, Transforming Ceramics and Ceramic Composites," *Acta Metall.*, 35 [6] 1453-70 (1988).

<sup>22</sup>K. J. Bowman, P. E. Reyes-Morel, and I.-W. Chen, "Reversible Transformation Plasticity in Uniaxial Tension-Compression Cycling of Mg-PSZ"; in Materials Research Society Symposium Proceedings on Advanced Structural Ceramics. Edited by P. F. Becher, M. V. Swain, and S. Somiya. Materials Research Society, Pittsburgh, PA, 1986.

<sup>23</sup>R. H. Dauskardt, W. Yu, and R. O. Ritchie, "Fatigue Crack Propagation in Transformation-Toughened Ceramic," *J. Am. Ceram. Soc.*, 70 [10] C-248-C-252 (1987).

<sup>24</sup>R. O. Ritchie, "Mechanisms of Fatigue Crack Propagation in Metals, Ceramics, and Composites: Role of Crack-Tip Shielding," *Mater. Sci. Eng.*, 103 [1] 15-28 (1988).

<sup>25</sup>L. A. Sylva and S. Suresh, "Crack Growth in Transforming Ceramics under Cyclic Tensile Loads," *J. Mater. Sci.*, 24 [5] 1729-38 (1989).

<sup>26</sup>M. J. Reece, F. Guiu and M. F. R. Sammuri, "Cyclic Fatigue Crack Propagation in Alumina under Direct Tension-Compression Loading," *J. Am. Ceram. Soc.*, 72 [2] 348-52 (1989).

<sup>27</sup>T. Hoshide, T. Ohara, and T. Yamada, "Fatigue Crack Growth from Indentation Flaw in Ceramics," *Int. J. Fract.*, 37 [1] 47-59 (1988).

<sup>28</sup>M. R. James, Rockwell International Science Center, Thousand Oaks, CA; unpublished work.

<sup>29</sup>L. X. Han and S. Suresh, "High-Temperature Failure of an Alumina-Silicon Carbide Composite under Cyclic Loads: Mechanisms of Fatigue Crack-Tip Damage," *J. Am. Ceram. Soc.*, 72 [7] 1233-38 (1989).

<sup>30</sup>R. H. Dauskardt and R. O. Ritchie, University of California, Berkeley, CA; unpublished work.

<sup>31</sup>R. O. Ritchie, R. H. Dauskardt, W. Yu, and A. M. Brendzel, "Cyclic Fatigue-Crack Propagation, Stress-Corrosion and Fracture-Toughness Behavior in Pyrolytic Carbon-Coated Graphite for Prosthetic Heart Valve Applications"; to be published in *J. Biomed. Mater. Res.*

<sup>32</sup>A. G. Evans and R. M. Cannon, "Toughening of Brittle Solids by Martensitic Transformations," *Acta Metall.*, 34 [5] 761-800 (1986).

<sup>33</sup>R. H. J. Hannick and M. V. Swain, "Magnesia-Partially-Stabilized Zirconia: The Influence of Heat Treatment on Thermomechanical Properties," *J. Aust. Ceram. Soc.*, 18 [2] 53-62 (1982).

<sup>34</sup>D. B. Marshall, "Strength Characteristics of Transformation-Toughened Zirconia," *J. Am. Ceram. Soc.*, 69 [3] 173-80 (1986).

<sup>35</sup>D. B. Marshall and M. R. James, "Reversible Stress-Induced Martensitic Transformation in  $\text{ZrO}_2$ ," *J. Am. Ceram. Soc.*, 69 [3] 215-17 (1986).

<sup>36</sup>D. B. Marshall and M. V. Swain, "Crack Resistance Curves in Magnesia-Partially-Stabilized Zirconia," *J. Am. Ceram. Soc.*, 71 [6] 399-407 (1988).

<sup>37</sup>R. M. MacMeeding and A. G. Evans, "Mechanics of Transformation Toughening in Brittle Materials," *J. Am. Ceram. Soc.*, 65 [5] 242-46 (1982).

<sup>38</sup>B. Budiansky, J. W. Hutchinson, and J. C. Lambropoulos, "Continuum Theory of Dilatant Transformation Toughening in Ceramics," *Int. J. Solids Struct.*, 19 [4] 337-53 (1983).

<sup>39</sup>J. C. Lambropoulos, "Shear, Shape, and Orientation Effects in Transformation Toughening," *Int. J. Solids Struct.*, 22, 1083-106 (1986).

<sup>40</sup>I.-W. Chen and P. E. Reyes-Morel, "Implications of Transformation Plasticity in  $\text{ZrO}_2$ -Containing Ceramics: I. Shear and Dilatation Effects," *J. Am. Ceram. Soc.*, 69 [3] 181-89 (1986).

<sup>41</sup>L. R. F. Rose, "The Mechanics of Transformation Toughening," *Proc. R. Soc. London, A*, 412 169-97 (1987).

<sup>42</sup>J. W. Hutchinson, "Crack Tip Shielding by Micro-Cracking in Brittle Solids," *Acta Metall.*, 35 [7] 1603-19 (1987).

<sup>43</sup>D. B. Marshall, B. N. Cox, and A. G. Evans, "The Mechanics of Matrix Cracking in Brittle-Matrix Fiber Composites," *Acta Metall.*, 33 [11] 2013-21 (1985).

<sup>44</sup>S. Suresh and R. O. Ritchie, "Near-Threshold Fatigue Crack Propagation: A Perspective on the Role of Crack Closure," pp. 227-61 in Fatigue Crack Growth Threshold Concepts. Edited by D. L. Davidson and S. Suresh. The Metallurgical Society of the American Institute of Mining, Metallurgical, and Petroleum Engineers, Warrendale, PA, 1984.

<sup>45</sup>"ASTM Standard E. 647-86a, "Standard Test Method for Measurement of Fatigue Crack Growth Rates"; pp. 899-926 in 1987 ASTM Annual Book of Standards, Vol. 3.01. American Society for Testing and Materials, Philadelphia, PA, 1987.

<sup>46</sup>P. K. Liaw, H. R. Hartmann, and W. A. Lodgson, "A New Transducer to Monitor Fatigue Crack Propagation," *J. Test. Eval.*, 11 [3] 202-207 (1983).

<sup>47</sup>R. O. Ritchie and W. Yu, "Short Crack Effects in Fatigue: A Consequence of Crack-Tip Shielding"; pp. 167-89 in Small Fatigue Cracks. Edited by R. O. Ritchie and J. Lankford. The Metallurgical Society of the American Institute of Mining, Metallurgical, and Petroleum Engineers, Warrendale, PA, 1986. □

by R. O. Ritchie and J. Lankford. The Metallurgical Society of the American Institute of Mining, Metallurgical, and Petroleum Engineers, Warrendale, PA, 1986.

<sup>48</sup>R. O. Ritchie, "Near-Threshold Fatigue Crack Propagation," *Int. Met. Rev.*, 20 [5-6] 205-30 (1979).

<sup>49</sup>A. Saxena, S. J. Hudak, Jr., J. K. Donald, and D. W. Schmidt, "Computer-Controlled Decreasing Stress Intensity Technique for Low Rate Fatigue Crack Growth Testing," *J. Test. Eval.*, 6 [3] 167-74 (1978).

<sup>50</sup>J. C. Newman, Jr., "Stress Analysis of the Compact Specimen Including the Effects of Pin Loading"; pp. 105-21 in Fracture Analysis (8th Conference), ASTM STP 560. American Society for Testing and Materials, Philadelphia, PA, 1974.

<sup>51</sup>J. E. Srawley, "Wide Range Stress Intensity Factor Expressions for ASTM Method E 399 Standard Fracture Toughness Specimens," *Int. J. Fract.*, 12 [6] 475-76 (1976).

<sup>52</sup>R. H. Dauskardt and R. O. Ritchie, "Cyclic Fatigue Crack Growth Behavior in Ceramics," *Closed Loop*, 17, 7-17 (1989).

<sup>53</sup>ASTM Standard E. 399-83, "Standard Test Method for Plane-Strain Fracture Toughness of Metallic Materials"; pp. 680-715 in 1987 ASTM Annual Book of Standards, Vol. 3.01. American Society for Testing and Materials, Philadelphia, PA, 1987.

<sup>54</sup>P. C. Paris and F. Erdogan, "A Critical Analysis of Crack Propagation Laws," *J. Basic Eng. Trans. ASME*, 85, 528-34 (1963).

<sup>55</sup>W. Elber, "The Significance of Fatigue Crack Closure"; pp. 230-42 in Damage Tolerance in Aircraft Structures, ASTM STP 486. American Society for Testing and Materials, Philadelphia, PA, 1971.

<sup>56</sup>N. Walker and C. E. Beevers, "A Fatigue Crack Closure Mechanism in Titanium," *Fatigue Eng. Mater. Struct.*, 1 [1] 135-48 (1979).

<sup>57</sup>K. Minakawa and A. J. McEvily, Jr., "On Crack Closure in the Near-Threshold Region," *Scr. Metall.*, 15 [6] 633-36 (1981).

<sup>58</sup>S. Suresh and R. O. Ritchie, "A Geometric Model for Fatigue Crack Closure Induced by Fracture Surface Roughness," *Metall. Trans. A*, 13A [9] 1627-31 (1982).

<sup>59</sup>D. R. Clarke and F. Adar, "Measurement of the Crystallographically Transformed Zone Produced by Fracture in Ceramics Containing Tetragonal Zirconia," *J. Am. Ceram. Soc.*, 65 [6] 284-88 (1982).

<sup>60</sup>D. B. Marshall, M. C. Shaw, R. H. Dauskardt, R. O. Ritchie, M. Readey, and A. H. Heuer, "Crack Tip Transformation Zones in Toughened Zirconia"; unpublished work.

<sup>61</sup>R. H. Dauskardt, D. K. Viers, and R. O. Ritchie, "Spatially-Resolved Raman Spectroscopy of Transformed Zones in MgO-Partially-Stabilized Zirconia," *J. Am. Ceram. Soc.*, 72 [7] 1124-30 (1989).

<sup>62</sup>B. N. Cox, D. B. Marshall, D. Kouris, and T. Mura, "Surface Displacement Analysis of the Transformed Zone in Magnesia Partially Stabilized Zirconia," *J. Eng. Mater. Technol.*, 110, 105-109 (1988).

<sup>63</sup>D. B. Marshall, A. G. Evans, and M. Drory, "Transformation Toughening in Ceramics"; pp. 289-307 in Fracture Mechanics of Ceramics, Vol. 6. Edited by R. C. Bradt, A. G. Evans, D. P. H. Hasselman, and F. F. Lange. Plenum Press, New York, 1983.

<sup>64</sup>L. S. Williams, "Fatigue and Ceramics"; Chapter 18 in Mechanical Properties of Engineering Ceramics. Edited by W. W. Kriegel and H. Palmour III. Interscience Publishers, New York, 1961.

<sup>65</sup>D. A. Krohn and D. P. H. Hasselman, "Static and Cyclic Fatigue Behavior of a Polycrystalline Alumina," *J. Am. Ceram. Soc.*, 55 [4] 208-11 (1972).

<sup>66</sup>A. H. Heuer, M. J. Readey, and R. Steinbrech, "Resistance Curve Behavior of Supertough MgO-Partially-Stabilized  $\text{ZrO}_2$  (Mg-PSZ)"; to be published in *J. Am. Ceram. Soc.*

<sup>67</sup>R. W. Hertzberg, Deformation and Fracture Mechanics of Engineering Materials, 3d ed. Wiley, New York, 1989.

<sup>68</sup>R. H. Dauskardt, W. C. Carter, D. K. Viers, and R. O. Ritchie, "Transient Subcritical Crack Growth Behavior in Transformation-Toughened Ceramics"; to be published in *Acta Metall.*

<sup>69</sup>P. L. Swanson, C. J. Fairbanks, B. R. Lawn, Y.-W. Mai, and B. J. Hockey, "Crack-Interface Grain Bridging as a Fracture Resistance Mechanism in Ceramics: I. Experimental Study on Alumina," *J. Am. Ceram. Soc.*, 70 [4] 279-89 (1987).

<sup>70</sup>R. Knechess and R. W. Steinbrech, "Effect of Grain Size on the Crack Resistance Curves of  $\text{Al}_2\text{O}_3$  Bend Specimens"; pp. 613-19 in Science of Ceramics, Vol. 8. Edited by R. C. Bradt, A. G. Evans, D. P. H. Hasselman, and F. F. Lange. Plenum Press, New York, 1986.

<sup>71</sup>B. R. Lawn, "Physics of Fracture," *J. Am. Ceram. Soc.*, 66 [2] 83-91 (1983).

<sup>72</sup>O. Grathwohl, "Fatigue of Ceramics under Cyclic Loading" (in Ger.). Materialwiss. Werkstofftech., 19, 113-24 (1988).

<sup>73</sup>V. Tvergaard and J. W. Hutchinson, "Microcracking in Ceramics Induced by Thermal Expansion or Elastic Anisotropy," *J. Am. Ceram. Soc.*, 71 [3] 157-66 (1988).

<sup>74</sup>Small Fatigue Cracks. Edited by R. O. Ritchie and J. Lankford. The Metallurgical Society of the American Institute of Mining, Metallurgical, and Petroleum Engineers, Warrendale, PA, 1986.



**Rockwell International  
Science Center**

**SC71002.FR**

## **6.0 TRANSFORMATION THERMODYNAMICS AND REVERSIBILITY**



Rockwell International  
Science Center  
SC71002.FR

**6.1 RECOVERY OF CRACK-TIP TRANSFORMATION ZONES IN ZIRCONIA  
AFTER HIGH TEMPERATURE ANNEALING**

published in J. Am. Ceram. Soc.

# Recovery of Crack-Tip Transformation Zones in Zirconia After High-Temperature Annealing

Michael C. Shaw\* and David B. Marshall\*

Rockwell International Science Center, Thousand Oaks, California 91360

Arthur H. Heuer\* and Eric Inghels\*

Department of Materials Science and Engineering, Case Western Reserve University, Cleveland, Ohio 44106

Annealing at temperatures between 500° and 1000°C reverses the stress-induced tetragonal-to-monoclinic phase transformation in precipitates within crack-tip zones in MgO-partially-stabilized ZrO<sub>2</sub> (Mg-PSZ). The stability of such reverse-transformed tetragonal precipitates during subsequent room-temperature aging has been examined using Raman spectroscopy, surface displacement measurements, and crack-opening measurements. Partial spontaneous retransformation of material within the original zone from tetragonal-to-monoclinic symmetry occurred over periods of several months. [Key words: zirconia, partially stabilized (PSZ), magnesium, crack tip, transformations, annealing.]

## I. Introduction

RECENT studies have shown that large residual crack openings are associated with the presence of transformation zones surrounding cracks in MgO-partially-stabilized ZrO<sub>2</sub> (Mg-PSZ).<sup>1,2</sup> The residual opening is a result of the dilatation associated with the stress-induced tetragonal-to-monoclinic (*t* → *m*) transformation, which causes both wedging near the tip of the crack and bending of the arms of fracture-mechanics test specimens. The magnitude of the residual opening is dependent on the toughness of the material, the specimen geometry, and the size and growth history of the crack.<sup>1</sup> The opening is largest in high-toughness materials and, if the crack begins with no transformation zone, increases with crack extension. Removal of the transformation zone by cutting along the crack with a saw blade eliminates the residual opening displacements, as does annealing in the temperature range 500° to 1000°C for times as short as 20 min.<sup>1</sup>

This last observation provides evidence that heat treatment in this temperature range causes the reverse monoclinic-to-tetragonal (*m* → *t*) transformation. In this paper, we use several techniques to examine the subsequent stability, at room temperature, of precipitates within such a zone that had undergone transformation to tetragonal symmetry during heat treatments at 600° and 800°C. During this room-temperature aging, complete recovery of the original residual crack-opening displacement occurred, whereas only partial recovery

was observed in surface uplift and monoclinic content (as determined by Raman spectroscopy).

## II. Experimental Procedure

The material examined was a commercial 9-mol%-Mg-PSZ (MS grade Mg-PSZ, Nilcra Ceramics, Ltd., Victoria, Australia) that had been heat-treated by us at 1100°C for 20 min (subeutectoid aging<sup>3,4</sup>) to promote ready transformation of tetragonal precipitates to monoclinic symmetry and, thus, formation of large transformation zones around cracks. The specimen geometry and loading conditions used to introduce cracks are described in detail elsewhere.<sup>1,5</sup> A "short DCB" specimen was polished on one side and notched using a 100-μm-thick saw blade. After loading to form a stable crack, the specimen was unloaded and annealed at 1000°C to retransform any material that had transformed to monoclinic symmetry back to the tetragonal structure, then reloaded to grow the crack a further 4 mm. During reloading the measured fracture resistance increased from an initial value of ~11 MPa · m<sup>1/2</sup> to ~15 MPa · m<sup>1/2</sup>, after ~2 mm of crack extension (*R*-curve behavior), and remained constant thereafter.

The transformation zone was then characterized using several methods. The residual crack opening was measured at two locations: (1) the root of the notch and (2) along the loading line 15 mm from the notch root. Raman spectroscopy<sup>6-9</sup> was used to measure the fraction of monoclinic phase as a function of distance from the crack plane at several locations behind the crack tip. Finally, from optical interference micrographs of the polished specimen surface, the out-of-plane displacements due to the transformation zone were measured in the region surrounding the crack.<sup>10</sup>

The specimen was then annealed at 600°C for 20 min, and the measurements were repeated 7 d after cooling. The specimen was annealed again at 800°C for 20 min, and the measurements were repeated 17 d later. These results indicated that partial recovery of the transformation zone had occurred. Therefore, to characterize the effect systematically, the specimen was annealed again at 800°C and the measurements were repeated at various intervals during the succeeding 15 months.

## III. Results

Both Raman spectroscopy and measurements of surface uplift indicated that a transformation zone with dimensions approximately as shown in Fig. 1 surrounded the crack in its initial state. The zone width increased over the first 2 mm of crack growth corresponding to the measured increase in crack resistance and consistent with previous observations of zone

D. R. Clarke—contributing editor

Manuscript No. 196381. Received July 5, 1991; approved October 28, 1991. Supported at Rockwell by the U.S. Air Force Office of Scientific Research under Contract No. F49620-89-C-0031 and at CWRU by the National Science Foundation under Grant No. DMR90-19383.

\*Member, American Ceramic Society.

<sup>†</sup>Present address: 17 Rue de Bazy, 27200 Vernon, France.

<sup>1</sup>Similar to a compact tension specimen, but with dimensions 30 mm × 25 mm × 4 mm.

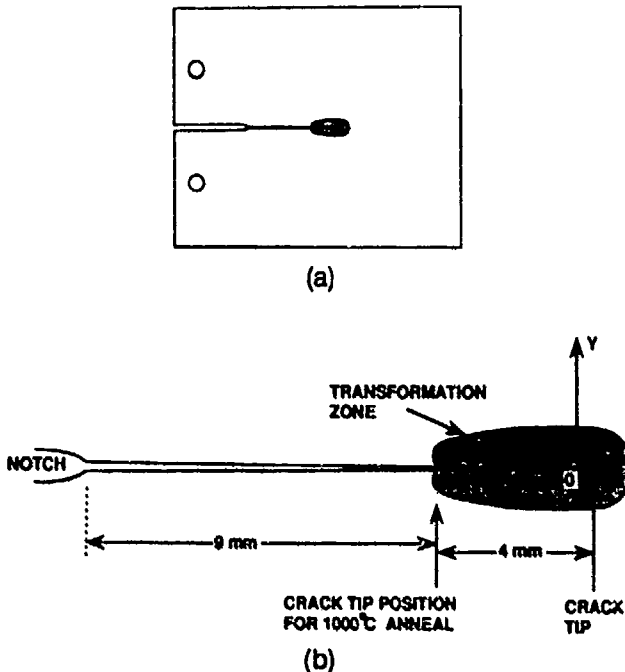


Fig. 1. Schematic diagram of (a) test specimen and (b) crack geometry showing dimensions and shape of transformation zone.

development in nominally identical material.<sup>9</sup> Measurements of the surface uplift and the fraction of monoclinic phase along a line normal to the crack within the steady-state region, as indicated in Fig. 1, are shown in Fig. 2. These are also similar to previous observations.<sup>9</sup>

The variation of the crack-opening displacement at the notch root during the sequence of room-temperature aging and repeated annealing is shown in Fig. 3. After the first anneal at 600°C, the displacement was reduced from the initial value of 54  $\mu\text{m}$  to 38  $\mu\text{m}$ , consistent with results in Ref. 1. The specimen was then annealed at 800°C and left for 17 d at room temperature, whereupon the displacement had increased to 50  $\mu\text{m}$ , close to its original value. Immediately after the second 800°C anneal, the displacement was reduced to 29  $\mu\text{m}$ . Measurements at regular intervals during room-temperature aging over the next 17 months (Fig. 3) showed that the residual crack-opening displacement completely recovered, the recovery being most rapid during the first several days.

Interference measurements of the surface uplift along the line OY normal to the steady-state crack of Fig. 1 are shown in Fig. 2(a) for several stages during the room-temperature aging. Corresponding measurements of the volume fraction of monoclinic phase by Raman spectroscopy are shown in Fig. 2(b). Both measurements indicated that most of the transformation zone was eliminated after annealing at 800°C, consistent with the observed reduction in residual crack opening. The subsequent surface uplift measurements provided clear evidence that partial recovery of dilatation within the original zone (associated with the  $\text{t} \rightarrow \text{m}$  transformation) occurred spontaneously during room-temperature aging. The Raman results also suggested that some forward  $\text{t} \rightarrow \text{m}$  transformation occurred during aging. However, the results were not as clear in this case because of microstructural nonuniformity; the Raman measurements indicated that the volume fraction of monoclinic phase varied from grain to grain (i.e., over distances of  $\sim 50 \mu\text{m}$ ) by up to 0.05, as in measurements reported previously in a similar material.<sup>9</sup> The data for each scan are represented in Fig. 2(b) by a smoothed curve with the "error bars" indicating this  $\pm 0.025$  fluctuation. Moreover, with the background subtraction method used in analyzing the data, the smoothed curves in Fig. 2(b) are true representations of the decrease in locally averaged monoclinic content along a given scan, but there is an error of  $\pm 0.025$  in the

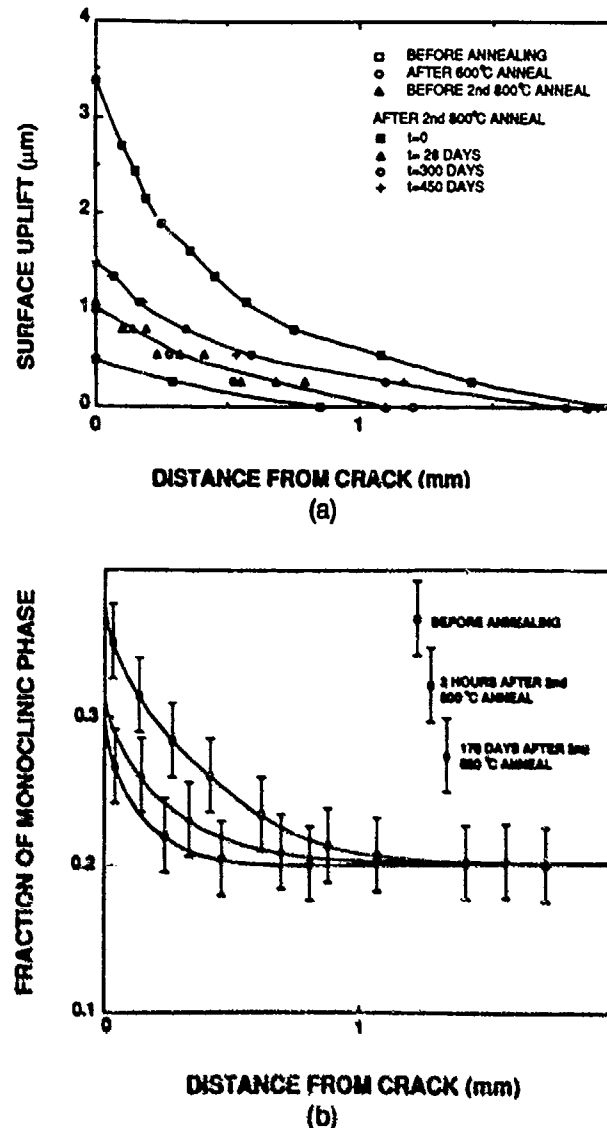


Fig. 2. (a) Out-of-plane surface displacements along the line OY in Fig. 1(b). Measurements from optical interference micrographs. (b) Volume fraction of monoclinic phase along the line OY in Fig. 1(b). Measurements from Raman spectroscopy. Curves are smoothed representations of scans which showed local fluctuations of  $\pm 0.025$  in the fraction of monoclinic phase (indicated by error bars) over a scale of  $\sim 50 \mu\text{m}$ .

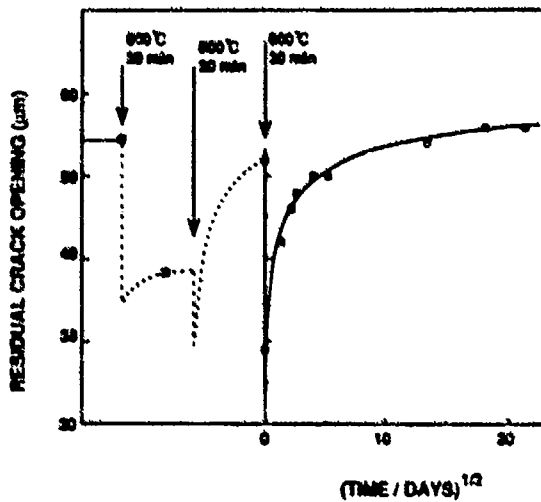


Fig. 3. Residual crack-opening displacements measured at the root of the notch in Fig. 1 after various sequences of high-temperature annealing and room-temperature aging.

absolute values. Thus, to allow comparison, the curves in Fig. 2(b) were shifted vertically to coincide in the region far from the crack.

The results in Figs. 2 and 3 suggest a correlation between the recovery of the residual crack-opening displacement and the retransformation of material within the original crack-tip zone to monoclinic symmetry. However, the magnitudes of the relative recovery of the surface uplift and the Raman signal are both much smaller than the relative recovery in crack opening. After 17 months the recovery in crack-opening displacement was complete, whereas less than one-half of the original surface uplift adjacent to the crack was recovered, and the increase in the fraction of monoclinic phase in regions around the crack (compared with those remote from the crack) was smaller than it was before annealing.

To test whether this apparent discrepancy arises because of differences in the transformation zone at the surface of the specimen and in the bulk, the specimen was sectioned and polished parallel to the line OY in Fig. 1(b), along which the Raman and surface uplift measurements had been made. The Raman measurements were then repeated along lines on this new surface parallel to OY and corresponding to different depths in the original specimen. The resultant zone profiles did not differ significantly from that measured at the specimen surface.

#### IV. Discussion

The measurements of the previous section suggest that, whereas annealing of Mg-PSZ at 600° to 800°C causes the reverse  $m \rightarrow t$  transformation, and thus removal of the transformation zone surrounding a crack, subsequent aging at room temperature without any applied stress causes partial retransformation of some precipitates within the original zone to monoclinic symmetry. This implies that defects associated with the forward stress-induced martensitic transformation must remain after annealing in order to provide nucleation sites (or driving forces) for retransformation. Microcracks, which are known to accompany the transformation of tetragonal precipitates to monoclinic symmetry in this and other transformation-toughened  $\text{ZrO}_2$  materials,<sup>1</sup> are a likely source of such defects.<sup>1</sup>

The overall macroscopic shape change of the specimen, as characterized by the residual crack-opening displacement, is similar to that of a two-way shape memory effect,<sup>11,12</sup> albeit with an activation barrier to the transformation that occurs after cooling. However, the crack-opening displacement measurements alone do not necessarily imply a true shape memory effect (which requires recovery of shear strains<sup>13</sup>) in the material, since the observed displacement variations could be induced by purely hydrostatic transformation strains within the confines of the crack-tip zone. However, complete recovery of the residual crack opening in this case would require complete recovery of the transformation within the zone, contrary to the observations from Raman spectroscopy and interference microscopy. Therefore, the shape strains associ-

ated with the initial stress-induced transformation appear to be different from those associated with the thermal transformation occurring after subsequent annealing cycles—a given extent of transformation during crack growth causes less residual opening than the same amount of transformation during room-temperature aging. This could occur because of a directional bias imposed by the crack-tip stress field on the shape strain of individual precipitates. Such bias would be absent during the transformation that occurs during aging.

The isothermal character of the transformation occurring during room-temperature aging is also interesting. Previous examples of isothermal room-temperature transformation in  $\text{ZrO}_2$  alloys have been noted (Mg-PSZ, Ref. 5 and Ca-PSZ, Ref. 16). In all cases, autocatalytic nucleation appears to be involved.<sup>16</sup> Unfortunately, the precipitates in these "super-tough"  $\text{ZrO}_2$  materials are so transformable that transmission electron microscopy is not useful to study this phenomenon—parasitic stresses occurring during foil-making cause transformation of any untransformed particles. However, this subject is certainly worthy of further study.

#### References

- R.W. Steinbrech, E. Inghels, and A.H. Heuer, "Residual Displacement Effects During Crack Propagation Studies in High-Toughness Magnesia-Partially-Stabilized Zirconia," *J. Am. Ceram. Soc.*, **73** [7] 2016-22 (1990).
- S.J. Burns and M.V. Swain, "Fracture Toughness of MgO-Partially Stabilized  $\text{ZrO}_2$  Specimens with  $K_a$ -Curve Behavior from Transformation Toughening," *J. Am. Ceram. Soc.*, **69** [3] 226-30 (1986).
- R.H.J. Hannink and M.V. Swain, "Magnesia-Partially-Stabilized Zirconia: The Influence of Heat Treatment on Thermomechanical Properties," *J. Aust. Ceram. Soc.*, **10** [2] 53-62 (1982).
- M.J. Readey, A.H. Heuer, and R.W. Steinbrech, "Annealing of Test Specimens of High-Toughness Magnesia-Partially-Stabilized Zirconia," *J. Am. Ceram. Soc.*, **71** [1] C-2-C-6 (1988).
- A.H. Heuer, M.J. Readey, and R.W. Steinbrech, "Resistance Curve Behavior of Supertough MgO-Partially-Stabilized  $\text{ZrO}_2$ ," *Mat. Sci. Eng.*, **A105/106**, 83-89 (1988).
- D.R. Clarke and F. Adar, "Measurement of the Crystallographically Transformed Zone Produced by Fracture in Ceramics Containing Tetragonal Zirconia," *J. Am. Ceram. Soc.*, **65** [6] 284-88 (1982).
- R.H. Dauskardt, D.K. Veirs, and R.O. Ritchie, "Spatially Resolved Raman Spectroscopy Study of Transformed Zones in Magnesia-Partially-Stabilized Zirconia," *J. Am. Ceram. Soc.*, **72** [7] 1124-31 (1989).
- O. Katagiri, H. Iida, A. Ishitani, and T. Masaki, "Direct Determination by a Raman Microprobe of the Transformation Zone Size in  $\text{Y}_2\text{O}_3$  Containing Tetragonal  $\text{ZrO}_2$  Polycrystals," pp. 537-48 in *Advances in Ceramics, Vol. 24, Science and Technology of Zirconia III*, Edited by S. Sōmiya and N. Yamamoto, American Ceramic Society, Westerville, OH, 1988.
- D.B. Marshall, M.C. Shaw, R.H. Dauskardt, R.O. Ritchie, M.J. Readey, and A.H. Heuer, "Crack-Tip Transformation Zones in Toughened Zirconia," *J. Am. Ceram. Soc.*, **73** [9] 2659-66 (1990).
- M.S. Dadkhah, D.B. Marshall, W.L. Morris, and B.N. Cox, "Direct Measurement of Transformation Zone Strains in Toughened Zirconia," *J. Am. Ceram. Soc.*, **74** [3] 584-92 (1991).
- A.H. Heuer, M. Rühle, and D.B. Marshall, "On the Thermoelastic Martensitic Transformation in Tetragonal Zirconia," *J. Am. Ceram. Soc.*, **73**, [4] 1084-93 (1990).
- C.M. Wayman, "Martensitic Transformations: An Overview," pp. 1119-44, in *Solid-Solid Phase Transformations*, Edited by H.I. Aaronson, D.B. Laughlin, R.F. Sekora, and C.M. Wayman, The Metallurgical Society, AIME, Warrendale, PA, 1982.
- T. Saburi and S. Nenno, "The Shape Memory Effect and Related Phenomena," *ibid.*, pp. 1435-79.
- P.E. Reyes-Morel, J.-S. Cherng, and I.-W. Chen, "Transformation Plasticity of CeO<sub>2</sub>-Stabilized Tetragonal Zirconia Polycrystals: II. Pseudoelasticity and Shape Memory Effect," *J. Am. Ceram. Soc.*, **71** [8] 648-57 (1988).
- M.V. Swain, "Shape Memory Behavior in Partially Stabilized Zirconia Ceramics," *Nature (London)*, **322**, 234-36 (1986).
- R.M. Dickerson, M.V. Swain, and A.H. Heuer, "Microstructural Evolution in Ca-PSZ and the Room-Temperature Instability of Tetragonal  $\text{ZrO}_2$ ," *J. Am. Ceram. Soc.*, **70** [4] 214-20 (1987). □

<sup>1</sup>We have also considered, and rejected, the possibility that defects generated from or associated with the large crack-tip stresses, such as dislocations, might be involved in the transformation during room-temperature aging. No such dislocations have ever been observed in the extensive TEM studies of transformation-toughened  $\text{ZrO}_2$  materials.



Rockwell Internationa

Science Center

SC71002.FR

**6.2 ON THE THERMOELASTIC MARTENSITIC TRANSFORMATION IN  
TETRAGONAL ZrO<sub>2</sub>**

published in J. Am. Ceram. Soc.

# On the Thermoelastic Martensitic Transformation in Tetragonal Zirconia

Arthur H. Heuer,\* Manfred Ruhle,† and David B. Marshall\*‡

Department of Materials Science and Engineering, Case Western Reserve University, Cleveland, Ohio 44106

Recent evidence is summarized showing that the tetragonal (*t*)  $\rightarrow$  monoclinic (*m*) martensitic transformation in  $\text{ZrO}_2$  can occur *thermoelastically* in certain  $\text{ZrO}_2$ -containing ceramics, and that microcracking accompanying the transformation is more common than had previously been recognized. The implications of these new data for the conditions under which the stress-induced transformation is irreversible, and for the particle size dependence of the transformation start ( $M_s$ ) temperature, are discussed. [Key words: martensite, zirconia, transformations, particle size, nucleation.]

## I. Introduction

TRANSFORMATION toughening via the martensitic tetragonal (*t*)  $\rightarrow$  monoclinic (*m*) transformation in  $\text{ZrO}_2$  is one of the most effective ways of improving the reliability and structural integrity of engineering ceramics. The martensitic nature of the *t*  $\rightarrow$  *m* transformation itself has not been an issue for a number of years,<sup>1</sup> but the crystallographic, thermodynamic, and kinetic aspects of the transformation remain areas of considerable research interests<sup>2-10</sup> and even of some controversy.

One subject that is still not thoroughly understood is the particle size dependence of the "martensitic start" or  $M_s$  temperature. In the past, it has been argued that, like martensitic transformations in metallic systems, the martensitic transformation temperature must be understood in relation to the effect of particle morphology (both size and shape) on the nucleation of the transformation, and possibly on the presence of defects to permit heterogeneous nucleation.<sup>7-9</sup> The notion of nucleation control appears to be widely shared,<sup>4</sup> although contrary opinions do exist.<sup>10,11</sup>

The purpose of this paper is to discuss a variety of new data, in particular the discoveries that (1) the transformation exhibits a degree of stress reversibility,<sup>12-14</sup> (2) that in some partially stabilized  $\text{ZrO}_2$ 's (PSZ's) an apparent general transformation of a fraction of *t*- $\text{ZrO}_2$  particles occurs under load prior to fracture and causes inelastic stress-strain curves and permanent deformation ( $\sim 0.1\%$  strain),<sup>12,15-17</sup> and (3) that microcracking associated with transformation is more common than has been previously appreciated. During this discussion, we will reexamine the particle size dependence of  $M_s$ .

## II. Reversible Transformation

Lee and Heuer<sup>13</sup> and Mecartney and Ruhle<sup>14</sup> induced the *t*  $\rightarrow$  *m* transformation in thin foils using stresses introduced

R. Rice—contributing editor

Manuscript No. 198549. Received March 10, 1989; approved August 30, 1989.

Supported at Case Western Reserve University by the National Science Foundation under Contract No. DMR-87-15622 and at the Rockwell Science Center by the Air Force Office of Scientific Research under Contract No. F4960-85-C-0143.

\*Member, American Ceramic Society.

†Max-Planck Institute für Metallforschung, Stuttgart, FRG.  
‡Rockwell International Science Center, Thousand Oaks, CA.

by electron illumination in the transmission electron microscope (TEM). In  $\text{Y}_2\text{O}_3$ -containing *t*- $\text{ZrO}_2$  polycrystals (YTZP),<sup>14</sup> martensitic laths nucleated at grain boundaries (Fig. 1), presumably at sites where stress concentrations existed, and grew in apparent thermoelastic equilibrium across individual grains. When a martensite lath grew completely across a grain, it was stopped at a grain boundary and the resulting stress concentration caused a differently oriented lath to nucleate and begin to grow, sometimes back into the partially transformed grain. If, on the other hand, the lath extended only partly across the grain, and the electron beam was defocused to reduce the beam-induced stresses, the lath shrank and left a defect-free untransformed grain without any evidence that the grain had been partially transformed (Fig. 1(d)). In fact, repeated stressing of the foil by refocusing the electron beam sometimes caused differently oriented martensite laths to form, presumably because of differences in the biaxial stress distribution from one focusing experiment to the next.

Similar experiments were done on both *t*- $\text{ZrO}_2$  grains and *t*- $\text{ZrO}_2$  precipitates in a ternary  $\text{MgO}-\text{Y}_2\text{O}_3-\text{ZrO}_2$  alloy.<sup>13</sup> The *t*- $\text{ZrO}_2$  precipitates in this alloy were platelike and could also be made to transform by beam-induced stresses, and strong autocatalytic transformation occurred. Transformation of a single particle generated a stress field which caused neighboring particles to transform until the entire illuminated region contained monoclinic (*m*) particles in the cubic (*c*)  $\text{ZrO}_2$  matrix. The *m*- $\text{ZrO}_2$  was invariably twinned, with the twin spacing being much smaller at the end of each transformed precipitate than in the bulk of the precipitate (see Fig. 7 of Ref. 13(b)). Partially transformed precipitates also existed. More significantly, several examples were shown of the *t*/*m* interface of partially transformed precipitates retreating when the foil was removed from the microscope and "aged" at room temperature for several days; it is clear that reversible transformations can occur in either *t*- $\text{ZrO}_2$  grains or in *t*- $\text{ZrO}_2$  precipitates in *c*- $\text{ZrO}_2$  matrices.

A reversible *t*  $\rightarrow$  *m* transformation under stress in bulk Mg-PSZ has been detected from *in situ* X-ray diffraction experiments.<sup>1,12</sup> The material had a background *m*- $\text{ZrO}_2$  content of approximately 13 vol%, but the *m*- $\text{ZrO}_2$  content was reversibly increased (or decreased) by  $\sim 3$  vol% during tensile loading (or unloading) using a fixture mounted on the X-ray diffraction apparatus. When these same specimens were mounted on a loading stage in an optical microscope and viewed with Nomarski interference, reversible surface roughness appeared on loading. The surface roughness was interpreted<sup>12</sup> as indicating the onset of *t*  $\rightarrow$  *m* transformation in favorably oriented grains; the scale of the surface roughness corresponded roughly with the grain size ( $\sim 50\ \mu\text{m}$ ). Calculations showed that the magnitude of the surface distortions in these experiments was consistent with that expected from the transformation strain associated with the fraction of *t*  $\rightarrow$  *m* transformation measured in the X-ray experiments.<sup>12</sup>

<sup>1</sup>The X-ray experiments sample approximately 3 mm  $\times$  3 mm  $\times$  20  $\mu\text{m}$  of material.

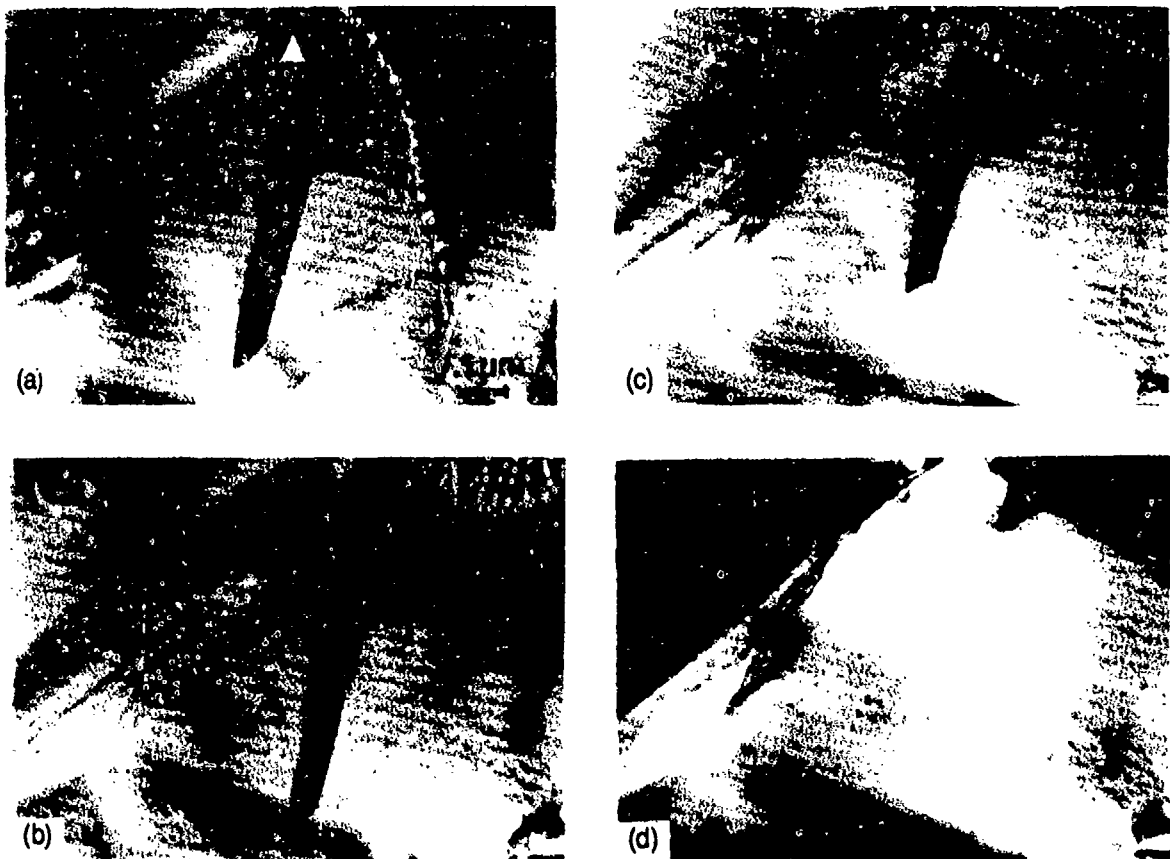


Fig. 1. *In situ* TEM observations of growth (a, b) and shrinkage (c, d) of a martensitic lath with monoclinic symmetry in Y-TZP.

More recent measurements<sup>15</sup> have demonstrated that the surface distortions are a combination of displacements due to the  $t \rightarrow m$  transformation and to elastic anisotropy (Fig. 2). The contribution from elastic anisotropy arises because an applied stress parallel to the free surface of a polycrystalline body causes contraction normal to the surface by an amount that is dependent upon the grain orientation. The results in Fig. 2, which compares distortions in toughened and non-toughened materials, indicate that at stresses below  $\sim 200$  MPa the distortions are due solely to elastic anisotropy, whereas, at higher stresses, anisotropy and transformation contribute about equally to the displacements in the toughened material. Calculations of the directions of maximum and minimum Young's moduli and Poisson's ratios indicate that the orientation dependences of the distortions due to elastic anisotropy and the  $t \rightarrow m$  transformation are similar if the transformation strain and the applied stress are coupled (see the Appendix). This is consistent with observations that the same

grains are uplifted or depressed throughout the load range of Fig. 2; i.e., the magnitudes of the relative surface displacements increased monotonically with load everywhere. Hysteresis in the magnitudes of the surface displacements upon unloading could not be detected from interference measurements, provided the applied load did not exceed  $\sim 350$  MPa. This observation suggests that the transformation occurs close to thermoelastic equilibrium.

The reversible transformation in Mg-PSZ has also been observed in regions under compressive loading. This is illustrated in Fig. 3, which shows the area between inner loading points of a beam loaded in four-point flexure. (The inner loading points are at the upper right and lower right corners of Fig. 3(a); i.e., the tensile and compressive surfaces are the left and right borders of the photo.) The applied stress increases linearly with distance from center (neutral axis) of the beam, with the outer fiber stress being 300 MPa. Corresponding increases in surface distortions are evident in Fig. 3 on both the tensile and compressive sides of the beam, and the surface distortions are of similar magnitudes on both sides. Reversing the sense of loading, as in Figs. 3(b) and (c), causes grains which are "proud" of the surface in tension to be depressed in compression and vice versa (see the arrowed grains in Figs. 3(b) and 3(c)). These observations suggest that the reversible transformation is governed by the applied shear stress and is relatively insensitive to the hydrostatic stress component.

Reversible surface transformation has also been observed in a series of heat-treated Mg-PSZ materials with fracture toughnesses that ranged between 8 and 14 MPa·m<sup>1/2</sup>.<sup>14</sup> The lowest toughness material in this series exhibited neither inelastic yielding nor stable microcrack growth, whereas the highest toughness material showed both. The amount of reversible transformation at given applied stress did not vary within this series of materials with vastly different mechanical properties. Instead, an inverse correlation was found

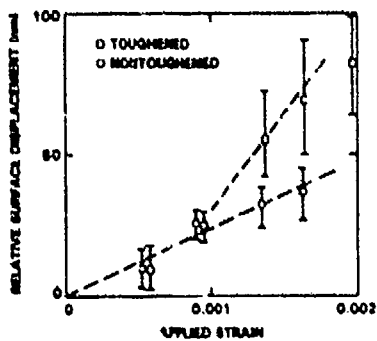


Fig. 2. Surface distortions measured by optical interference microscopy from toughened and nontoughened Mg-PSZ (Ref. 15).

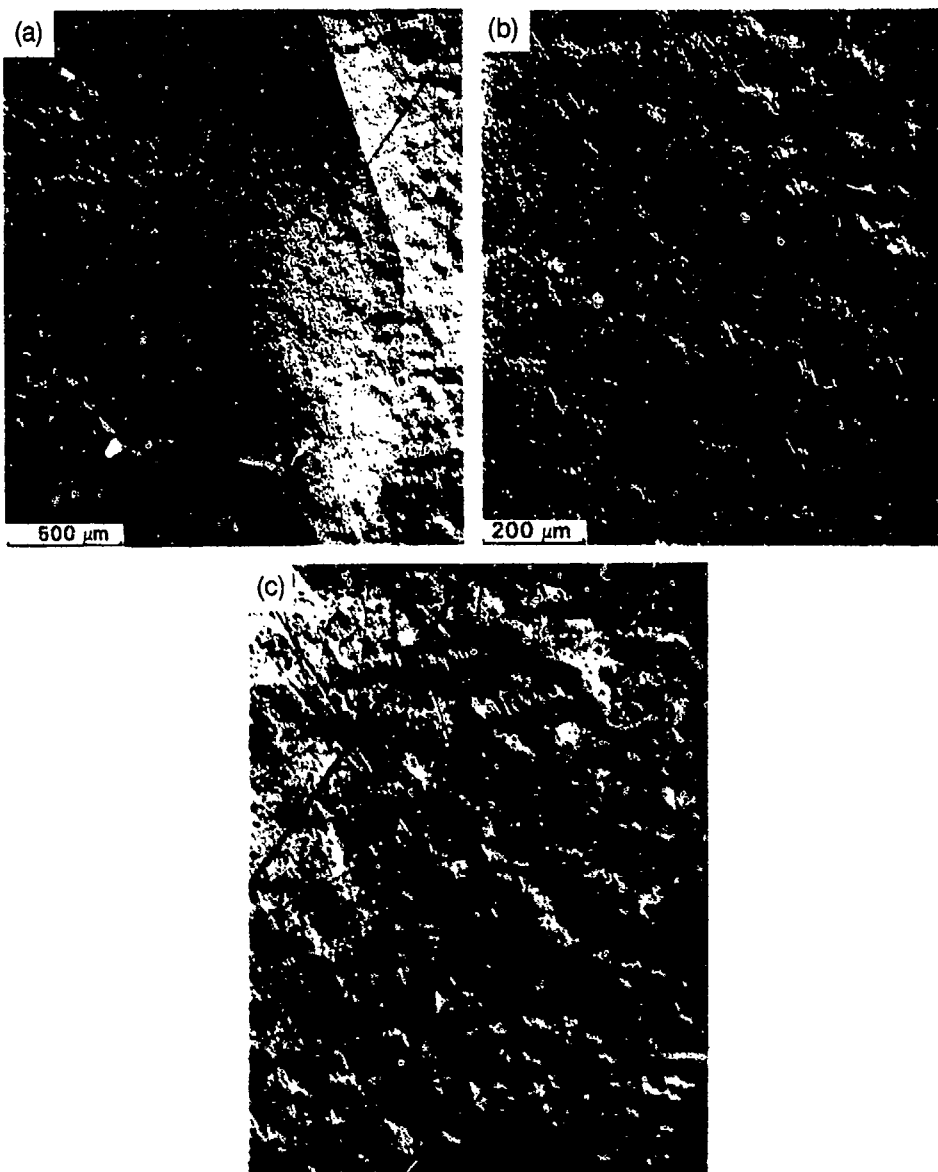


Fig. 3. (a) Optical micrograph from side of beam of Mg-PSZ loaded in four-point flexure (area between inner load lines), showing surface distortions on both the tensile and compressively loaded regions. Outer fiber stress 300 MPa. (b) Enlargement of (a) showing area from tensile side of beam. (c) Same area as (b), but after unloading and reloading, with the sign of bending reversed to generate compressive stress. (The arrowed grains show the reversal of the sense of uplift on reversing the stress.) The Nomarski imaging conditions were identical for the micrographs of (b) and (c), giving the impression of low-angle illumination from the top right of the micrographs.

between the fracture toughness and the stress required to cause permanent or irreversible transformation, indicating that it is the stabilization of the transformation product that is the key to obtaining high toughness and good damage tolerance.<sup>17</sup>

### III. Irreversible Transformation in Mg-PSZ

Tensile loading of the high-toughness Mg-PSZ causes only reversible transformation, provided the applied stress does not exceed  $\sim 350$  MPa. At higher stresses, permanent transformation and microcracking develop (see the arrowed features in Fig. 4(a)), which appear to be correlated. The permanent transformation occurs in localized regions (encompassing several grains), which are elongated on the surface in the direction normal to the applied stress. Etching of the surface with HF reveals that these regions are composed of a substructure of well-defined, parallel-sided bands (Fig. 4(b)). Individual bands are confined to single grains, and the uplifted areas visible without etching contain arrays of adjacent grains with

near-parallel bands. The surface traces of the bands are all oriented approximately normal to the applied stress.

Loading in compression also causes permanent transformation, but the stress required is considerably higher ( $\sim 1200$  MPa) than in tension. Therefore, the critical stress to cause permanent transformation is strongly dependent on the hydrostatic stress component, in contrast to the response of the reversible transformation. The development of permanent transformation in compressive loading can be seen in the series of micrographs in Fig. 5, taken at various stages during load/unload cycles<sup>1</sup> (Fig. 5(d)). The surface roughening in

<sup>1</sup>The stresses appropriate for the load-time curves of Fig. 5(d) cannot be specified with certainty. The specimen was a disk loaded along a diameter, with a strain gauge mounted in the center and the micrographs taken from an area about 1/4 of the distance between the strain gauge and the loading point. The stress-strain curve after the onset of transformation is nonlinear, so stresses calculated from linear elasticity at low loads, and subsequent scale up, would be misleading. The stress at which transformation began (point A) is  $\sim 1200$  MPa.

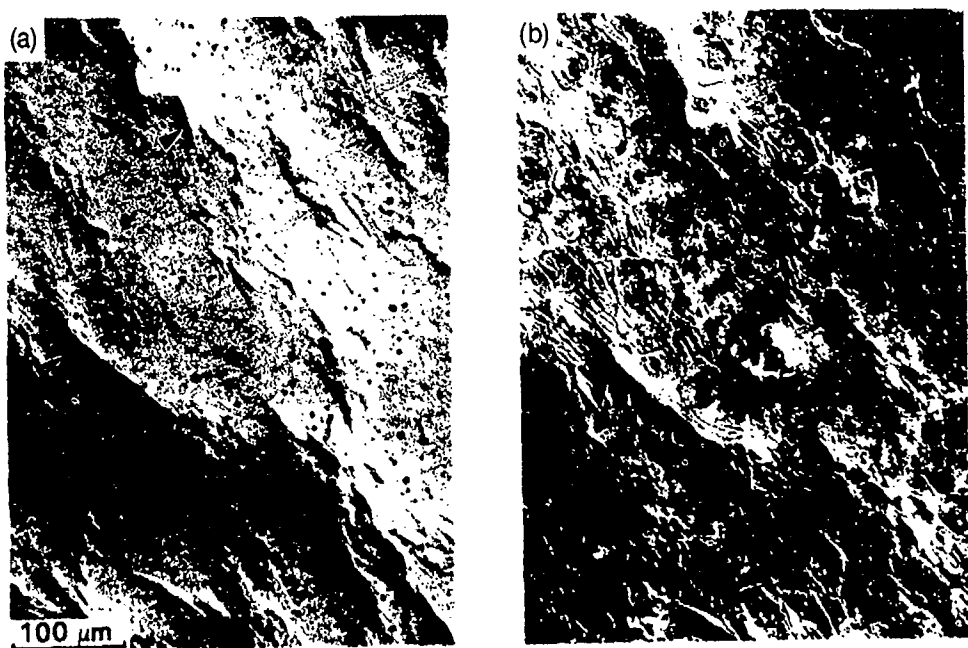


Fig. 4. (a) Polished surface of Mg-PSZ after applying tensile stress of 420 MPa, showing uplifted regions and microcracks (arrowed feature) due to permanent transformation. (b) surface in (a) after etching for 4 min in HF, showing grain boundaries and transformation bands within individual grains.

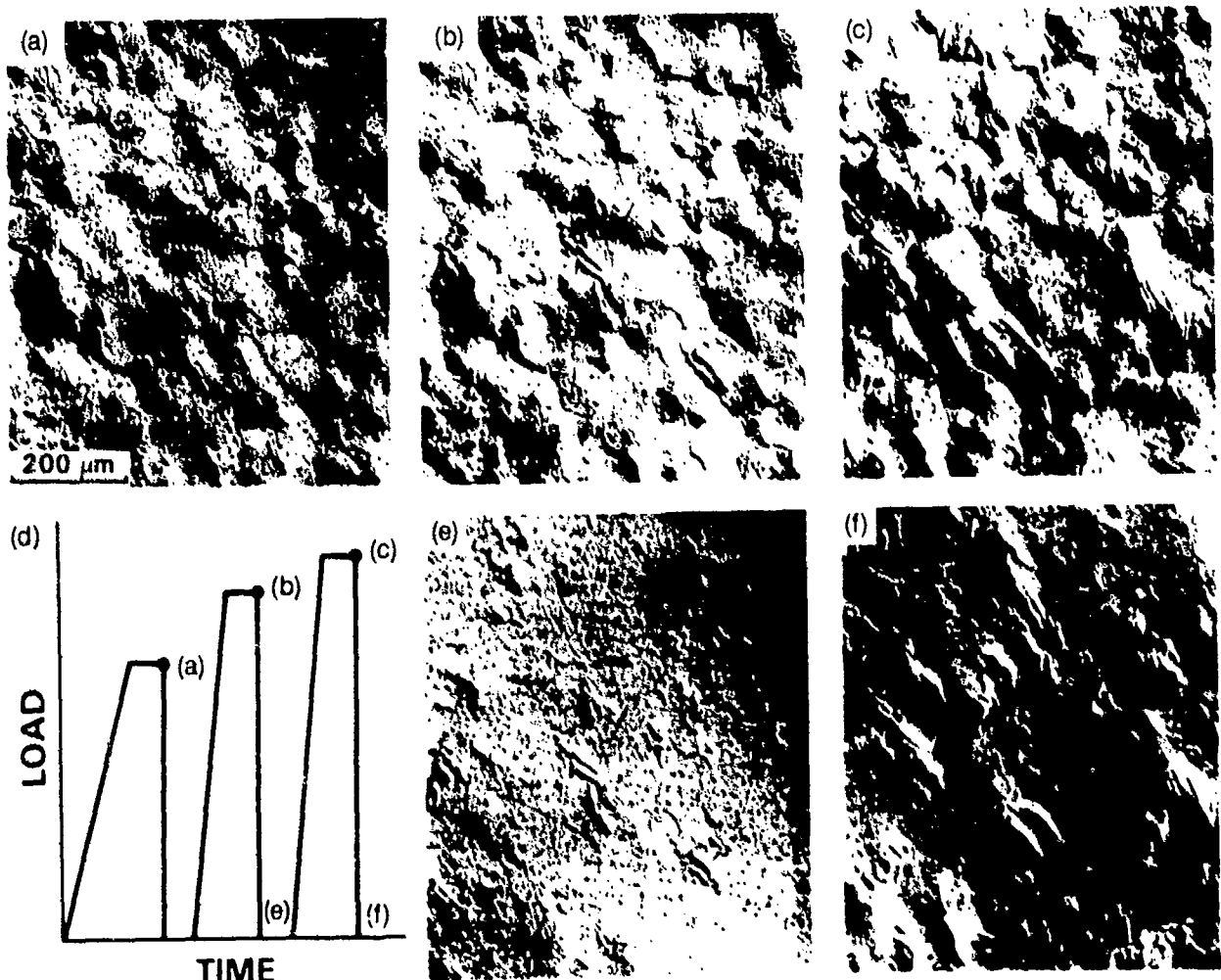


Fig. 5. Optical micrographs from the surface of a disk of Mg-PSZ that was loaded in diametral compression during load cycling. The loading sequence and conditions under which the micrographs were obtained are indicated in (d). (A) corresponds to a stress of 1200 MPa.

Fig. 5(a) was similar to that shown quantitatively in Fig. 2 and was reversible upon unloading. At increasing applied load (Figs. 5(a) to (c)), well-defined bands with more severe surface uplift than that associated with the reversible transformation developed within certain grains. With continued loading, individual bands increased in width and length, the number of bands within individual grains increased, and bands formed in new grains. Upon unloading (Figs. 5(e) and (f)), all of the transformation bands remained, but all of the other surface distortions disappeared.

The surface traces of the bands all lie at angles between  $\sim 30^\circ$  and  $90^\circ$  to the direction of the applied stress (horizontal in Fig. 5). Therefore, if these traces represent the intersections of the specimen surface with planar transformation bands, all of the bands could lie on planes of high resolved shear stress.

The shear nature of these transformation bands is also suggested by the shape of the associated surface distortions. An optical interference micrograph from the area of Fig. 5(f) is shown in Fig. 6; the dark fringes in this micrograph represent contours of constant height separated by  $\lambda/2 = 270$  nm. The surface uplift along A-B is plotted in Fig. 6(b). Within the bright bands in Fig. 5(f), the surface is tilted at a constant angle, thus implying a large component of shear in the transformation strain.

A one-to-one correlation is evident in Figs. 5(a) to (c) between grains that were uplifted in Fig. 5(a) and grains that subsequently developed transformation bands in Figs. 5(b)

and (c). This observation establishes a direct connection between the reversible and permanent transformations.

#### IV. Microcracking and Twinning

A martensitic transformation proceeding in thermoelastic equilibrium generates very large residual stresses which oppose further transformation and lead to reverse transformation on unloading. To prevent the reverse transformation, relief of these residual stresses must occur, which in the present systems involves twinning and microcracking.

Microcracking has been observed around transformed  $m\text{-ZrO}_2$  particles in the three types of transformation-toughened  $\text{ZrO}_2$ -containing ceramics of commercial significance. Examples from  $\text{ZrO}_2$ -toughened  $\text{Al}_2\text{O}_3$  (ZTA), Mg-PSZ, and YTZP are shown in Fig. 7. In ZTA and Mg-PSZ, both tangential and radial microcracks can occur (radial and tangential are defined with respect to the  $\text{Al}_2\text{O}_3/\text{ZrO}_2$  or precipitate/matrix interfaces). Tangential microcracking is the more common, with the microcracks appearing to be nucleated by stress concentrations at the intersections of twin or variant boundaries with the  $\text{Al}_2\text{O}_3/\text{ZrO}_2$  or precipitate/matrix interfaces. Observations by several authors<sup>18-20</sup> indicate that tangential microcracking occurs if the thickness of individual twin plates exceeds  $\sim 50$  nm and if no "domains of closure"<sup>20</sup> form. Analysis of the singular stresses associated with the termination of such twin plates<sup>21</sup> indicated that spontaneous initiation of microcracks cannot be explained using linear

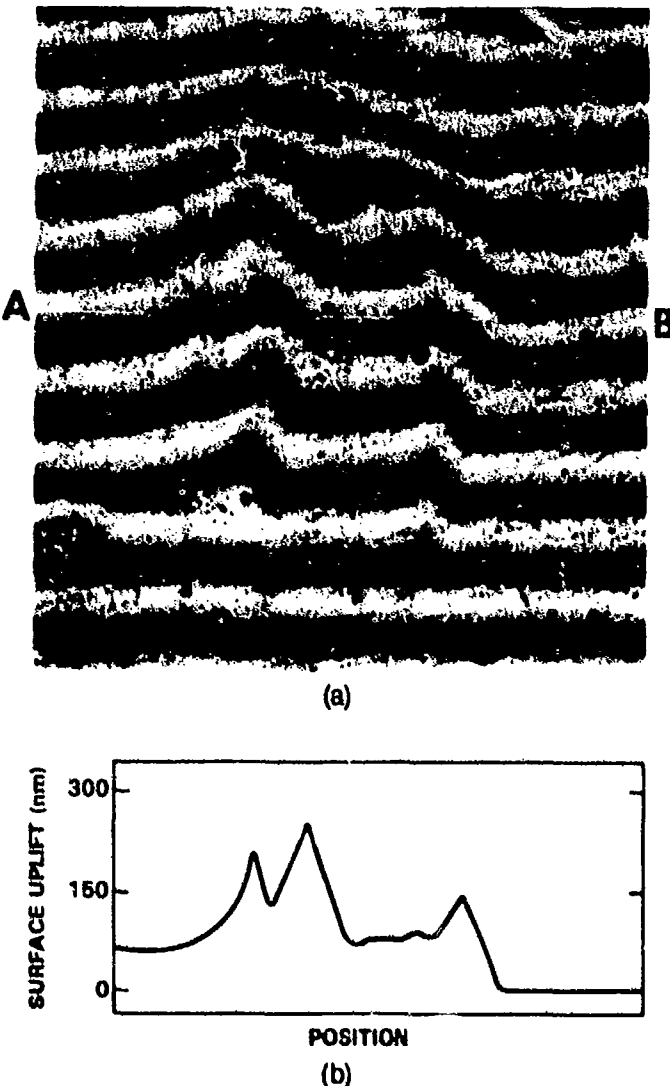


Fig. 6. (a) Optical interference micrograph ( $\lambda = 540$  nm) from area of Fig. 5(f).  
(b) Surface uplift along line A-B in (a).

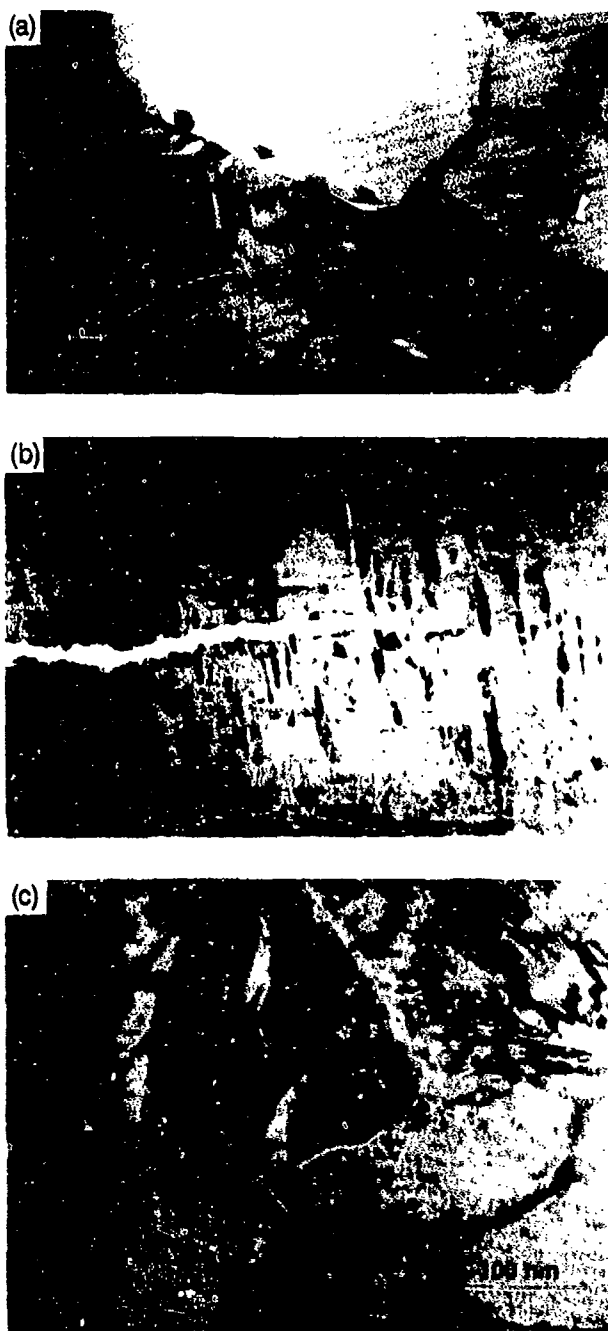


Fig. 7. Microcracking (arrowed features) associated with transformed  $m\text{-ZrO}_2$  particles in (a) ZTA, (b) Mg-PSZ, and (c) Y-TZP.

elasticity. Microcrack nucleation either requires the presence of lattice defects (e.g., dislocations) or involves nonlinear bond displacement in response to the very high stress concentrations.<sup>21</sup> Further nucleation studies are needed to address these possibilities.

In Y-TZP, radial microcracking is observed around transformed grains. In the example of Fig. 7(c), the material had been heat-treated in the two-phase ( $t\text{-ZrO}_2 + c\text{-ZrO}_2$ ) phase field to form some high-solute-content (~10.5 wt%  $\text{Y}_2\text{O}_3$ )  $c\text{-ZrO}_2$  grains in equilibrium with some low-solute-content (~3.5 wt%  $\text{Y}_2\text{O}_3$ )  $t\text{-ZrO}_2$  grains, with  $M_s$  above room temperature. Microcracks are visible around the transformed, low- $\text{Y}_2\text{O}_3$ -content grains. The cracks are evidently caused by transformation-induced stresses, augmented by thermal expansion anisotropy stresses which are enhanced at grain facet corners.

Alternatively, the transformation stresses can be relaxed by the formation of closure twins<sup>20</sup> or by twinning occurring subsequent to the transformation.<sup>22</sup> These have been ob-

served in ZTA, Y-TZP, and Mg-PSZ. An example already cited and identified by high-resolution lattice imaging in a low-solute precipitate in a ternary Mg,Y-PSZ is shown in Fig. 8.

## V. Transformation Reversibility and Size Dependence of $M_s$

The *in situ* transformation experiments (e.g., Fig. 1) clearly demonstrate that stress-induced reversibility in thin foils can arise from partial transformation. The glissile nature of the martensitic interfaces between parent and product ( $t$ - and  $m\text{-ZrO}_2$ ) is one of the hallmarks of martensitic transformations, and this phenomenon is not surprising. These examples further demonstrated that partial reversible transformation did not lead to any transformation debris. It is clear that the strains resulting from partial transformation cause stresses which oppose the applied stresses, leading to a state of *thermoelastic equilibrium*.<sup>2,23</sup> We now discuss the implications of such thermoelastic equilibrium on (i) the size dependence of  $M_s$ , and (ii) the conditions under which permanent irreversible transformation can occur.<sup>††</sup>

### (I) Size Dependence of $M_s$

In certain Mg-PSZ samples, the matrix contains some particles of  $m\text{-ZrO}_2$ , which had transformed during cooling (in the absence of any applied stress), and some particles of  $t\text{-ZrO}_2$  capable of reversible transformation. These observations may imply an intrinsic size dependence. However, rather than a surface energy argument for this size dependence of  $M_s$ , as suggested by Garvie and Swain,<sup>10</sup> we postulate that the difference may involve the effect of particle morphology on the strain energy arising from the transformation.

The elastic strain energy,  $F$ , associated with a transformed inclusion is in general dependent upon its size and shape. For an oblate spheroid (axes  $a = b < c$ ) with unconstrained dilation and shear transformation strains,  $\epsilon^T$  and  $\epsilon_{13}^T$ , the elastic energy in the matrix and inclusion after transformation can be expressed (after Eshelby)<sup>24</sup> as

$$F = [VE(\epsilon^T)^2/9(1 - \nu)] \left[ 1 + \frac{9\gamma(1 - \nu)}{(1 + \nu)} \left( \frac{\epsilon_{13}^T}{\epsilon^T} \right)^2 \right] \quad (1)$$

<sup>††</sup>We use a simplified approach in which an isolated particle in an isotropic matrix is considered. Important considerations such as elastic anisotropy<sup>14</sup> and thermal expansion and elastic modulus mismatch<sup>13,14</sup> between particle and matrix are ignored. While these simplifications prohibit a quantitative treatment, they should not obscure the physics underlying transformation reversibility or the size dependence of  $M_s$ .



Fig. 8. High-resolution TEM image showing closure twins in (Mg,Y) PSZ. (Ref. 13.)

where  $V$  is the inclusion volume,  $E$  Young's modulus (assumed equal for inclusion and matrix),  $\nu$  Poisson's ratio, and  $\gamma$  is a function of the aspect ratio  $a/c$ . The first term in Eq. (1) is the contribution due to the dilation component of the transformation strain, and the second term arises from the shear component. The variation of  $F/F_0$  (the strain energy normalized by the zero shear case) with aspect ratio is shown in Fig. 9 for several values of the ratio  $e_{13}^T/e^T$ ;  $e_{13}^T/e^T = 0$  corresponds to pure dilational transformation (i.e., complete relief of shear strains by twinning), whereas  $e_{13}^T \approx 0.07$ ,  $e \approx 0.04$  is appropriate for the unit cell shape strain. For pure dilation, the strain energy per unit volume is independent of inclusion shape, whereas the contribution due to the shear strain decreases with increasing aspect ratio. Since this elastic strain energy provides the resistance to transformation, and the chemical driving force per unit volume is independent of inclusion shape, the degree of undercooling needed for the transformation to become thermodynamically favorable decreases with increasing aspect ratio. Therefore, this effect could provide a rationale for an apparent size-dependence of  $M$ , if the precipitate aspect ratio increases with precipitate size.

Observations of Farmer and Heuer<sup>23</sup> are consistent with this hypothesis. They found that in Mg-PSZ,  $t$ -ZrO<sub>2</sub> particles with aspect ratios  $\leq 4$  had  $M$ , well below room temperature, those with aspect ratios between 4 and 5 still had  $M$ ,  $<$  room temperature but were sufficiently unstable that they often transformed to an orthorhombic ( $\alpha$ ) form of ZrO<sub>2</sub> during TEM examination,<sup>24,25</sup> and specimens that were heat-treated to encourage some precipitate growth had transformed particles with aspect ratios  $> 5$ .

Of course, this explanation is restricted to precipitation-toughened systems such as Mg-PSZ and is not applicable to the equiaxed TZP's.

## (2) Stabilization of the Stress-Induced Transformation Product

From the *in situ* TEM observations (e.g., Fig. 1), it is clear that reversible transformation in YTZP and Mg,Y-PSZ involves reversible, stress-induced movement of tetragonal/monoclinic interfaces. Stabilization of the monoclinic phase in these experiments was observed only when a lath grew

<sup>23</sup>This diffusionless  $t \rightarrow \alpha$  transformation occurs artificially in TEM thin foil specimens, and is discussed elsewhere.<sup>24,25</sup>

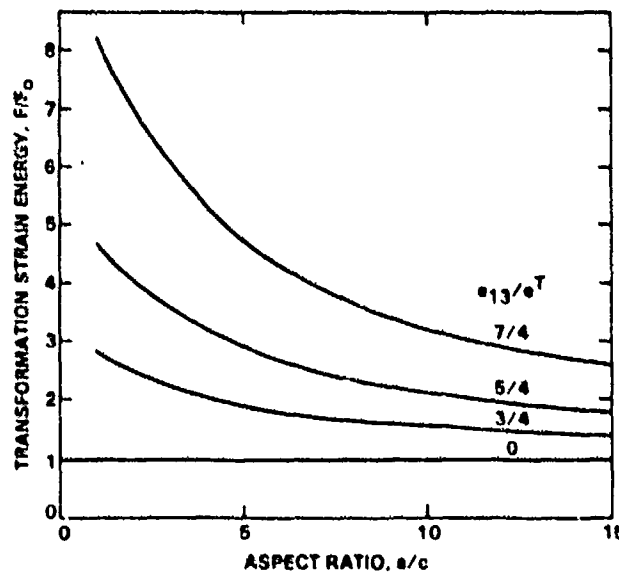


Fig. 9. Plot of elastic strain energy in matrix and inclusion for an oblate spheroidal inclusion with aspect ratio  $a/c$  and unconstrained dilation and shear transformation strains  $e^T$  and  $e_{13}^T$ .

completely across a grain in the YTZP, and when the precipitates in the Mg,Y-PSZ transformed completely. These observations are consistent with the notion that permanent transformation requires microcracking or the formation of closure twins, as discussed in Section IV.

Similar observations of partially transformed precipitates have not been made in Mg-PSZ. Therefore, experiments to date cannot distinguish whether the reversible transformation seen in the X-ray experiments involves partial transformation of all precipitates or complete transformation of some individual precipitates. However, the direct connection between reversible and permanent transformation (Fig. 5) does confirm a previous suggestion<sup>12</sup> that irreversible transformation requires a higher applied stress than does initiation of the forward transformation. Moreover, stabilization of the monoclinic phase in Mg-PSZ is always associated with bands that traverse grains, suggesting that precipitate interactions leading to strain localization are associated with the stabilization event, either as the cause or as a consequence.

If the reversible transformation in Mg-PSZ involves complete transformation of some individual precipitates, the observed continuous increase in surface distortions with increasing applied stress must be due to increasing numbers of transformed precipitates, according to a distribution of transformation stresses. In this case, stabilization would require irreversible, stress-relieving events to reduce the driving force for reverse transformation. This could be achieved by twinning and microcracking, both of which have been found by TEM to be evident at transformed precipitates in thin foils (Section IV). However, a connection between this mechanism of stabilization and the formation of transformation bands is not apparent. A more likely critical event for stabilization is the actual formation of a shear band of transformed precipitates; Fig. 10 shows schematically the basic idea, in that spatially correlated transformation, i.e., a transformation shear band, is necessary for irreversible transformation; the shear band would lead to a reduction in the shear strain energy associated with each precipitate. Formation of the shear band requires interaction between precipitates and would be dictated by the statistical occurrence of a nucleus composed of a critical number of adjacent transformed precipitates. The mechanism does not preclude subsequent twinning and microcrack formation and is therefore consistent with all of the observations.

If, instead, the reversibility involves partial transformation of many or all precipitates, with reversible movement of the tetragonal/monoclinic interface under an applied stress, then stabilization could also occur by microcracking or twinning. However, again, it is not evident why such a mechanism would lead to the bands of transformation observed in the experiments discussed in Section III.

It is useful at this point to consider the thermodynamics of transformation. The total change in free energy,  $\Delta F$ , of the system upon transformation of a volume,  $V$ , can be written<sup>22-25</sup>

$$\Delta F = \Delta G + \Delta U_T + \Delta U_{\omega} + \Delta U, \quad (2)$$

where  $\Delta G$  is the decrease in chemical free energy,  $\Delta U_T$  is the transformation strain energy,  $\Delta U_{\omega}$  is the interaction energy under an applied stress  $\sigma_{\omega}$ , and  $\Delta U$  is the change in surface energy (which may include strain energy associated with twin terminations at the precipitate boundary). The variations of the individual energy terms and the total energy with transformed volume,  $V$ , are shown schematically in Figs. 11(a) and (b). If the shape of the transformed volume remains geometrically similar with increasing size, the first three terms in Eq. (1) are proportional to  $V$ , whereas  $\Delta U$  is proportional to  $V^2$ , and a size effect exists, (i.e., the energy change  $\Delta F$  is negative for volumes larger than a critical value,  $V_c$ , and positive for  $V < V_c$ , Fig. 11(b)). This is the argument used by

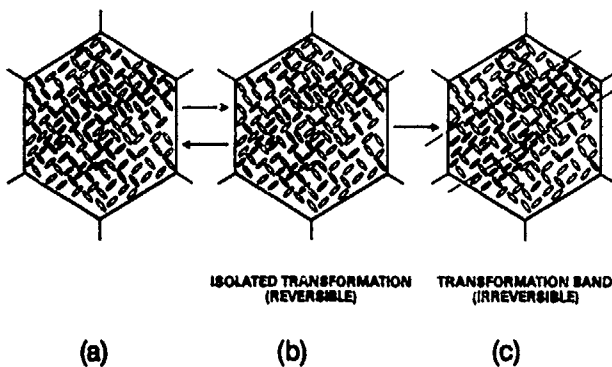


Fig. 10. Schematic diagram illustrating reversible and irreversible transformation of precipitates in Mg-PSZ: (a) zero stress, (b) reversible transformation (isolated precipitates transformed), (c) permanent transformation (autocatalysis causes formation of transformation band).

Garvie and Swain to explain the observed size effect in spontaneous transformation (i.e., in the  $M_s$  temperature). Alternatively, if the particle shape does not remain constant with increasing volume, the size effect is obtained without invoking the surface energy term, because  $\Delta U_T$  increases more slowly with increasing  $V$ , as discussed in Section V(1). The requisite increasing aspect ratio with increasing transformed volume is exhibited by a growing lath, as in Fig. 1, and by partly transformed precipitates, as in Mg-Y-PSZ and Mg-PSZ.

In either case, the total energy change varies with volume and applied stress, as indicated in Fig. 11(b). The energy maxima,  $\Delta F^*$ , in these plots represent a homogeneous nucleation barrier, and the curves predict complete transformation of precipitates with volumes larger than the critical value,  $V_c$  ( $V_c$  decreases with increasing applied stress), provided  $\Delta F^*$  is overcome. This is consistent with the response depicted in Fig. 10. However, stable movement of a transformation interface within a precipitate (Fig. 11(e)) is not consistent with Fig. 11(b). Such a response requires an additional energy term  $\Delta U_i$ , with the form represented in Fig. 11(c), as would arise from an interaction strain energy with a localized stress concentration. In Mg-PSZ, stress concentrations have been observed at very small precipitates of Mg-rich  $\delta$ -phase that form near the surfaces of the tetragonal precipitates.<sup>26</sup> It has also been suggested that stress concentrations occur at the edges of the precipitates because the profile is sharper than that of an oblate spheroid.<sup>27</sup> The total energy change in this case is shown schematically in Fig. 11(d). Spontaneous transformation is predicted for restricted volumes less than  $V_0$  within a particle. Moreover,  $V_0$  increases continuously (and reversibly) with applied stress, as required for stable movement of the transformation interface. At the applied stress  $\sigma_a^*$  represented in Fig. 11(d), the transformation extends indefinitely and irreversibly, thus defining the condition for permanent transformation. This description of the reversible transformation is simply the nucleation stage of transformation. For this mechanism to be consistent with the observations of Section III, it would be necessary for the stress field surrounding the precipitate after unstable transformation to cause transformation at adjacent precipitates, leading to the formation of a transformation band. Such autocatalytic transformation has been observed in *in situ* experiments in Mg-Y-PSZ (Section II), and is postulated to occur also in bulk Mg-PSZ.

## VI. Conclusions

The stress-induced  $t \rightarrow m$  transformation in  $\text{ZrO}_2$  can occur either reversibly or irreversibly. The irreversible transformation requires microcracking or twinning to avoid retransformation on unloading. The thermodynamics of stress-induced transformation require inclusion of an interaction energy term with a localized stress concentration for explanation of

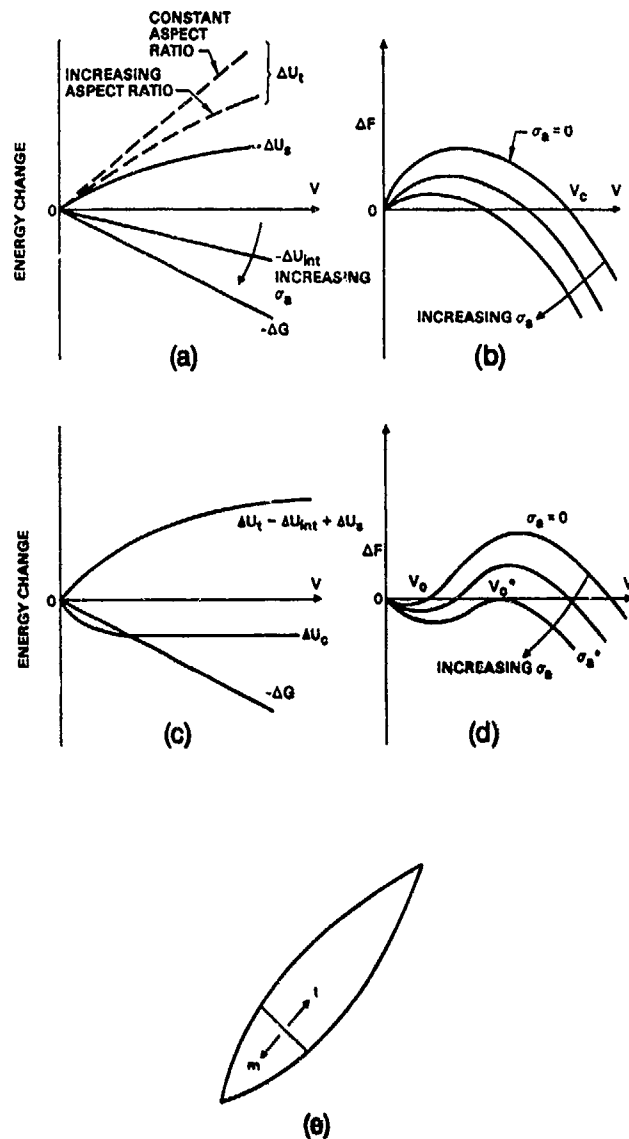


Fig. 11. (a) Variation of energy changes associated with tetragonal-to-monoclinic transformation in a constraining matrix with the volume transformed. (b) Change of total free energy of system with volume transformed. (c, d) Energy changes in the presence of a localized stress concentration. (e) Mechanism of reversible transformation by stress-induced movement of the tetragonal/monoclinic interface within a precipitate.

all experimental observations. We have also suggested that the particle size dependence of  $M_s$  involves variation of particle shape with particle size, rather than an intrinsic size effect due to surface energy arguments.

## APPENDIX

### Relations between Surface Distortions and Transformation Strains

The surface distortions associated with the reversible transformation were of opposite sign in uniaxial tension and compression. This observation is consistent with a simple consideration of the transformation strains, assuming coupling of the strains to the applied shear stress. Each grain in Mg-PSZ contains small, lens-shaped precipitates of tetragonal  $\text{ZrO}_2$  in a solute-rich cubic  $\text{ZrO}_2$  matrix. The tetragonal  $c$  axis of the precipitates is parallel to their smallest dimension. The precipitates are in three orientations, each with the tetragonal  $c$  axis parallel to one of the cube axes. If we assume a single lattice correspondence for the martensitic  $t \rightarrow m$  transformation, (e.g., lattice correspondence C for which the tetragonal

*c* axis becomes the monoclinic *c* axis,<sup>38</sup> then an applied stress along a [110] cube direction (Fig. A1) provides the most favorable orientation for coupling with the shear strains. Then two sets of precipitates are oriented with Schmid factors of 0.5 for (001)/[100] transformation shear, and the third set has zero shear stress on the (001) plane. In this orientation, transformation of equal numbers of the two sets of favorably oriented precipitates to single untwinned variants uniformly throughout the grain causes a total unconstrained strain of the grain

$$\begin{aligned}\epsilon_x &= f(\pm\gamma/2 + e^T/3) \\ \epsilon_y &= f(\mp\gamma/2 + e^T/3) \\ \epsilon_z &= fe^T/3\end{aligned}\quad (A-1)$$

where the upper sign refers to tensile and lower one to compressive loading, *f* is the volume fraction of the grain that transformed, and  $\gamma$  ( $\equiv\epsilon_x^T$ ) and  $e^T$  are the unconstrained shear and dilation strains of the transformation (0.16 and 0.04, respectively).<sup>38,39</sup> The magnitudes of the strains for tension and compression are shown in Fig. A1.

Surface distortions arise from variations in the transverse strains,  $\epsilon_y$  and  $\epsilon_z$ , in adjacent grains. In compressive loading, both of the transverse strains are positive, indicating that the surfaces of transformed grains are always *uplifted*. In tensile loading, on the other hand, transformed grains can be either uplifted or depressed ( $\epsilon_y < 0$ ,  $\epsilon_z > 0$ ). However, the grains which experience the largest surface distortions (i.e., those oriented with  $\epsilon_y$  normal to the specimen surface) are depressed in tensile loading and uplifted in compression, consistent with the observations of Section III. Moreover, equal volume fractions of transformation in tension and compression (as would be implied by a critical shear stress criterion) would cause larger distortions in compression than in tension, as observed.

Relative axial and transverse transformation strains resulting from permanent transformation have been measured directly by Chen and Reyes-Morel<sup>40</sup> using strain gauges in uniaxial compression experiments. From the measured ratio of  $\sim 2/3$  (i.e.,  $2\epsilon_z/(\epsilon_y + \epsilon_z)$ ), the shear strain calculated from Eq. (A-1) is  $\gamma = (5/3)e^T \approx 0.07$ . Therefore as concluded by these workers,  $\sim 50\%$  of the available shear strain appeared in the macroscopic strain measurements in this case.

It is interesting to note that for the volume fraction of reversible transformation in uniaxial tension measured previously using X-ray diffraction ( $\sim 3\%$ ),<sup>12</sup> the magnitudes of the strains in the direction of the applied load ( $\epsilon_x = -0.0018$  in compression and  $\epsilon_x = 0.0027$  in tension) are similar (but of opposite sign) to the applied strain ( $\sim \pm 0.0015$ ). This implies

that in a fixed grips loading, the applied stress would be approximately relaxed by the transformation. Moreover, as shown previously,<sup>12</sup> the corresponding transverse strains  $\epsilon_y \sim 0.002$  over a depth of about one grain diameter ( $\sim 50 \mu\text{m}$ ) would produce surface displacements  $\sim 100 \text{ nm}$ , consistent with observations.

## References

- G. M. Wolten, "Diffusionless Phase Transformation in Zirconia and Hafnia," *J. Am. Ceram. Soc.*, **46** [9] 418-22 (1963).
- E. C. Subbarao, H. S. Maiti, and K. K. Srivastava, "Martensitic Transformation in Zirconia," *Phys. Status Solidi A*, **21**, 9-40 (1974).
- Advances in Ceramics, Vol. 3, *Science and Technology of Zirconia I*. Edited by A. H. Heuer and L. W. Hobbs, American Ceramic Society, Columbus, OH, 1981.
- Advances in Ceramics, Vol. 12, *Science and Technology of Zirconia II*. Edited by N. Claussen, M. Ruhle, and A. H. Heuer. American Ceramic Society, Columbus, OH, 1985.
- Advances in Ceramics, Vol. 24, *Science and Technology of Zirconia III*. Edited by S. Soma, N. Yamamoto, and H. Yanagida. American Ceramic Society, Westerville, OH, 1988.
- A. G. Evans and R. M. Cannon, "Toughening of Brittle Solids by Martensitic Transformations," *Acta Metall.*, **34** [5] 761-800 (1986).
- J.-W. Chen and Y.-H. Chiao, "Theory and Experiment of Martensitic Nucleation of  $\text{ZrO}_2$ -Containing Ceramics and Ferrous Alloys," *Acta Metall.*, **33** [10] 1827-45 (1985).
- J.-W. Chen, Y.-H. Chiao, and K. Tsuzaki, "Statistics of Martensitic Nucleation," *Acta Metall.*, **33** [10] 1847-59 (1985).
- A. H. Heuer and M. Ruhle, "On the Nucleation of the Martensitic Transformation in Zirconia ( $\text{ZrO}_2$ )," *Acta Metall.*, **33** [12] 2101-12 (1985).
- R. C. Garvie and M. V. Swain, "Thermodynamics of the Tetragonal to Monoclinic Phase Transformation in Constrained Zirconia Microcrystals," *J. Mater. Sci.*, **20** 1193-1200 (1985).
- R. C. Garvie and M. F. Goss, "Intrinsic Size Dependence of the Phase Transformation Temperature in Zirconia Microcrystals," *J. Mater. Sci.*, **21** 1253-57 (1986).
- D. B. Marshall and M. R. James, "Reversible Stress-Induced Martensitic Transformation in  $\text{ZrO}_2$ ," *J. Am. Ceram. Soc.*, **69** [3] 215-17 (1986).
- R. R. Lee and A. H. Heuer, "In Situ Martensitic Transformation in a Ternary  $\text{MgO}-\text{Y}_2\text{O}_3-\text{ZrO}_2$  Alloy: I. Transformation in Tetragonal  $\text{ZrO}_2$  Grains," *J. Am. Ceram. Soc.*, **71** [8] 694-700 (1988); II, "Transformation in Tetragonal  $\text{ZrO}_2$  Precipitates," *ibid.*, **71** 701-706.
- M. L. McCartney and M. Ruhle, "In Situ Transmission Electron Microscopy Observations of the Monoclinic to Tetragonal Phase Transformation in Tetragonal  $\text{ZrO}_2$ ," *Acta Metall.*, **37** [7] 1859-64 (1989).
- D. B. Marshall and M. V. Swain, "Reversible Transformation and Elastic Anisotropy in  $\text{Mg}-\text{ZrO}_2$ ," *J. Am. Ceram. Soc.*, **72** [8] 1530-32 (1989).
- D. B. Marshall and M. V. Swain, "Crack Resistance Curves in Magnesia-Partially-Stabilized Zirconia," *J. Am. Ceram. Soc.*, **71** [6] 399-407 (1988).
- D. B. Marshall, "Strength Characteristics of Transformation-Toughened Zirconia," *J. Am. Ceram. Soc.*, **69** [3] 173-80 (1986).
- M. Ruhle, A. Strecker, and D. Waldeich, "In Situ Observations of Stress-Induced Phase Transition in  $\text{ZrO}_2$ -Containing Ceramics," pp. 256-82 in *Advances in Ceramics, Vol. 12, Science and Technology of Zirconia II*. Edited by N. Claussen, M. Ruhle, and A. H. Heuer. American Ceramic Society, Columbus, OH, 1985.
- M. Ruhle, N. Claussen, and A. H. Heuer, "Transformation and Microcrack Toughening as Complementary Processes in  $\text{ZrO}_2$ -Toughened  $\text{Al}_2\text{O}_3$ ," *J. Am. Ceram. Soc.*, **69** [3] 195-97 (1986).
- E. Bischoff and M. Ruhle, "Twin Boundaries in Monoclinic  $\text{ZrO}_2$  Particles Confined in a Mullite Matrix," *J. Am. Ceram. Soc.*, **64** [2] 123-27 (1981).
- Y. Fu, A. G. Evans, and W. M. Kriven, "Microcrack Nucleation in Ceramics Subject to a Phase Transformation," *J. Am. Ceram. Soc.*, **67** [9] 626-30 (1984).
- W. M. Kriven, "Martensitic Theory and Twinning in Composite Zirconia Ceramics," pp. 168-83 in *Advances in Ceramics, Vol. 3, Science and Technology of Zirconia I*. Edited by A. H. Heuer and L. W. Hobbs. American Ceramic Society, Columbus, OH, 1981.
- A. H. Heuer, "Alloy Design in Partially Stabilized  $\text{ZrO}_2$ ," pp. 98-115 in *Advances in Ceramics, Vol. 3, Science and Technology of Zirconia I*. Edited by A. H. Heuer and L. W. Hobbs. American Ceramic Society, Columbus, OH, 1981.
- R. Ingel and D. Lewis III, "Elastic Anisotropy in Zirconia Single Crystals," *J. Am. Ceram. Soc.*, **71** [4] 265-71 (1988).
- J. W. Adams, H. H. Nakamura, R. P. Ingel, and R. W. Rice, "Thermal Expansion Behavior of Single Crystal Zirconia," *J. Am. Ceram. Soc.*, **68** [9] C-228-C-231 (1985).
- R. W. Rice, "Ceramic Matrix Composite Toughening Mechanisms: An Update," *Ceram. Eng. Sci. Proc.*, **6** [7-8] 589-607 (1985).
- J. D. Eshelby, "The Determination of the Elastic Field of an Ellipsoidal Inclusion and Related Problems," *Proc. R. Soc. London, A*, **241**, 376 (1957).
- S. C. Farmer, "Diffusional Decomposition of Magnesia Partially-Stabilized Zirconia," Ph.D. Thesis, Case Western Reserve University, Cleveland, OH, 1987.
- A. H. Heuer, V. Lanteri, S. C. Farmer, R. Chaim, R.-R. Lee, B. W. Kibbel, and R. M. Dickerson, "In Situ Formation of  $\alpha\text{-ZrO}_2$  in TEM Foils,"

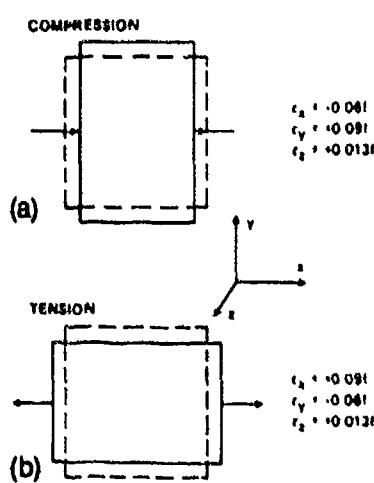


Fig. A1. Schematic diagram indicating transformation strains in tension and compression.

*J. Mater. Sci.*, **24** [1] 124–32 (1989).

<sup>30</sup>H. Bestgen, R. Chaim, and A. H. Heuer, "Thin-Foil Phase Transformations of Tetragonal  $ZrO_2$  in a  $ZrO_2$ –8 wt%  $Y_2O_3$  Alloy," *J. Am. Ceram. Soc.*, **71** [10] 826–31 (1988).

<sup>31</sup>A. H. Heuer, L. H. Schoenlein, and S. Farmer, "New Microstructural Features in Mg-PSZ"; pp. 257–67 in Proceedings of the 12th International Conference "Science of Ceramics," European Ceramic Association, Saint-Vincent, Italy, June, 1983. Edited by P. Vincenzini. Ceramurgica s.r.l., Italy, 1984.

<sup>32</sup>A. G. Evans and A. H. Heuer, "Review—Transformation Toughening in Ceramics: Martensitic Transformation in Crack Tip Stress Fields," *J. Am. Ceram. Soc.*, **63** (5–6) 241–48 (1980).

<sup>33</sup>A. G. Evans, N. Burlingame, M. Drory, and W. M. Kriven, "Martensitic Transformation in Zirconia—Particle Size Effects and Toughening," *Acta Metall.*, **29** 447–56 (1981).

<sup>34</sup>F. F. Lange, "Transformation Toughening—Part I: Size Effects Associated with the Thermodynamics of Constrained Transformation," *J. Mater. Sci.*, **17** [10] 225–34 (1982).

<sup>35</sup>D. B. Marshall, A. G. Evans, and M. Drory, "Transformation Toughening in Ceramics"; pp. 289–307 in *Fracture Mechanics of Ceramics*, Vol. 6. Edited by R. C. Bradt, A. G. Evans, D. P. H. Hasselman, and F. F. Lange. Plenum Press, New York, 1983.

<sup>36</sup>R. H. J. Hannink, "Microstructural Development of Sub-Eutectoid Aged  $MgO$ – $ZrO_2$  Alloys," *J. Mater. Sci.*, **18**, 457–65 (1983).

<sup>37</sup>M. Ruhle and W. M. Kriven, "Analysis of Strain Around Tetragonal and Monoclinic Zirconia Inclusion"; pp. 1569–73 in *Solid → Solid Phase Transformation*. Edited by H. A. Aaronson, D. E. Laughlin, R. F. Sekula, and C. M. Waymar. Metallurgical Society of AIME, Warrendale, PA, 1982.

<sup>38</sup>W. M. Kriven, W. L. Fraser, and S. W. Kennedy, "The Martensite Crystallography of Tetragonal Zirconia"; pp. 82–97 in *Advances in Ceramics*, Vol. 3, *Science and Technology of Zirconia I*. Edited by A. H. Heuer and L. W. Hobbs. American Ceramic Society, Columbus, OH, 1981.

<sup>39</sup>B. C. Muddle and R. H. J. Hannink, "Crystallography of the Tetragonal to Monoclinic Transformation in  $MgO$ -Partially-Stabilized Zirconia," *J. Am. Ceram. Soc.*, **69** [7] 547–55 (1986).

<sup>40</sup>I.-W. Chen and P. E. Reyes-Morel, "Implications of Transformation Plasticity in  $ZrO_2$ -Containing Ceramics: I, Shear and Dilation Effects," *J. Am. Ceram. Soc.*, **69** [3] 181–89 (1986). □



Rockwell International  
Science Center

SC71002.FR

### 6.3 REVERSIBLE TRANSFORMATION AND ELASTIC ANISOTROPY IN Mg-ZrO<sub>2</sub>

published in J. Am. Ceram. Soc.

## Reversible Transformation and Elastic Anisotropy in Mg-ZrO<sub>2</sub>

David B. Marshall\*

Rockwell International Science Center,  
Thousand Oaks, California 91360

Michael V. Swain\*

Division of Materials Science,  
Commonwealth Scientific and Industrial Research Organization, Clayton, Victoria 3168, Australia

Commonwealth Scientific and Industrial Research Organization, Clayton, Victoria 3168, Australia

**Mechanical loading of polycrystalline ZrO<sub>2</sub> ceramics causes reversible, out-of-plane distortions at free surfaces that are parallel to the direction of applied stress. These distortions have been measured using optical interference microscopy, and the separate contributions due to elastic anisotropy and reversible martensitic transformation have been identified. [Key words: zirconia, magnesium, mechanical properties, phase transformations, stress.]**

SEVERAL studies have shown that the martensitic transformation in ZrO<sub>2</sub>, between tetragonal and monoclinic phases,

can occur reversibly with stress under certain conditions.<sup>1-4</sup> This observation is important for understanding the initiation condition for the transformation, which in turn determines the extent of the transformation zone around a crack and hence the degree of toughening.

The first indication of reversibility came from observations, by Nomarski interference, of surface distortions caused by varying amounts of transformation in adjacent grains. These measurements, from the polished surface of polycrystalline Mg-ZrO<sub>2</sub>, were confirmed by *in situ* X-ray diffraction.<sup>1</sup> *In situ* TEM observations have also revealed reversible transformations in other ZrO<sub>2</sub> alloys.<sup>2-4</sup> Although the surface distortion measurement remains the most sensitive of these methods for detecting small amounts of transformation, it is complicated by the fact that distortion of the surface under applied load can also be caused by elastic anisotropy. In this paper, measurements of the separate contributions to surface distortions in Mg-PSZ from elastic anisotropy and reversible transformation are presented.

### EXPERIMENTAL OBSERVATIONS

Surface distortions were compared in one transformation-toughened 9 mol% MgO-ZrO<sub>2</sub> material\* and four related, nontoughened materials: (1) a fully stabilized cubic Mg-ZrO<sub>2</sub> (14 mol% MgO); (2) 10.9 mol% MgO-ZrO<sub>2</sub> which contained tetragonal precipitates that were not sufficiently transformable to cause significant transformation toughening; (3) an overaged 9 mol% MgO-ZrO<sub>2</sub> in which all precipitates were of monoclinic phase; and (4) the toughened 9 mol% MgO-ZrO<sub>2</sub> which had undergone a cooling cycle in liquid nitrogen to transform most tetragonal precipitates to orthorhombic phase.<sup>5</sup> Of the nontoughened materials, the 9 mol% MgO-ZrO<sub>2</sub> cooled in liquid nitrogen possessed the highest strength (500 MPa, compared with approximately 250 MPa for the others) and therefore allowed comparisons with the toughened material over the widest range of stresses. It was also closest to having a microstructure identical to that of the toughened material, but with the transformability switched off.

Beams of each material (~50×3×3 mm) were loaded in bending using a fix-

A. O. Evans — contributing editor

Manuscript No. 198693. Received January 6, 1989. Approved March 10, 1989.

Supported by the Office of Scientific Research, U.S. Air Force, under Contract No. F49620-85-C-0143.

\*Member, American Ceramic Society.

\*MS grade Mg-PSZ, Nilco Ceramics (USA), Inc., Elmhurst, IL.

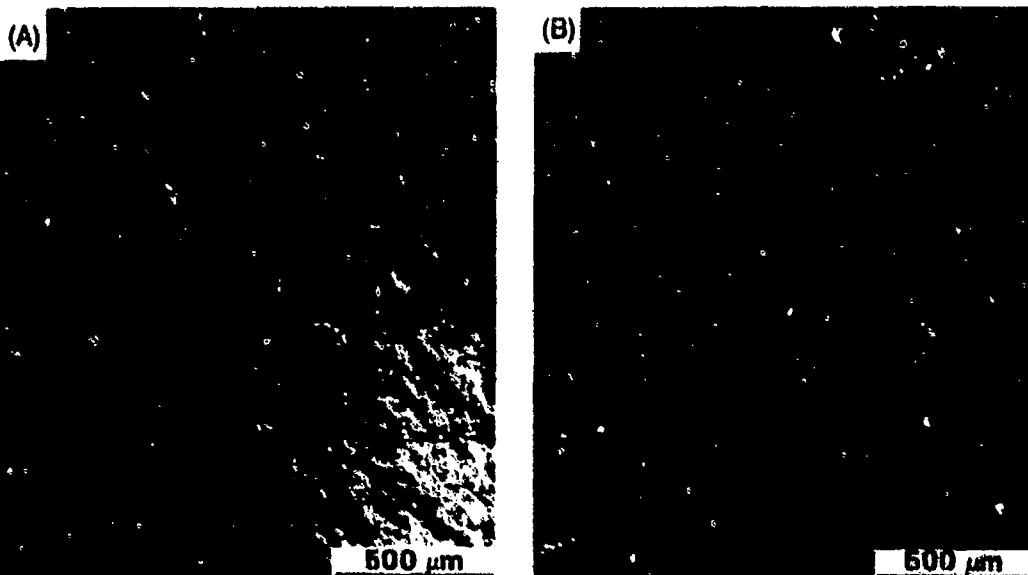


Fig. 1. Optical micrographs (Nomarski interference), comparing out-of-plane surface distortions in (A) transformation-toughened Mg-PSZ and (B) nontoughened Mg-PSZ. Applied load horizontal, average strain 0.0015.

ture on the stage of an optical microscope, while being viewed either with Nomarski interference or with conventional interference using monochromatic light. While Nomarski interference is the more convenient and possibly the more sensitive of these two methods of observing surface distortions, it is only qualitative. On the other hand, quantitative measurements of surface displacements are obtained from the conventional interference measurements. In the present experiments comparisons of the different materials were made using micrographs obtained with identical measurements settings and film/print processing. Applied stresses were monitored in all cases, using strain gages attached to the surfaces of the beams.

The tensile surfaces of all five materials exhibited reversible distortions during loading. Observations in the fully stabilized, overaged, and 10.9 mol% MgO materials were limited (by their strengths) to applied stresses below approximately 200 MPa (i.e., strain <0.001). Over this range of stresses the magnitudes of the surface distortions were indistinguishable in all of the materials. However, at larger applied stresses the magnitudes of the surface distortions were higher in the toughened material than in the material that had been cooled in liquid N<sub>2</sub>. Nomarski interference micrographs from these two materials are compared in Fig. 1 and measured surface displacements from conventional interference micrographs are shown in Fig. 2. (The relative surface displacements in Fig. 2 represent measurements of the largest height difference within subareas approximately 200×200 μm on the tensile surfaces.) These results suggest that, at stresses below ~200 MPa, the surface distortions result from elastic anisotropy, but that at higher stresses in the toughened material, transformation strains and elastic anisotropy contribute about equally to the surface distortions.

In situ observation during continuous loading of the toughened material indicated that the same grains were either uplifted or depressed over the entire range of strains in Fig. 2; i.e., the magnitudes of the surface displacements increased monotonically with load everywhere. This indicates that the crystallographic orientations of distortions due to elastic anisotropy and transformation strains are similar.

## DISCUSSION

### Elastic Anisotropy

An applied stress parallel to the surface of a polycrystalline body causes contraction normal to the surface by an amount which, because of elastic anisotropy, is dependent upon the grain orientation. Therefore, the surface must become distorted where grains of different orientations meet. A detailed calculation of the magnitude of these distortions would be complex because all components of local stress and strain are nonuniform and dependent upon

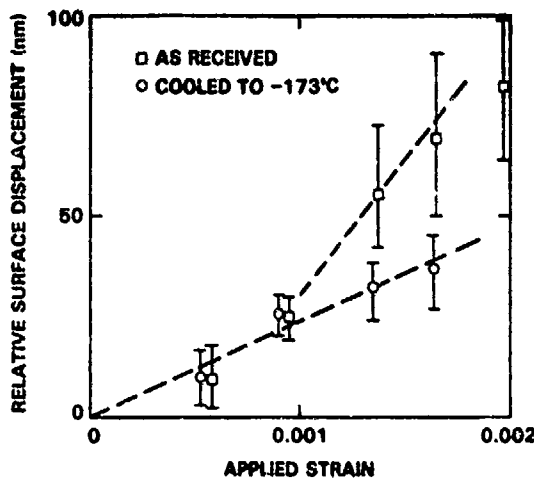


Fig. 2. Relative surface displacements, measured by optical interference microscopy, for toughened (as-received) and non-toughened (cooled in liquid N<sub>2</sub>) Mg-PSZ.

relative orientations of all adjacent grains. However, a rough estimate of the maximum distortion can be obtained by calculating the maximum and minimum Poisson ratios assuming uniform strain parallel to the applied stress.

For cubic ZrO<sub>3</sub> with elastic stiffness constants  $C_{11}=417$  GPa,  $C_{12}=82$  GPa, and  $C_{44}=47$  GPa,<sup>4,7</sup> Young's moduli and maximum and minimum Poisson ratios for applied stresses in the directions [100], [110], and [111] are listed in Table I. Qualitatively, the elastic response of this material is similar to that of a structure composed of rods along the edges of a cube and hinged at the corners; it is stiffest when loaded along [100], soft when loaded along [111] and [110], and the transverse contraction (for tensile load) when loaded along [110] is large along [110] and very small along [001]. Therefore, the largest difference in contraction should be between grains with [110] parallel to the applied stress and [110] or [001] normal to the surface. For strain of 0.0015 parallel to [110], the difference in contraction (unconstrained) of the two grains would be  $\Delta e=0.0007$ . The grain size of this material is ~50 μm. Therefore, the difference in surface displacements would be ~350 Å (~35 nm), consistent with the measurements in Fig. 2 for the material that had been cooled in liquid N<sub>2</sub>.

### Surface Distortions and Transformation Strains

In the spirit of the approximate calcu-

lations of the previous section, an upper bound can be estimated for the relative surface displacements due to transformation, assuming coupling between the transformation strain and the applied shear stress. Each grain in Mg-PSZ contains small, lens-shaped precipitates of tetragonal ZrO<sub>3</sub> in a solute-rich cubic matrix, with the tetragonal *c* axis of the precipitates parallel to their smallest dimension. The precipitates are in three orientations, each with the tetragonal *c* axis parallel to one of the cubic axes. If a single-lattice correspondence for the martensitic  $\text{t} \rightarrow \text{m}$  transformation is assumed (e.g., lattice correspondence C for which the tetragonal *c* axis becomes the monoclinic *c* axis),<sup>8</sup> then applied stress along a [110] direction provides the most favorable orientation for coupling with the shear strains. Then two sets of precipitates are oriented with Schmidt factors of 0.5 for (001)/[100] transformation shear, and the third set have zero shear stress on the (001) plane. In this orientation, transformation of equal numbers of the two sets of favorably oriented precipitates uniformly throughout the grain causes total unconstrained strains of the grain.

$$c_z = f(\epsilon_x^2/3 + \gamma/2) \quad (1a)$$

$$c_y = f(\epsilon_x^2/3 - \gamma/2) \quad (1b)$$

$$c_x = \epsilon_x/3 \quad (1c)$$

where *x*, *y*, and *z* correspond to [110], [110], and [001], *f* is the volume fraction

Table I. Young's Modulus and Poisson's Ratio of Cubic ZrO<sub>3</sub>

Stress direction	<i>E</i> (GPa)	<i>v</i>	
		Max	Min
[100]	390	0.16	
[110]	156	0.66 (110)	0.08 (001)
[111]	130	0.39	

of transformed precipitates, and  $\gamma$  and  $\epsilon^T$  are the unconstrained shear and dilation strains of the transformation. The dilation strain is fixed at  $\sim 0.04$ , whereas the shear strain, which can be partly relieved by twinning, could take any value between zero and that of a single untwinned variant (0.15). Therefore, the largest depression of the surface occurs at grains with untwinned precipitates and oriented with  $[110]$  parallel to the applied stress and  $(\bar{1}\bar{1}0)$  normal to the surface. This is the same orientation as for the largest depression from elastic anisotropy, and is therefore consistent with the observations of the previous section. An upper bound for the magnitude of the surface distortion (unconstrained) due to transformation in these grains is given by the difference of  $\epsilon_x$  and  $\epsilon_y$  in Eq. (1): with  $f=0.03$  at applied strain 0.0015, as measured previously using X-ray diffraction,<sup>1</sup> this gives  $\Delta\epsilon=0.002$ . Therefore, for a grain size of 50  $\mu\text{m}$  the difference in surface displacement is  $\approx 1000 \text{ \AA}$  ( $\approx 100 \text{ nm}$ ). This is adequate to account for the observed displacements due to transformation (Fig. 2).

## CONCLUSIONS

Mechanical load applied parallel to the free surface of polycrystalline  $\text{Mg-ZrO}_2$  ceramics causes reversible distortions of the surface. In nontoughened materials, and in transformation-toughened material at low loads ( $\le 200 \text{ MPa}$ ), the distortions are a result of elastic anisotropy and relative grain misorientations. At higher loads in the transformation-toughened material, reversible martensitic transformation causes superimposed displacements with a similar magnitude and grain orientation dependence as the displacement due to elastic anisotropy. Therefore, although in situ observation of these distortions is a convenient method for detecting reversible transformation, care is needed to separate the influence of elastic anisotropy when interpreting the results. Furthermore, the observations of surface distortions due to elastic anisotropy serve to illustrate the nonuniformity of local stresses in polycrystalline bodies, even those with cubic structure, and the potential role of these local stresses in initiation of strength-limiting cracks.

## REFERENCES

- D. B. Marshall and M. R. James, "Reversible Stress-Induced Martensitic Transformation in  $\text{ZrO}_2$ ," *J. Am. Ceram. Soc.*, **69** [3] 215-17 (1986).
- M. L. McCartney and M. Rühle, "In Situ Transmission Electron Microscopy Observations of the Monoclinic-to-Tetragonal Phase Transformation in Tetragonal  $\text{ZrO}_2$ "; to be published in *Acta Metall.*
- R. R. Lee and A. H. Heuer, "In Situ Martensitic Transformation in a Ternary  $\text{MgO-Y}_2\text{O}_3-\text{ZrO}_2$  Alloy: I. Transformation in Tetragonal  $\text{ZrO}_2$  Grains," *J. Am. Ceram. Soc.*, **71** [8] 694-700 (1988).
- R. R. Lee and A. H. Heuer, "In Situ Martensitic Transformation in a Ternary  $\text{MgO-Y}_2\text{O}_3-\text{ZrO}_2$  Al": II. Transformation in Tetragonal  $\text{ZrO}_2$  Precipitates," *J. Am. Ceram. Soc.*, **71** [8] 701-706 (1988).
- D. B. Marshall, M. R. James, and J. R. Porter, "Structural and Mechanical Property Changes in Toughened Magnesia-Partially-Stabilized Zirconia at Low Temperatures," *J. Am. Ceram. Soc.*, **72** [2] 218-27 (1989).
- A. H. Heuer and M. Rühle, "On the Nucleation of the Martensitic Transformation in Zirconia ( $\text{ZrO}_2$ )," *Acta Metall.*, **33** [12] 2101-12 (1985).
- R. P. Ingel and D. Lewis III, "Elastic Anisotropy in  $\text{ZrO}_2$  Single Crystals," *J. Am. Ceram. Soc.*, **71** [4] 265-71 (1988).
- W. M. Kriven, W. L. Fraser, and S. W. Kennedy, "The Martensitic Crystallography of Tetragonal Zirconia," pp. 82-97 in *Advances in Ceramics, Vol. 3, Science and Technology of Zirconia*, Edited by A. H. Heuer and L. W. Hobbs, American Ceramic Society, Columbus, OH, 1981. □

SC71002.FR

**6.4 STRUCTURAL AND MECHANICAL PROPERTY CHANGES IN  
TOUGHENED MAGNESIA-PARTIALLY-STABILIZED ZIRCONIA AT  
LOW TEMPERATURES**

published in J. Am. Ceram. Soc.

Reprinted from the *Journal of the American Ceramic Society*, Vol. 72, No. 2, February 1989  
Copyright © 1989 by The American Ceramic Society, Inc.

Journal

*J. Am. Ceram. Soc.*, 72 [2] 218-27 (1989)

## Structural and Mechanical Property Changes in Toughened Magnesia-Partially-Stabilized Zirconia at Low Temperatures

David B. Marshall,\* Michael R. James, and John R. Porter\*

Rockwell International Science Center, Thousand Oaks, California 91360

The mechanical properties of high-toughness magnesia-partially-stabilized zirconia were found to be dramatically altered by a single cooling cycle between room temperature and  $-196^{\circ}\text{C}$ . Raman spectroscopy and X-ray diffraction were used to correlate the changes in mechanical properties with structural changes that occur at temperatures below  $\sim -100^{\circ}\text{C}$ . Most of the tetragonal precipitates that are responsible for toughening transformed to an orthorhombic phase with unit-cell volume intermediate between those of the tetragonal and monoclinic phases. The orthorhombic phase was stable with heating to  $300^{\circ}\text{C}$ , but it transformed back to the tetragonal structure when heated to  $400^{\circ}\text{C}$ . Surprisingly, the orthorhombic phase was not readily transformable by stress, with the consequence that, after the cooling cycle, most of the high-toughness properties of the original tetragonal-containing material were lost. [Key words: mechanical properties, zirconia, magnesia, phase transformations, heat treatment.]

### I. Introduction

ZIRCONIA-CONTAINING ceramics can be toughened dramatically by the martensitic tetragonal-monoclinic transformation in localized zones around cracks.<sup>1-11</sup> However, high toughening requires a very narrow range of microstructures in which  $\text{ZrO}_2$  grains or precipitates are on the verge of spontaneous transformation. Since the transformability of constrained  $\text{ZrO}_2$  particles is sensitive to the degree of undercooling from the unconstrained  $M_s$  (martensitic start) temperature, both the degree of toughening and the stability of the microstructure are expected to be very sensitive to temperature changes.

The highest-toughness  $\text{ZrO}_2$  ceramics are from the magnesia-partially-stabilized zirconia system (Mg-PSZ).<sup>9-15</sup> In optimally aged materials, with toughness up to  $18 \text{ MPa} \cdot \text{m}^{1/2}$ , the tetragonal precipitates are so close to spontaneous transformation at room temperature that a fraction do transform during cooling, and others begin to transform under applied tensile stresses as low as  $300 \text{ MPa}$ .<sup>10,11</sup> The purpose of this paper is to examine whether cooling below room temperature causes further transformation of these precipitates, and thereby a loss of toughening at cryogenic temperatures, or even more importantly, degradation of room-temperature mechanical properties after a single cooling cycle. Swain<sup>16,17</sup> has shown previously that the fracture toughness of such materials is reduced at temperatures below about  $-100^{\circ}\text{C}$  and that thermal expansion measurements indicate a volume increase in the temperature range  $-80^{\circ}$  to  $-100^{\circ}\text{C}$ . Moreover, the tetragonal-monoclinic transformation after cooling in liquid nitrogen has been inferred from X-ray measurements in several Mg-PSZ ceramics,<sup>18</sup> although the measured phase differences in that work approached the limits of experimental error. We will show that cooling does indeed cause a transformation, but that the transformation product is not the monoclinic structure. Instead, it is an orthorhombic phase of  $\text{ZrO}_2$ .

### II. Experimental Procedure

The material of primary interest in this study is a high-toughness, 9-mol-%-MgO-partially-stabilized zirconia (Mg-PSZ), which was fabricated by sintering at  $1700^{\circ}\text{C}$ , with controlled cooling to room temperature, followed by subeutectoid heat treatment at  $1100^{\circ}\text{C}$ . Specimens that had been given several different heat treatments to produce various degrees of transformation toughening were examined (Table I). These materials contained lens-shaped, MgO-depleted precipitates,  $\sim 200 \text{ nm}$  in diameter, in a fully stabilized (MgO-rich) cubic matrix. In the high-toughness material, most of the precipitates were of the tetragonal structure, but some ( $\sim 13 \text{ vol\%}$ ) had transformed to the monoclinic phase

Manuscript No. 499161. Received May 3, 1988, approved August 5, 1988.  
Supported by the Air Force Office of Scientific Research under Contract No. F49620-85-C-0333.

\*Member, American Ceramic Society.

Table I. Materials Tested

Material	Heat treatment		Steady-state toughness (MPa · m <sup>1/2</sup> )	Apparent flexural strength (MPa) <sup>2</sup>	True strength (MPa)
	1100°C	1400°C			
High toughness*	24 h		13	620	400
High toughness <sup>1</sup>	By manufacturer <sup>1</sup>		13	620	400
Intermediate toughness*	7 h		10	700	600
Low toughness*	0		6	540	540
Overaged <sup>1</sup>		48 h	3		

\*Specimens supplied by M. V. Swain, Nilcra Ceramics (USA), Inc., St. Charles, IL. <sup>1</sup>Calculated from elastic beam theory; larger than true strength for material with nonlinear stress-strain response in tensile loading (Ref. 11).

during cooling. Some of this material was overaged by heating to 1400°C for 2 d, resulting in transformation of all precipitates to monoclinic structure upon cooling. Two other Mg-ZrO<sub>2</sub> ceramics, with different compositions and heat treatments, were also tested for comparison: 14 mol% MgO-ZrO<sub>2</sub> which was all stabilized cubic phase, and 11 mol% MgO-PSZ which contained tetragonal precipitates that cannot be transformed to monoclinic phase by applied stress.

The room-temperature mechanical properties of the 9 mol% MgO materials were reported in detail elsewhere.<sup>19</sup> In tensile loading of specimens of the high-toughness material with polished surfaces, the stress-strain response was nonlinear because of stress-induced transformation and microcracking at stresses above ~300 MPa. The sequence of damage development is shown in Fig. 1. Stresses below 300 MPa caused reversible surface roughening, which was correlated with tetragonal-monoclinic transformation, whereas higher stresses resulted in permanent transformation and the formation and stable growth of microcracks to lengths up to 1 mm. The stable crack growth was attributed to a resistance curve (*R* curve) that increased with crack extension. The steady-state fracture toughness was ~13 MPa · m<sup>1/2</sup>, and transformation zones ~100 μm in width around cracks were readily observed because of surface uplift due to transformation strains (Fig. 1(B)). The material with 9-h heat treatment had a steady-state fracture toughness of ~9 MPa · m<sup>1/2</sup> and also exhibited nonlinear stress-strain response, *R*-curve behavior, and transformation zones around cracks, but all less extensive than in the 24-h heat-treated material. The material that was not heat-treated at 1100°C did not show nonlinear load-deflection response or stable microcrack growth during failure testing, but a small transformation zone was observed around the crack that caused failure. Transformation zones were not detected around cracks in the 11 and 14 mol% MgO-ZrO<sub>2</sub> materials.

Structural changes occurring during cooling to ~196°C were monitored *in situ* for some materials by optical microscopy and

Raman spectroscopy, using a small cooling stage with a quartz window. Optical microscopy was done with both Nomarski interference and conventional interference methods to allow detection and measurement of surface distortions produced by transformation strains. Raman spectroscopy was done using a microprobe with a spot size of ~20 μm when the specimen was in the cooling stage and ~1 to 2 μm otherwise.

X-ray diffraction was done at room temperature, using Cu or Cr radiation and an energy-dispersive detector. Step scanning was used with counting times ~20 h over the range  $2\theta = 10^\circ$  to  $90^\circ$  and with 5000 counts accumulated at each 0.05° step. Diffraction peak positions and peak half-breadths were obtained by fitting the profiles to Pearson VII functions after background subtraction. Angles were calibrated using a silicon standard.

### III. Results

#### (1) Optical Observations

The polished surface of a peak-toughness Mg-PSZ after cooling in liquid N<sub>2</sub> is shown in Fig. 2. Surface distortions similar to those produced by stress-induced tetragonal-monoclinic transformation (Fig. 1) are evident in the Nomarski interference micrograph. Quantitative measurements using conventional interference microscopy indicated that the amplitude of the distortion (~50 nm) was larger than that due to the reversible transformation at low applied stresses (~20 nm) (Fig. 1(A)), but smaller than that due to permanent transformation (~100 to 200 nm) (Fig. 1(B)).

The stress-induced transformation caused relatively uniform uplift of areas that span several grains (presumably, those grains most favorably oriented relative to the applied stress), whereas cooling to liquid N<sub>2</sub> caused general uplift of most of the surface except for isolated areas ~20 μm in diameter. The areas of surface depression were found to correspond to regions, usually near the centers of grains, that contained comparatively large precipitates which transformed to monoclinic structure during cooling

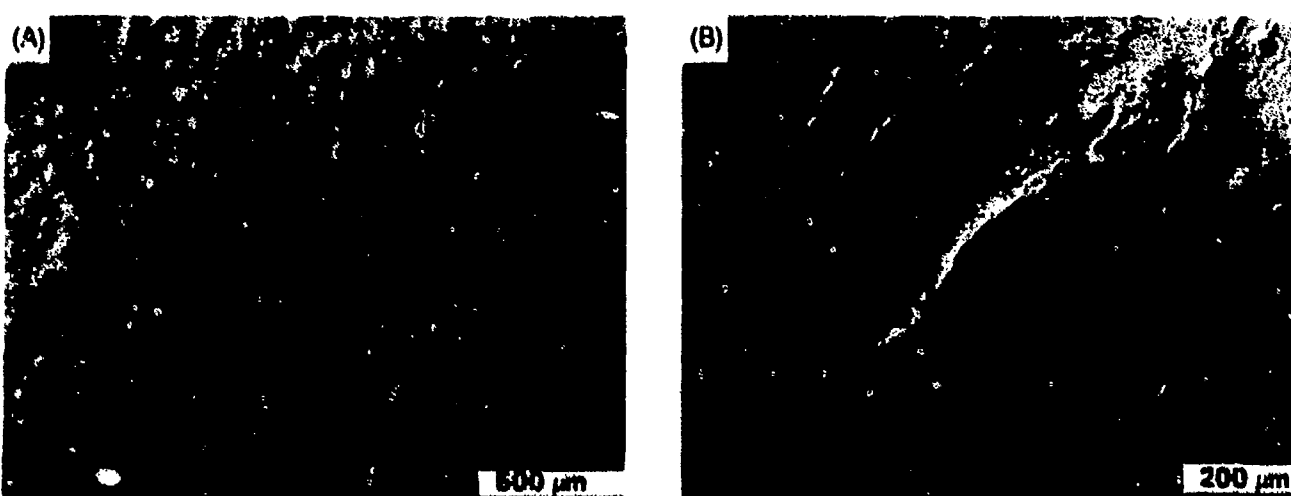


Fig. 1. Nomarski interference micrographs of polished surface of high-toughness Mg-PSZ: (A) during loading with tensile stress 300 MPa; (B) stress increased to 380 MPa.

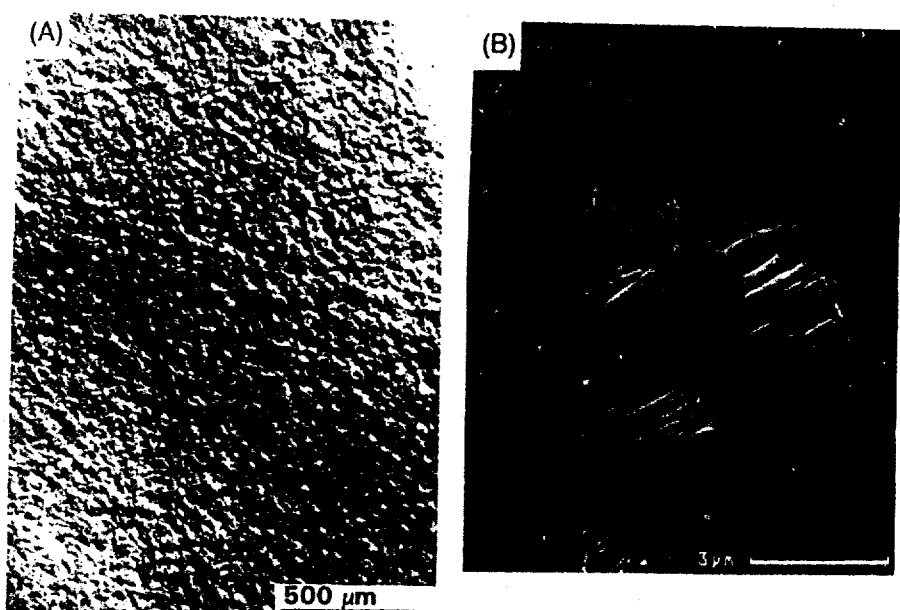


Fig. 2. (A) Polished surface of high-toughness Mg-PSZ after cooling to  $-196^{\circ}\text{C}$ ; Nomarski interference micrograph. (B) Scanning electron micrograph showing large precipitates within a region of surface depression in (A).

(Fig. 2(B)). Formation of these large precipitate regions has been discussed by Hughan and Hannink.<sup>20</sup>

During *in situ* experiments using the cooling stage, the distortions in Fig. 2 were found to develop over the temperature range  $-80^{\circ}$  to  $-120^{\circ}\text{C}$  and then remain unchanged as the temperature was lowered to  $-196^{\circ}\text{C}$  and increased to  $+96^{\circ}\text{C}$ . Subsequent heating in a separate furnace for 10 min at  $300^{\circ}\text{C}$  also left the surface distortions unaltered. However, after 3 min at  $400^{\circ}\text{C}$ , most of the distortion disappeared. The temperature range over which surface uplift developed coincides with the temperature range over which Swain<sup>17</sup> previously observed a volume increase from thermal expansion measurements. The persistence of the volume expansion upon heating to room temperature is also consistent with Swain's results.

Similar response was observed in the intermediate-toughness Mg-PSZ, but the surface distortions appeared at lower tempera-

tures ( $-120^{\circ}$  to  $-160^{\circ}\text{C}$ ), again consistent with Swain's thermal expansion measurements. Comparison of polished surfaces of the other materials in Table I did not reveal any surface distortions.

### (2) Raman Spectroscopy

Raman spectra from the high-toughness Mg-PSZ before and after immersion in liquid  $\text{N}_2$  are shown in Fig. 3. Also shown for comparison are spectra from 14% Mg-ZrO<sub>2</sub> (cubic structure) and the overaged PSZ (cubic matrix with monoclinic precipitates). The spectrum obtained after cooling to  $-196^{\circ}\text{C}$  contains at least 11 peaks in the range 100 to  $700\text{ cm}^{-1}$  that were not present before cooling, and the original tetragonal peaks are all present, but greatly reduced in intensity. Two of the new peaks ( $338$  and  $480\text{ cm}^{-1}$ ) coincide with peaks of the monoclinic phase (Fig. 3(C)), but the remaining nine do not belong to any of the tetragonal, monoclinic, or cubic phases. Moreover, there are several strong peaks in the monoclinic spectrum of Fig. 3(C) that do not appear in Fig. 3(B) (e.g.,  $177$ ,  $384\text{ cm}^{-1}$ ). Therefore, cooling to  $-190^{\circ}\text{C}$  caused transformation of most of the tetragonal precipitates to a phase that does not have the monoclinic structure.

Results from *in situ* Raman measurements during cooling of the high-toughness Mg-PSZ are shown in Fig. 4. The transformation occurred over the temperature range  $-80^{\circ}$  to  $-120^{\circ}\text{C}$ , corresponding to the temperature range over which volume expansions and surface roughening were observed. Moreover, after the heat treatment at  $400^{\circ}\text{C}$ , when the surface distortions disappeared, the Raman spectrum returned to the same as before cooling (Fig. 5). In *in situ* measurements from the intermediate-toughness Mg-PSZ yielded similar results, with the transformation occurring over the range  $-120^{\circ}$  to  $-160^{\circ}\text{C}$ , again consistent with the surface roughening and thermal expansion results. Raman measurements from the other materials in Table I did not reveal any changes in the spectra before and after immersion in liquid  $\text{N}_2$ .

### (3) X-ray Measurements

X-ray diffraction patterns obtained at room temperature for the high-toughness material before and after cooling in liquid  $\text{N}_2$  are compared in Fig. 6. The specimen was located in the same position and orientation for both X-ray scans. Before cooling, the material contained  $\sim 13\%$  monoclinic precipitates,  $\sim 30\%$  tetragonal precipitates, and the remainder cubic matrix. After cooling, there was no change in the intensities of the monoclinic peaks (e.g.,  $(1\bar{1}\bar{1})$  and  $(1\bar{1}\bar{1})$ ) and very little change in the superimposed cubic-tetragonal peaks. However, the tetragonal peaks that were separated from the cubic peaks (i.e.,  $(002)$ ,  $(02\bar{2})$ ,  $(11\bar{3})$ , and  $(004)$ ) almost disappeared, and many new peaks appeared (shaded in Fig. 6 and listed in Table II).

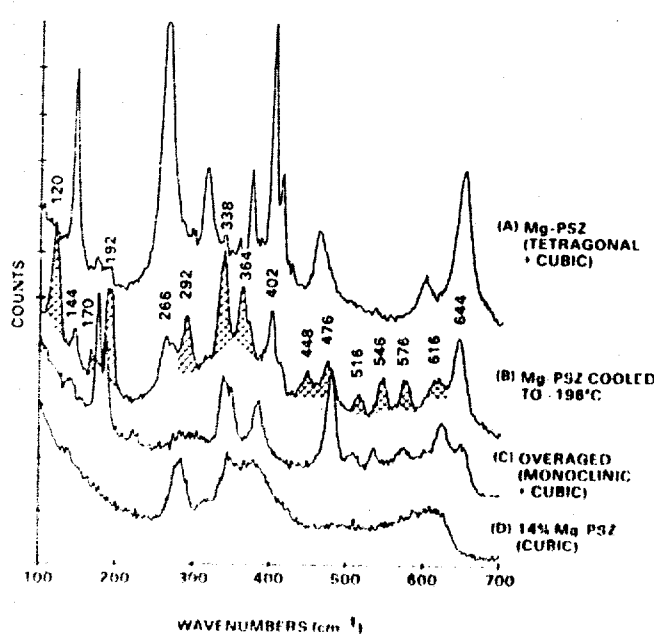


Fig. 3. Raman spectra (from temperature) from high-toughness Mg-PSZ (polished surface) before and after cooling to  $-196^{\circ}\text{C}$ , overaged Mg-PSZ (monoclinic and cubic phases), and 14% Mg-PSZ (fully stabilized cubic phase).

All of the new reflections could be accounted for by indexing a tetragonal (or orthorhombic) unit cell with dimensions  $a = b = 0.5073$  nm and  $c = 0.5260$  nm. The comparisons between observed and calculated  $d$  spacings are shown in Table II. Also shown in Table II are the calculated positions of reflections that overlapped with cubic peaks and reflections that were missing, but which if present would not overlap with cubic peaks. The optimum cell dimensions were obtained using a cell-fitting routine with observed reflections that did not overlap with cubic peaks. The cell-fitting routine was constrained to a unit cell with  $a = b$ , because none of the reflections that would split for  $a \neq b$  were observed to do so. Two further approaches were taken to determine whether a difference between  $a$  and  $b$  could be resolved. In one, Cr radiation was used to measure the (310)/(130) peak at higher resolution than with Cu radiation; a single peak was obtained and an upper bound for the difference between  $a$  and  $b$  was estimated to be 0.0005 nm. The second approach was to plot the peak half-widths (determined by fitting Pearson VII functions to the profiles) as a function of  $2\theta$ : peak broadening should exist for reflections of the type  $(hkl)$ ,  $(khl)$  if  $a \neq b$ , whereas reflections of the type  $(hhl)$  would not be broadened. However, a significant difference between the peak widths of these two types of reflections was not observed. This result also placed an upper bound of approximately 0.0005 nm on the difference between  $a$  and  $b$ .

The absence of any restrictions on the allowed non-zero  $(hkl)$  indicates that the lattice is primitive, with either tetragonal or orthorhombic space groups. The missing reflections of the type (odd, odd, zero) indicate the existence of a glide plane,  $a/2$ , and/or  $b/2$  on (001). However, a tetragonal space group would require both of these glide directions, which would restrict the allowed  $(hk0)$  reflections to those with both  $h$  and  $k$  even. Therefore, the existence of the (230)/(320) reflection eliminates a tetragonal space group. Analysis of the other allowed reflections (i.e., (011) and (013) present, (001) and (003) missing) indicates either a glide plane  $c/2$  on (100) with mirror plane (010), or a glide plane  $c/2$  on (010) with mirror plane (100). Therefore, the possible space groups relative to the above axes are  $Pmca$ ,  $Pcm$ ,  $Pcm$ , or  $Pmc$ . Rotation of the axes converts each of these to one of the standard forms  $Pbcm$  or  $Pbam$ . These two space groups cannot be distinguished using our data.

Close examination of the X-ray diffraction patterns revealed that the orthorhombic phase was present in the as-received mate-

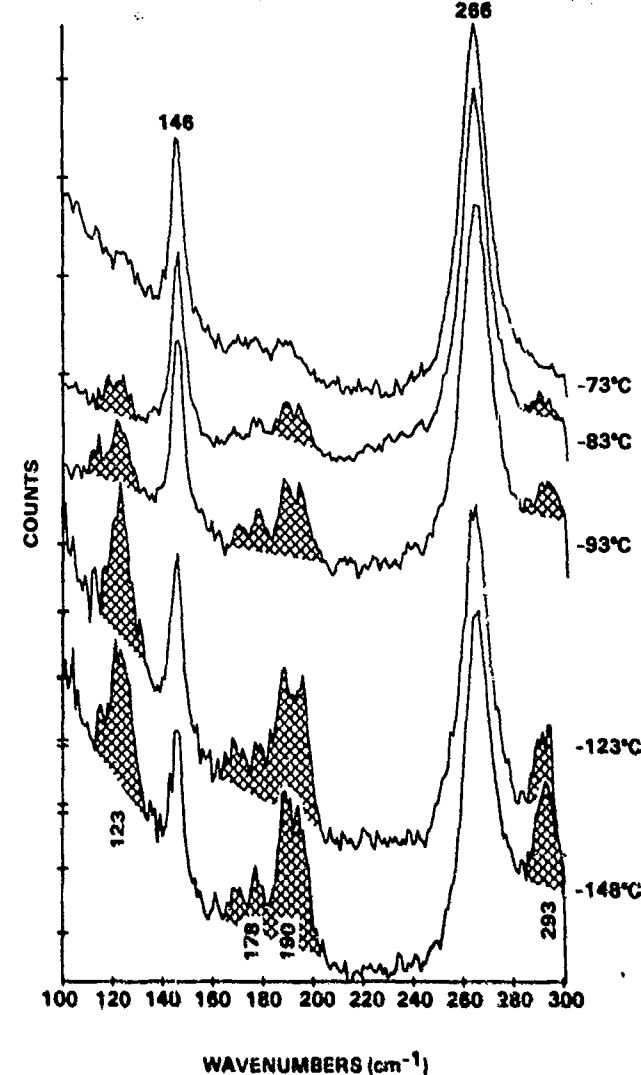


Fig. 4. In situ Raman spectra from high-toughness Mg-PSZ during cooling.

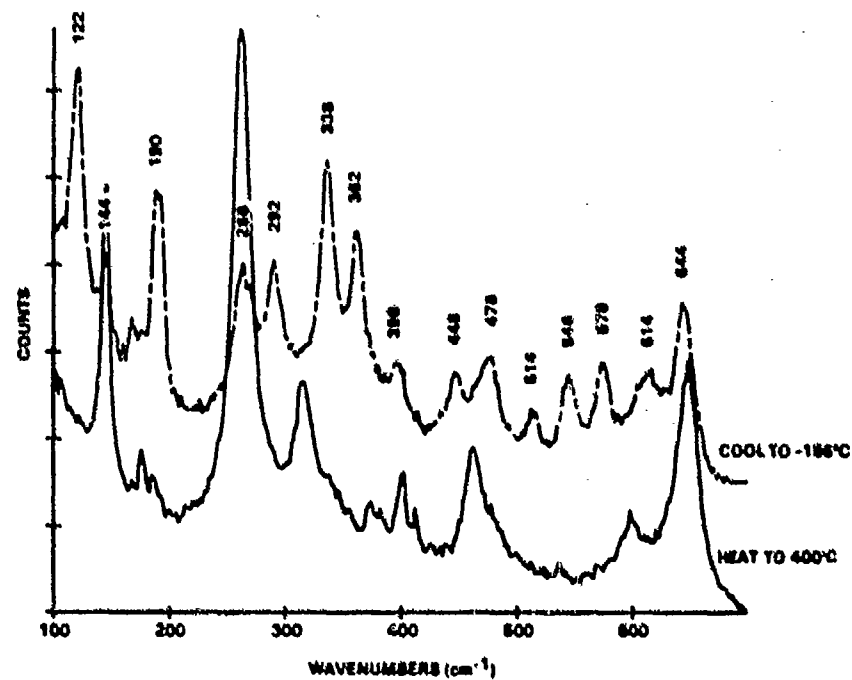


Fig. 5. Raman spectra from high-toughness Mg-PSZ after cooling to  $\sim 196^\circ\text{C}$ , then heating to  $400^\circ\text{C}$  and cooling to room temperature.

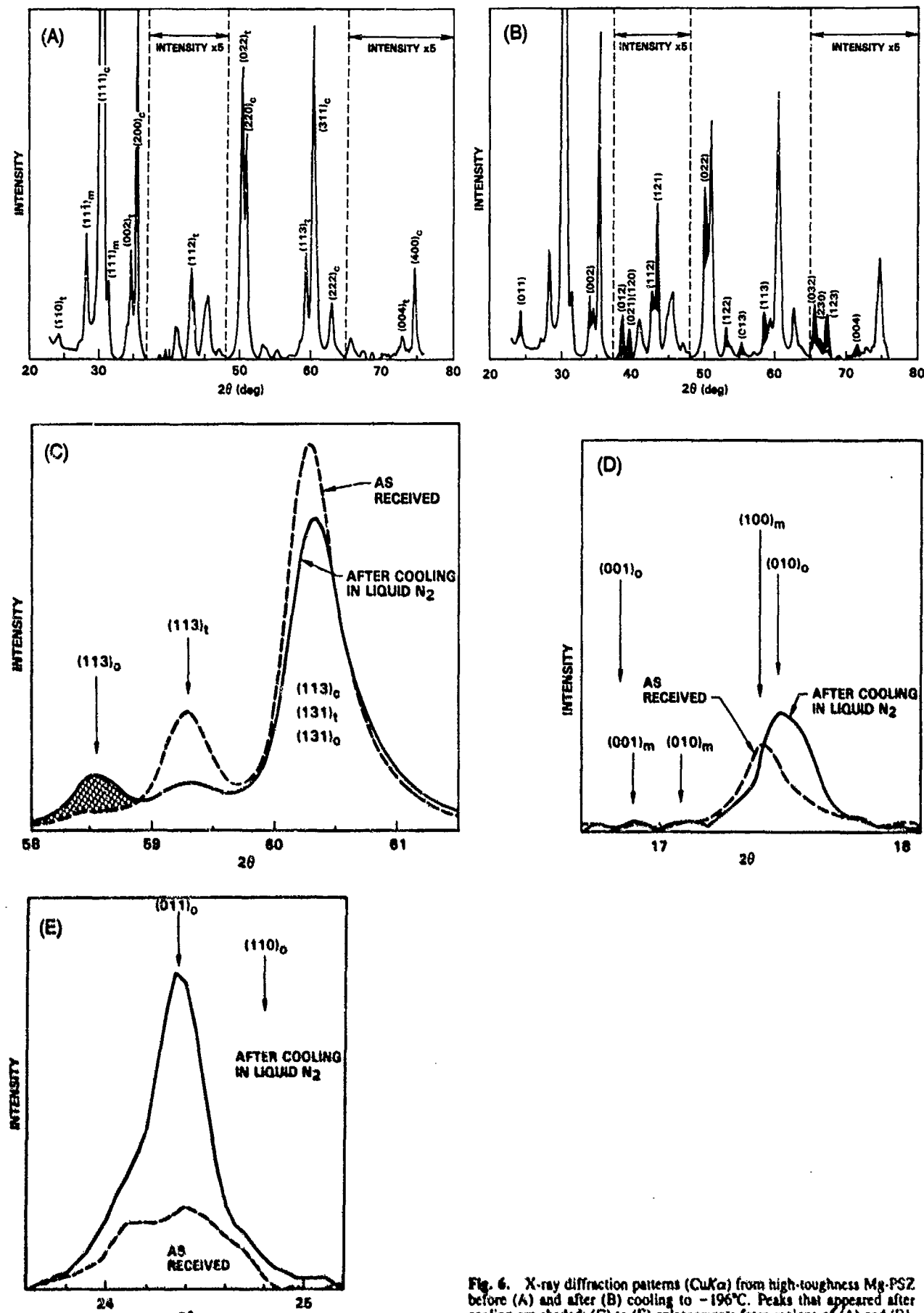


Fig. 6. X-ray diffraction patterns (CuK $\alpha$ ) from high-toughness Mg-PSZ before (A) and after (B) cooling to -196°C. Peaks that appeared after cooling are shaded: (C) to (E) enlargements from regions of (A) and (B).

rial in very small quantities which may normally go unnoticed. An enlargement of the region around the (113) peaks is shown in Fig. 6(C): peaks of similar relative size, just above the limit of detection, were identified in the as-received material for all of the other orthorhombic reflections. From the relative peak areas, the initial volume fraction of orthorhombic phase is estimated to be  $\leq 2\%$ . Similarly, the amount of residual tetragonal phase remaining after cooling in liquid  $N_2$  was estimated to be  $\sim 6$  vol%.

#### (4) Mechanical Properties

The steady-state fracture toughness of the high-toughness Mg-PSZ was recently measured<sup>16</sup> at  $-196^\circ C$  and found to be reduced from  $\sim 13 \text{ MPa} \cdot \text{m}^{1/2}$  at room temperature to  $\sim 7 \text{ MPa} \cdot \text{m}^{1/2}$ . This toughness is higher than that of the overaged material ( $3 \text{ MPa} \cdot \text{m}^{1/2}$ , Table I), indicating that, although the degree of transformation toughening was reduced at  $-196^\circ C$ , toughening was not completely eliminated. The steady-state toughness is similar to that of the low-toughness Mg-PSZ (Table I) that was not given the subeutectoid heat treatment.

(A) *Flexural Loading:* Flexural loading of the high-toughness Mg-PSZ after cooling to  $-196^\circ C$  and warming to room temperature resulted in a linear stress-strain curve to failure and a strength of 520 MPa. There was no permanent transformation or stable microcrack growth during loading, although in one experiment a microcrack  $\sim 50 \mu\text{m}$  in length initiated and was stable for  $\sim 2$  s at constant load before extending unstably. Postfailure examination of the surface that was stressed in tension revealed surface uplift, indicative of the presence of a transformation zone, around the crack that caused failure, and around several cracks that branched from the main one (Fig. 7(A)). However, the width of the transformation zone was substantially smaller ( $\sim 10 \mu\text{m}$ ) than in the specimen which had not been cooled to  $-196^\circ C$  ( $100 \mu\text{m}$ ). The transformation zone width was about the same as in the low-toughness Mg-PSZ that was not heat-treated at  $1100^\circ C$ , implying that the steady-state toughness is  $\sim 6 \text{ MPa} \cdot \text{m}^{1/2}$  and therefore similar to the toughness measured at  $-196^\circ C$ .

After heating to  $400^\circ C$  for 3 min, mechanical behavior that is characteristic of the high-toughness Mg-PSZ was restored. During loading, permanent transformation developed and stable microcracks grew to  $\sim 1 \text{ mm}$  before failure. The stress-strain curve was nonlinear, with the apparent flexural strength of 600 MPa and a true failure stress of 400 MPa.\* Stable microcracks and permanent trans-

\*For Mg-PSZ with nonlinear stress-strain response in tension, the stress-strain curve in compression is linear, with the result that the apparent flexural stress calculated from beam theory is larger than the actual stress on the tensile surface (Ref. 11).

Table II. Comparison of Observed and Calculated  $d$  Values for Orthorhombic  $\text{ZrO}_2$ ;  $a = b = 0.5073 \text{ nm}$ ,  $c = 0.5260 \text{ nm}$

$hkl^*$		$d$ (nm)	
Overlap with cubic reflections	Not overlapping with cubic reflections	Measured	Calculated
(111)	(011)	†	0.5260
	(010)	0.506	0.5073
	(011)	0.3654	0.3651
	(110)	†	0.3587
	(002)	0.2634	0.2630
	(020)	0.2536	0.2535
	(012)	0.2338	0.2335
	(021)	0.2285	0.2285
	(120)	0.227	0.2269
	(112)	0.2120	0.2121
(220)	(121)	0.2083	0.2083
	(023)	0.1824	0.1826
	(003)	†	0.1793
	(122)	0.1718	0.1718
	(221)	†	0.1697
	(030)	†	0.1691
	(013)	0.1657	0.1657
	(031)	†	0.1610
	(130)	†	0.1604
	(113)	0.1575	0.1575
(131)	(131)	0.1534	0.1534
	(222)	0.1482	0.1482
	(023)	†	0.1442
	(032)	0.1422	0.1422
	(230)	0.1407	0.1407
	(123)	0.1387	0.1387
	(132)	†	0.1369
	(231)	†	0.1359
	(004)	0.1314	0.1315
	(040)	0.1268	0.1268

\* $(hkl)$  is understood to mean  $(hkl)$  and/or  $(h\bar{k}\bar{l})$ . <sup>†</sup>Orthorhombic peak not detected but calculated position overlaps with monoclinic peaks. <sup>‡</sup>Peak not detected and calculated position does not overlap with any preexisting peaks in the as-received material.

formation, as well as a larger transformation zone around the main crack, are evident in the postfailure micrograph of Fig. 7(B).

(B) *Indentation Experiments:* Indentations (300-N Vickers) made in the high-toughness Mg-PSZ before and after cooling to  $-196^\circ C$  and after heating to  $400^\circ C$  are compared in Figs. 8(A) to (F). Cooling of the high-toughness material containing an inden-

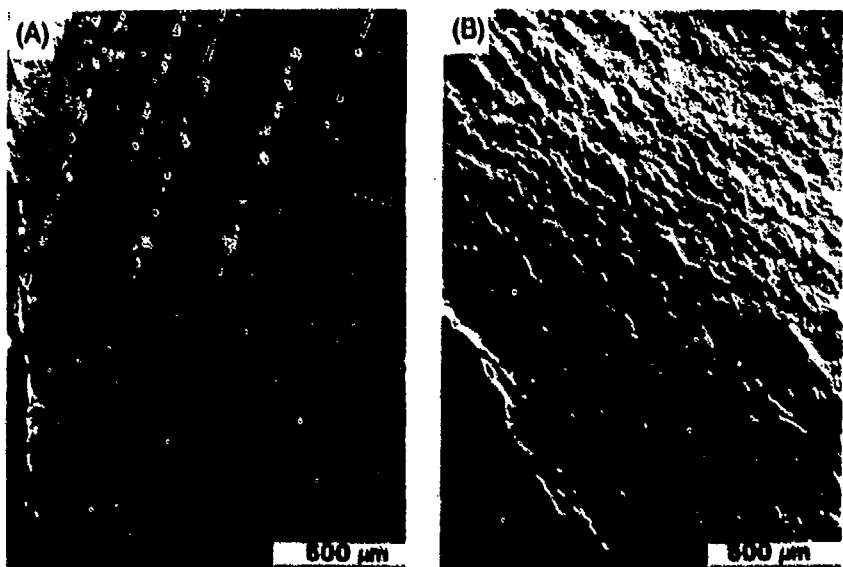


Fig. 7. Nomarski interference micrographs from tensile surfaces of bars of high-toughness Mg-PSZ that were broken in flexure: (A) after being cooled to  $-196^\circ C$ , warmed to room temperature, and polished; (B) after being cooled to  $-196^\circ C$ , heated to  $400^\circ C$  for 3 min, cooled to room temperature, and polished.

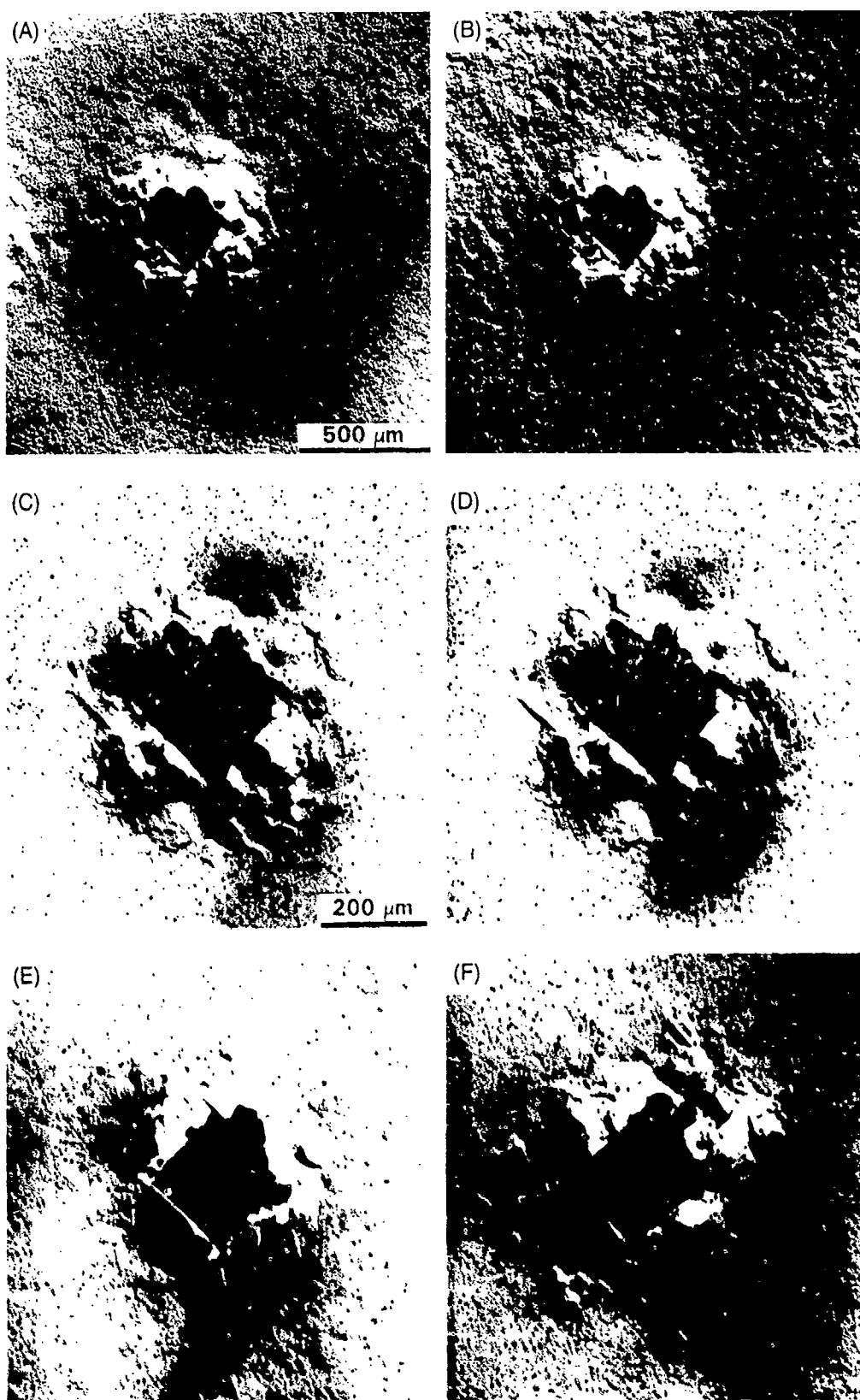


Fig. 8. Vickers indentations (300 N load) in high toughness Mg PSZ (Nomarski interference micrographs). (A) as received, surface polished before indentation, (B) same indentation as (A) after cooling to  $-196^{\circ}\text{C}$ , (C) higher magnification of (A) (note that contrast due to Nomarski interference is lower with the higher power objective lens), (D) higher magnification of (B), (E) indentation made in another area of the specimen used for (A) to (D), but after cooling to  $-196^{\circ}\text{C}$  and warming to room temperature, (F) indentation made after cooling to  $-196^{\circ}\text{C}$ , heating to  $400^{\circ}\text{C}$ , and cooling to room temperature.

Table III. Comparison of Lattice Parameters of Orthorhombic and Tetragonal Phases of Zirconia\*

	<i>a</i> (nm)	<i>b</i> (nm)	<i>c</i> (nm)
Low-temperature (Mg-PSZ) ortho	0.5073	0.5073	0.5260
TEM foil (Mg-PSZ) ortho <sup>†</sup>	0.5088	0.5071	0.5184
TEM foil (Mg-PSZ) ortho <sup>‡</sup>	0.508	0.508	0.518
High-pressure ( $ZrO_2$ and $Y_2O_3-ZrO_2$ ) ortho <sup>§</sup>	0.5042	0.5092	0.5257
Tetragonal Mg-PSZ	0.5080		0.5190

\*Note that in this table cell dimensions have been chosen with  $a < b < c$ . To express the space group of the orthorhombic phases in the standard form,  $Pbcm$ , it is necessary to rotate the axes so that  $b$  is the largest. <sup>†</sup>Data from Hannink.<sup>21</sup> <sup>‡</sup>Data from Heuer *et al.*<sup>22</sup> <sup>§</sup>Data from Suyama *et al.*<sup>23</sup>

tation (Fig. 8(B)) caused surface distortions as in Fig. 2(B) remote from the indentation, but did not change the surface distortions associated with the tetragonal-monoclinic transformation around the indentation (compare Figs. 8(C) and (D)). These surface distortions around the indentation are also much larger than those due to the tetragonal-orthorhombic transformation, consistent with the observations in Section III(1). Indentation after a cooling cycle to  $-196^\circ C$  and back to room temperature induced a much smaller area of tetragonal-monoclinic transformation (Fig. 8(E)), similar in size to that in the low-toughness Mg-PSZ.<sup>19</sup> Indentation after subsequent heating to  $400^\circ C$  and cooling to room temperature (Fig. 8(F)) resulted in a transformation zone similar in size to that in the original material. These results indicate that the propensity for stress-induced transformation decreases upon cooling to  $-196^\circ C$  and is restored by heating to  $400^\circ C$ , consistent with the results obtained in flexural loading.

#### IV. Discussion

The results of the previous section have directly linked the formation of an orthorhombic phase of  $ZrO_2$  to dramatic changes in mechanical properties of high-toughness Mg-PSZ. A single cooling cycle from room temperature to  $-100^\circ C$  results in transformation of tetragonal precipitates to the orthorhombic phase, with an accompanying reduction in fracture toughness and elimination of both nonlinear stress-strain response and *R*-curve behavior. However, the original high-toughness properties can be restored by a subsequent heating cycle to  $400^\circ C$ , which causes transformation of the orthorhombic back to the tetragonal structure.

Orthorhombic phases of  $ZrO_2$  have been observed by transmission electron microscopy (TEM) in thin foils of all of the transformation-toughened  $ZrO_2$  ceramics.<sup>21-23</sup> A high-pressure orthorhombic phase has also been observed in  $ZrO_2$ , both at high pressure<sup>24,25</sup> and at atmospheric pressure after quenching from high pressure and temperature<sup>26,27</sup> (although a high-pressure modified tetragonal structure has also been proposed<sup>28</sup>). In both the thin foil and high-pressure studies, the space group  $Pbcm$  was assigned; this is one of the two possible space groups for the present low-temperature orthorhombic phase. Moreover, there are some similarities (but also some significant differences) in the cell parameters (Table III); the *a* and *b* dimensions for the orthorhombic phase in thin foils of Mg-PSZ are close to the values for the low-temperature phase, but *c* is smaller, whereas the largest dimension for the high-pressure phase (*c* = 0.5257) is close to that of the low-temperature phase, but *a* and *b* differ. Raman spectra have also been obtained for the high-pressure phase, both at high pressure using a diamond anvil cell<sup>24,25</sup> and at atmospheric pressure in materials with quenched high-pressure phase.<sup>27</sup> These spectra differ from that of the low-temperature phase (Fig. 3). However, the total number of peaks is similar, consistent with the space group determinations.

The tetragonal-orthorhombic transformation in the present experiments is accompanied by an increase in unit-cell volume of 1.1% (unit-cell dimensions listed in Table III), which is about a quarter of the volume increase accompanying the tetragonal-monoclinic transformation. Combined with the measured volume fraction of transformation ( $\sim 30\%$ ), this implies a total volume change of 0.4% upon cooling the material through the phase transformation. This agrees well with the thermal expansion data of Swain,<sup>17</sup> who measured 0.13% linear expansion when cooling

similar material through the temperature range  $-70^\circ$  to  $-160^\circ C$ . It is also consistent with the magnitude of the surface distortion observed after cooling (Fig. 2). The surface distortions are associated with regions  $\sim 20 \mu m$  in diameter which were monoclinic phase and did not transform during cooling. A volume strain of 0.4% in a region of this size would correspond to linear expansion of 30 nm, which is reasonably close to the measured depression depth of  $\sim 50$  nm.

The present experiments are the first to have identified the formation of an orthorhombic phase in bulk material at atmospheric pressure. In the TEM foils, the transformation occurred at atmospheric pressure, but it was observed only in the thinnest regions (i.e., thickness  $<$  precipitate diameter), thus leading to the suggestion that it was an artifact of the special constraint configuration of the thin foil and the foil preparation techniques. In support of this suggestion, Muddle and Hannink<sup>23</sup> showed directly that ion beam thinning can induce the tetragonal-orthorhombic transformation. The transformation in the present experiments is believed to occur throughout the bulk rather than only at free surfaces for the following reasons: (1) the bulk volume change calculated above on the basis of the measured unit-cell parameters agrees with bulk expansion measurements; and (2) the penetration depths for the X-ray measurements were  $\sim 10 \mu m$ , and the amount of orthorhombic phase detected by Raman spectroscopy was the same using either high- or low-magnification lens systems that collect from depths of  $\sim 2$  and  $\sim 20 \mu m$ , respectively. For these depths, which are up to 2 orders of magnitude larger than the precipitate size, the effect of the free surface on the elastic strain energy associated with a transformation is negligible.

The stability of the orthorhombic phase determines its influence on mechanical properties of the ceramic. In both TEM foils and quenched high-pressure materials, the stress-induced orthorhombic-monoclinic transformation occurred readily (in the TEM foils by stresses caused by thermal cycling of adjacent regions with the electron beam,<sup>22,23</sup> and in the quenched material by grinding in a mortar<sup>26</sup>). In contrast, the low-temperature orthorhombic phase appears to be very resistant to stress-induced transformation to monoclinic structure, as reflected in the changes in room-temperature mechanical properties after cooling in liquid  $N_2$ . Moreover, the orthorhombic-monoclinic transformation could not be detected by Raman spectroscopy on surfaces that had been ground after the cooling cycle to  $-196^\circ C$ . Since the tetragonal phase in this material transforms very readily to the monoclinic structure, the formation of the orthorhombic phase cannot be an essential intermediate step in the tetragonal-monoclinic transformation.

There is, however, some indirect evidence to suggest that the orthorhombic-monoclinic transformation can occur at high stresses. After cooling in liquid  $N_2$ , the degree of toughening is reduced, but toughening is not eliminated altogether, and small transformation zones adjacent to cracks are evident. These zones could arise from transformation of either the orthorhombic precipitates or the small fraction of tetragonal precipitates that survive the cooling cycle. Since transformation during cooling occurs only in the two Mg-PSZ materials that exhibit high toughness, it may be argued that the precipitates that transform to the new phase during cooling are the same ones that are most easily transformed by stress, and which give rise to the large toughening. Raman measurements from regions adjacent to cracks in the high-toughness Mg-PSZ indicate that only some of the tetragonal precipitates (approximately half) transform to monoclinic structure. More

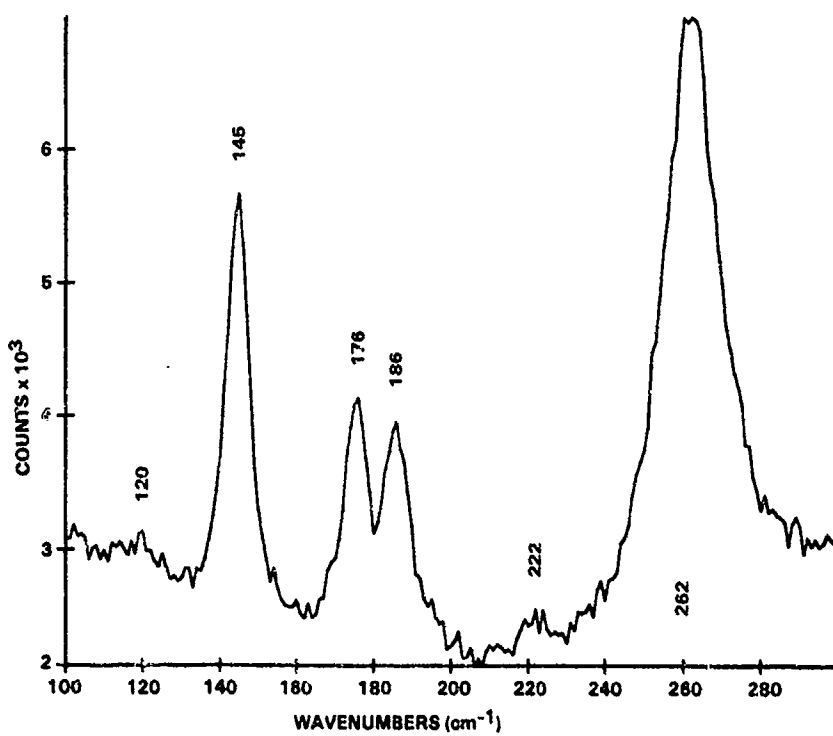


Fig. 9. Raman spectrum from region adjacent to crack in high-toughness Mg-PSZ.

over, the fraction of tetragonal phase remaining in the crack tip zone is larger than the fraction remaining after cooling to  $-196^{\circ}\text{C}$  (compare Figs. 3(B) and 9). These results imply that all of the tetragonal precipitates remaining after cooling should also remain untransformed in the crack tip zone and therefore that the crack tip transformation zone arises from the stress-induced orthorhombic-monoclinic transformation.

An attempt was made to identify the source of residual toughening after cooling to  $-196^{\circ}\text{C}$  by comparing Raman spectra from areas adjacent to, and remote from, the crack that caused failure in flexural loading (Fig. 10). An increase in the signal from the monoclinic phase is evident (shaded peaks), confirming that it is indeed transformation to the monoclinic phase that gives rise to the transformation zone. However, the sensitivity is not sufficiently

high to determine whether this transformation corresponded to a decrease in tetragonal or orthorhombic phase.

## V. Conclusions

A single cooling cycle for high-toughness Mg-PSZ to temperature below  $\sim -100^{\circ}\text{C}$  causes severe degradation of room-temperature mechanical properties. The fracture toughness is reduced from  $\sim 13$  to  $\sim 6 \text{ MPa} \cdot \text{m}^{1/2}$ , the tensile stress-strain response becomes linear up to failure instead of being nonlinear, and the *R*-curve characteristic of high-toughness Mg-PSZ is lost. However, the original high-toughness properties are restored by heating to  $400^{\circ}\text{C}$ .

The degradation in mechanical properties coincides with the

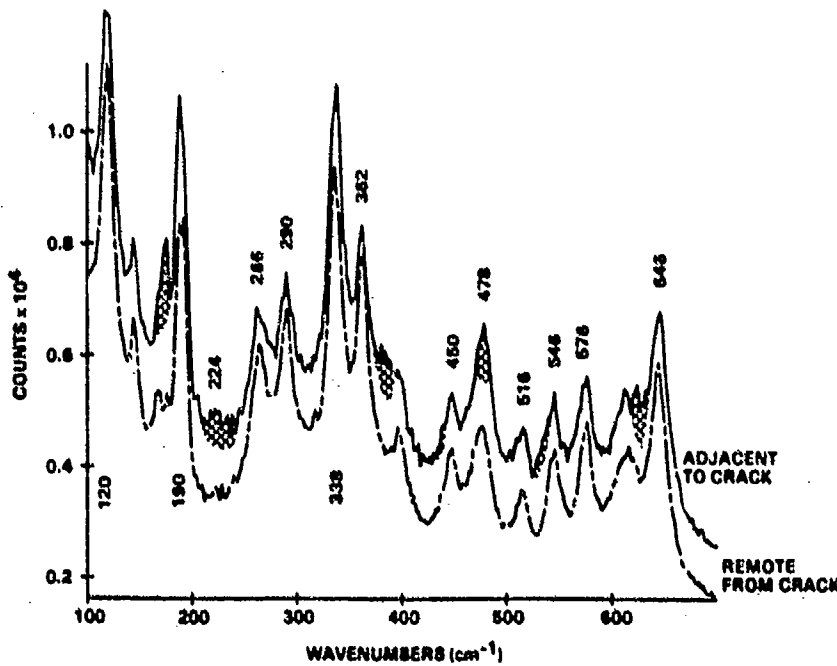


Fig. 10. Raman spectra from regions adjacent to and remote from the crack in Fig. 7(A) (high-toughness Mg-PSZ cooled to  $\sim -196^{\circ}\text{C}$ , polished, then broken in flexure). Shaded areas represent monoclinic peaks from area adjacent to crack.

transformation of most of the tetragonal precipitates to an orthorhombic phase with unit-cell volume between those of the tetragonal and monoclinic phases. The orthorhombic phase is stable upon heating to at least 300°C, but at 400°C (for 3 min), it transforms back to the tetragonal structure. Traces of the orthorhombic phase were also detected in the as-received material that had not been cooled below room temperature.

**Acknowledgments:** Some of the materials studied were kindly supplied by M. V. Swain. The authors are grateful to P. E. D. Morgan for use of a cell-fitting routine to optimize the cell dimensions, and to K. T. Miller for collecting some of the in situ Raman data.

## References

- 1 R. S. Garvie, R. H. J. Hannink, and R. T. Pascoe, "Ceramic Steel?," *Nature (London)*, **258** [5537] 703-704 (1975).
- 2 D. L. Porter and A. H. Heuer, "Mechanisms of Toughening Partially Stabilized Zirconia," *J. Am. Ceram. Soc.*, **60** [3-4] 183-84 (1977).
- 3 F. F. Lange, "Transformation Toughening: Part 5. Effect of Temperature and Alloy on Fracture Toughness," *J. Mater. Sci.*, **17**, 255-63 (1982).
- 4 F. F. Lange, "Transformation Toughening: Part 4. Fabrication, Fracture Toughness and Strength of  $\text{Al}_2\text{O}_3$ - $\text{ZrO}_2$  Composites," *J. Mater. Sci.*, **17**, 247-54 (1982).
- 5 N. Claussen and M. Rühle, "Design of Transformation-Toughened Ceramics"; pp. 137-63 in *Advances in Ceramics*, Vol. 3, *Science and Technology of Zirconia*. Edited by A. H. Heuer and L. W. Hobbs. American Ceramic Society, Columbus, OH, 1981.
- 6 M. V. Swain, R. H. J. Hannink, and R. C. Garvie; pp. 339-54 in *Fracture Mechanics of Ceramics*, Vol. 6. Edited by R. C. Bradt, A. G. Evans, D. P. H. Hasselman, and F. F. Lange. Plenum Press, New York, 1983.
- 7 R. H. J. Hannink, "Growth Morphology of the Tetragonal Phase in Partially Stabilized Zirconia," *J. Mater. Sci.*, **13**, 2487-96 (1978).
- 8 R. H. J. Hannink, K. A. Johnston, R. T. Pascoe, and R. C. Garvie, "Microstructural Changes During Isothermal Aging of a Calcia Partially Stabilized Zirconia Alloy"; pp. 116-36 in *Advances in Ceramics*, Vol. 3, *Science and Technology of Zirconia*. Edited by A. H. Heuer and L. W. Hobbs. American Ceramic Society, Columbus, OH, 1981.
- 9 M. V. Swain and R. H. J. Hannink, "R-Curve Behavior in Zirconia Ceramics"; pp. 225-39 in *Advances in Ceramics*, Vol. 12, *Science and Technology of Zirconia II*. Edited by N. Claussen, M. Rühle, and A. H. Heuer. American Ceramic Society, Columbus, OH, 1984.
- 10 M. V. Swain, "Inelastic Deformation of Mg-PSZ and Its Significance for Strength-Toughness Relationships of Zirconia Toughened Ceramics," *Acta Metall.*, **33** [11] 2083-91 (1985).
- 11 D. B. Marshall, "Strength Characteristics of Transformation-Toughened Zirconia," *J. Am. Ceram. Soc.*, **69** [3] 173-80 (1986).
- 12 R. H. J. Hannink and M. V. Swain, "Magnesia-Partially Stabilized Zirconia: The Influence of Heat Treatment on Thermomechanical Properties," *J. Aust. Ceram. Soc.*, **18** [2] 53-62 (1982).
- 13 M. J. Ready and A. H. Heuer, "Crack Development in Transformation-Toughened Mg-PSZ"; pp. 107-20 in *Advanced Structural Ceramics*, MRS Symposium Proceedings. Edited by P. F. Becher, M. V. Swain, and S. Sōmiya. Materials Research Society, Pittsburgh, PA, 1987.
- 14 M. J. Ready and A. H. Heuer, "On the Annealing of Test Specimens of High Toughness Mg-PSZ," *J. Am. Ceram. Soc.*, **71** [1] C-2-C-6 (1988).
- 15 A. H. Heuer, M. J. Ready, and R. Steinbrech, "Resistance Curve Behavior of Supertough MgO-Partially Stabilized  $\text{ZrO}_2$  (Mg-PSZ)"; to be published in *J. Mater. Sci.*
- 16 S. Veitch, M. Marmach, and M. V. Swain, "Strength and Toughness of Mg-PSZ and Y-TZP Materials at Cryogenic Temperatures"; pp. 97-106 in *Advanced Structural Ceramics*, MRS Symposium Proceedings. Edited by P. F. Becher, M. V. Swain, and S. Sōmiya. Materials Research Society, Pittsburgh, PA, 1987.
- 17 M. V. Swain; private communication.
- 18 J. A. Excell and M. Marmach, "Reversible Cryogenically Induced Tetragonal to Monoclinic Phase Transformation in Mg-PSZ," *J. Am. Ceram. Soc. Bull.*, **65** [10] 1404-407 (1986).
- 19 D. B. Marshall and M. V. Swain, "Crack Resistance Curves in Magnesia-Partially-Stabilized Zirconia," *J. Am. Ceram. Soc.*, **71** [6] 379-407 (1988).
- 20 R. R. Hughan and R. H. J. Hannink, "Precipitation During Controlled Cooling of Magnesia-Partially-Stabilized Zirconia," *J. Am. Ceram. Soc.*, **69** [7] 556-63 (1986).
- 21 A. H. Heuer, L. H. Schoenlein, and S. Farmer, "New Microstructural Features in Magnesia-Partially-Stabilized Zirconia (Mg-PSZ)"; pp. 257-66 in *Science of Ceramics 12*. Edited by P. Vincenzini. Cermurgica, Imola, Italy, 1984.
- 22 A. H. Heuer, V. Lauteri, S. C. Farmer, R. Chaim, R.-R. Lee, B. W. Kibble, and R. M. Dickerson, "On the Orthorhombic Phase in  $\text{ZrO}_2$ -Based Alloys"; to be published in *J. Mater. Sci.*
- 23 B. C. Muddli and R. H. J. Hannink, "Phase Transformation Involving an Orthorhombic Phase in MgO-PSZ"; pp. 89-102 in *Science and Technology of Zirconia III*. Edited by S. Sōmiya, N. Yamamoto, and H. Yanagida. American Ceramic Society, Westerville, OH, 1988.
- 24 A. Arashi and M. Ishigame, "Raman Spectroscopic Studies of the Polymorphism in  $\text{ZrO}_2$  at High Pressures," *Phys. Status Solidi A*, **71**, 313-21 (1952).
- 25 Y. Kudo, H. Takeda, and H. Arashi, "In-Situ Determination of Crystal Structure for High Pressure Phase of  $\text{ZrO}_2$  using a Diamond Anvil and Single Crystal X-Ray Diffraction Method," *Phys. Chem. Mineral.*, **3**, 233-37 (1986).
- 26 R. Suyama, T. Ashida, and S. Kume, "Synthesis of the Orthorhombic Phase of  $\text{ZrO}_2$ ," *J. Am. Ceram. Soc.*, **68** [12] C-314-C-315 (1985).
- 27 O. Ohtaka, S. Kume, T. Awami, and K. Urabe, "Synthesis of Orthorhombic Phase of  $2\text{Y}\cdot\text{ZrO}_2$ ," *J. Am. Ceram. Soc.*, **71** [3] C-164-C-166 (1988).
- 28 B. Alzyab, C. H. Perry, and R. P. Ingel, "High Pressure Phase Transitions in Zirconia and Yttria-Doped Zirconia," *J. Am. Ceram. Soc.*, **70** [10] 760-65 (1987). □